Journal of
Mechanics of Materials and Structures

JOURNAL OF MECHANICS OF MATERIALS AND STRUCTURES

http://www.jomms.org

Founded by Charles R. Steele and Marie-Louise Steele

THIRD-ORDER SHEAR DEFORMATION THEORY FOR STRESS ANALYSIS OF A THICK CONICAL SHELL UNDER PRESSURE

HAMID REZA EIPAKCHI

The stresses and displacements of a thick conical shell with varying thickness under nonuniform internal pressure have been calculated analytically using third-order shear deformation theory. The governing equations, which are a system of differential equations with variable coefficients, have been solved analytically with the matched asymptotic expansion of the perturbation theory. The effects of higher-order approximations on the radial and axial displacements, von Mises stress, and shear stress have been studied. The results have been compared with the finite elements analysis.

1. Introduction

Shear deformation theory is a popular model in structural analysis. The displacement field is assumed as a polynomial of the thickness variable (z), which results in a system of differential equations without parameter z. By increasing the number of terms in the polynomial functions, it is possible to improve the approximate solution. Obviously, this leads to systems of differential equations which are more complex. The general form for displacement components in shear deformation theory is $U(x, y, z) = \sum_{i=0}^{n} u_i(x, y) z^i$ where $U(x, y, z)$ is the displacement component and $u_i(x, y)$ are unknown functions of the coordinates. For $i = 1$, one obtains first-order shear deformation theory (FSDT); $i = 2$ corresponds to second-order shear deformation theory (SSDT), and $i = 3$ gives third-order shear deformation theory (TSDT).

Although higher-order shear deformation theories can be used in the analysis of conical shells as well, most reported studies in this field are based on the classical theory of shells or the three-dimensional theory of elasticity and the governing equations have been solved numerically. Sundarasivarao and Ganesan [1991] analyzed a conical shell subjected to uniform internal pressure and various boundary conditions to find an optimum thickness variation by the finite element (FE) method. Sivadas and Ganesan [1991] studied the effects of thickness variation on the natural frequencies of laminated conical shells using a semianalytical FE method and Love's first approximation thin shell theory.

Panferov [1992] used the method of successive approximations and a perturbation of the shape of the boundary to determine the stress state of thick-walled conical isotropic shells with constant thickness subjected to thermal loading. Thambiratnam and Zhuge [1993] presented a simple FE method for the axisymmetric free vibration analysis of conical shells with uniform or varying wall thickness. Tong [1994] extracted equilibrium equations for the free vibration of composite laminated conical shells including transverse shear deformation and extension-bending coupling using a particularly convenient coordinate system. The solutions for the governing equations are in the form of a power series. Tavares [1996]

determined the stresses, strains, and displacements of a thin conical shell with constant thickness and axisymmetric load by the construction of a Green's function for the homogeneous differential equation based on bending theory. Buchanan and Wong [2001] employed FE analysis to study the vibration of truncated thick hollow cones, using three-dimensional strain-displacement equations in a conical coordinate system.

Cui et al. [2001] introduced a new variable transformation to solve the basic governing differential equations for conical shells. By neglecting quantities with order of magnitude of h/R, the authors transformed the basic governing differential equations for conical shells into a second-order differential equation with complex coefficients. This equation has an accurate solution which is simpler than the exact solution because it does not use Bessel functions. Wu and Chiu [2002] investigated thermally induced dynamic instability of laminated composite conical shells subjected to static and periodic thermal loads by means of the multiple scales method of perturbation theory. Correia et al. [2003] presented a numerical method for the structural analysis of laminated conical shell panels using a quadrilateral isoparametric FE based on higher-order shear deformation theory. The displacement expressions used for the longitudinal and circumferential components of the displacement field were given by power series and a condition of zero stress on the top and bottom surfaces of the shell was imposed.

Garg et al. [2006] presented a FE model based on a TSDT for free vibration analysis of laminates. He concluded that applying the shear correction factor is not necessary. Ramesh et al. [2008] derived a triangular plate element based on higher-order shear deformation theory with superior performance through bending analysis of plates and examining the distribution of the stress resultants.

In this paper, displacements and stresses of a thick conical shell with varying thickness subjected to nonuniform internal pressure have been calculated using a TSDT for the homogeneous, isotropic, and axisymmetric cases. The governing equations, which are a system of differential equations with variable coefficients, have been solved analytically using the matched asymptotic expansion (MAE) of perturbation theory. The effects of different shear deformation theories on the displacements, von Mises stress, and shear stress have been studied. The results have been compared with FE analysis.

2. Governing equations

The coordinates of a point on the longitudinal section of a conical shell can be defined by the two parameters r and x, where x is the vertical coordinate, and r is the radius, which is perpendicular to x and satisfies $r = R(x) + z$. $R(x)$ is the middle surface radius, and z is the thickness variable, which is measured from the middle surface (see Figure 1). The displacement field in the axisymmetric case, based on TSDT, is assumed as

$$
\begin{aligned}
U_x(x, z) &= U_{x3} = u_0(x) + zu_1(x) + z^2 u_2(x) + z^3 u_3(x), \\
U_z(x, z) &= U_{z3} = w_0(x) + zw_1(x) + z^2 w_2(x) + z^3 w_3(x).
\end{aligned}
\tag{1}
$$

U_x and U_z are the approximate axial and radial displacements, respectively, and u_0, u_1, u_2, u_3, w_0, w_1, w_2, and w_3 are the unknown functions of x. According to (1), the displacements vary cubically with respect to z and a cross section remains neither straight nor normal to the middle surface. The small-strain components are

$$e_x = \frac{dU_x}{dx} = \frac{du_0}{dx} + z\frac{du_1}{dx} + z^2\frac{du_2}{dx} + z^3\frac{du_3}{dx},$$

$$e_z = \frac{dU_z}{dz} = w_1 + 2zw_2 + 3z^2w_3,$$

$$e_\theta = \frac{U_z}{r} = \frac{w_0 + zw_1 + z^2w_2 + z^3w_3}{R + z},$$

$$\gamma_{xz} = \frac{dU_x}{dz} + \frac{dU_z}{dx} = u_1 + \frac{dw_0}{dx} + z\left(2u_2 + \frac{dw_1}{dx}\right) + z^2\left(3u_3 + \frac{dw_2}{dx}\right) + z^3\frac{dw_3}{dx}.$$

$$(2)$$

For an isotropic, homogeneous, linear elastic material, the stress-strain relations are

$$\sigma_x = Ae_x + \lambda(e_\theta + e_z), \qquad \sigma_z = Ae_z + \lambda(e_\theta + e_x),$$

$$\sigma_\theta = Ae_\theta + \lambda(e_x + e_z), \qquad \sigma_{xz} = \mu\gamma_{xz}.$$

$$(3)$$

Here λ and μ are the Lamé's constants and $A = \lambda + 2\mu$. The governing equations can be derived using the principal of virtual work which states that $\delta U = \delta W$. U is the strain energy and W is the external work. The variation of the strain energy for an axisymmetric elastic body is

$$\delta U = \int_V (\sigma_{xx}\delta e_x + \sigma_{\theta\theta}\delta e_{\theta\theta} + \sigma_{zz}\delta e_{zz} + \sigma_{xz}\delta\gamma_{xz})\,dV, \tag{4}$$

where V is the shell volume, $dV = r\,d\theta\,dx\,dz$, $0 \le \theta \le 2\pi$, $-h/2 \le z \le h/2$, and $0 \le x \le L$, with L the shell length and h the thickness. The external work variation due to internal pressure is

$$\delta W = \iint_S (f_x\delta U_x + f_z\delta U_z)\,ds. \tag{5}$$

ds is a surface element and f_x and f_z are the vertical and horizontal components of the pressure. After substituting (1)–(5) into the principal of virtual work and considering the coefficients of δu_0, δu_1, δu_2,
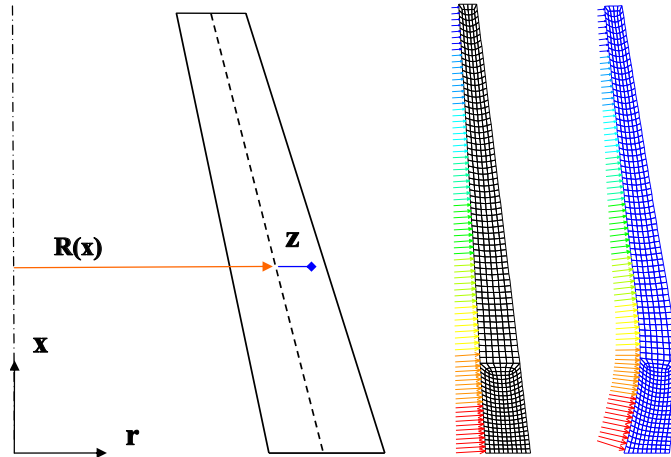
Figure 1. Shell geometry (left), loading (center), and deformation (right).

δu_3, δw_0, δw_1, δw_2, and δw_3, the results are

$$\frac{d}{dx}(RN_x) + RF_{x_0} = 0, \qquad\qquad \frac{d}{dx}(RQ_x) - N_\theta + RF_{z_0} = 0,$$

$$\frac{d}{dx}(RM_x) - RQ_x + RF_{x_1} = 0, \qquad \frac{d}{dx}(RM_{xz}) - (M_\theta + RN_z) + RF_{z_1} = 0,$$

$$\frac{d}{dx}(RP_x) - 2RM_{xz} + RF_{x_2} = 0, \qquad \frac{d}{dx}(RP_{xz}) - (P_\theta + 2RM_z) + RF_{z_2} = 0, \tag{6}$$

$$\frac{d}{dx}(RS_x) - 3RP_{xz} + RF_{x_3} = 0, \qquad \frac{d}{dx}(RS_{xz}) - (S_\theta + 3RP_z) + RF_{z_3} = 0,$$

where $F_{x_n} = f_x z^n \left(1 + \frac{z}{R}\right)\Big|_{z=\pm\frac{h}{2}}$ and $F_{z_n} = f_z z^n \left(1 + \frac{z}{R}\right)\Big|_{z=\pm\frac{h}{2}}$ for $n = 0, 1, 2, 3$, and the boundary conditions are

$$\left[R(N_x \delta u_0 + M_x \delta u_1 + P_x \delta u_2 + S_x \delta u_3 + Q_x \delta w_0 + M_{xz} \delta w_1 + P_{xz} \delta w_2 + S_{xz} \delta w_3)\right]_{x=0}^{L} = 0. \tag{7}$$

The first equation in (6) can be rewritten as $RN_x + \int RF_{x_0}dx + C_0 = 0$, and likewise the others.

The stress resultants are

$$N_x = \int_{-h/2}^{h/2} \sigma_x \left(1 + \frac{z}{R}\right) dz$$
$$= Ah\frac{du_0}{dx} + \frac{Ah^3}{12R}\frac{du_1}{dx} + \frac{Ah^3}{12}\frac{du_2}{dx} + \frac{Ah^5}{80R}\frac{du_3}{dx} + \frac{\lambda h}{R}w_0 + \lambda h w_1 + \frac{3\lambda h^3}{12R}w_2 + \frac{3\lambda h^3}{12}w_3,$$

$$M_x = \int_{-h/2}^{h/2} \sigma_x z \left(1 + \frac{z}{R}\right) dz$$
$$= \frac{Ah^3}{12R}\frac{du_0}{dx} + \frac{Ah^3}{12}\frac{du_1}{dx} + \frac{Ah^5}{80R}\frac{du_2}{dx} + \frac{Ah^5}{80}\frac{du_3}{dx} + \frac{2\lambda h^3}{12R}w_1 + \frac{2\lambda h^3}{12}w_2 + \frac{4\lambda h^5}{80R}w_3,$$

$$P_x = \int_{-h/2}^{h/2} \sigma_x z^2 \left(1 + \frac{z}{R}\right) dz$$
$$= \frac{Ah^3}{12}\frac{du_0}{dx} + \frac{Ah^5}{80R}\frac{du_1}{dx} + \frac{Ah^5}{80}\frac{du_2}{dx} + \frac{Ah^7}{448R}\frac{du_3}{dx} + \frac{\lambda h^3}{12R}w_0 + \frac{\lambda h^3}{12}w_1 + \frac{3\lambda h^5}{80R}w_2 + \frac{3\lambda h^5}{80}w_3,$$

$$S_x = \int_{-h/2}^{h/2} \sigma_x z^3 \left(1 + \frac{z}{R}\right) dz$$
$$= \frac{Ah^5}{80R}\frac{du_0}{dx} + \frac{Ah^5}{80}\frac{du_1}{dx} + \frac{Ah^7}{448R}\frac{du_2}{dx} + \frac{Ah^7}{448}\frac{du_3}{dx} + \frac{2\lambda h^5}{80R}w_1 + \frac{2\lambda h^5}{80}w_2 + \frac{4\lambda h^7}{448R}w_3,$$

$$N_\theta = \int_{-h/2}^{h/2} \sigma_\theta \, dz = A\alpha_0 w_0 + A\alpha_1 w_1 + \lambda h w_1 + A\alpha_2 w_2 + A\alpha_3 w_3 + \frac{3\lambda h^3}{12}w_3 + \lambda h\frac{du_0}{dx} + \frac{\lambda h^3}{12}\frac{du_2}{dx},$$

$$M_\theta = \int_{-h/2}^{h/2} \sigma_\theta z \, dz = A\alpha_1 w_0 + A\alpha_2 w_1 + A\alpha_3 w_2 + A\alpha_4 w_3 + \frac{2\lambda h^3}{12}w_2 + \frac{\lambda h^3}{12}\frac{du_1}{dx} + \frac{\lambda h^5}{80}\frac{du_3}{dx},$$

$$P_\theta = \int_{-h/2}^{h/2} \sigma_\theta z^2 \, dz = A\alpha_2 w_0 + A\alpha_3 w_1 + A\alpha_4 w_2 + A\alpha_5 w_3 + \frac{\lambda h^3}{12}w_1 + \frac{3\lambda h^5}{80}w_3 + \frac{\lambda h^3}{12}\frac{du_0}{dx} + \frac{\lambda h^5}{80}\frac{du_2}{dx},$$

$$S_\theta = \int_{-h/2}^{h/2} \sigma_\theta z^3 \, dz = A\alpha_3 w_0 + A\alpha_4 w_1 + A\alpha_5 w_2 + A\alpha_6 w_3 + \frac{2\lambda h^5}{80}w_2 + \frac{\lambda h^5}{80}\frac{du_1}{dx} + \frac{\lambda h^7}{488}\frac{du_3}{dx},$$

$$N_z = \int_{-h/2}^{h/2} \sigma_z \left(1 + \frac{z}{R}\right) dz$$
$$= \frac{\lambda h}{R} w_0 + Ah w_1 + \frac{(2A+\lambda)h^3}{12R} w_2 + \frac{3Ah^3}{12} w_3 + \lambda h \frac{du_0}{dx} + \frac{\lambda h^3}{12R} \frac{du_1}{dx} + \frac{\lambda h^3}{12} \frac{du_2}{dx},$$

$$M_z = \int_{-h/2}^{h/2} \sigma_z z \left(1 + \frac{z}{R}\right) dz$$
$$= \frac{(A+\lambda)h^3}{12R} w_1 + \frac{2Ah^3}{12} w_2 + \frac{(3A+\lambda)h^5}{80R} w_3 + \frac{\lambda h^3}{12R} \frac{du_0}{dx} + \frac{\lambda h^3}{12} \frac{du_1}{dx} + \frac{\lambda h^5}{80R} \frac{du_2}{dx} + \frac{\lambda h^5}{80} \frac{du_3}{dx},$$

$$P_z = \int_{-h/2}^{h/2} \sigma_z z^2 \left(1 + \frac{z}{R}\right) dz$$
$$= \frac{\lambda h^3}{12R} w_0 + \frac{Ah^3}{12} w_1 + \frac{(2A+\lambda)h^5}{80R} w_2 + \frac{3Ah^5}{80} w_3 + \frac{\lambda h^3}{12} \frac{du_0}{dx} + \frac{\lambda h^5}{80R} \frac{du_1}{dx} + \frac{\lambda h^5}{80} \frac{du_2}{dx} + \frac{\lambda h^7}{448R} \frac{du_3}{dx},$$

$$Q_x = \int_{-h/2}^{h/2} \sigma_{xz} \left(1 + \frac{z}{R}\right) dz$$
$$= \mu \left\{ hu_1 + \frac{2h^3}{12R} u_2 + \frac{3h^3}{12} u_3 + h \frac{dw_0}{dx} + \frac{h^3}{12R} \frac{dw_1}{dx} + \frac{h^3}{12} \frac{dw_2}{dx} + \frac{h^5}{80R} \frac{dw_3}{dx} \right\},$$

$$M_{xz} = \int_{-h/2}^{h/2} \sigma_{xz} z \left(1 + \frac{z}{R}\right) dz$$
$$= \mu \left\{ \frac{h^3}{12R} u_1 + \frac{2h^3}{12} u_2 + \frac{3h^5}{80R} u_3 + \frac{h^3}{12R} \frac{dw_0}{dx} + \frac{h^3}{12} \frac{dw_1}{dx} + \frac{h^5}{80R} \frac{dw_2}{dx} + \frac{h^5}{80} \frac{dw_3}{dx} \right\},$$

$$P_{xz} = \int_{-h/2}^{h/2} \sigma_{xz} z^2 \left(1 + \frac{z}{R}\right) dz$$
$$= \mu \left\{ \frac{h^3}{12} u_1 + \frac{2h^5}{80R} u_2 + \frac{3h^5}{80} u_3 + \frac{h^3}{12} \frac{dw_0}{dx} + \frac{h^5}{80R} \frac{dw_1}{dx} + \frac{h^5}{80} \frac{dw_2}{dx} + \frac{h^7}{448R} \frac{dw_3}{dx} \right\},$$

$$S_{xz} = \int_{-h/2}^{h/2} \sigma_{xz} z^3 \left(1 + \frac{z}{R}\right) dz$$
$$= \mu \left\{ \frac{h^5}{80R} u_1 + \frac{2h^5}{80} u_2 + \frac{3h^7}{448R} u_3 + \frac{h^5}{80R} \frac{dw_0}{dx} + \frac{h^5}{80} \frac{dw_1}{dx} + \frac{h^7}{448R} \frac{dw_2}{dx} + \frac{h^7}{448} \frac{dw_3}{dx} \right\}. \tag{8}$$

By assuming $v = du_0/dx$ and using (6) and (8), we derive the governing equations in terms of the displacement parameters:

$$\frac{d}{dx}\left([A_1]\frac{d\{Y\}}{dx}\right) + \frac{d}{dx}\left([A_2]\{Y\}\right) + [A_3]\frac{d\{Y\}}{dx} + [A_4]\{Y\} + \{F_p\} = \{0\}_{8\times1}, \tag{9a}$$

where

$$\{F_p\} = \{RF_{x_0} + C_0, RF_{x_1}, RF_{x_2}, RF_{x_3}, RF_{z_0}, RF_{z_1}, RF_{z_2}, RF_{z_3}\}^T,$$

$$A_1 = \begin{bmatrix} [A_{11}]_{4*4} & [0]_{4*4} \\ [0]_{4*4} & \theta_2[A_{14}]_{4*4} \end{bmatrix}, \qquad A_2 = \begin{bmatrix} [0]_{4*4} & \theta_1[A_{22}]_{4*4} \\ \theta_2[A_{23}]_{4*4} & [0]_{4*4} \end{bmatrix},$$

$$A_3 = \begin{bmatrix} [A_{31}]_{4*4} & -\theta_2[A_{32}]_{4*4} \\ -\theta_1[A_{33}]_{4*4} & [0]_{4*4} \end{bmatrix}, \qquad A_4 = \begin{bmatrix} -\theta_2[A_{41}]_{4*4} & \theta_1[A_{42}]_{4*4} \\ -\theta_1[A_{42}]_{4*4}^T & -[A_{44}]_{4*4} \end{bmatrix},$$

$$[A_{11}]_{4*4} = \begin{bmatrix} 0 & 0 & 0 & 0 \\ 0 & \dfrac{Rh^3}{12} & \dfrac{h^5}{80} & \dfrac{Rh^5}{80} \\ 0 & \dfrac{h^5}{80} & \dfrac{Rh^5}{80} & \dfrac{h^7}{448} \\ 0 & \dfrac{Rh^5}{80} & \dfrac{h^7}{448} & \dfrac{Rh^7}{448} \end{bmatrix}, \qquad [A_{14}]_{4*4} = \begin{bmatrix} Rh & \dfrac{h^3}{12} & \dfrac{Rh^3}{12} & \dfrac{h^5}{80} \\ \dfrac{h^3}{12} & \dfrac{Rh^3}{12} & \dfrac{h^5}{80} & \dfrac{Rh^5}{80} \\ \dfrac{Rh^3}{12} & \dfrac{h^5}{80} & \dfrac{Rh^5}{80} & \dfrac{h^7}{448} \\ \dfrac{h^5}{80} & \dfrac{Rh^5}{80} & \dfrac{h^7}{448} & \dfrac{Rh^7}{448} \end{bmatrix},$$

$$[A_{22}]_{4*4} = \begin{bmatrix} 0 & 0 & 0 & 0 \\ 0 & \dfrac{2h^3}{12} & \dfrac{2Rh^3}{12} & \dfrac{4h^5}{80} \\ \dfrac{h^3}{12} & \dfrac{Rh^3}{12} & \dfrac{3h^5}{80} & \dfrac{3Rh^5}{80} \\ 0 & \dfrac{2h^5}{80} & \dfrac{2Rh^5}{80} & \dfrac{4h^7}{448} \end{bmatrix}, \qquad [A_{23}]_{4*4} = \begin{bmatrix} 0 & Rh & \dfrac{2h^3}{12} & \dfrac{3Rh^3}{12} \\ 0 & \dfrac{h^3}{12} & \dfrac{2Rh^3}{12} & \dfrac{3h^5}{80} \\ 0 & \dfrac{Rh^3}{12} & \dfrac{2h^5}{80} & \dfrac{3Rh^5}{80} \\ 0 & \dfrac{h^5}{80} & \dfrac{2Rh^5}{80} & \dfrac{3h^7}{448} \end{bmatrix},$$

$$[A_{31}]_{4*4} = \begin{bmatrix} 0 & \dfrac{h^3}{12} & \dfrac{Rh^3}{12} & \dfrac{h^5}{80} \\ 0 & 0 & 0 & 0 \\ 0 & 0 & 0 & 0 \\ 0 & 0 & 0 & 0 \end{bmatrix}, \qquad [A_{32}]_{4*4} = \begin{bmatrix} 0 & 0 & 0 & 0 \\ Rh & \dfrac{h^3}{12} & \dfrac{Rh^3}{12} & \dfrac{h^5}{80} \\ \dfrac{2h^3}{12} & \dfrac{2Rh^3}{12} & \dfrac{2h^5}{80} & \dfrac{2Rh^5}{80} \\ \dfrac{3Rh^3}{12} & \dfrac{3h^5}{80} & \dfrac{3Rh^5}{80} & \dfrac{3h^7}{448} \end{bmatrix},$$

$$[A_{33}]_{4*4} = \begin{bmatrix} 0 & 0 & \dfrac{h^3}{12} & 0 \\ 0 & \dfrac{2h^3}{12} & \dfrac{Rh^3}{12} & \dfrac{2h^5}{80} \\ 0 & \dfrac{2Rh^3}{12} & \dfrac{3h^5}{80} & \dfrac{2Rh^5}{80} \\ 0 & \dfrac{4h^5}{80} & \dfrac{3Rh^5}{80} & \dfrac{4h^7}{448} \end{bmatrix}, \qquad [A_{41}]_{4*4} = \begin{bmatrix} \dfrac{-Rh}{\theta_2} & 0 & 0 & 0 \\ 0 & Rh & \dfrac{2h^3}{12} & \dfrac{3Rh^3}{12} \\ 0 & \dfrac{2h^3}{12} & \dfrac{4Rh^3}{12} & \dfrac{6h^5}{80} \\ 0 & \dfrac{3Rh^3}{12} & \dfrac{6h^5}{80} & \dfrac{9Rh^5}{80} \end{bmatrix},$$

$$[A_{42}]_{4*4} = \begin{bmatrix} h & Rh & \dfrac{h^3}{4} & \dfrac{Rh^3}{4} \\ 0 & 0 & 0 & 0 \\ 0 & 0 & 0 & 0 \\ 0 & 0 & 0 & 0 \end{bmatrix}, \quad \theta_1 = \dfrac{\lambda}{A}, \quad \theta_2 = \dfrac{\mu}{A}, \quad \alpha_n = \int_{-h/2}^{h/2} \dfrac{z^n dz}{R+z}, \quad n = 0, \ldots, 6,$$

$$[A_{44}]_{4*4} = \begin{bmatrix} \alpha_0 & \alpha_1 + \theta_1 h & \alpha_2 & \alpha_3 + \theta_1 \dfrac{3h^3}{12} \\ \alpha_1 + \theta_1 h & \alpha_2 + Rh & \alpha_3 + (3\theta_1 + 2)\dfrac{h^3}{12} & \alpha_4 + \dfrac{3Rh^3}{12} \\ \alpha_2 & \alpha_3 + (3\theta_1 + 2)\dfrac{h^3}{12} & \alpha_4 + \dfrac{4Rh^3}{12} & \alpha_5 + (5\theta_1 + 6)\dfrac{h^5}{80} \\ \alpha_3 + \theta_1 \dfrac{3h^3}{12} & \alpha_4 + \dfrac{3Rh^3}{12} & \alpha_5 + (5\theta_1 + 6)\dfrac{h^5}{80} & \alpha_6 + \dfrac{9Rh^5}{80} \end{bmatrix}. \tag{9b}$$

Equations (9a) and (9b) were derived by assuming (1) as the displacement field, but it is possible to consider different theories of shear deformation, and in each case only the coefficient matrices A_i change. In this paper the results of nine cases have been studied. By the definition of the functions, we have

$$
\begin{aligned}
U_{x2} &= u_0(x) + z u_1(x) + z^2 u_2(x), & U_{x1} &= u_0(x) + z u_1(x), \\
U_{z2} &= w_0(x) + z w_1(x) + z^2 w_2(x), & U_{z1} &= w_0(x) + z w_1(x).
\end{aligned}
\tag{10}
$$

These are the nine cases studied:

$$
\begin{array}{lllll}
\text{Case 1:} & U_x(x,z) = Ux_3, & Uz(x,z) = Uz_3 & \rightarrow & \text{VMS}_{33}, Sxz_{33}, \\
\text{Case 2:} & U_x(x,z) = Ux_3, & Uz(x,z) = Uz_2 & \rightarrow & \text{VMS}_{32}, Sxz_{32}, \\
\text{Case 3:} & U_x(x,z) = Ux_3, & Uz(x,z) = Uz_1 & \rightarrow & \text{VMS}_{31}, Sxz_{31}, \\
\text{Case 4:} & U_x(x,z) = Ux_2, & Uz(x,z) = Uz_3 & \rightarrow & \text{VMS}_{23}, Sxz_{23}, \\
\text{Case 5:} & U_x(x,z) = Ux_2, & Uz(x,z) = Uz_2 & \rightarrow & \text{VMS}_{22}, Sxz_{22}, \\
\text{Case 6:} & U_x(x,z) = Ux_2, & Uz(x,z) = Uz_1 & \rightarrow & \text{VMS}_{21}, Sxz_{21}, \\
\text{Case 7:} & U_x(x,z) = Ux_1, & Uz(x,z) = Uz_3 & \rightarrow & \text{VMS}_{13}, Sxz_{13}, \\
\text{Case 8:} & U_x(x,z) = Ux_1, & Uz(x,z) = Uz_2 & \rightarrow & \text{VMS}_{12}, Sxz_{12}, \\
\text{Case 9:} & U_x(x,z) = Ux_1, & Uz(x,z) = Uz_1 & \rightarrow & \text{VMS}_{11}, Sxz_{11},
\end{array}
\tag{11}
$$

where VMS stands for the von Mises stress and Sxz is the shear stress due to the selected displacement field. The governing equations for all nine cases are (9a) but the coefficient matrices A_i will change by the removal of some entries. For example, by applying $w_3 = 0$ to (9a), the equilibrium equations for case 2 are obtained. This corresponds to omitting the eighth column and row of the coefficient matrices and neglecting the eighth element of the force and displacement vectors, or, for case 7, removing the third and fourth rows and columns of the matrices and the third and fourth elements of the displacement and force vectors. This is in agreement with the results obtained in [Eipakchi et al. 2008].

Equation (9a) is a system of ordinary differential equations with variable coefficients. Frobenius series are the usual method for solving this kind of equations. This method has slow convergence and needs a lot of calculations. Also, one must know the inner and outer profiles of the shell and loading distribution, *before formulation*.

3. Analytical solution

In this paper, the MAE method has been used for solving the governing equations, which are a system of differential equations with variable coefficients. This method does not require knowledge of the inner and outer profiles of the shell and loading distribution before formulation, and can explain the behavior of the shell successfully even near the boundaries. The convergence of the solution is quick. The method involves solving a system of algebraic equations and two systems of differential equations with constant coefficients. These systems of equations have closed-form solutions.

We start by making the governing equations dimensionless, using the following characteristic scales:

$$
x^* = \frac{x}{L}, \quad R^* = \frac{R}{h_0}, \quad h^* = \frac{h}{h_0}, \quad u_2^* = u_2 h_0, \quad u_3^* = u_3 h_0^2, \quad w_0^* = \frac{w_0}{h_0}, \quad w_2^* = w_2 h_0, \quad w_3^* = w_3 h_0^2, \tag{12}
$$

where h_0 is the thickness characteristic and u_2^*, u_3^*, w_2^*, and w_3^* are the unknown dimensionless functions of x^*. By using these functions, the displacement field (1) converts to a nondimensional form as $U_z^* = U_z/h_0$ and $U_x^* = U_x/h_0$. By substituting (12) into (9), the nondimensional form of (9) is obtained:

$$\varepsilon^2 \frac{d}{dx^*}\left([A_1^*]\frac{d\{Y^*\}}{dx^*}\right) + \varepsilon\left(\frac{d}{dx^*}\left([A_2^*]\{Y^*\}\right) + [A_3^*]\frac{d\{Y^*\}}{dx^*}\right) + [A_4^*]\{Y^*\} + \frac{1}{\varepsilon}\{F_1^*\} + \{F_2^*\} = \{0\}. \quad (13a)$$

Here $\varepsilon = h_0/L$ is assumed small and will be taken as the perturbation parameter; The matrices $[A_i^*]$, $i = 1, \ldots, 4$, which are functions of x^*, are determined by replacing R with R^* and h with h^* in the matrices $[A_i]$, $i = 1, \ldots, 4$. The vectors $\{Y^*\}$, $\{F_1^*\}$, and $\{F_2^*\}$ are

$$\{Y^*\} = \{v, u_1, u_2^*, u_3^*, w_0^*, w_1, w_2^*, w_3^*\}^T, \qquad \{F_1^*\} = \left\{\left[\int \frac{R^*}{A} F_{x_0}\, dx^*, 0, 0, 0, 0, 0, 0, 0\right]\right\}^T,$$

$$\{F_2^*\} = \{C_0^*, F_{x_1}^*, F_{x_2}^*, F_{x_3}^*, F_{z_0}^*, F_{z_1}^*, F_{z_2}^*, F_{z_3}^*\}^T, \qquad F_k^* = \frac{R^* F_k}{A}, \quad k = x_1, x_2, x_3, z_0, z_1, z_2, z_3,$$

(13b)

where C_0^* is a constant.

Equation (13a) suggest that there are two boundary layers, one at each end of the shell. So, the solution of the problem contains an outer expansion away from the boundaries and two inner expansions near the two boundaries [Nayfeh 1981, Chapter 12].

3.1. *Outer expansion.*
This solution is considered as a uniform series of ε:

$$\{Y_{\text{out}}^*\} = \frac{1}{\varepsilon^\nu}\left(\{y_0(x^*)\} + \varepsilon\{y_1(x^*)\} + \varepsilon^2\{y_2(x^*)\} + \cdots\right). \quad (14)$$

Substituting (14) into (13) and considering the dominant terms, one obtains $\nu = 1$ (distinguished limit), so the equations with the same orders are

$$O(\varepsilon^{-1}): \qquad [A_4^*]\{y_0\} + \{F_1^*\} = \{0\}_{8*1},$$

$$O(\varepsilon^0): \qquad [A_4^*]\{y_1\} + \frac{d}{dx^*}\left([A_2^*]\{y_0\}\right) + [A_3^*]\frac{d\{y_0\}}{dx^*} + \{F_2^*\} = \{0\}_{8*1}, \quad (15)$$

$$O(\varepsilon^1): \qquad [A_4^*]\{y_2\} + \frac{d}{dx^*}\left([A_2^*]\{y_1\}\right) + [A_3^*]\frac{d\{y_1\}}{dx^*} + \frac{d}{dx^*}\left([A_1^*]\frac{d\{y_0\}}{dx^*}\right) = \{0\}_{8*1}.$$

Equations (15) are systems of algebraic equations, which are responsible for the shell away from the boundaries.

3.2. *Inner expansion at $x^* = 0$.*
The fast variable $\eta = x^*/\varepsilon$ is taken as the new variable for this region. The Taylor expansions of the coefficient matrices around $\varepsilon = 0$ are as follows:

$$[A_i^*(x^*)] = [A_i^*(0)] + \varepsilon\eta[a_i] + \varepsilon^2\eta^2[d_i] + \cdots, \qquad\qquad i = 1, \ldots, 4,$$

$$\{F_j^*(x^*)\} = \{F_j^*(0)\} + \varepsilon\eta\frac{d\{F_j^*\}}{dx^*}\bigg|_{x^*=0} + \frac{1}{2}\varepsilon^2\eta^2\frac{d^2\{F_j^*\}}{dx^{*2}}\bigg|_{x^*=0} + \cdots, \qquad j = 1, 2,$$

(16)

where

$$[a_k] = \frac{d[A_k^*]}{dx^*}\bigg|_{x^*=0}, \qquad [d_k] = \frac{1}{2}\frac{d^2[A_k^*]}{dx^{*2}}\bigg|_{x^*=0}, \qquad k = 1, \ldots, 4.$$

The solution in this region is sought in the form

$$\{Y_{\text{in}}^*\} = \frac{1}{\varepsilon}\big(\{y_0(\eta)\} + \varepsilon\{y_1(\eta)\} + \varepsilon^2\{y_2(\eta)\} + \cdots\big), \tag{17}$$

and by substituting (16) and (17) into (13a), the terms of same order are collected as

$$O(\varepsilon^{-1}) : \big\{L_1(\{y_0\}, \eta, 0)\big\} + \{F_1^*(0)\} = \{0\}_{8*1}, \tag{18a}$$

$$O(\varepsilon^0) : \big\{L_1(\{y_1\}, \eta, 0)\big\} + \big\{M_1(\{y_0\}, \eta, [a_1], [a_2], [a_3], [a_4], 0)\big\} + \eta \frac{d\{F_1^*\}}{dx^*}\bigg|_{x^*=0} + \{F_2^*(0)\}$$
$$= \{0\}_{8*1}, \tag{18b}$$

$$O(\varepsilon^1) : \big\{L_1(\{y_2\}, \eta, 0)\big\} + \big\{M_1(\{y_1\}, \eta, [a_1], [a_2], [a_3], [a_4], 0)\big\}$$
$$+ \big\{M_1(\{y_0\}, \eta, [d_1], [d_2], [d_3], [d_4], 0)\big\} + \eta \frac{d\{F_2^*\}}{dx^*}\bigg|_{x^*=0} + \frac{1}{2}\eta^2 \frac{d^2\{F_1^*\}}{dx^{*2}}\bigg|_{x^*=0} = \{0\}_{8*1}, \tag{18c}$$

where the differential operators $\{L_1\}$ and $\{M_1\}$ are given by

$$\big\{M_1(\{y\}, x, [a_1], [a_2], [a_3], [a_4], j)\big\} = [a_1]\frac{d}{dx}\Big(x\frac{d\{y\}}{dx}\Big) + [a_2]\frac{d}{dx}(x\{y\}) + [a_3]x\frac{d\{y\}}{dx} + [a_4]x\{y\},$$
$$\{L_1(\{y\}, x, i)\} = [A_1^*(i)]\frac{d^2\{y\}}{dx^2} + \big([A_2^*(i)] + [A_3^*(i)]\big)\frac{d\{y\}}{dx} + [A_4^*(i)]\{y\}; \tag{19}$$

Equations (18), which are systems of ordinary differential equations with constant coefficients, are solved using the elementary theory of differential equations [Wylie 1979].

3.3. *Inner expansion at $x^* = 1$.* The fast variable $\xi = (x^* - 1)/\varepsilon$ is taken as the new variable for this region. The Taylor expansions of the coefficient matrices around $\varepsilon = 0$ are

$$[A_i^*(x^*)] = [A_i^*(1)] + \varepsilon\xi[a_i] + \varepsilon^2\xi^2[d_i] + \cdots, \qquad\qquad i = 1, \ldots, 4,$$
$$\{F_j^*(x^*)\} = \{F_j^*(1)\} + \varepsilon\xi\frac{d\{F_j^*\}}{dx^*}\bigg|_{x^*=1} + \frac{1}{2}\varepsilon^2\xi^2\frac{d^2\{F_j^*\}}{dx^{*2}}\bigg|_{x^*=1} + \cdots, \qquad j = 1, 2, \tag{20}$$

where

$$[a_k] = \frac{d[A_k^*]}{dx^*}\bigg|_{x^*=1}, \qquad [d_k] = \frac{1}{2}\frac{d^2[A_k^*]}{dx^{*2}}\bigg|_{x^*=1}, \qquad k = 1, \ldots, 4.$$

We consider the solution

$$\{Y_{IN}^*\} = \frac{1}{\varepsilon}\big(\{y_0(\xi)\} + \varepsilon\{y_1(\xi)\} + \varepsilon^2\{y_2(\xi)\} + \cdots\big). \tag{21}$$

By substituting (20) and (21) into (13a), the same-order terms are

$$O(\varepsilon^{-1}) : \big\{L_1(\{y_0\}, \xi, 1)\big\} + \{F_1^*(1)\} = \{0\}_{8*1}, \tag{22a}$$

$$O(\varepsilon^0) : \big\{L_1(\{y_1\}, \xi, 1)\big\} + \big\{M_1(\{y_0\}, \xi, [a_1], [a_2], [a_3], [a_4], 1)\big\} + \xi\frac{d\{F_1^*\}}{dx^*}\bigg|_{x^*=1} + \{F_2^*(1)\}$$
$$= \{0\}_{8*1}, \tag{22b}$$

$$O(\varepsilon^1) : \left\{L_1\big(\{y_2\}, \xi, 1\big)\right\} + \left\{M_1\big(\{y_1\}, \xi, [a_1], [a_2], [a_3], [a_4], 1\big)\right\}$$

$$+ \left\{M_1\big(\{y_0\}, \xi, [d_1], [d_2], [d_3], [d_4], 1\big)\right\} + \xi \frac{d\{F_2^*\}}{dx^*}\bigg|_{x^*=1} + \tfrac{1}{2}\xi^2 \frac{d^2\{F_1^*\}}{dx^{*2}}\bigg|_{x^*=1} = \{0\}_{8*1}. \quad (22c)$$

Equations (22) forms a set of coupled ordinary differential equations with constant coefficients, and one can solve these equations as in the last section.

3.4. Composite solution. In the MAE method, the composite solution is the summation of these three calculated solutions minus the overlapping parts of them:

$$\{Y^*\} = \{Y_{\text{in}}^*\} + \{Y_{\text{IN}}^*\} + \{Y_{\text{out}}^*\} - \big(\{J_0\} + \{J_L\}\big). \quad (23)$$

$\{J_0\}$ and $\{J_L\}$ are the common parts of the inner and outer solutions at the two ends of the shell and can be determined by van Dyke's matching principle [Nayfeh 1981, pp. 282–283].

4. Case studies

A thick cylinder with constant thickness subjected to constant internal pressure. By solving this problem, it is possible to find a validation range of thickness to use the shear deformation theory in the stress and displacement analysis of a thick cylinder. Away from the boundaries, the solution can be found with Lamé's formula, which is an exact solution. According to Lamé's formula, the radial and hoop stresses are $\sigma_r = c_1 + c_2/r^2$ and $\sigma_\theta = c_1 - c_2/r^2$. The constants c_1 and c_2 are determined from the boundary conditions: the inner wall is subjected to internal pressure and the outer wall is traction free. By using Hooke's law, the radial and axial displacements in the plane stress state are $U_z = c_3 r + c_4/r$ and $U_x = c_5 x$ where c_3, c_4, and c_5 are constants that depend on the geometrical and material properties of the cylinder. So, it is possible to estimate the von Mises stress easily. Away from the boundaries, the solution of this problem can be obtained with (15), which is the solution of the algebraic equations $[A_4]\{Y\} + \{F_p\} = \{0\}$. Thus the parameters in (1) are $u_1 = u_2 = u_3 = 0$, $u_0 = c_6 x$, and w_0, w_1, w_2, and w_3 are calculated. For this problem, the nine cases in (11) reduce to just the three following cases:

$$
\begin{aligned}
&\text{Case 1:} &&U_x(x, z) = c_6 x, &&U_z(x, z) = U_{z3} &&\rightarrow &&VMS_{33}, \\
&\text{Case 2:} &&U_x(x, z) = c_6 x, &&U_z(x, z) = U_{z2} &&\rightarrow &&VMS_{32}, \\
&\text{Case 3:} &&U_x(x, z) = c_6 x, &&U_z(x, z) = U_{z1} &&\rightarrow &&VMS_{31}.
\end{aligned}
\qquad (24)
$$

The axial displacement depends on the selected radial displacement field or it depends on z, implicitly. By comparing these solutions, one can determine the relative difference between exact and approximate solutions, that is, the quotient $(q_{\text{exact}} - q_{\text{shear}})/q_{\text{exact}}$ (expressed as a percentage), where q is the quantity of interest at the *inner wall* of the shell, and the subscripts "exact" and "shear" stand for the Lamé and shear deformation solutions. Figure 2, top, plots the relative difference in radial displacement versus $m = R/h$ for the theories listed in (24). As the thickness decreases, so does the relative difference; for $m > 4$ there is nearly no advantage to higher-order theories. For thick shells, TSDT shows a smaller difference.

Figure 2, bottom, shows the difference percentage of the von Mises stress for values of m. FSDT is a poor approximation for the von Mises stress, and TSDT is very good for thick shells. For moderately thick shells (for instance, $m > 4$), there is no difference between SSDT and TSDT.

Figure 3 compares the quantity $E \cdot U_x / (p \cdot x)$ with respect to m with different theories where p is the internal pressure. Approximately, TSDT and SSDT are the same for the axial displacement prediction.

A thick conical shell with varying thickness subjected to nonuniform internal pressure. Table 1, on the next page, lists the geometrical and material properties of the shell. The variation of the pressure is linear and the boundary conditions are clamped-free (see Figure 1). The MAE method has been used for the stress analysis of this shell. The calculations were performed on Maple 10 software, and were based on TSDT. From this solution, it is possible to extract the nine cases of (11).
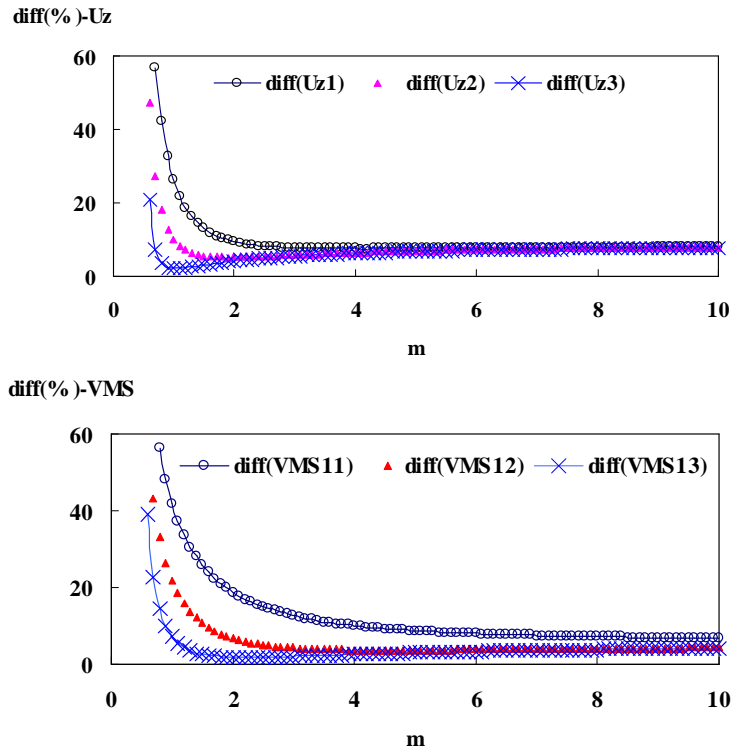
Figure 2. Relative difference in the radial displacement (top) and the von Mises stress (bottom) as a function of m. See (24) for the meaning of the three cases.
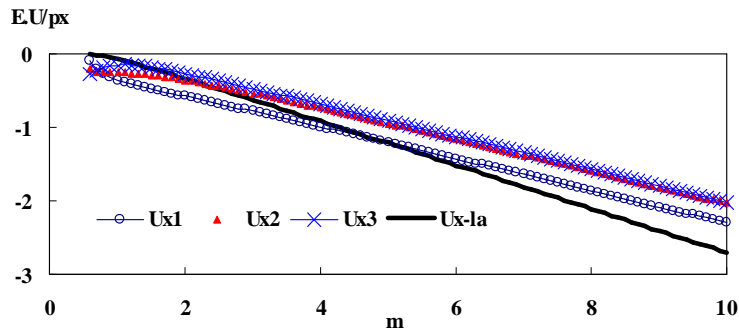
Figure 3. Nondimensional axial displacement as a function of m. See (24).

Shell length	$L = 50\,\text{cm}$
Inner radius at $x = 0$	$R_{i0} = 10\,\text{cm}$
Inner radius at $x = L$	$7\,\text{cm}$
Outer radius at $x = 0$	$15\,\text{cm}$
Outer radius at $x = L$	$9\,\text{cm}$
Internal pressure at $x = 0$	$P_0 = 200\,\text{MPa}$
Internal pressure at $x = L$	$50\,\text{MPa}$
Young's modulus	$E = 210\,\text{GPa}$
Poisson's ratio	0.3

Table 1. Shell properties.

Outer expansion. This is the solution of (15). Although the solution is straightforward, by increasing the order of ε, calculation time increases due to enlarging the nonhomogeneous part of equations. It is possible to decrease running time by special programming techniques.

Inner solution. At $x^* = 0$, this is the solution of (18). It is in the form of systems of nonhomogeneous ordinary differential equations with constant coefficients. The general solution is $\{y\} = \{V\}e^{\lambda_i \eta}$, where $\{V\}$ is the eigenvector and λ_i is the eigenvalue. By substituting the general solution in the homogeneous part of (18a), we find

$$\left(A_1^*(0)\lambda_i^2 + \left[A_2^*(0) + A_3^*(0)\right]\lambda_i + A_4^*(0)\right)\{V\} = \{0\}. \tag{25}$$

λ_i is calculated from the determinant of the system matrix, that is,

$$\det\left(A_1^*(0)\lambda_i^2 + \left[A_2^*(0) + A_3^*(0)\right]\lambda_i + A_4^*(0)\right) = 0.$$

This equation has 14 roots and for each root, an eigenvector can be calculated from (25). So the general solution is

$$\{y\}_g = \sum_{i=1}^{14} C_i \{V_i\} e^{\lambda_i \eta},$$

which is valid for (18). The particular solution of (18a) depends on the nonhomogeneous part, which is a constant vector and can be considered as $\{y\}_p = \{K_0\}$. By substituting this solution into (18a), $\{K_0\}$ is determined. The total solution is $\{y\} = \{y\}_g + \{y\}_p$. There are 14 constants. Seven constants, which correspond to eigenvalues with positive real parts, are zero, because the solution is finite at $\eta \to \infty$. The remaining constants are determined from the clamped boundary conditions at $x^* = 0$ for this case study, that is, $u_1 = u_2^* = u_3^* = w_0^* = w_1 = w_2^* = w_3^* = 0$. The condition $u_0 = 0$ is applied, later. The particular solution of (18b) is

$$\{y\}_p = \sum_{i=1}^{7} \left(\{K_{0i}\} + \{K_{1i}\}\eta + \{K_{2i}\}\eta^2\right)e^{\lambda_i \eta} + \{K_1\}\eta + \{K_0\},$$

and by substituting this solution into (18b), the unknown vectors can be determined. The boundary conditions are applied to the total solution of this order to determine seven constants. The particular

solution of (18c) is

$$\{y\}_p = \sum_{i=1}^{7}\big(\{K_{0i}\} + \{K_{1i}\}\eta + \{K_{2i}\}\eta^2 + \{K_{3i}\}\eta^3 + \{K_{4i}\}\eta^4\big)e^{\lambda_i\eta} + \{K_2\}\eta^2 + \{K_1\}\eta + \{K_0\},$$

and by substituting into (18c), the coefficient vectors are determined. Seven constants are determined from the clamped boundary conditions.

Inner solution. At $x^* = 1$, this is the solution of (22), which are in the form of systems of nonhomogeneous ordinary differential equations with constant coefficients. The general solution for each system is

$$\{y\}_g = \sum_{i=1}^{14} C_i\{V_i\}e^{\lambda_i\xi}.$$

The eigenvalues λ_i are the roots of algebraic equation

$$\det\big(A_1^*(1)\lambda_i^2 + \big[A_2^*(1) + A_3^*(1)\big]\lambda_i + A_4^*(1)\big) = 0,$$

and the eigenvectors $\{V\}$ are determined from

$$\big(A_1^*(1)\lambda_i^2 + \big[A_2^*(1) + A_3^*(1)\big]\lambda_i + A_4^*(1)\big)\{V\} = \{0\}.$$

The particular solution of (22a) is $\{y\}_p = \{K_0\}$ and the total solution is $\{y\} = \{y\}_g + \{y\}_p$. Seven constants, which correspond to eigenvalues with negative real parts, are zero because the solution is finite at $\xi \to -\infty$. The other constants are determined from the free boundary conditions at $x^* = 1$ for this case study, that is, $M_x = P_x = S_x = Q_x = M_{xz} = P_{xz} = S_{xz} = 0$. The condition $N_x = 0$ is applied later. The particular solutions of (22b) and (22c) are similar to the case of the previous section, except that the variable is ξ.

Composite solution. This solution is determined from (23) for each order of ε. The common parts were specified by removing the exponential terms of the inner solutions for this case study. By integrating the first element of (23), u_0 is calculated and a new constant of integration is found. This constant and C_0^* are calculated from the clamped-free boundary conditions. At $x = 0$, $u_0 = 0$, and at $x = L$, $N_x = 0$.

5. Numerical results

The ANSYS 5.4 FE package was used in the static analysis of this thick conical shell with varying thickness. The PLANE82 element in axisymmetric mode, which is an element with eight nodes and two translational degrees of freedom in the axial and radial directions per each node, was used for discretization. The boundary conditions were considered clamped-free and the characteristics of the shell have been listed in Table 1. Figure 1 shows the loading, mesh pattern, and deformation of the shell.

6. Comparison of results

Figure 4 shows the radial displacement of the inner wall for different orders of ε. It is seen that order (ε^{-1}) is not an acceptable solution, but orders $(\varepsilon^1, \varepsilon^0)$ have a good convergence. There is not any noticeable difference between these orders. This result is valid for the axial displacement and the von Mises stress. So, the displacements and the von Mises stress have been calculated with the order (ε^0) expansion for

Uz/h0
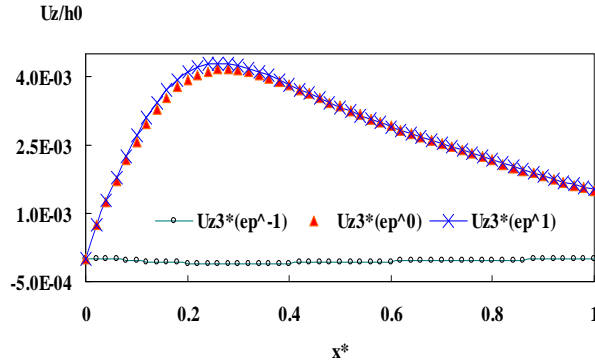
Figure 4. Convergence procedure for radial displacement by different expansions.

Ux/h0

Uz/h0
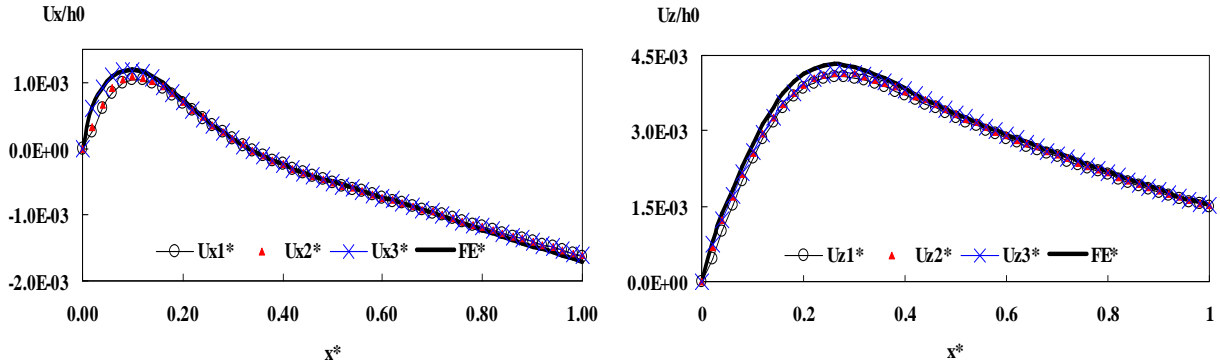
Figure 5. Axial (left) and radial (right) displacement for various approximations. See (11).

the inner wall of the shell. $x^* = x/L$ in the graphs is the vertical position of each point on the inner wall of the shell.

Figure 5 shows that, by using higher-order theories (Uz_2, Uz_3, Ux_2, and Ux_3), the displacements do not change significantly. The maximum percentage of difference between the FE and shear deformation results is 7% for Uz_1, 5% for Uz_2, and 4.8% for Uz_3, which is in agreement with Figure 2, top, for this case study ($3 < m < 4.5$). In Figure 6, it is seen that by using Uz_2 and Uz_3, for the radial displacement,

VMS/P0

Figure 6. Von Mises stress for different theories. See (11).
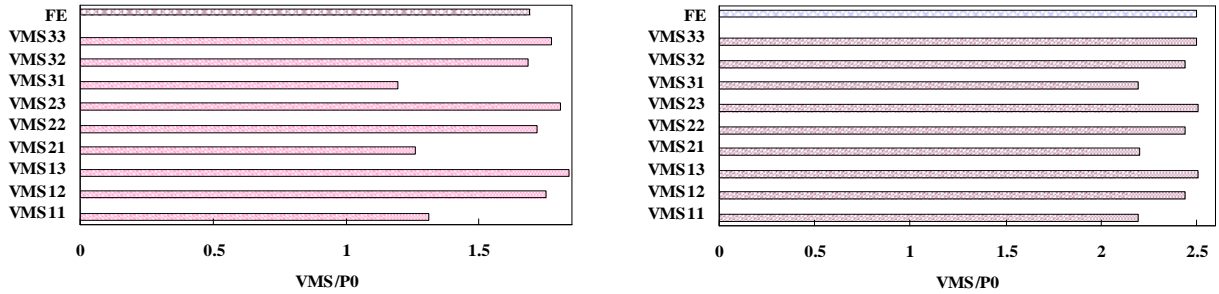
Figure 7. Effect of various theories on von Mises Stress at $x^* = 0.08$ (left) and $x^* = 0.4$ (right).
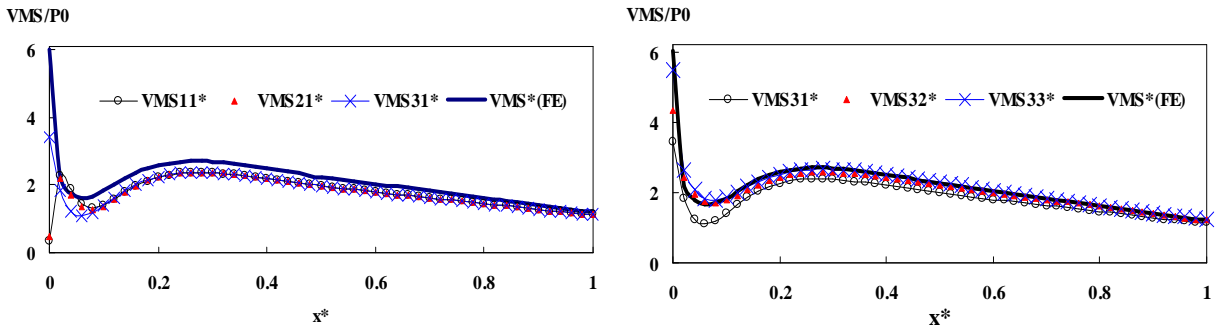
Figure 8. Comparison of different axial displacements for Uz_1 (left) and radial displacements for Ux_3 (right) on von Mises stress.
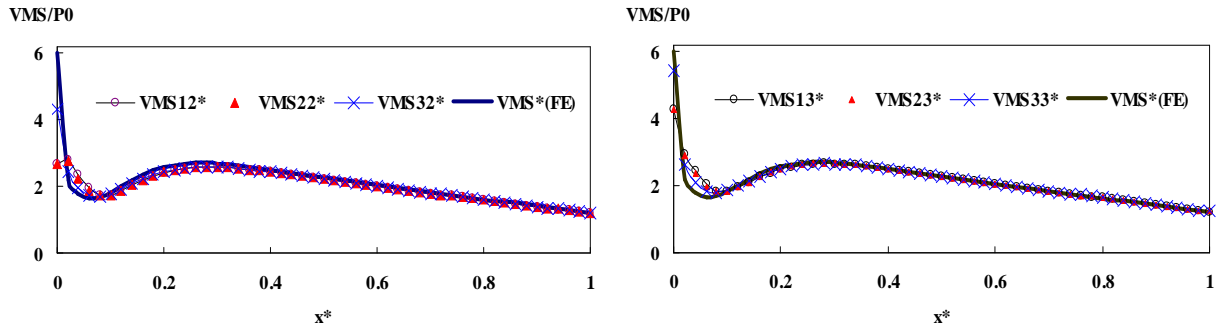
Figure 9. Comparison of different axial displacements on von Mises stress for Uz_2 (left) and Uz_3 (right).
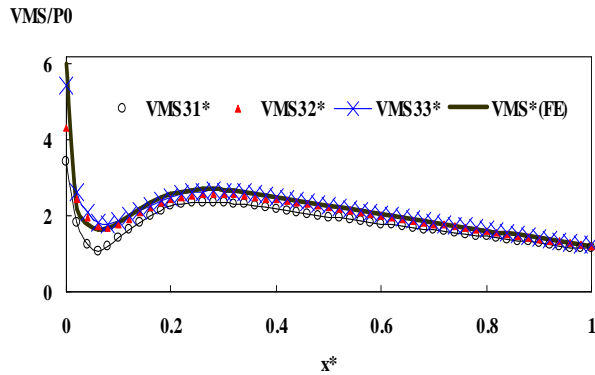
the von Mises stress will improve. This result has been shown in Figure 7 for the point $x^* = 0.08$ (a point on the inner wall, near the boundary, and so related to the inner solution) and at $x^* = 0.4$ (a point away from the boundaries, and so related to the outer solution). Also, the difference between the Uz_2 and Uz_3 approximations is not noticeable on the von Mises stress.

Figure 8, left, compares the von Mises stress for the cases 3, 6 and 9 listed in (11). The higher-order theories in axial displacement (Ux_2 and Ux_3) do not affect the stress distribution except near the boundaries. Figure 9 shows the effect of higher-order radial displacements on the von Mises stress distribution. There is no significant difference between the Uz_2 and Uz_3 solutions but Uz_2 and Uz_3 are
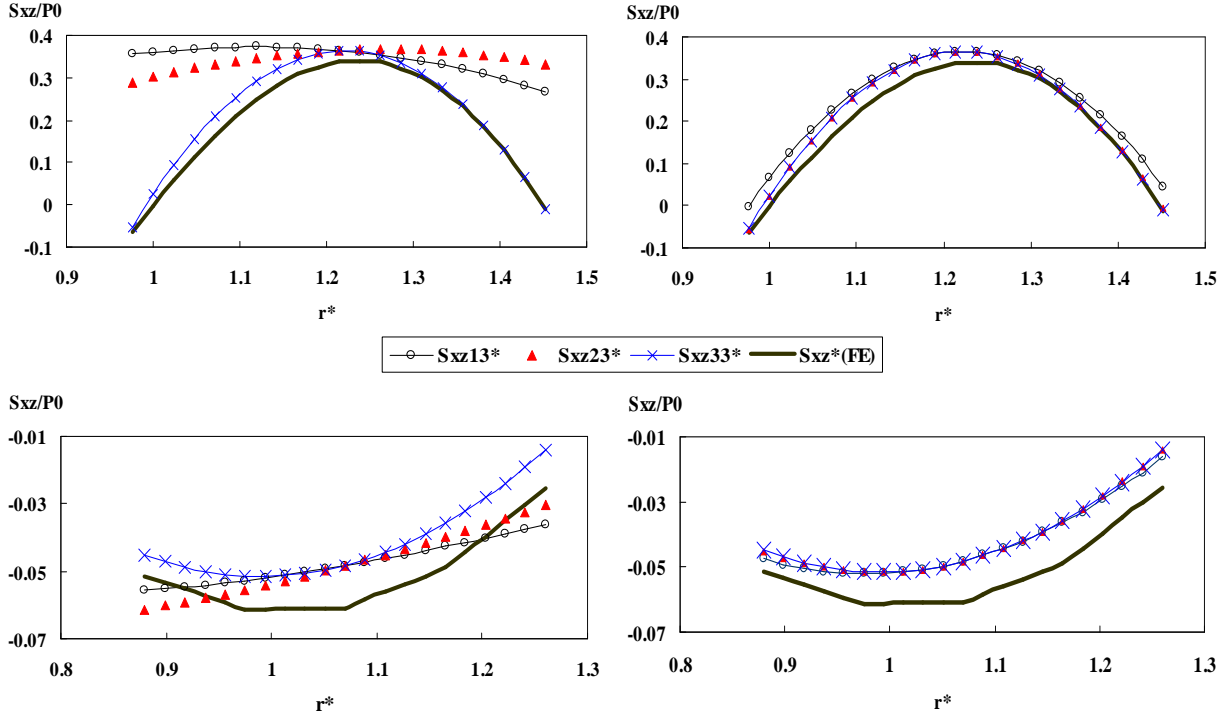
Figure 10. Comparison of different axial displacements on shear stress at $x^* = 0.08$ (top) and $x^* = 0.4$ (bottom), for Uz_3 (left) and for Ux_3 (right).

more accurate than Uz_1 for calculating the von Mises stress. Figure 8, right, suggests that Uz_3 is a very good approximation with respect to the FE results.

Figure 10, top, compares different axial approximations on the shear stress distribution at the section $x^* = 0.08$ in terms of $r^* = r/R_{i0}$ where R_{i0} is the inner radius at $x^* = 0$ (see Table 1). Ux_3 improves the shear stress distribution; the results using Ux_1 and Ux_2 are not suitable. According to Figure 10, right, the higher-order approximations for radial displacement do not change significantly the shear stress distribution at this section. Similar results can be found when one uses Ux_1 or Ux_2 as the axial displacement.

The effect of different theories on the shear stress at section $x^* = 0.4$ is shown in the bottom row of Figure 10. The higher-order approximations are more important for the axial displacement than for the radial displacement in the shear stress distribution at this section.

7. Conclusion

By dividing the solution region into three parts and finding a closed-form solution for each region using the MAE method, it is possible to determine an analytical solution for the governing equations with fast convergence and good accuracy.

The calculations show that the relative difference between the presented results and FE (or elasticity) is not due to the MAE technique but it relates to the selected displacement field.

The results show that FSDT is sufficient for determining the displacements, but that for calculating the von Mises Stress it is necessary to use a higher-order approximation for the radial displacements. The shear stress is small compared to the von Mises stress. The shear stress is sensitive to the selected axial displacement, and Ux_1 and Ux_2 cannot predict its distribution as well, especially at the sections near the boundaries.

As a result, TSDT for the axial and radial displacements is a good approximation for both von Mises and shear stresses; see Equation (1).

References

[Buchanan and Wong 2001] G. R. Buchanan and F. T.-I. Wong, "Frequencies and mode shapes for thick truncated hollow cones", *Int. J. Mech. Sci.* **43**:12 (2001), 2815–2832.

[Correia et al. 2003] I. F. P. Correia, C. M. Mota Soares, C. A. Mota Soares, and J. Herskovits, "Analysis of laminated conical shell structures using higher order models", *Compos. Struct.* **62**:3–4 (2003), 383–390.

[Cui et al. 2001] W. Cui, J. Pei, and W. Zhang, "A simple and accurate solution for calculating stresses in conical shells", *Comput. Struct.* **79**:3 (2001), 265–279.

[Eipakchi et al. 2008] H. R. Eipakchi, S. E. Khadem, and G. H. Rahimi S., "Axisymmetric stress analysis of a thick conical shell with varying thickness under nonuniform internal pressure", *J. Eng. Mech.* (*ASCE*) **134**:8 (2008), 601–610.

[Garg et al. 2006] A. K. Garg, R. K. Khare, and T. Kant, "Free vibration of skew fiber-reinforced composite and sandwich laminates using a shear deformable finite element model", *J. Sandw. Struct. Mater.* **8**:1 (2006), 33–53.

[Nayfeh 1981] A. H. Nayfeh, *Introduction to perturbation techniques*, Wiley, New York, 1981.

[Panferov 1992] I. V. Panferov, "Stresses in a transversely isotropic conical elastic pipe of constant thickness under a thermal load", *J. Appl. Math. Mech.* **56**:3 (1992), 410–415.

[Ramesh et al. 2008] S. S. Ramesh, C. M. Wang, J. N. Reddy, and K. K. Ang, "Computation of stress resultants in plate bending problems using higher-order triangular elements", *Eng. Struct.* **30**:10 (2008), 2687–2706.

[Sivadas and Ganesan 1991] K. R. Sivadas and N. Ganesan, "Vibration analysis of laminated conical shells with variable thickness", *J. Sound Vib.* **148**:3 (1991), 477–491.

[Sundarasivarao and Ganesan 1991] B. S. K. Sundarasivarao and N. Ganesan, "Deformation of varying thickness of conical shells subjected to axisymmetric loading with various end conditions", *Eng. Fract. Mech.* **39**:6 (1991), 1003–1010.

[Tavares 1996] S. A. Tavares, "Thin conical shells with constant thickness and under axisymmetric load", *Comput. Struct.* **60**:6 (1996), 895–921.

[Thambiratnam and Zhuge 1993] D. P. Thambiratnam and Y. Zhuge, "Axisymmetric free vibration analysis of conical shells", *Eng. Struct.* **15**:2 (1993), 83–89.

[Tong 1994] L. Tong, "Free vibration of laminated conical shells including transverse shear deformation", *Int. J. Solids Struct.* **31**:4 (1994), 443–456.

[Wu and Chiu 2002] C.-P. Wu and S.-J. Chiu, "Thermally induced dynamic instability of laminated composite conical shells", *Int. J. Solids Struct.* **39**:11 (2002), 3001–3021.

[Wylie 1979] C. R. Wylie, "Simultaneous linear differential equations", Chapter 5, pp. 147–181 in *Differential equations*, McGraw-Hill, New York, 1979.

HAMID REZA EIPAKCHI: hamidre_2000@yahoo.com
Mechanical Engineering Faculty, Shahrood University of Technology, P.O. Box 316, Shahrood, Iran

FINITE ELEMENT IMPLEMENTATION OF NONLINEAR CONSTITUTIVE MODELS FOR PIEZOCERAMIC MATERIALS

BERND LASKEWITZ AND MARC KAMLAH

The objective of this work was the finite element implementation of constitutive material models for piezoceramic materials. A phenomenological material model was implemented by means of a customized radial return mapping algorithm into an open source finite element program, and the problem was reduced to the solution of a single nonlinear algebraic equation. This led to a significant reduction in computation time for simulations compared to an implementation by means of an explicit higher order integration scheme for the constitutive differential equations. Furthermore, a microscopically motivated material model was implemented by means of a radial return mapping algorithm based on the backward Euler scheme.

Apart from simulations of the principal behavior of the material models and their finite element implementations, simulations of applied examples are discussed which demonstrate the properties of the models and the performance of the implementations.

1. Introduction

The *piezoelectric* effect describes a linear relationship between strain and polarization on the one hand, and electric field and stress on the other. Nowadays, this effect is commonly utilized by a class of ferroelectric ceramics, also called piezoceramics for short. The electromechanical coupling properties of these polycrystalline materials are caused by distinct features of their perovskite microstructure. Below the Curie temperature, each grain possesses a substructure of *domains*, these being regions of uniform orientation of the microdipoles of the crystallographic unit cells. Upon application of electric fields and mechanical stresses of sufficient magnitude, the domains can be reoriented. The macroscopic hysteresis properties resulting from microscopic domain switching processes under a cyclic electric field and mechanical stress loading in such a *ferroelectric* material are called *ferroelectricity* and *ferroelasticity*, respectively. In particular, the so-called poling process caused by strong electric fields leads to the orientation of the domains in the direction of the field resulting in a macroscopic piezoelectric effect from the microscopic piezoelectric contributions of the domains.

Piezoceramic materials are used for actuation in various technical fields requiring challenging properties. They facilitate highly accurate positioning, show fast response times, and allow for large actuation forces. Examples of technical applications are diesel injection valves (which in 2005 won the Deutscher Zukunftspreis awarded by the President of the Federal Republic of Germany[1]), as well as positioners in nano- and microtechnology.

[1] See announcement at http://www.deutscher-zukunftspreis.de/en/nominierter/piezo-injectors-new-technologybr-clean-and-economical-diesel-and-gasoline-engines

The composition of piezoceramic materials is subject to constant improvement in optimizing the piezo-electric properties. On the other hand, with respect to modeling, in commercial finite element codes only a linear relationship between the quantities is taken into account for simulation of the electromechanical behavior. As an important example, the above mentioned poling process and the resulting residual stresses after poling as part of manufacturing piezoelectric devices made of ferroelectrics cannot be simulated. Furthermore, mechanical depolarization cannot be taken into account in computations based on linear piezoelectric behavior. This lack of capability to represent the electromechanical fields correctly leads to increasing difficulties in predicting malfunctions and failures of devices in complex applications. The current paper deals with providing such finite element tools taking into account the complete spectrum of electromechanically coupled large signal hysteresis behavior of ferroelectrics. Such tools are needed as basis for the assessment of the reliability of piezoceramic devices, for example.

This paper is organized as follows: In Section 2, the literature regarding constitutive modeling of piezoceramic materials and finite element implementations will be reviewed. At the beginning of Section 3, the phenomenological constitutive model developed earlier will be described [Kamlah and Tsakmakis 1999; Kamlah 2001; Kamlah and Boehle 2001]. The finite element tool described in these papers is among the very earliest capable of taking into account the complete coupled ferroelectric and ferroelastic large signal hysteresis properties of piezoceramics. On the other hand, the implementation algorithm, based on a higher order explicit integration scheme for the constitutive differential equations, lacked computational efficiency.

In the first main section (Section 3) we present a significantly improved integration algorithm for the phenomenological constitutive model in the open source finite element code PSU [PSU 2000]. This implementation is verified by comparing simulated curves to experimentally measured behavior. In addition, the poling of a stack actuator is discussed as a simulation example.

In the second main section (Section 4), we introduce a microscopically motivated material model [Kamlah and Jiang 1999; Kamlah and Wang 2003]. This model operates at the same length scale as the previously mentioned phenomenological model. However, it is based on the orientation distribution function of ferroelectric domains, and its evolution due to domain switching. Thus, it possesses a clear micromechanical foundation. The finite element implementation of this model is based on a backward Euler scheme. Verification examples and an example simulation demonstrate the capability of the obtained computation tool. The computation time is longer due to the complexity of the model and the integration algorithm, but, on the other hand, it can describe poling processes more realistically than the phenomenological model. This leads to a better understanding of the behavior of ferroelectric materials.

2. Constitutive modeling of ferroelectrics

2.1. *Phenomenological approach.* The phenomenological approach is an efficient way to describe the complex behavior of piezoceramic materials. The disadvantages of this approach result from the fact that the material behavior is described phenomenologically which means in general that a calibration is necessary. Outside of the range of loadings considered in developing such a model, there is always the danger that it may be inaccurate or even qualitatively wrong. In the field of phenomenological models some significant improvements have been made since the work of Chen [1980] which will be described subsequently.

McMeeking and Landis [2002] proposed a phenomenological model for ferroelectric switching processes subject to multiaxial mechanical and electrical loadings. It is based on a kinematic hardening theory with a switching surface in the space of stress and electric field. McMeeking and Landis [2002] express the remanent strain by means of a function of remanent polarization. This approach simplifies the model significantly, but excludes purely ferroelastic hysteretic behavior.

Such an restriction does not apply to the model of Landis [2002]. It is based on the Helmholtz free energy of the material. A domain switching surface and flow rules for the internal variables in the space of stress and electric field are introduced. The derived constitutive law has a symmetric material tangent. This leads to faster computation time and lower memory demand for the finite element implementation compared to models which rely on asymmetric tangents.

Huber and Fleck [2001] proposed — in addition to their crystal plasticity type theory [Huber et al. 1998; Huber and Fleck 2004], see Section 2.2 — a phenomenological model. The computation time for this model is short, but it is specialized to nearly uniaxial cyclic loadings.

Kessler and Balke [2001] derived an expression for the local and average energy release rate during polarization orientation processes. On this basis, they developed a repolarization model which can describe pure rotation of the polarization at a fixed magnitude.

Schroeder and Gross [2004] developed a fully coupled electromechanical formulation for transversally isotropic materials for reversible material behavior. A variational and finite element formulation for fully coupled problems with small deformations is presented. Schroeder and Romanowski [2005] enhanced the model with consideration of domain switching to be able to describe fundamental hysteresis effects. However, only the magnitude of polarization can change while its direction is fixed in space, and strain is just a function of polarization.

Belov and Kreher [2005] proposed two viscoplasticity type models without loading conditions for the onset of switching. The evolution of the structure of domains is described by means of rate-dependent equations of the volume fractions of orientation variants. The first model offers six different domain orientations and is proposed for uniaxial loadings. The second model has 42 possible domain orientations and can be applied to multiaxial simulations.

Elhadrouz et al. [2005a; 2005b] used the material law of Kamlah and Boehle [Boehle 1999; Kamlah and Tsakmakis 1999; Kamlah 2001; Kamlah and Boehle 2001]. They coded an element for the finite element implementation of the model in a commercially available finite element code.

Klinkel [2006] has developed on the basis of a thermodynamically consistent approach a 1D model for ferroelastic and ferroelectric hysteresis effects of piezoceramics. He made use of the Helmholtz free energy and a domain switching surface for the thermodynamical framework of his work. As a specific feature, he introduced, besides irreversible strain, an irreversible electric field as a state variable. This simplifies the finite element implementation, but doesn't have an immediate physical interpretation.

2.2. *Micromechanical modeling.* Many available theoretical studies are based on micromechanical material models [Hwang et al. 1995; 1998; Chen et al. 1997; Chen and Lynch 1998; Huber et al. 1998; Hwang 2000; Smith et al. 2003; Huber and Fleck 2004; Seemann et al. 2004; Delibas et al. 2005; Kamlah et al. 2005; Semenov et al. 2006] which have led to a better understanding of the behavior of ferroelectrics. In general an application of micromechanical models to common engineering problems is difficult because the models are mostly very complex and computationally expensive. But, they have

significant advantages compared to phenomenological models because the range of validity of microme-
chanical models is mostly more general as basic mechanisms on the microscopic level are taken into
consideration.

On the basis of the constitutive behavior of single crystals Chen and Lynch [1998] have developed a
micromechanical model for polycrystalline, ferroelectric ceramics. The model simulates tetragonal and
rhombohedral crystal structures in which a saturation of the linear piezoelectric effect is implemented.
Furthermore the interaction between the different grains of the polycrystal is considered. A switching
criterion was developed which takes into consideration the domain switching processes of the tetragonal
and rhombohedric crystal structure.

Huber et al. [1998] and Huber and Fleck [2004] describe a micromechanical model based on crystal
plasticity theory. A grain is a mixture of variants, a variant representing all domains of equal orientation
of the spontaneous polarization inside a grain. Switching processes transform a variant into another
variant. The polycrystalline properties are then obtained by a self-consistent scheme to yield irreversible
polarization and irreversible strain, as well as the average linear electromechanical properties. In [Kamlah
et al. 2005], grain to grain interaction is modeled explicitly by means of the finite element method.

Seemann et al. [2004] and Delibas et al. [2005] have derived a model on the level of the grains of a
polycrystal in which they assume that after poling the domains in a grain have the same orientation. The
basis of the model is an energetic approach from [Hwang et al. 1998] in which the potential energy of a
single domain is taken into consideration. If the potential energy rises beyond a certain limit, the domain
switches. The response of the polycrystal is the average of all domain processes. Mutual interaction of
domain processes is accounted for by some probabilistic functions.

Smith et al. [2003] developed a micromechanical model on the basis of the Helmholtz and Gibbs free
energy at the lattice level of the crystal structure of a single crystal. The embedding in polycrystalline
structures is carried out by means of a stochastic homogenization to include the inhomogeneous structure
of polycrystals. This model provides an excellent thermodynamical basis to simulate the macroscopic
behavior of ferroelectric polycrystals.

3. Phenomenological material model and its finite element implementation

The phenomenological material model used in this work was developed in [Kamlah and Tsakmakis
1999; Kamlah and Boehle 2001; Kamlah 2001]. Here, we will give only an outline of the basic fea-
tures. The model can describe ferroelectric and ferroelastic hysteresis behavior including mechanical
depolarization and polarization rotation. The finite element implementation reported in [Kamlah and
Boehle 2001] is computationally expensive since it relies on the solution of a system of nine ordinary
differential equations by means of an explicit Runge–Kutta algorithm. Therefore, a customized radial
return mapping algorithm was developed where computing the constitutive model was reduced to solving
a single nonlinear algebraic equation (see also [Laskewitz and Kamlah 2004]). This new implementation
reduced the computation time significantly and made it possible to simulate the poling processes of
structures consisting of tens of thousands of elements.

3.1. *Formulation of the phenomenological material model.* A constitutive model for ferroelectric ma-
terials relates strain S_{ij} and polarization P_i to the histories of stress T_{ij} and electric field E_i [Kamlah
2001]. Analogously to plasticity theory the hysteretic behavior of piezoceramic materials motivates a

decomposition of strain S_{ij} and polarization P_i into reversible and irreversible parts [Zhou et al. 2005a; 2005b]:

$$S_{ij} = S_{ij}^{\mathrm{r}} + S_{ij}^{\mathrm{i}}, \qquad P_i = P_i^{\mathrm{r}} + P_i^{\mathrm{i}}. \tag{1}$$

The irreversible parts represent volume averages of spontaneous strain and polarization, respectively, over some representative volume element. The reversible parts are related to the *stress tensor T_{ij}* and the *electric field vector E_i* by

$$S_{ij}^{\mathrm{r}} = C_{ijkl}^{-1} T_{kl} + d_{kij} E_k, \qquad P_i^{\mathrm{r}} = d_{ijk} T_{jk} + \kappa_{ij} E_j, \tag{2}$$

with C_{ijkl} as the *tensor of elasticity*, d_{ijk} as the *tensor of piezoelectricity* and κ_{ij} as the *tensor of susceptibility*. These equations possess the structure of linear piezoelectricity theory, in which the tensor of piezoelectricity is anisotropic and depends on the loading history in terms of the irreversible polarization P_i^{i}:

$$d_{kij} = \frac{\|P_i^{\mathrm{i}}\|}{P^{\mathrm{sat}}} \left\{ d^{\|} e_i e_j e_k + d^{\perp} (\delta_{ij} - e_i e_j) e_k + d^{=} \frac{1}{2} [(\delta_{ki} - e_k e_i) e_j + (\delta_{kj} - e_k e_j) e_i] \right\}. \tag{3}$$

Here, $\|P_i^{\mathrm{i}}\| = \sqrt{P_i^{\mathrm{i}} P_i^{\mathrm{i}}}$ and

$$e_i = \frac{P_i^{\mathrm{i}}}{\|P_i^{\mathrm{i}}\|} \tag{4}$$

is the unit vector in the direction of irreversible polarization, while the piezoelectric constants can be identified as $d^{\|} = d_{33}$, $d^{\perp} = d_{31}$, $d^{=} = \frac{1}{2} d_{15}$, and P^{sat} is the saturation value of irreversible polarization. We adopt the common simplification of assuming C_{ijkl} and κ_{ij} to be isotropic.

The loading history is represented in terms of irreversible strain S_{ij}^{i} and irreversible polarization P_i^{i} as internal variables. Irreversible strain S_{ij}^{i} is divided according to

$$S_{ij}^{\mathrm{i}} = S_{ij}^{\mathrm{ie}} + S_{ij}^{\mathrm{im}} \tag{5}$$

into electrically and mechanically induced parts. The electrically induced part is given as a function of irreversible polarization as

$$S_{ij}^{\mathrm{ie}} = \frac{3}{2} S^{\mathrm{sat}} \frac{\|P_i^{\mathrm{i}}\|}{P^{\mathrm{sat}}} \left(e_i e_j - \frac{1}{3} \delta_{ij} \right). \tag{6}$$

As will be sketched in the following, irreversible mechanically induced strain S_{ij}^{im} and irreversible polarization P_i^{i} are computed from evolution equations derived from switching criteria and saturation criteria.

The electrical switching function is expressed by

$$f^{\mathrm{e}}(E_i, P_i^{\mathrm{i}}) = \|E_i - c^{\mathrm{e}} P_i^{\mathrm{i}}\| - E^{\mathrm{c}}, \tag{7}$$

in which E^{c} and c^{e} are nonnegative material parameters. Condition $f^{\mathrm{e}} = 0$ defines the point where the coercive field is reached and domains begin to switch in the direction of the electric field, that is, irreversible polarization P_i^{i} starts to evolve. The evolution is limited such that the magnitude stays below the saturation polarization $\hat{P}^{\mathrm{sat}}$ with the help of the electrical saturation function

$$h^{\mathrm{e}}(E_i, P_i^{\mathrm{i}}, T_{ij}) = \|P_i^{\mathrm{i}}\| - \hat{P}^{\mathrm{sat}}(E_i, P_i^{\mathrm{i}}, T_{ij}), \tag{8}$$

in accordance with the condition $h^{\mathrm{e}} = 0$. Here, the saturation polarization is defined by

$$\hat{P}^{\mathrm{sat}}(T_{ij}, E_i, P_i^{\mathrm{i}}) = (P^{\mathrm{sat}} - P^{\delta}) \left\langle 1 - \frac{1}{m} \langle -\tfrac{3}{2} e_i T_{ij}^{\mathrm{D}} e_j - \hat{T}^{\mathrm{c}} \rangle \right\rangle + P^{\delta}, \tag{9}$$

with the constant $P^{\delta} \geq 0$ being the part of the remanent polarization which remains after the maximum mechanical depolarization and m a positive material constant. Furthermore, A_{ij}^{D} is the deviator of tensor A_{ij}, while $\langle x \rangle = 0$ for $x \leq 0$ and $\langle x \rangle = x$ for $x \geq 0$.

The mechanical switching function,

$$f^{\mathrm{m}}(E_i, P_i^{\mathrm{i}}, T_{ij}, S_{ij}^{\mathrm{im}}) = \|(T_{ij} - c^{\mathrm{m}} S_{ij}^{\mathrm{im}})^{\mathrm{D}}\| - \hat{T}^{\mathrm{c}}(E_i, P_i^{\mathrm{i}}), \tag{10}$$

is used to define at $f^{\mathrm{m}} = 0$ the point where the coercive stress $\hat{T}^{\mathrm{c}}$ is reached and the evolution of the mechanically induced irreversible strain S_{ij}^{im} is initiated. Here c^{m} is a nonnegative material parameter and $\|A_{ij}\| = \sqrt{A_{ij} A_{ij}}$. The coercive stress depends on the superposed electric field according to

$$\hat{T}^{\mathrm{c}}(E_i, P_i^{\mathrm{i}}) = \left\langle T^{\mathrm{c}} + n \frac{E_i}{E^{\mathrm{c}}} e_i \right\rangle \tag{11}$$

with n as a nonnegative material constant. The mechanical saturation function,

$$h^{\mathrm{m}}(P_i^{\mathrm{i}}, S_{ij}^{\mathrm{im}}) = \sqrt{\tfrac{2}{3}} \|S_{ij}^{\mathrm{im}}\| - \left(S^{\mathrm{sat}} - \sqrt{\tfrac{2}{3}} \|S_{ij}^{\mathrm{ie}}\| \right), \tag{12}$$

is used to limit by the condition $h^{\mathrm{m}} = 0$ the evolution of the total irreversible strain S_{ij}^{i} to the saturation strain S^{sat}.

The irreversible polarization and the irreversible strain are computed by evolution equations which are derived from the normality rule and the consistency condition for the respective active switching or saturation condition. By introducing the notation

$$\lfloor x \rceil = \begin{cases} 1, & x \geq 0, \\ 0, & x < 0, \end{cases} \qquad \lceil x \rfloor = \begin{cases} 1, & x > 0, \\ 0, & x \leq 0, \end{cases} \tag{13}$$

and

$$\overset{*}{f}{}^{\mathrm{e}} = \frac{d}{dt} f^{\mathrm{e}} \Big|_{\dot{P}_i^{\mathrm{i}} = 0}, \qquad \overset{*}{h}{}^{\mathrm{e}} = \frac{d}{dt} h^{\mathrm{e}} \Big|_{\dot{P}_i^{\mathrm{i}} = \lfloor f^{\mathrm{e}} \rceil \lfloor \overset{*}{f}{}^{\mathrm{e}} \rceil \lambda_f^{\mathrm{e}} \frac{\partial f^{\mathrm{e}}}{\partial E_i}},$$

$$\overset{*}{f}{}^{\mathrm{m}} = \frac{d}{dt} f^{\mathrm{m}} \Big|_{\dot{S}_{ij}^{\mathrm{i}} = 0}, \qquad \overset{*}{h}{}^{\mathrm{m}} = \frac{d}{dt} h^{\mathrm{m}} \Big|_{\dot{S}_{ij}^{\mathrm{i}} = \lfloor f^{\mathrm{m}} \rceil \lfloor \overset{*}{f}{}^{\mathrm{m}} \rceil \lambda_f^{\mathrm{m}} \frac{\partial f^{\mathrm{m}}}{\partial T_{ij}}}, \tag{14}$$

as well as

$$F^{\mathrm{k}} = \lfloor f^{\mathrm{i}} \rceil \lfloor \overset{*}{f}{}^{\mathrm{k}} \rceil, \qquad H^{\mathrm{k}} = \left\lceil \lfloor h^{\mathrm{k}} \rceil \lceil \overset{*}{h}{}^{\mathrm{k}} \rfloor + \lceil f^{\mathrm{k}} \rfloor \right\rceil, \qquad \mathrm{k} = \mathrm{e, m}, \tag{15}$$

and finally

$$n_i^{\mathrm{e}} = \frac{\partial h^{\mathrm{e}} / \partial P_i^{\mathrm{i}}}{\|\partial h^{\mathrm{e}} / \partial P_i^{\mathrm{i}}\|}, \qquad N_{ij}^{\mathrm{m}} = \frac{\partial h^{\mathrm{m}} / \partial S_{ij}^{\mathrm{i}}}{\|\partial h^{\mathrm{m}} / \partial S_{ij}^{\mathrm{i}}\|}, \tag{16}$$

the evolution equations for the state variables can be written as

$$\dot{P}_i^{\mathrm{i}} = (\delta_{ij} - H^{\mathrm{e}} n_i^{\mathrm{e}} n_j^{\mathrm{e}}) \left(F^{\mathrm{e}} \lambda_f^{\mathrm{e}} \frac{\partial f^{\mathrm{e}}}{\partial E_i} \right) + H^{\mathrm{e}} \lambda_h^{\mathrm{e}} \frac{\partial h^{\mathrm{e}}}{\partial P_i^{\mathrm{i}}}, \tag{17}$$

and

$$\dot{S}_{ij}^{\mathrm{im}} = (\delta_{ik}\delta_{jl} - H^{\mathrm{m}} N_{ij}^{\mathrm{m}} N_{kl}^{\mathrm{m}}) \Big(F^{\mathrm{m}} \lambda_{\mathrm{f}}^{\mathrm{m}} \frac{\partial f^{\mathrm{m}}}{\partial T_{ij}} \Big) + H^{\mathrm{m}} \lambda_h^{\mathrm{m}} \frac{\partial h^{\mathrm{m}}}{\partial S_{ij}^{\mathrm{im}}}. \tag{18}$$

The factors of proportionality λ_f^{e}, λ_h^{e}, λ_f^{m}, and λ_h^{m} are defined by the consistency conditions $\dot{f}^{\mathrm{e}} = 0$, $\dot{h}^{\mathrm{e}} = 0$, $\dot{f}^{\mathrm{m}} = 0$, and $\dot{h}^{\mathrm{m}} = 0$, respectively. For further details on this model, the reader is referred to [Kamlah and Tsakmakis 1999; Kamlah and Boehle 2001; Kamlah 2001].

3.2. *Finite element implementation.*

In [Kamlah and Boehle 2001], a finite element implementation of the phenomenological constitutive model sketched in the previous section is presented, where the system (17), (18) is solved by an explicit higher order integration scheme considering all combinations of cases that may occur. This scheme turned out to be too slow and not very reliable. In the following, we will describe a customized radial return mapping algorithm exploiting the hierarchy of switching and saturation criteria.

The electromechanical finite element formulation of Allik and Hughes [1970], which employs displacement and electric potential as primary nodal variables, is used. In the nonlinear finite element method, the loading history is divided into increments. In the following, the indices n and $n + 1$ describe the states at the beginning and end of the current increment, respectively. At the beginning of increment n, the state of all variables is known. We assume that trial values ${}^{n+1}S_{ij}$ and ${}^{n+1}E_i$ for strain and electric field, respectively, have been computed by the global Newton method. The irreversible polarization ${}^{n+1}P_i^{\mathrm{i}}$ and mechanically induced strain ${}^{n+1}S_{ij}^{\mathrm{im}}$ corresponding to the trial values have to be calculated. Once all state variables at the end of the increment are known, ${}^{n+1}T_{ij}$ and ${}^{n+1}D_i$ can be computed to check equilibrium, $T_{ij,j} = 0$, and Gauss' law, $D_{i,i} = 0$. Here, $D_i = \varepsilon_0 E_i + P_i$ is the electric displacement and ε_0 is the dielectric constant of vacuum.

In this work, the irreversible polarization and the irreversible strain at the end of the increment are obtained from a two step corrector scheme by

$$^{n+1}P_i^{\mathrm{i}} = {}^{n}P_i^{\mathrm{i}} + \Delta P_i^{\mathrm{i,f}} + \Delta P_i^{\mathrm{i,h}}, \qquad {}^{n+1}S_{ij}^{\mathrm{im}} = {}^{n}S_{ij}^{\mathrm{im}} + \Delta S_{ij}^{\mathrm{im,f}} + \Delta S_{ij}^{\mathrm{im,h}}. \tag{19}$$

The correctors $\Delta P_i^{\mathrm{i,f}}$, $\Delta P_i^{\mathrm{i,h}}$, $\Delta S_{ij}^{\mathrm{im,f}}$, and $\Delta S_{ij}^{\mathrm{im,h}}$ of irreversible polarization and mechanically induced irreversible strain in the radial return mapping algorithm are obtained from the corresponding electric and mechanical switching and saturation criteria, respectively. The calculation of the correctors for the example of irreversible polarization is explained with the help of Table 1 and Figure 1.

First, the criterion for the onset of electrically induced domain switching according to Equation (7) is checked. For $f^{\mathrm{e}}({}^{n+1}E_i, {}^{n}P_i^{\mathrm{i}}) \leq 0$, no switching occurs and, thus, there is no evolution of irreversible polarization in the current load step, that is, $\Delta P_i^{\mathrm{i,f}} = 0$. For $f^{\mathrm{e}}({}^{n+1}E_i, {}^{n}P_i^{\mathrm{i}}) > 0$, the trial value ${}^{n+1}E_i$ for the electric field violates the electric switching criterion, and a nontrivial corrector $\Delta P_i^{\mathrm{i,f}}$ needs to be calculated such that $f^{\mathrm{e}}({}^{n+1}E_i, {}^{n}P_i^{\mathrm{i}} + \Delta P_i^{\mathrm{i,f}}) = 0$ is satisfied. According to the first term in (17), we make the ansatz that the corrector $\Delta P_i^{\mathrm{i,f}}$ is in the direction normal to the electric switching criterion. The normal is calculated on the basis of the trial value for the electric field and irreversible polarization from the last load step,

$$\Delta P_i^{\mathrm{i,f}} = \alpha^{\mathrm{e}} \frac{\partial f^{\mathrm{e}}({}^{n+1}E_i, {}^{n}P_i^{\mathrm{i}})}{\partial E_i}, \tag{20}$$

Criterion	Ansatz for corrector	Condition for magnitude
Onset of switching		
$f^e(^{n+1}E_i, {}^nP_i^i) \leq 0$	$\Delta P_i^{i,f} = 0$	
$f^e(^{n+1}E_i, {}^nP_i^i) > 0$	$\Delta P_i^{i,f} = \alpha^e \dfrac{\partial f^e(^{n+1}E_i, {}^nP_i^i)}{\partial E_i}$	$f^e(^{n+1}E_i, {}^nP_i^i + \Delta P_i^{i,f}) = 0$
Saturation		
$h^e(^{n+1}S_{ij}, {}^{n+1}E_i, {}^nP_i^i + \Delta P_i^{i,f}) \leq 0$	$\Delta P_i^{i,h} = 0$	
$h^e(^{n+1}S_{ij}, {}^{n+1}E_i, {}^nP_i^i + \Delta P_i^{i,f}) > 0$	$\Delta P_i^{i,h} = \beta^e \dfrac{\partial h^e(^{n+1}S_{ij}, {}^{n+1}E_i, {}^nP_i^i + \Delta P_i^{i,f})}{\partial P_i^i}$	$h^e(^{n+1}S_{ij}, {}^{n+1}E_i, {}^nP_i^i + \Delta P_i^{i,f} + \Delta P_i^{i,h}) = 0$

Table 1. Conditions for the calculation of the correctors for irreversible polarization. Condition $f^e = 0$ can be solved analytically for α^e, while $h^e = 0$ has to be solved numerically for β^e.

where the factor of proportionality α^e gives the magnitude of the corrector. Plugging this into the condition $f^e(^{n+1}E_i, {}^nP_i^i + \Delta P_i^{i,f}) = 0$ leads to a nonlinear equation which can be solved analytically to yield

$$\alpha^e = \frac{1}{c^e} f^e(^{n+1}E_i, {}^nP_i^i), \tag{21}$$

and, thus, the corrector $\Delta P_i^{i,f}$ is completely determined.

Next, the criterion for the saturation of irreversible polarization according to (8) has to be checked. For this, the stresses have to be eliminated by the trial strains with the help of $(1)_1$, (2), and (5). For $h^e(^{n+1}S_{ij}, {}^{n+1}E_i, {}^nP_i^i + \Delta P_i^{i,f}) \leq 0$, saturation polarization has not yet been reached in the current load step, and, consequently, $\Delta P_i^{i,h} = 0$. On the other hand, for $h^e(^{n+1}S_{ij}, {}^{n+1}E_i, {}^nP_i^i + \Delta P_i^{i,f}) > 0$, the magnitude of the possibly once corrected polarization vector ${}^nP_i^i + \Delta P_i^{i,f}$ calculated from the trial strain and trial electric field is beyond its stress dependent saturation value. A corresponding corrector $\Delta P_i^{i,h}$ is calculated from the condition $h^e(^{n+1}S_{ij}, {}^{n+1}E_i, {}^nP_i^i + \Delta P_i^{i,f} + \Delta P_i^{i,h}) = 0$. For this, we obtain from the second term in evolution (17) the ansatz for corrector $\Delta P_i^{i,h}$ to be normal to the saturation criterion $h^e(^{n+1}S_{ij}, {}^{n+1}E_i, {}^nP_i^i + \Delta P_i^{i,f}) = 0$ given by the trial values for strain and electric field and the once corrected irreversible polarization vector:

$$\Delta P_i^{i,h} = \beta^e \frac{\partial h^e(^{n+1}S_{ij}, {}^{n+1}E_i, {}^nP_i^i + \Delta P_i^{i,f})}{\partial P_i^i}. \tag{22}$$

Requiring the saturation criterion to be satisfied yields the nonlinear algebraic equation

$$h^e\left({}^{n+1}S_{ij}, {}^{n+1}E_i, {}^nP_i^i + \Delta P_i^{i,f} + \beta^e \frac{\partial h^e(^{n+1}S_{ij}, {}^{n+1}E_i, {}^nP_i^i + \Delta P_i^{i,f})}{\partial P_i^i}\right) = 0, \tag{23}$$

which needs to be solved numerically for the only unknown scalar parameter β^e.

In a similar way as just described, correctors $\Delta S_{ij}^{im,f}$ and $\Delta S_{ij}^{im,h}$ are computed for the irreversible strain. The corresponding conditions $f^m = 0$ and $h^m = 0$ for α^m and β^m, respectively, can both be solved analytically. Special care has to be taken, as the two saturation criteria are electromechanically coupled, such that, depending on the loading, they might be considered separately or have to be considered together.
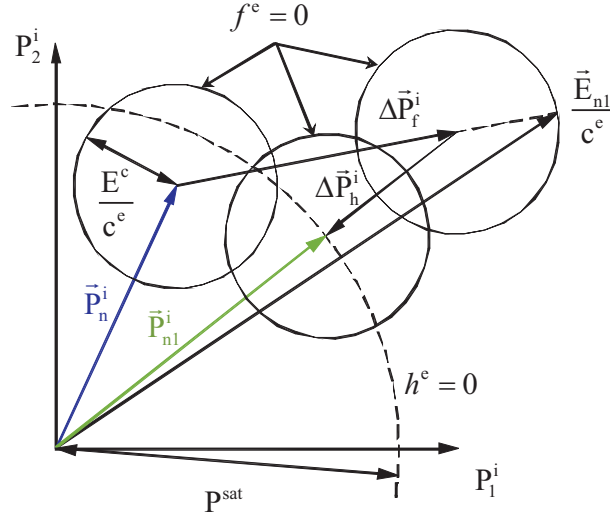
Figure 1. The radial return mapping algorithm used for the finite element implementation of the phenomenological material model for the dielectric hysteresis: In case the predictor $^{n+1}E_i/c^e$ violates the electrical switching condition f^e (the solid circle with irreversible polarization $^nP_i^i$ of the last increment as its center), the corrector $\Delta P_i^{i,f}$ is found. In the situation where all domains are switched into the direction of the electric field, the electrical saturation condition h^e (the dashed circle) becomes active meaning the new predictor $^nP_i^i + \Delta P_i^{i,f}$ has to be checked. If it is outside the saturation condition, an additional corrector $\Delta P_i^{i,h}$ has to be computed which lies on the line of action of $^nP_i^i + \Delta P_i^{i,f}$.

Nevertheless, in any case the problem can be reduced to solving numerically at most a single nonlinear scalar algebraic equation for a single scalar parameter. For the numerical solution, Newton's method and the regula falsi method are used. For the full set of equations including all details on the solution algorithm the reader is referred to [Laskewitz 2007].

3.3. *Verification of the finite element implementation.* This section describes the verification of the material model and its finite element implementation. Simple experiments were carried out [Laskewitz 2007] and compared to simulation results. Table 2 shows the values of the material parameters. Because of the usually ill conditioned electromechanical stiffness matrix, the material parameters are recalculated in units which lead to a better conditioned matrix.

Figure 2 shows the dielectric and the butterfly hysteresis of the simulations and experiments. The corner points of the simulation results represent the electrical switching and saturation conditions of the phenomenological model. A good agreement is observed between the simulation and the experimental results.

3.4. *Simulation example: stack actuator.* To demonstrate the capability of the presented finite element tool a simulation example is presented in this section. It deals with the poling process of a common stack actuator (see Figure 3) which consists of many thin layers with inner electrodes. The basic idea of a stack actuator is to provide large longitudinal displacements at moderate voltages. To reduce the danger of

E^{c} (MV/mm)	1.0×10^3
P^{sat} (kN/(MVmm))	310×10^{-3}
σ^{c} (kN/mm^2)	40.0×10^{-3}
S^{sat}	0.00225
Y (kN/mm^2)	60.0
ν	0.37
$d^{\parallel}$ (mm/MV)	6.75×10^{-1}
$d^{\perp}$ (mm/MV)	-3.15×10^{-1}
$d^{=}$ (mm/MV)	4.35×10^{-1}
c^{e} (MV^2/kN)	1.0×10^{-3}
c^{m} (kN/mm^2)	20.0
P^{δ} (kN/(MVmm))	100×10^{-3}
n (kN/mm^2)	20.0×10^{-3}
m (kN/mm^2)	150×10^{-3}

Table 2. Material parameters used in simulations.
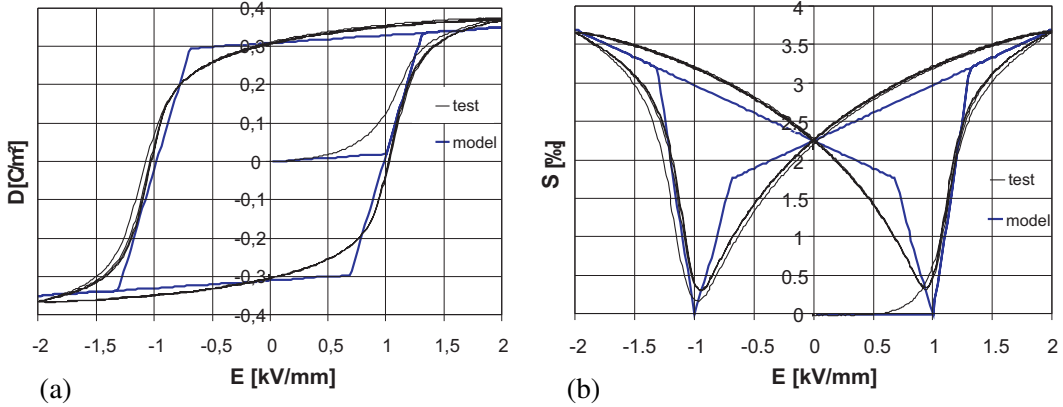
Figure 2. Comparison of simulation results with experiments: (a) dielectric hysteresis and (b) butterfly hysteresis.

electrical arcing and to eliminate the need for a high voltage source, the actuator is composed of a large number of thin piezoceramic layers ($< 100 \, \mu$m) sandwiched between alternately contacted electrodes. The inner electrodes end at a certain distance from the side opposite to the so-called termination electrode by which they are connected to the voltage source. Common usages of stack actuators are diesel injection valves or positioners because of the short response time and the ability for very accurate positioning.

We consider a 2D finite element model representing half of a piezoceramic layer. Figure 3 also shows a sketch of the electric field lines to be expected. The finite element discretization and the geometry are depicted in Figure 4. The model consists of approximately 1000 elements (plane strain). The nodes at the top of the model are coupled to have equal displacement in the vertical direction as a symmetry condition. On the left hand side of the model, we use fixed horizontal displacements as an approximation
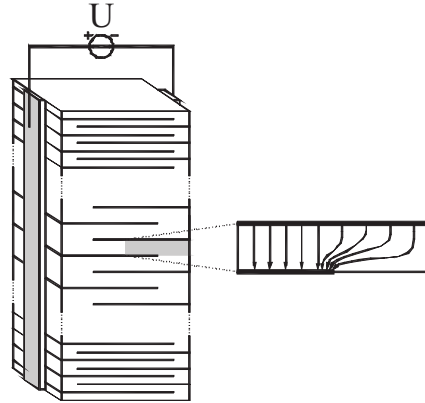
**Figure 3.** Simplified sketch of a stack actuator.
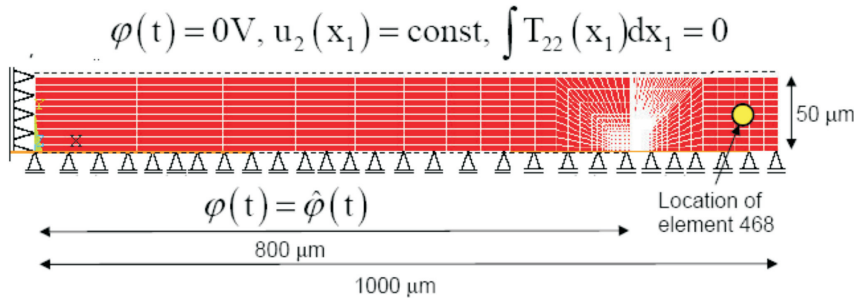
Figure 4. Finite element discretization of a part of the layer of a stack actuator.

of the antisymmetry along this line. This seems to be satisfied as the distance to the field intensification at the electrode tip is much larger than the thickness of the layer. The electrode at the bottom ends at a distance of $200\,\mu$m from the right border. To simulate the poling process of such devices, an electric potential is applied to the top line of the model to reach a maximum voltage of $150\,$V (an average electric field of $3\,$kV/mm). Afterwards the actuator is electrically unloaded.

Figure 5 shows the simulation results of the electric potential at maximum load and after unloading.

For linear simulations with commercial finite element codes, usually a homogeneous polarization state in the vertical direction is assumed. In contrast to this, the poling state in the nonlinear ferroelectric simulations is computed here and not assumed. There is no evolution of irreversible polarization in the region to the right of the tip of the lower electrode, because there is a nearly homogeneous electric potential (see Figure 5a) and, consequently, the tensor of piezoelectricity is still zero (see Equation (4)). After unloading (see Figure 5b) there remains a significant electric potential around the electrode tip which can be explained by the divergence of the irreversible polarization vector in the neighborhood of the tip. Figure 6 shows the irreversible polarization at maximum load around the electrode tip.

Figure 7 shows the distribution of the normal stress in the vertical direction plotted along the bottom line of the model at maximum load and after unloading. At the electrode tip, there is a stress intensification. More importantly, the level of tensile stress in the unpoled area even after unloading remains at $40\,$MPa. This tensile stress is caused by the vertical extension of the active region to the left of the
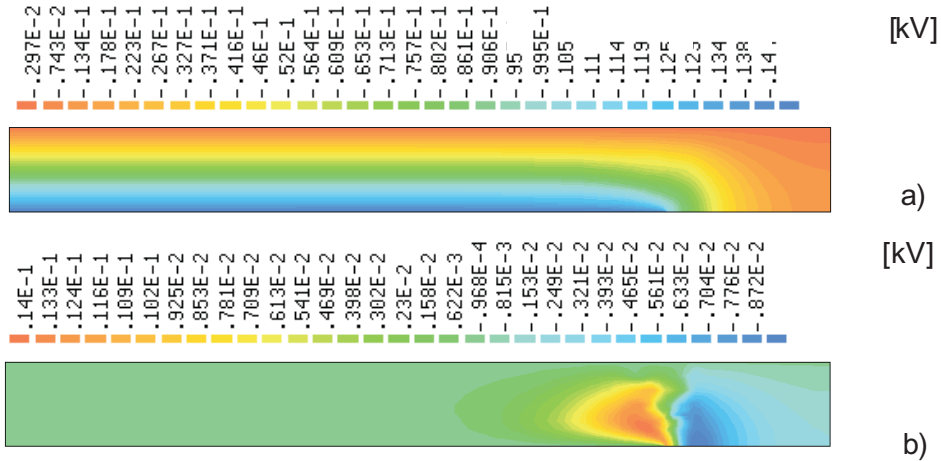
Figure 5. Distribution of the electric potential of a part of a layer of a stack actuator: (a) ferroelectric simulation at maximum voltage and (b) ferroelectric simulation after unloading.
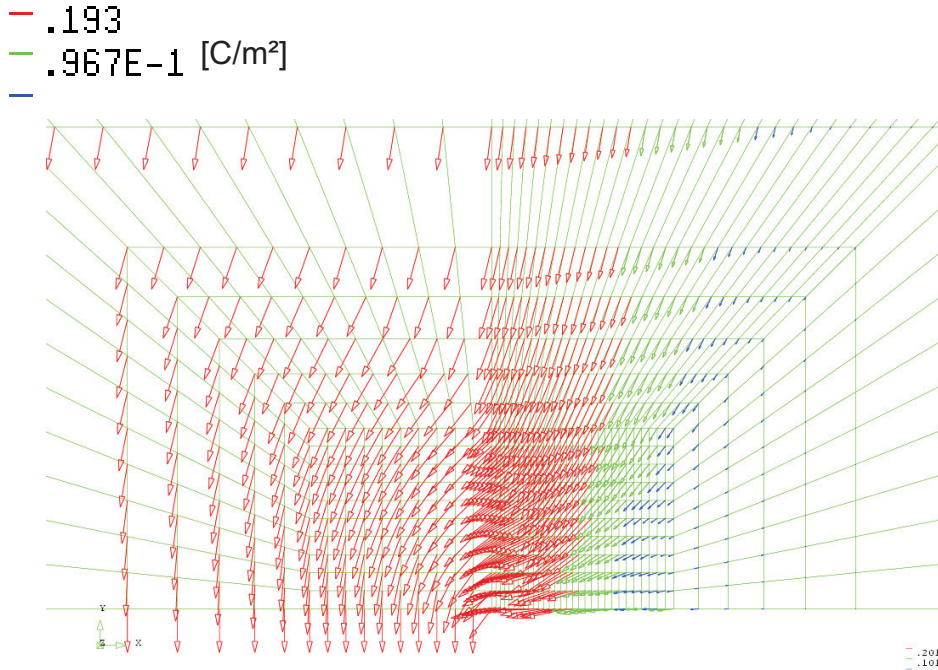
Figure 6. Vector plot of the irreversible polarization around the electrode tip.

electrode tip during poling. By equilibrium, these tensile stresses give rise to compressive stresses along the lower electrode to the left of its tip. For wider actuators with a larger active region of the layer between the electrodes this compressive stress would be smaller. The tensile stresses are in the range of the tensile strength of the material and can lead to cracks while poling the device. Moreover, after poling there is cyclic loading which increases the danger of fatigue because of the residual tensile stress in the
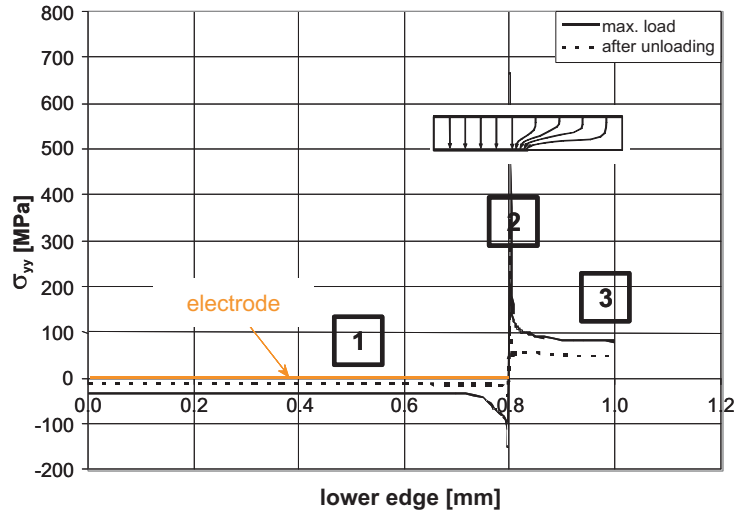
Figure 7. Stress distribution in the vertical direction at the bottom line of the finite element model at maximum load and after unloading.

passive region to the right to the electrode tip. In practice the actuators are prestressed in applications to avoid cracking. By using our finite element tool the magnitude of the prestress and the geometries of the devices may be optimized. On the one hand, the tensile stresses have to be minimized by means of the prestress. On the other hand, too large a prestress has to be avoided, so no mechanical depolarization can occur, which would reduce the performance of the actuator. An optimum between minimal depolarization and minimal tensile stress has to be found.

Further simulation examples from experimental practice can be found in [Laskewitz et al. 2006] (piezoceramic thin walled tubes) and [Westram et al. 2007] (electrically driven crack growth).

4. Microscopically motivated material model and its finite element implementation

4.1. *Formulation of the microscopically motivated material model.* In this section, we present a microscopically motivated constitutive model for ferroelectrics, the development of which started with [Kamlah and Jiang 1999; Kamlah and Wang 2003]. Just as with the model introduced in the previous section, this model is applied at macroscopic length scales, that is, at the level of engineering components. In contrast to the previous model which is formulated by methods of classical phenomenological modeling, the model in this section relies on quantities of clear micromechanical meaning. For a tetragonal structure of the unit cells, the microscopically motivated model is based on the orientation distribution of lattice axes and spontaneous polarization. A tetragonal unit cell possesses two distinct lattice constants, the c-axis which is up to 1% larger than the other axis, called the a-axis. For each orientation of the c-axis, there are still two possible orientations of the spontaneous polarization, and regions in a grain which have the same orientation of c-axes and spontaneous polarizations are called domains.

As with the phenomenological model, the current model relies on an additive decomposition. However, for the microscopically motivated constitutive model, irreversible strain and polarization themselves are not taken as internal or state variables. Rather, they are assumed to be functions of some microstructural

parameters $q^1, \ldots, q^n$, which represent the microscopic domain state at the macroscopic level, and in this way act as the state variables:

$$S^{\mathrm{i}}_{ij} = S^{\mathrm{i}}_{ij}(q^1, \ldots, q^n), \qquad P^{\mathrm{i}}_i = P^{\mathrm{i}}_i(q^1, \ldots, q^n). \tag{24}$$

The model is based on the Gibbs free energy

$$g = \tfrac{1}{2} T_{ij} C^{-1}_{ijkl} T_{kl} + E_i d_{ijk} T_{jk} + \tfrac{1}{2} E_i \kappa_{ij} E_j + \mathrm{gi}(q^1, \ldots, q^n). \tag{25}$$

By exploiting the Clausius–Duhem inequality, this leads to relations (2) with the definition of the material tensors as before, in particular (3). Furthermore, we obtain the driving forces

$$\phi^\alpha = E_i \frac{\partial P^{\mathrm{i}}_i}{\partial q^\alpha} + T_{ij} \frac{\partial S^{\mathrm{i}}_{ij}}{\partial q^\alpha} + \rho \frac{\partial g}{\partial q^\alpha}, \quad \alpha = 1, \ldots, n, \tag{26}$$

being thermodynamically conjugate to the corresponding state variable q^α. Further details on the thermodynamical framework can be found in [Kamlah and Wang 2003].

By means of a convex switching function $f = f(\phi^1, \ldots, \phi^n)$, which includes the origin, the normality rule

$$\dot{q}^\alpha = \lambda \frac{\partial f}{\partial \phi^\alpha} \tag{27}$$

leads to evolution equations for the state variables which satisfy the dissipation inequality in a sufficient manner. Here, for a rate independent theory, the irreversible multiplier λ can be determined by means of the consistency condition:

$$\lambda \begin{cases} \text{solves } \dot{f} = \sum_{\alpha=1}^{n} \frac{\partial f}{\partial \phi^\alpha} \frac{\partial \phi^\alpha}{\partial q^\beta} \dot{q}^\beta = 0 & \text{for } f(\phi^1, \ldots, \phi^n) = 0 \text{ and } \dot{f}|_{\dot{q}^1, \ldots, \dot{q}^n = 0} > 0, \\ = 0 & \text{else.} \end{cases} \tag{28}$$

4.1.1. *1D approach.* For a better understanding, the choice of internal state variables of the model is motivated by means of a 1D approach. Figure 8 shows a projection of a unit sphere with two inner cones, where the cones axes are parallel the loading direction (x_3) and the cones have an opening angle θ^{e}. The continuous straight lines represent the orientation of selected c-axes and the direction of the spontaneous polarization is indicated by the arrow tips. The sphere represents the distribution of the orientation of c-axes and spontaneous polarization in some representative volume element in the neighborhood of a point in a macrocontinuum. Figure 8b symbolizes the thermally depolarized initial state where the distribution c-axes and spontaneous polarization is uniform over the sphere. For this initial state, the average macroscopic irreversible polarization and strain are zero.

The first state variable to be identified is $q^1 = \beta$, which is the fraction of c-axes within the cones. The range of β is $\beta \in [0; 1]$, in which zero is the case where no c-axes are inside the cones. For $\beta = 1$, all c-axes are within the cones in which case the irreversible strain reaches its saturation value $S^{\mathrm{i}}_{33} = S^{\mathrm{sat}}$. For the initial state of random distribution of the c-axes β assumes its reference value β^{ref}. The opening angle θ^{e} of the cones and the state variable β can also be interpreted as parameters of a step function approximation of the orientation distribution function (ODF) of the c-axes. This distribution would be transversely isotropic meaning that it is invariant for arbitrary rotations about the axis of loading. The

poloidal variation of this approximate ODF can be written as

$$p(\theta) = \begin{cases} \dfrac{\beta}{4\pi\,(1-\cos\theta^{\mathrm{e}})} & \text{for } 0 \le \theta \le \theta^{\mathrm{e}} \text{ and } \pi - \theta^{\mathrm{e}} \le \theta \le \pi, \\[2mm] \dfrac{1-\beta}{4\pi\,\cos\theta^{\mathrm{e}}} & \text{for } \theta^{\mathrm{e}} < \theta < \pi - \theta^{\mathrm{e}}, \end{cases} \qquad 0 \le \beta \le 1. \tag{29}$$

For the initial random state, that is, a uniform distribution of the c-axes, β assumes its reference value $\beta^{\mathrm{ref}} = 1 - \cos\theta^{\mathrm{e}}$. A graphical representation of the ODF is shown in Figure 9 for the range $0 \le \theta \le \frac{\pi}{2}$.

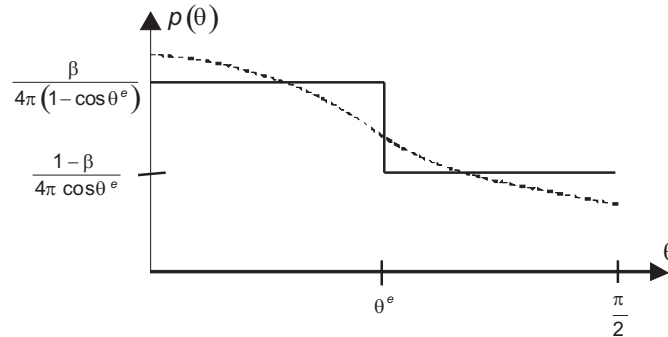By integration over the approximate ODF [Kamlah and Wang 2003], we obtain immediately

$$S_{33}^{\mathrm{i}}(\beta) = S^{\mathrm{sat}} \frac{\beta - \beta^{\mathrm{ref}}}{1 - \beta^{\mathrm{ref}}} \tag{30}$$

for the dependence of irreversible strain on the microstructural parameter β.

For each fixed orientation of the c-axes of a domain, there are still two possible directions for the corresponding spontaneous polarization. From this it is quite obvious, that variable β is not sufficient to describe the macroscopic state within the unit sphere, see Figure 8. Rather, a second state variable
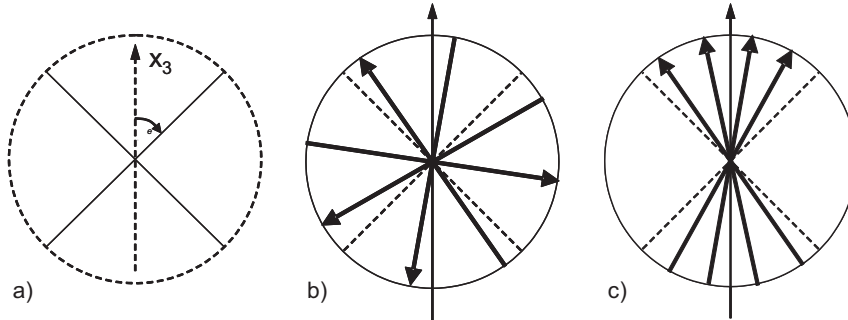
Figure 8. Projection of a sphere with two inner cones around the loading axis x_3.

Figure 9. Transversally isotropic ODF $p(\theta)$ for the domain density. The dashed line represents the real function, while the solid line is the simplification used in the material model.

$q^2 = \gamma$ needs to be introduced, describing the relative macroscopic polarization:

$$\gamma = \frac{\|P_i^{\mathrm{i}}\|}{P^{\mathrm{sat}}}. \tag{31}$$

Of course, $\gamma = 0$ holds for the thermally depolarized initial state, as there is no polarization at the macroscopic level. It has to be noted that state variable γ is not completely independent of β. Integration over the approximate ODF [Kamlah and Wang 2003] yields the maximum irreversible polarization belonging to a given orientation state of the c-axes. One obtains

$$\gamma^{\mathrm{max},\|}(\beta) = \frac{\beta + \cos\theta^{\mathrm{e}}}{1 + \cos\theta^{\mathrm{e}}} = \frac{\beta - \beta^{\mathrm{ref}} + 1}{2 - \beta^{\mathrm{ref}}} \tag{32}$$

for the maximum relative irreversible polarization in the loading direction that can be attained for a given orientation state of the c-axes characterized by β. The maximum or minimum ($\gamma = \pm 1$) can only be reached if all c-axes are within the cones, that is, $\beta = 1$. If all c-axes are outside of the cones, a maximum polarization magnitude of $\gamma^{\mathrm{max},\|}(0)$ is still possible. For $0 \le \beta \le 1$ the maximum irreversible polarization is a function of β:

$$|\gamma| \le \gamma^{\mathrm{max},\|}(\beta). \tag{33}$$

Thus, β and γ may assume values only from a range of admissible values defined by

$$G = \left\{(\beta, \gamma) \,\middle|\, |\gamma| \le \gamma^{\mathrm{max},\|}(\beta),\, 0 \le \beta \le 1\right\}. \tag{34}$$

Figure 10 shows region G with border ∂G which β and γ are not allowed to leave. To compare both, the phenomenological and the microscopically motivated constitutive models, we consider the simple simulation in Figure 11, showing dielectric and butterfly hysteresis, respectively. It clearly can be seen that the evolution of the state variables initiates at reaching the coercive field. After this, the plots of the curves differ significantly. In the microscopically motivated material model, 90 and 180 switching processes and saturation are taken into account more realistically. After reaching the saturation both models follow the linear piezoelectric behavior.

4.1.2. *3D generalization of the material model.* In the following, the material model will be generalized for 3D loadings. Therefore, two additional state variables are introduced. The first one $q^3 = e_i^{\beta}$ is a unit
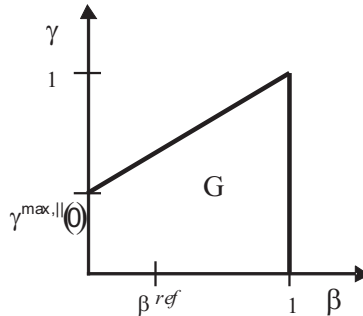
Figure 10. Range G of admissible values for the state variables β and γ.
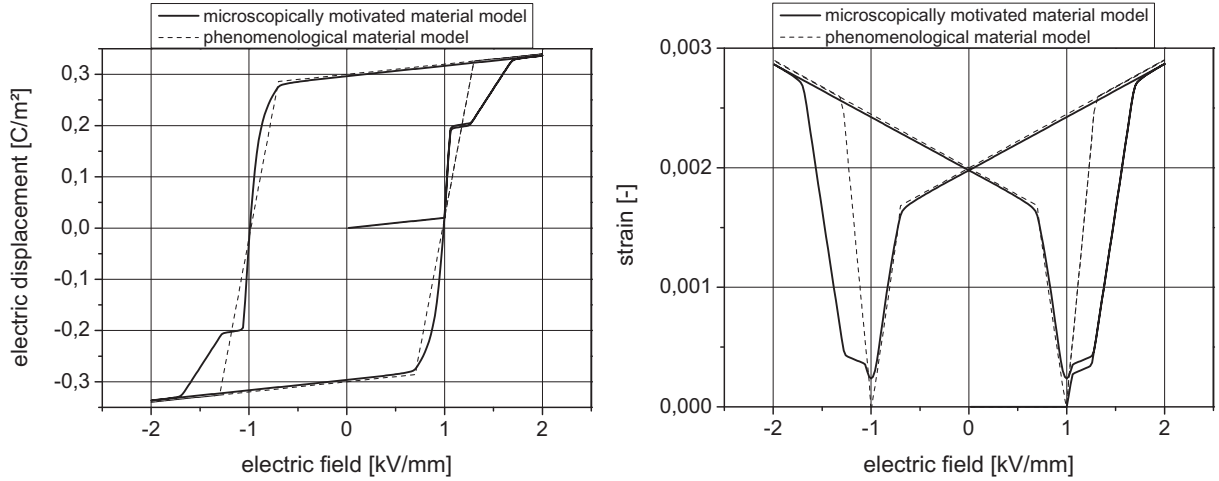
Figure 11. Dielectric and butterfly hysteresis for both material models.

vector representing the direction of the axis of the transversely isotropic ODF in 3D space. This direction depends on the loading history. Then, the irreversible strain is written as

$$S_{ij}^{\mathrm{i}} = \frac{3}{2} S^{\mathrm{sat}} \frac{\beta - \beta^{\mathrm{ref}}}{1 - \beta^{\mathrm{ref}}} \left(e_i^{\beta} e_j^{\beta} - \frac{1}{3} \delta_{ij} \right), \tag{35}$$

where δ_{ij} is the Kronecker symbol. This tensor represents an irreversible strain state with a normal strain according to Equation (30) in the direction of unit vector e_i^{β}. The normal strains perpendicular to e_i^{β} then follow from the requirement that the total irreversible strain tensor must be isochoric. This requirement is motivated by switching processes being the underlying mechanism.

Depending on the loading history, the direction of the ODF and the direction of the irreversible polarization need not be the same. Therefore, another unit vectorial state variable $q^4 = e_i^{\gamma}$ is introduced by which the irreversible polarization vector is expressed as $P_i^{\mathrm{i}} = \gamma\, P^{\mathrm{sat}} e_i^{\gamma}$.

Since in general e_i^{β} and e_i^{γ} include an angle resulting in $|e_i^{\beta} e_i^{\gamma}| < 1$, the region G of admissible values for our internal variables has to be reformulated. If $e_i^{\beta} = e_i^{\gamma}$, we have $|\gamma| \leq \gamma^{\mathrm{max},\|}(\beta)$. If e_i^{β} and e_i^{γ} are perpendicular to each other, one finds $|\gamma| \leq \gamma^{\mathrm{max},\perp}(\beta)$, where $\gamma^{\mathrm{max},\perp}$ is obtained from integration over the ODF [Kamlah and Wang 2003] yielding

$$\gamma^{\mathrm{max},\perp}(\beta) = \frac{\pi - 2\theta^{\mathrm{e}} + \sin 2\theta^{\mathrm{e}}}{\pi \cos \theta^{\mathrm{e}}(1 + \cos \theta^{\mathrm{e}})} + \left(\frac{2\theta^{\mathrm{e}} - \sin 2\theta^{\mathrm{e}}}{\pi(1 - \cos^2 \theta^{\mathrm{e}})} - \frac{\pi - 2\theta^{\mathrm{e}} + \sin 2\theta^{\mathrm{e}}}{\pi \cos \theta^{\mathrm{e}}(1 + \cos \theta^{\mathrm{e}})} \right) \beta. \tag{36}$$

For an arbitrary angle with $0 \leq \cos|e_i^{\beta} e_i^{\gamma}| \leq 1$, the linear interpolation,

$$\gamma^{\mathrm{max}}(\beta, e_i^{\beta}, e_i^{\gamma}) = \gamma^{\mathrm{max},\perp}(\beta) + \left(\gamma^{\mathrm{max},\|}(\beta) - \gamma^{\mathrm{max},\perp}(\beta) \right) |e_i^{\beta} e_i^{\gamma}|, \tag{37}$$

is used for the maximum magnitude of relative irreversible polarization. In summary, the region of admissible values for the set $\{\beta, \gamma, e_i^{\beta}, e_i^{\gamma}\}$ of internal state variables in 3D reads as

$$G = \left\{ (\beta, \gamma, e_i^{\beta}, e_i^{\gamma}) \;\middle|\; |\gamma| \leq \gamma^{\mathrm{max}}(\beta, e_i^{\beta}, e_i^{\gamma}), 0 \leq \beta \leq 1 \right\}. \tag{38}$$

4.1.3. *3D formulation of the evolution equations.* As a hardening parameter, an energy barrier function is introduced which satisfies the conditions

$$
F^G \to \infty \qquad\qquad\qquad \text{for } (\beta, \gamma, e_i^\beta, e_i^\gamma) \to \partial G,
$$
$$
F^G = 0, \frac{\partial F^G}{\partial \beta} = 0, \text{ and } \frac{\partial F^G}{\partial \gamma} = 0 \quad \text{for } (\beta, \gamma) = (\beta^{\text{ref}}, 0) \text{ and all } (e_i^\beta, e_i^\gamma).
\tag{39}
$$

While the first condition implies that the region of admissible values is surrounded by an energy wall of infinite height, the second condition ensures that there is no effect from the energy barrier function F^G in the unpoled initial state. The energy barrier function was chosen as

$$
F^G = A\Big(b(\beta)\big(\beta^{-N} + (1-\beta)^{-N}\big) + g(\gamma)\big(\gamma^{\max} - |\gamma|\big)^{-N}\Big),
\tag{40}
$$

in which A und N are positive constants and, for example, $b(\beta) = (\beta - \beta^{\text{ref}})^4$ and $g(\gamma) = \gamma^4$ to enforce the second set of conditions (39).

By means of the Gibbs free energy, the driving forces for the internal variables can be obtained from expression (26) as

$$
\phi^\beta = \frac{3}{2} \frac{S^{\text{sat}}}{1-\beta^{\text{ref}}}\Big(e_i^\beta e_j^\beta - \frac{1}{3}\delta_{ij}\Big)T_{ij} + \frac{1}{2}\frac{\partial C_{jklm}^{-1}}{\partial \beta}T_{jk}T_{lm} + \frac{1}{2}\frac{\partial \kappa_{jk}}{\partial \beta}E_j E_k - c^\beta(\beta - \beta^{\text{ref}}) - \frac{\partial F^G}{\partial \beta},
$$
$$
\phi^\gamma = P^{\text{sat}}E_i e_i^\gamma + \frac{\partial d_{kij}}{\partial \gamma}E_k T_{ij} - c^\gamma \gamma - \frac{\partial F^G}{\partial \gamma},
$$
$$
\phi_i^{\vec{e}\beta} = 3S^{\text{sat}}\frac{\beta - \beta^{\text{ref}}}{1-\beta^{\text{ref}}}T_{ij}e_j^\beta + \frac{1}{2}\frac{\partial C_{jklm}^{-1}}{\partial e_i^\beta}T_{jk}T_{lm} + \frac{1}{2}\frac{\partial \kappa_{jk}}{\partial e_i^\beta}E_j E_k - \frac{\partial F^G}{\partial e_i^\beta},
$$
$$
\phi_i^{\vec{e}\gamma} = P^{\text{sat}}\gamma E_i + \gamma \frac{\partial d_{krs}^{\text{sat}}}{\partial e_i^\gamma}E_k T_{rs} - \frac{\partial F^G}{\partial e_i^\gamma}.
\tag{41}
$$

Since e_i^β and e_i^γ have to remain unit vectors, only the component of the driving force perpendicular to the corresponding unit vector must be taken into account for the respective evolution equation:

$$
\phi_i^{\vec{e}\beta,\perp} = (\delta_{ij} - e_i^\beta e_j^\beta)\phi_j^{\vec{e}\beta}, \qquad \phi_i^{\vec{e}\gamma,\perp} = (\delta_{ij} - e_i^\gamma e_j^\gamma)\phi_j^{\vec{e}\gamma}.
\tag{42}
$$

This is by analogy to incremental plasticity, where only the stress deviator contributes to the evolution of volume preserving plastic strain.

As a simple choice, the convex switching function is then given by

$$
f = \sqrt{\Big(\frac{\phi^\beta}{\phi^{\beta,0}}\Big)^2 + \Big(\frac{\phi^\gamma}{\phi^{\gamma,0}}\Big)^2 + \Big(\frac{|\vec{\phi}^{\vec{e}\beta,\perp}|}{\phi^{\vec{e}\beta,0}}\Big)^2 + \Big(\frac{|\vec{\phi}^{\vec{e}\gamma,\perp}|}{\phi^{\vec{e}\gamma,0}}\Big)^2} - 1,
\tag{43}
$$

in which

$$
\phi^{\beta,0} = \frac{S^{\text{sat}}\sigma^{\text{c}}}{1-\beta^{\text{ref}}}, \qquad \phi^{\gamma,0} = P^{\text{sat}}E^{\text{c}}, \qquad \phi^{\vec{e}\beta,0} = \sqrt{3}\sigma^{\text{c}}S^{\text{sat}}\frac{\beta - \beta^{\text{ref}}}{1-\beta^{\text{ref}}}, \qquad \phi^{\vec{e}\gamma,0} = \gamma P^{\text{sat}}E^{\text{c}}.
\tag{44}
$$

For pure electric loadings, this criterion is satisfied (that is, $f = 0$) if the magnitude of the electric field vector E_i is equal to the coercive field strength E^c. For pure mechanical loadings, this switching function is equivalent to a *von Mises* type criterion.

By the normality rule (27), the evolution equations for the internal variables are obtained as

$$
\dot{\beta} = \lambda \frac{\partial f}{\partial \phi^\beta} = \frac{\lambda}{1+f} \left(\frac{1}{\phi^{\beta,0}} \right)^2 \phi^\beta, \qquad\qquad \dot{\gamma} = \lambda \frac{\partial f}{\partial \phi^\gamma} = \frac{\lambda}{1+f} \left(\frac{1}{\phi^{\gamma,0}} \right)^2 \phi^\gamma,
$$

$$
\dot{\vec{e}}^\beta = \lambda \frac{\partial f}{\partial \phi^{\vec{e}^\beta}} = \frac{\lambda}{1+f} \left(\frac{1}{\phi^{\vec{e}^\beta,0}} \right)^2 \vec{\phi}^{\vec{e}^\beta,\perp}, \qquad \dot{\vec{e}}^\gamma = \lambda \frac{\partial f}{\partial \phi^{\vec{e}^\gamma}} = \frac{\lambda}{1+f} \left(\frac{1}{\phi^{\vec{e}^\gamma,0}} \right)^2 \vec{\phi}^{\vec{e}^\gamma,\perp}.
$$

(45)

This system of eight ordinary differential equations has to be solved in the finite element implementation. To remove redundant equations, the formulation of the material law was rewritten in generalized variables, where the unit vectors are represented by two polar variables instead of three cartesian components [Laskewitz 2007].

4.2. *Finite element implementation.* First of all, coming from the elastic region, initial values for the state variables e_i^β and e_i^γ have to be found before switching starts for the first time. Several cases have to be taken into consideration, which are presented in Table 3.

Due to the nonlinearity of the problem, the loading history is subdivided into increments. In the following, we consider the general case of a computation for some time instant $^{n+1}t = t + \Delta t$. We depart from some known state at time $^nt = t$ (the last increment), meaning the state variables $^nq^\alpha$ are known (besides strain $^nS_{ij}$ and electric field ^nE_i, of course). Furthermore, trial values $^{n+1}S_{ij}$ and $^{n+1}E_i$ for strain and electric field, respectively, are given from the global Newton iteration. The task is to find the state variables $^{n+1}q^\alpha$ from which the stress $^{n+1}T_{ij}$ and the electric displacement $^{n+1}D_i$ can be computed. Furthermore, the algorithmic consistent tangents

$$
^{n+1}\left(\frac{\partial D_i}{\partial E_j} \right), \qquad ^{n+1}\left(\frac{\partial T_{ij}}{\partial E_k} \right), \qquad ^{n+1}\left(\frac{\partial D_i}{\partial S_{jk}} \right), \qquad ^{n+1}\left(\frac{\partial T_{ij}}{\partial S_{kl}} \right),
$$

have to be provided to guarantee quadratic convergence of the global Newton iteration.

Case	Initial value
$\|^{n+1}T_{ij}^{\text{rev}}\| = 0$ and $\|^{n+1}E_i\| = 0$	Undefined
$\|^{n+1}T_{ij}^{\text{rev}}\| = 0$ and $\|^{n+1}E_i\| > 0$	$e_i^\beta = \dfrac{^{n+1}E_i}{\|^{n+1}E_i\|}$ $e_i^\gamma = \dfrac{^{n+1}E_i}{\|^{n+1}E_i\|}$
$\|^{n+1}T_{ij}^{\text{rev}}\| > 0$ and $\|^{n+1}E_i\| = 0$	e_i^β, e_i^γ : eigenvector of $^{n+1}T_{ij}^{\text{rev}}$ belonging to largest eigenvalue
$\|^{n+1}T_{ij}^{\text{rev}}\| > 0$ and $\|^{n+1}E_i\| > 0$	e_i^β : eigenvector of $^{n+1}T_{ij}^{\text{rev}}$ $e_i^\gamma = \dfrac{^{n+1}E_i}{\|^{n+1}E_i\|}$

Table 3. Initial values for e_i^β and e_i^γ ($^{n+1}T_{ij}^{\text{rev}}$ is the elastic stress tensor (trial stress) at the end of the increment).

The bases for this computation are the evolution equations (27) which are solved by a backward Euler scheme yielding

$$^{n+1}q^\alpha(t+\Delta t) = {}^n q^\alpha(t) + \Delta t \cdot {}^{n+1}\lambda(t+\Delta t) {}^{n+1}\left(\frac{\partial f}{\partial \phi^\alpha}\big(q^\beta(t+\Delta t), t+\Delta t\big)\right). \tag{46}$$

By means of the notation $^{n+1}q^\alpha = q^\alpha(t+\Delta t)$ and $^{n+1}\lambda = \lambda(t+\Delta t)$ for the state variables and the so-called irreversible multiplier, (46) can be rewritten as

$$F^\alpha = q^\alpha(t+\Delta t) - q^\alpha(t) - \Delta t \lambda(t+\Delta t)\frac{\partial f}{\partial \phi^\alpha}\big(q^\beta(t+\Delta t), t+\Delta t\big) = 0. \tag{47}$$

The switching condition

$$f\big(q^\alpha(t+\Delta t), t+\Delta t\big) = 0. \tag{48}$$

completes the system of equations.

From Taylor series expansion and linearization of functions F^α and f, the iteration scheme

$$^{j+1}F^\alpha = {}^j F^\alpha + {}^j\left(\frac{\partial F^\alpha}{\partial q^\beta}\right) \cdot {}^{j+1}\delta q^\beta + {}^j\left(\frac{\partial F^\alpha}{\partial \lambda}\right) \cdot {}^{j+1}\delta\lambda = 0,$$

$$^{j+1}f = {}^j f + {}^j\left(\frac{\partial f}{\partial q^\alpha}\right) \cdot {}^{j+1}\delta q^\alpha = 0, \tag{49}$$

can be found in which

$$^j F^\alpha = {}^j q^\alpha - q^\alpha(t) - \Delta t \cdot {}^j\lambda \frac{\partial f}{\partial \phi^\alpha}({}^j q^\beta, t+\Delta t), \qquad {}^j f = f({}^j q^\alpha, t+\Delta t). \tag{50}$$

This procedure is equivalent to the Newton–Kantorovich method. As a consequence, a second local Newton iteration has been established to solve the constitutive law at each integration station in each load step.

To achieve quadratic convergence in the global Newton iteration during nonlinear computation of switching processes, it is necessary to employ the so-called algorithmic consistent tangent moduli. For such a complex constitutive model as the one considered in this paper, it is not possible to derive these moduli in closed form. Approximations may be used, such as the material tensors from the linear constitutive law, yielding a quasi-Newton method with only linear convergence guaranteed. Otherwise, numerical differentiation may be employed:

$$^{n+1}\left(\frac{\partial D_i}{\partial E_j}\right) = \frac{D_i(E_j+h) - D_i(E_j)}{h}, \qquad {}^{n+1}\left(\frac{\partial T_{ij}}{\partial E_k}\right) = \frac{T_{ij}(E_k+h) - T_{ij}(E_k)}{h},$$

$$^{n+1}\left(\frac{\partial D_i}{\partial S_{jk}}\right) = \frac{D_i(S_{ik}+h) - D_i(S_{ik})}{h}, \qquad {}^{n+1}\left(\frac{\partial T_{ij}}{\partial S_{kl}}\right) = \frac{T_{ij}(S_{kl}+h) - T_{ij}(S_{kl})}{h}, \tag{51}$$

in which $h = \sqrt{eps} \approx 1,5 \cdot 10^{-8}$ should be chosen, where *eps* is the accuracy of the computer.

4.2.1. *Methods to improve convergence.* In the finite element solution, occasional convergence problems occurred. This section describes some methods to enhance the convergence of the finite element implementation. The convergence problems occur mainly because of the form of the energy barrier function which is a hyperbola. There is a possibility for the state variables to take values outside the region of

admissible values because of inaccuracies during the iteration procedures. In this case, a physically incorrect solution is obtained. Therefore, it should be ensured that the state variables cannot leave the region of admissible values. The Newton method needs a start vector which is sufficiently close to the solution for an accurate convergence to the physically correct roots of the system (47)–(48). To improve convergence, several methods have been studied and tested. An overview of the most important methods is given in Table 4. It has to be mentioned that sometimes convergence still could not be achieved.

4.2.2. *Verification of the implementation of the microscopically motivated material model.* Based on the material parameters in Table 5, the microscopically motivated constitutive model and its finite element implementation are verified in comparison to experimental results.

Figure 12 shows the dielectric and the butterfly hysteresis from experiments and simulations. The microscopically motivated model can represent the material behavior very well.

4.3. *Simulation example: hollow cylinder.* In experiments, hollow cylinders are often used to investigate multiaxial loading states. Figure 13a shows a piezoceramic circular ring which is poled in the radial direction. The axisymmetric finite element model shown in Figure 13b represents a cylinder of infinite axial length, since all vertical displacements at the top of the model are forced to be equal. The maximum electric potential loading is equivalent to an average electric field of $3E^c$. Following poling, the cylinder is unloaded again. The material parameters are adjusted to a soft lead-zirconate-titanate (soft PZT) and are presented in Table 6.

Figure 14 presents the deformed and undeformed finite element mesh. The electrical loading induces a decrease of the inner radius accompanied by a shortening in the vertical direction in comparison to the

| Method to improve convergence	Advantages and disadvantages
Consistent tangent moduli	$+$ Improvement of global convergence $+$ In general local convergence better $-$ Computationally expensive
Enforcing admissible range for β and γ	$+$ Improvement of convergence $-$ Limitation in finding suitable start vectors
Damped Newton method for local Newton iteration	$+$ Significant improvement of convergence $+$ Computationally inexpensive $-$ Strong dependence on the maximum number of iterations for the damped local Newton method (different roots can be found for different maximum numbers of iterations)
Systematic search for suitable start vector (Euler forward, linear interpolation)	$+$ Improvement of convergence $-$ Can be computationally expensive
Subincrementing the time step, solution with backward Euler method or forward Euler method	$+$ Significant improvement of convergence $-$ Computationally very expensive

Table 4. Methods to improve convergence of the Newton method.

E^c (MV/mm)	1.0×10^3
P^{sat} (kN/(MVmm))	310×10^{-3}
σ^c (kN/mm^2)	40.0×10^{-3}
S^{sat}	0.00225
Y (kN/mm^2)	60.0
ν	0.37
$d^{\parallel}$ (mm/MV)	6.75×10^{-1}
$d^{\perp}$ (mm/MV)	-3.15×10^{-1}
$d^{=}$ (mm/MV)	4.35×10^{-1}
c^{γ} (kN/mm^2)	3.0×10^{-5}
c^{β} (kN/mm^2)	1.0×10^{-4}
N	2.0
A (kN/mm^2)	5.0×10^{-11}

Table 5. Material parameters for the microscopically motivated material model.
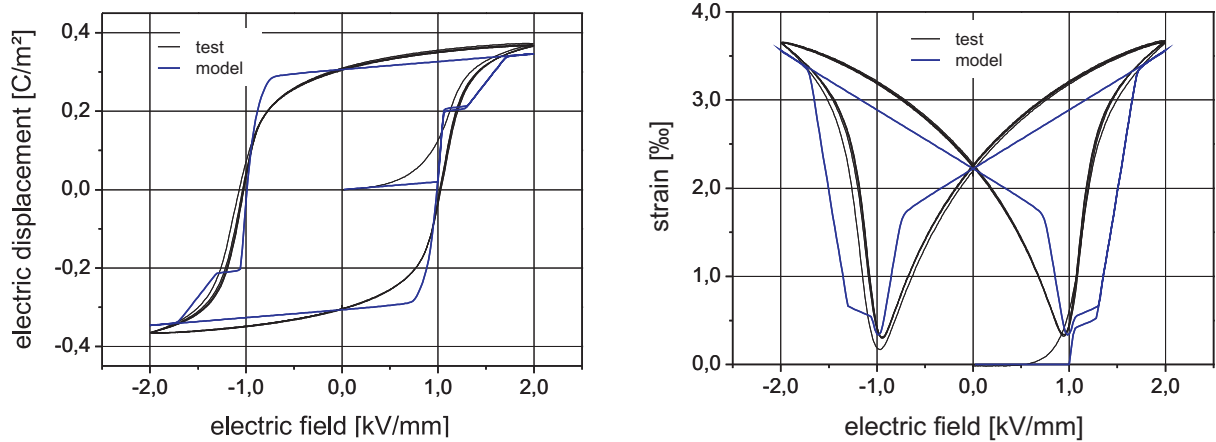
Figure 12. Dielectric (left) and butterfly hysteresis (right) from experiments and simulations.
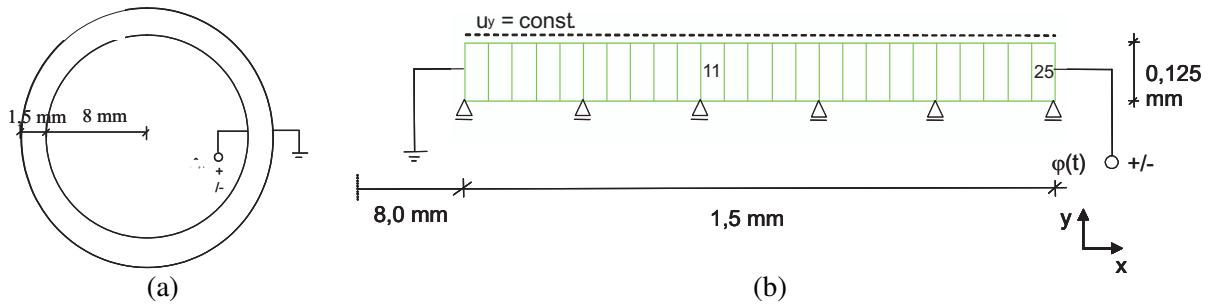
Figure 13. (a) Radial poled circular cylinder, top view, and (b) axisymmetric finite element model.

|	
Y (GPa)	60.0
ν	0.396
σ^c (MPa)	40.0
S^{sat}	0.002
E^c (kV/mm)	1.0
P^{sat} (C/m^2)	0.29
d_{33} (mm/MV)	4.5×10^{-1}
d_{31} (mm/MV)	-2.1×10^{-1}
d_{15} (mm/MV)	5.8×10^{-1}

Table 6. Material parameters used in the simulations.
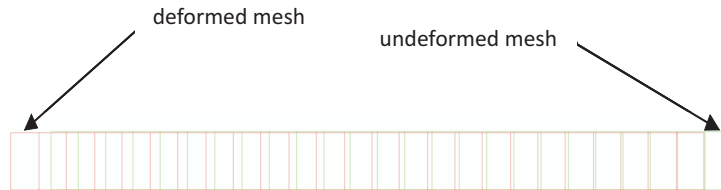
**Figure 14.** Undeformed and deformed finite element mesh (scale factor 5.27).
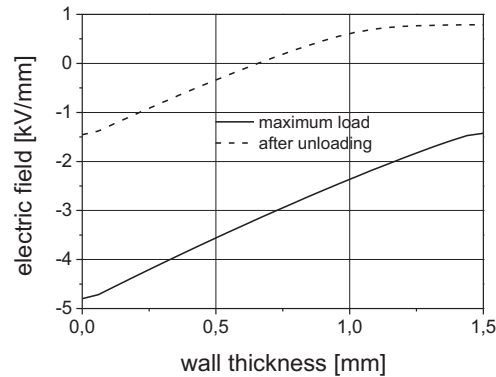
Figure 15. Electric field in the radial direction at maximum load and after unloading over the wall thickness.

initial state. In Figure 15, the electric field versus the wall thickness at the maximum electric potential and after unloading is depicted. At the inner surface of the cylinder the local electric field reaches approximately -5 kV/mm, while at the outer surface, it is just above the coercive field at maximum load. After unloading, there remains a local electric field at the inner surface of approximately -1.5 kV/mm. In contrast to this, the local electric field at the outer surface changes sign and is just below the initial critical field strength for the onset of switching, that is, E^c.

In Figure 16 the axial stress over the wall thickness is presented. The distribution of the axial stress is almost linear at maximum voltage. At the inner surface of the cylinder, there are tensile stresses, while at the outer surface there are compressive stresses. The tensile stress is in the range of the tensile strength
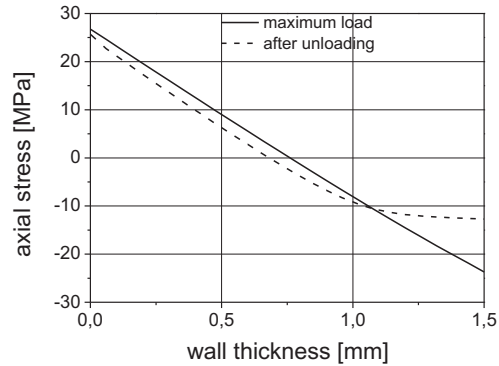
Figure 16. Axial stress over the wall thickness at maximum load and after unloading.
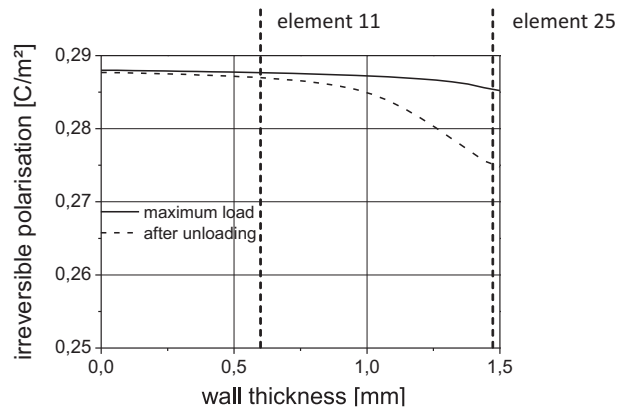
Figure 17. Irreversible polarization over wall thickness at maximum load and after unloading.

of the material and may lead to cracks. After unloading, there remain stresses in the cylinder. At the inner surface there is almost no reduction of the stresses, but at the outer surface, there is a decrease in the axial stresses observed. Because of the inhomogeneous distribution of the electric field, the coercive field is reached earlier in regions near the inner surface initiating domain switching in the radial direction while at the outer surface the coercive field has not yet been reached. This leads to compressive axial stresses close to the outer surface and, as a consequence of equilibrium, to tensile axial stresses near the inner surface. The circumferential stresses (not shown) exhibit a nonlinear distribution as well and do not vanish after unloading. The radial stresses are approximately zero.

Figure 17 shows the irreversible polarization at maximum voltage and after unloading. At maximum load, the saturation polarization is almost reached in all regions of the cylinder. Only at the outer surface, there is a small decrease observed. During unloading the irreversible polarization is decreasing especially at the outer surface. While the stresses in the cylinder wall are significant, they can not explain this effect by means of some mechanical depolarization. As they are compressive, these stresses rather would stabilize the poled state close to the outer surface. To have a closer look at the depolarization effect, the local electric displacement over the local electric field is depicted in Figure 18 for two elements. Element 11 is approximately at the position where the electric field is zero after unloading. Element 25 is at the outer surface of the cylinder (see Figure 17).
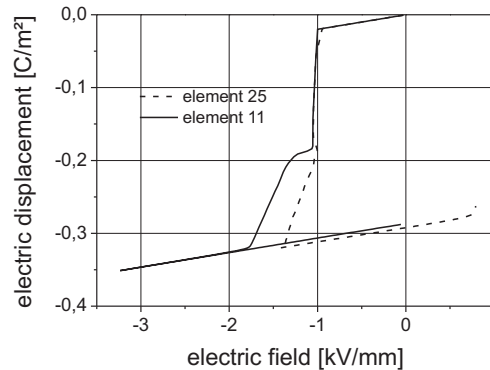
Figure 18. Local electric displacement over local electric field for two positions in the cylinder wall.

In element 11, saturation of the local irreversible polarization is clearly reached, while for element 25 the saturation level is just touched. After unloading, the local electric field in element 11 is reduced to nearly zero, while the local electric displacement approaches P^{sat} as the linear dielectric contribution vanishes. In contrast to this, the local electric field in element 25 changes sign and takes significant values in the opposite direction of the initial poling. As a matter of fact, it reaches the critical electric field for the onset of electrically induced repoling in opposite direction. Around this critical field strength, small changes of the electric field lead to significant changes in the irreversible polarization. Due to the large slope of the polarization changing parts of the hysteresis electrical depolarization takes place. Because of that, after unloading, an obvious reduction of the irreversible polarization is observed near the outer surface of the cylinder, though the electric field is nearly constant with respect to position in this region. The actual critical field strength for the repoling process is dependent on the previous loading history. In particular, it has been reduced close to the outer surface compared to the initial coercive field strength E^{c} due to what we may call a ferroelectric Bauschinger effect. As a consequence, even an arbitrarily high electric voltage during poling is not able to ensure fully saturated polarization over the whole wall thickness after unloading.

By means of this simulation example it could be shown that the implementation of the microscopically motivated material model is very powerful. It can describe the polarization behavior of piezoceramic materials in more detail than the phenomenological model. This statement results from a comparison to simulations in [Laskewitz et al. 2006], where the finite element analysis of piezoceramic hollow cylinders based on the phenomenological model is presented.

5. Conclusion

After motivating this work and giving an overview of the state of the art in the literature, a phenomenological constitutive model for ferroelectrics and its finite element implementation was described. A customized, computationally time efficient integration algorithm (radial return mapping method) was introduced. The model and its finite element implementation was verified by simulation examples and comparison to experiments. As a simulation example, poling of a stack actuator was considered showing the capability of the finite element tool.

Next, a microscopically motivated constitutive model and its finite element implementation by a more complex radial return mapping algorithm was described and verifications by means of experimental data were performed. Lastly, a simulation example using a hollow cylinder showed the applicability of the this finite element tool for practical problems.

In summary, the phenomenological material model is well suited to simulate realistically the overall behavior of large systems. The microscopically motivated material model has its field of application in simulating the detailed electromechanically fields of smaller piezoceramic (sub)systems, because of the higher computation time consumed by the more complex integration algorithm.

References

[Allik and Hughes 1970] H. Allik and T. J. R. Hughes, "Finite element method for piezoelectric vibration", *Int. J. Numer. Meth. Eng.* **2** (1970), 151–157.

[Belov and Kreher 2005] A. Y. Belov and W. Kreher, "Viscoplastic models for ferroelectric ceramics", *J. Eur. Ceramic Soc.* **25**:12 (2005), 2567–2571.

[Boehle 1999] U. Boehle, "Phänomenologische Modellierung und Finite-Elemente-Simulationen von nichtlinearen elektromechanischen Vorgängen in ferroelektrischen Materialien", technical report FZKA 6347, Forschungszentrum Karlsruhe, 1999.

[Chen 1980] P. J. Chen, "Three dimensional dynamic electromechanical constitutive relations for ferroelectric materials", *Int. J. Solids Struct.* **16** (1980), 1059–1067.

[Chen and Lynch 1998] W. Chen and C. S. Lynch, "A micro-electro-mechanical model for polarization switching of ferroelectric materials", *Acta Mater.* **46** (1998), 5303–5311.

[Chen et al. 1997] X. Chen, D. N. Fang, and K. C. Hwang, "Micromechanics simulation of ferroelectric polarization switching", *Acta Mater.* **45** (1997), 3181–3189.

[Delibas et al. 2005] B. Delibas, A. Arockiarajan, and W. Seemann, "A nonlinear model of piezoelectric polycrystalline ceramics under quasi-static electromechanical loading", *J. Materials Science: Materials in Electronics* **16** (2005), 507–515.

[Elhadrouz et al. 2005a] M. Elhadrouz, T. B. Zineb, and E. Patoor, "Constitutive law for ferroelastic and ferroelectric piezoceramics", *J. Intell. Mater. Syst. Struct.* **16** (2005), 221–236.

[Elhadrouz et al. 2005b] M. Elhadrouz, T. B. Zineb, and E. Patoor, "Finite element modeling of piezoelectric actuators and sensors: local analysis of the ferroelectric and ferroelastic effects", in *Proceedings of MRS Spring Meeting* (San Francisco, 2005), vol. CC4.7, edited by R. M. McMeeking et al., 2005.

[Huber and Fleck 2001] J. E. Huber and N. A. Fleck, "Multi-axial electrical switching of a ferroelectric theory vs. experiment", *J. Mech. Phys. Solids* **49** (2001), 785–811.

[Huber and Fleck 2004] J. E. Huber and N. A. Fleck, "Ferroelectric switching: a micromechanics model versus measured behaviour", *Eur. J. Mech. A/Solids* **23** (2004), 203–217.

[Huber et al. 1998] J. E. Huber, N. A. Fleck, C. M. Landis, and R. M. McMeeking, "Constitutive model of ferroelectrics", *J. Mech. Phys. Solids* **47** (1998), 1663–1697.

[Hwang 2000] S. Hwang, "Switching in ferroelectric polycrystals", *J. Appl. Physics* **87** (2000), 869–875.

[Hwang et al. 1995] S. C. Hwang, C. S. Lynch, and R. M. McMeeking, "Ferroelectric/ferroelastic interactions and a polarization switching model", *Acta Metall. Mater.* **43** (1995), 2073–2084.

[Hwang et al. 1998] S. C. Hwang, S. C., and R. M. McMeeking, "A finite element model of ferroelectric polycrystals", *Ferroelectrics* **211** (1998), 177–194.

[Kamlah 2001] M. Kamlah, "Ferroelectric and ferroeleastic piezoceramics: modeling of electromechanical hysteresis phenomena", *Continuum Mech. Thermodyn.* **13** (2001), 219–268.

[Kamlah and Boehle 2001] M. Kamlah and U. Boehle, "Finite element analysis of piezoceramic components taking into account ferroelectric hysteresis behaviour", *Int. J. Solids Struct.* **38** (2001), 605–633.

[Kamlah and Jiang 1999] M. Kamlah and Q. Jiang, "A constitutive model for ferroelectric ceramics under uniaxial loading", *Smart Materials Struct.* **9** (1999), 441–451.

[Kamlah and Tsakmakis 1999] M. Kamlah and C. Tsakmakis, "Phenomenological modeling of the non-linear electro-mechanical coupling in ferroelectrics", *Int. J. Solids Struct.* **36** (1999), 669–695.

[Kamlah and Wang 2003] M. Kamlah and Z. Wang, "A thermodynamically and microscopically motivated constitutive model for piezoceramics", technical report FZKA 6880, Forschungszentrum Karlsruhe, 2003.

[Kamlah et al. 2005] M. Kamlah, A. C. Liskowsky, R. M. McMeeking, and H. Balke, "Finite element simulation of a polycrystalline ferroelectric based on a multidomain single crystal switching model", *Int. J. Solids Struct.* **42** (2005), 2949–2964.

[Kessler and Balke 2001] H. Kessler and H. Balke, "On the local and average energy release in polarization switching phenomena", *J. Mech. Phys. Solids* **49** (2001), 953–978.

[Klinkel 2006] S. Klinkel, "A thermodynamic consistent 1D model for ferroelastic and ferroelectric hysteresis effects in piezoceramics", *Comm. Numer. Meth. Eng.* **22** (2006), 727–739.

[Landis 2002] C. M. Landis, "Fully coupled, multi-axial, symmetric constitutive laws for polycrystalline ferroelectric ceramics", *J. Mech. Phys. Solids* **50** (2002), 127–152.

[Laskewitz 2007] B. Laskewitz, "Finite-Elemente-Implementierung konstitutiver nichtlinearer Stoffgesetze für piezokeramische Werkstoffetitle", technical report FZKA 7359, Forschungszentrum Karlsruhe, 2007.

[Laskewitz and Kamlah 2004] B. Laskewitz and M. Kamlah, "Nonlinear Finite Element Simulations of Poling Processes in Piezoceramic Devices", *Proceedings in Appl. Math. Mech.* **4**:1 (2004), 286–287.

[Laskewitz et al. 2006] B. Laskewitz, M. Kamlah, and C. Chen, "Investigations of the nonlinear behavior of piezoceramic hollow cylinders", *J. Intell. Mater. Syst. Struct.* **17** (2006), 521–532.

[McMeeking and Landis 2002] R. M. McMeeking and C. M. Landis, "A phenomenological multi-axial constitutive law for switching in polycrystalline ferroelectric ceramics", *Int. J. Eng. Sci.* **40** (2002), 1553–1577.

[PSU 2000] PSU, Open-source finite element code, Institut für Statik und Dynamik in der Luft- und Raumfahrttechnik, Universität Stuttgart, 2000.

[Schroeder and Gross 2004] J. Schroeder and D. Gross, "Invariant formulation of the electromechanical enthalpy function of transversely isotropic piezoelectric materials", *Arch. Appl. Mech.* **73** (2004), 533–552.

[Schroeder and Romanowski 2005] J. Schroeder and H. Romanowski, "A thermodynamically consistent mesoscopic model for transversely isotropic ferroelectric ceramics in a coordinate-invariant setting", *Arch. Appl. Mech.* **74** (2005), 863–877.

[Seemann et al. 2004] W. Seemann, A. Arockiarajan, and B. Delibas, "Micromechanical simulation of piezoelectric materials using probability functions", 5387 (2004), 402–410.

[Semenov et al. 2006] A. S. Semenov, H. Kessler, A. Liskowsky, and H. Balke, "On a vector potential formulation for 3D electromechanical finite element analysis", *Comm. Numer. Meth. Eng.* **22** (2006), 357–375.

[Smith et al. 2003] R. C. Smith, S. Seelecke, Z. Ounaies, and J. Smith, "A free energy model for hysteresis in ferroelectric materials", *J. Intell. Mater. Syst. Struct.* **14** (2003), 719–739.

[Westram et al. 2007] I. Westram, B. Laskewitz, D. Lupascu, M. Kamlah, and J. Rödel, "Electric-field-induced crack initiation from a notch in a ferroelectric ceramic", *J. Amer. Ceramic Soc.* **90**:9 (2007), 2849–2854.

[Zhou et al. 2005a] D. Zhou, M. Kamlah, and D. Munz, "Effects of bias electric fields on the non-linear ferroelastic behavior of soft lead zirconate titanate piezoceramics", *J. Amer. Ceramic Soc.* **88** (2005), 867–874.

[Zhou et al. 2005b] D. Zhou, M. Kamlah, and D. Munz, "Effects of uniaxial prestress on the ferroelectric hysteretic response of soft PZT", *J. Eur. Ceramic Soc.* **25** (2005), 425–432.

BERND LASKEWITZ: laskewitz@imf.fzk.de
Karlsruhe Institute of Technology, Institute for Materials Research II, P.O. Box 3640, 76021 Karlsruhe, Germany
http://www.fzk.de/imf2

MARC KAMLAH: marc.kamlah@kit.edu
Karlsruhe Institute of Technology, Institute for Materials Research II, P.O. Box 3640, 76021 Karlsruhe, Germany
http://www.fzk.de/imf2

POROMECHANICS RESPONSE OF AN INCLINED BOREHOLE SUBJECT TO IN-SITU STRESS AND FINITE LENGTH FLUID DISCHARGE

YOUNANE N. ABOUSLEIMAN AND SHENGLI CHEN

The analytical approach developed in this paper calculates the poroelastic coupled time-dependent stress and pore pressure variations for an inclined borehole drilled in a fluid saturated porous medium and subjected to the far-field three-dimensional in-situ stresses in addition to a fluid discharge over a finite length of its surface. This problem is encountered in many engineering applications, in particular, in wellbore drilling, fluid injection, and production. A superposition scheme is employed to obtain the analytical solutions within the linear theory of poromechanics. The comparison with an earlier published solution shows a discrepancy in the poroelastic boundary conditions applied at the wellbore wall. In this solution a systematic analysis is being carried out to evaluate the effects of the mechanical parameters on the calculated time-dependent effective tangential stress and pore pressure in addition to the effects of the borehole inclination and the geometry of the flux loading area are also included.

1. Introduction

The generalized poromechanics solutions of an inclined borehole, which extend the isotropic plane strain solution of Carter and Booker [1982] and the one slightly modified by Detournay and Cheng [1988] to an anisotropic porous medium (coupled with thermal and chemical effects) [Abousleiman and Ekbote 2005; Ekbote and Abousleiman 2005; 2006], have seen many applications in engineering problems, in particular in the oil and gas industry [Abousleiman et al. 1999], where these problems are of great economic value to operations. Lately, these solutions have been extended for estimating stress and pore pressure distributions in a borehole drilled in naturally fractured fluid saturated medium [Abousleiman and Nguyen 2005] following the mixture theory approach in [Bowen 1982].

Poromechanics theory was first established by [Biot 1941] and has served as the basis for many of the later works on borehole problems. Cui et al. [1997; 1998; 1999] presented the analytical solutions for the general case, where the borehole is inclined to the three-dimensional principal axes of the far-field in-situ stresses using a loading decomposition scheme. In an earlier study, Rajapakse [1993] obtained a set of general stress solutions associated with free stress boundaries, yet a fluid source applied over a finite segment of the borehole wall.

For a wide range of engineering applications in the oil and gas industry it has been customary practice to inject fluid into a sealed segment of the borehole at great depth. In reservoir stimulation, hydraulic fracturing is one of the most widely used techniques, it also extends to applications in environmental

engineering for clean ups. In addition, from such geometries an extended leak-off test is commonly performed to estimate the far field in-situ stresses. For these important problems, the poromechanics solution does not exist in the literature. Although Rajapakse [1993] considered the fluid flowing into the finite length of the borehole, and its effects on the stress and pore pressure perturbation, the assumptions were that the formation is initially unstressed and consists of incompressible constituents. Moreover, it was clearly incorrect in his study to claim that the total radial stress be zero over the fluid injection segment of the borehole wall. While in the existing solutions [Cui et al. 1997; 1998; 1999; Abousleiman and Ekbote 2005], efforts were focused upon an infinite length inclined borehole with only stress and pore pressure boundary conditions. Therefore, a more general solution, which could take into account the fluid injection on a finite geometry of the wellbore coupled with the three-dimensional far field in-situ stresses is needed.

The purpose of this paper is to present the analytical stress analysis and pore pressures of an inclined borehole subjected to fluid discharge over a finite segment of the surface and to the three-dimensional in-situ far field state of stress. Based on linear poromechanics and a careful inspection of the boundary conditions, the problem is divided into two fundamental parts, specifically, a fluid discharge problem, and a stress boundary problem. These time-dependent problems are solved using the Laplace and Fourier integral transforms. The final stress solutions thus may be deduced by simple superposition. Comprehensive numerical analyses are carried out in the paper to present comparison with the existing solutions and to investigate the influences of the material properties, borehole inclination, as well as the flux loading area on the calculated effective tangential stress and pore pressure.

2. Governing equations

Consider an inclined borehole with radius R drilled in an infinite porous medium which is characterized by a nonhydrostatic in-situ stress field, see Figure 1a. The borehole is subjected to a radial fluid discharge over a segment of the surface. Using the cylindrical coordinates system (r, θ, z), see Figure 1b, the governing equations for deformations of the isotropic homogeneous saturated medium can be expressed as follows [Biot 1941; Rice and Cleary 1976; Wang 2000]:

$$\nabla^2 u_r + \frac{1}{1-2\nu_u} \frac{\partial e_v}{\partial r} - \frac{1}{r}\left(\frac{2}{r}\frac{\partial u_\theta}{\partial \theta} + \frac{u_r}{r}\right) - \frac{2B(1+\nu_u)}{3(1-2\nu_u)}\frac{\partial \varepsilon_v}{\partial r} = 0, \tag{1}$$
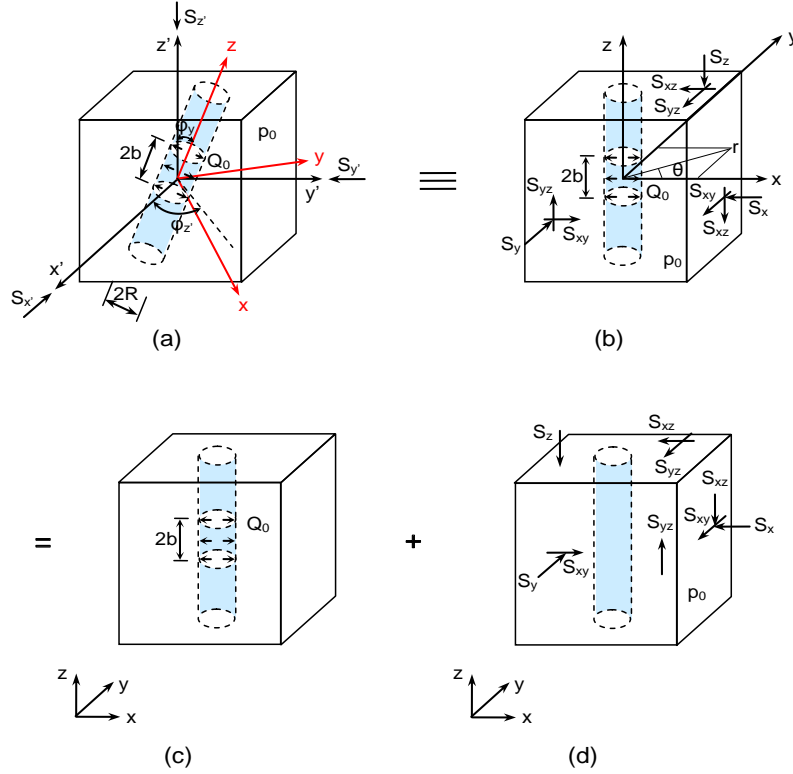
$$\nabla^2 u_\theta + \frac{1}{1-2\nu_u} \frac{\partial e_v}{r\partial \theta} - \frac{1}{r}\left(\frac{u_\theta}{r} - \frac{2}{r}\frac{\partial u_r}{\partial \theta}\right) - \frac{2B(1+\nu_u)}{3(1-2\nu_u)}\frac{\partial \varepsilon_v}{r\partial \theta} = 0, \tag{2}$$

$$\nabla^2 u_z + \frac{1}{1-2\nu_u} \frac{\partial e_v}{\partial z} - \frac{2B(1+\nu_u)}{3(1-2\nu_u)}\frac{\partial \varepsilon_v}{\partial z} = 0, \tag{3}$$

$$\nabla^2 \varepsilon_v = \frac{1}{c}\frac{\partial \varepsilon_v}{\partial t} \tag{4}$$

in which u_r, u_θ, and u_z are radial, circumferential, and vertical displacements of the solid matrix;

$$e_v = \frac{\partial u_r}{\partial r} + \frac{u_r}{r} + \frac{\partial u_\theta}{r\partial \theta} + \frac{\partial u_z}{\partial z}$$

Figure 1. Geometry of inclined borehole and decomposition scheme: (a) borehole inclined to principal stresses; (b) equivalent far field stresses in local coordinate system; (c) fluid discharge problem; (d) stress boundary problem.

is the matrix dilation and ε_v is the variation of fluid content per unit reference volume; B is Skempton pore pressure coefficient;

$$c = \frac{2G\kappa B^2 (1-\nu)(1+\nu_u)^2}{9(1-\nu_u)(\nu_u-\nu)}$$

is the diffusion coefficient, G is the shear modulus, ν and ν_u are the drained and undrained Poisson's ratios, and κ is defined by $\kappa = k/\mu$, with k denoting the intrinsic permeability (mD) and μ the fluid viscosity; and ∇^2 denotes the Laplacian operator which is given by

$$\nabla^2 = \frac{\partial^2}{\partial r^2} + \frac{1}{r}\frac{\partial}{\partial r} + \frac{1}{r^2}\frac{\partial^2}{\partial \theta^2} + \frac{\partial^2}{\partial z^2}.$$

The constitutive relations can be expressed as

$$\sigma_{ij} = 2Ge_{ij} + \frac{2G\nu}{1-2\nu}\delta_{ij}e_v - \alpha\delta_{ij}p, \quad (i,j=r,\theta,z), \tag{5}$$

$$p = -\frac{2GB(1+\nu_u)}{3(1-2\nu_u)}e_v - \frac{2GB^2(1-\nu)(1+\nu_u)^2}{9(\nu-\nu_u)(1-2\nu_u)}\varepsilon_v, \tag{6}$$

where σ_{ij} and e_{ij} are the total stress tension and strain tension, respectively;

$$\alpha = \frac{3(\nu_u - \nu)}{B(1 - 2\nu)(1 + \nu_u)}$$

is the Biot effective stress coefficient or the pore pressure coefficient (PPC); δ_{ij} is the Kronecker delta function; and p is the excess pore water pressure. Note that tension stress and compressive pore pressure are taken as positive in the present analysis.

3. Formulation of the problem

As shown schematically in Figure 1a, before drilling, the saturated medium is under in-situ compressive stress condition with the three principal stresses $S_{x'}$, $S_{y'}$, and $S_{z'}$ coinciding with the Cartesian coordinate system (x', y', z'). The initial pore pressure is assumed to be hydrostatic with a magnitude of p_0. Following the treatment by Cui et al. [1997] and Abousleiman and Nguyen [2005], a borehole local coordinate system (x, y, z), which is defined by a rotation of an azimuth angle $\varphi_{z'}$ about the z' axis and then by an inclination of a zenith angle φ_y towards the x-axis, is introduced for convenience of the solution presentation. The borehole axis is consistent with the z axis (Figure 1a). It is also assumed that the borehole is being pumped at a steady rate Q_0 (l/min) over a finite length $2b$.

The six components of the far-field stress tensor in the local coordinate system, S_x, S_y, S_z, S_{xy}, S_{yz}, and S_{xz} (See Figure 1b, where r and θ are the polar coordinates), are readily obtainable from the three principal stresses via a transformation matrix [Jaeger and Cook 1969]. So the stress boundary conditions at the far field $(r \to \infty)$, under the local coordinate system, can be written as

$$\sigma_{xx} = -S_x, \quad \sigma_{yy} = -S_y, \quad \sigma_{zz} = -S_z, \quad \sigma_{xy} = -S_{xy}, \quad \sigma_{yz} = -S_{yz}, \quad \sigma_{xz} = -S_{xz}, \quad p = p_0. \quad (7)$$

While on the surface of the wellbore, $r = R$,

$$\sigma_{rr} = \begin{cases} -p & 0 \le |z| \le b, \\ 0 & b < |z| < \infty, \end{cases} \tag{8a}$$

$$\sigma_{r\theta} = 0, \tag{8b}$$

$$\sigma_{rz} = 0, \tag{8c}$$

$$q = \begin{cases} Q_0/4\pi R b & 0 \le |z| \le b, \\ 0 & b < |z| < \infty, \end{cases} \tag{8d}$$

where $q = -\kappa \, dp/dr$ is the fluid flow rate in units of cm/min. Note that in [Rajapakse 1993], instead of (8a), a simpler but incorrect boundary condition for radial stress at the borehole wall was adopted ($\sigma_{rr} = 0$ for $|z| \le \infty$).

Equation (8d) identifies a flow boundary condition that the borehole is drilled with an impermeable casing but perforated over a length of $2b$ for fluid injection, a commonly encountered case in drilling practice. It must be noted that in the above the far field boundary conditions are expressed in the Cartesian coordinates, but at the borehole surface the polar coordinates are used for convenience.

Combining the governing equations (1)–(6) and boundary conditions (7)–(8) fully defines the concerned problem of an inclined borehole subjected to in-situ stresses and fluid loading. To simplify the

analysis it is better to employ the superposition method and decompose the problem into two fundamental parts, solving (1)–(6) separately with the incorporation of the following two boundary conditions:

I: Fluid discharge problem. In the far field ($r \to \infty$),

$$\sigma_{xx} = \sigma_{yy} = \sigma_{zz} = \sigma_{xy} = \sigma_{yz} = \sigma_{xz} = p = 0. \tag{9}$$

At the borehole wall ($r = R$),

$$\sigma_{r\theta} = \sigma_{rz} = 0, \qquad \sigma_{rr} = \begin{cases} -p & 0 \le |z| \le b, \\ 0 & b < |z| < \infty, \end{cases} \qquad q = \begin{cases} Q_0/4\pi\, Rb & 0 \le |z| \le b, \\ 0 & b < |z| < \infty. \end{cases} \tag{10}$$

II: Stress boundary problem. In the far field ($r \to \infty$),

$$\sigma_{xx} = -S_x, \quad \sigma_{yy} = -S_y, \quad \sigma_{zz} = -S_z, \quad \sigma_{xy} = -S_{xy}, \quad \sigma_{yz} = -S_{yz}, \quad \sigma_{xz} = -S_{xz}, \quad p = p_0. \tag{11}$$

At the borehole wall ($r = R$),

$$\sigma_{rr} = \begin{cases} -p & \text{if } |z| \le b, \\ 0 & \text{if } |z| > b, \end{cases} \qquad \sigma_{r\theta} = 0, \qquad \sigma_{rz} = 0, \qquad q = 0. \tag{12}$$

Figures 1c–1d illustrate the detailed decomposition scheme. It is obviously observed that after the addition of (9)–(12) the original boundary equations (7)–(8) are identically recovered.

4. Solutions for fundamental problems

The decomposition methodology demonstrated above enables us to find the solutions of individual problems and subsequently superpose the results yielding the final solution. Among them, problem I can be treated using the conventional integral transform technique, while the solutions of problem II will be approximated by directly employing the results of Cui et al. [1998] for an impermeable wellbore problem.

I: Fluid discharge problem. This problem is axially symmetric (all quantities independent of θ), so Equations (1)–(6) can be simplified as follows:

$$\frac{\partial^2 u_r^{(I)}}{\partial r^2} + \frac{1}{r}\frac{\partial u_r^{(I)}}{\partial r} - \frac{u_r^{(I)}}{r^2} + \frac{\partial^2 u_r^{(I)}}{\partial z^2} + \frac{1}{1 - 2\nu_u}\frac{\partial e_v^{(I)}}{\partial r} - \frac{2B(1 + \nu_u)}{3(1 - 2\nu_u)}\frac{\partial \varepsilon_v^{(I)}}{\partial r} = 0, \tag{13}$$

$$\frac{\partial^2 u_z^{(I)}}{\partial r^2} + \frac{1}{r}\frac{\partial u_z^{(I)}}{\partial r} + \frac{\partial^2 u_z^{(I)}}{\partial z^2} + \frac{1}{1 - 2\nu_u}\frac{\partial e_v^{(I)}}{\partial z} - \frac{2B(1 + \nu_u)}{3(1 - 2\nu_u)}\frac{\partial \varepsilon_v^{(I)}}{\partial z} = 0, \tag{14}$$

$$\frac{\partial^2 \varepsilon_v^{(I)}}{\partial r^2} + \frac{1}{r}\frac{\partial \varepsilon_v^{(I)}}{\partial r} + \frac{\partial^2 \varepsilon_v^{(I)}}{\partial z^2} = \frac{1}{c}\frac{\partial \varepsilon_v^{(I)}}{\partial t}, \tag{15}$$

$$p^{(I)} = -\frac{2GB(1 + \nu_u)}{3(1 - 2\nu_u)}e_v^{(I)} - \frac{2GB^2(1 - \nu)(1 + \nu_u)^2}{9(\nu - \nu_u)(1 - 2\nu_u)}\varepsilon_v^{(I)}, \tag{16}$$

$$\sigma_{rr}^{(I)} = 2G\frac{\partial u_r^{(I)}}{\partial r} + \frac{2G\nu}{1 - 2\nu}e_v^{(I)} - \frac{3(\nu_u - \nu)}{B(1 - 2\nu)(1 + \nu_u)}p^{(I)}, \tag{17}$$

$$\sigma_{zz}^{(I)} = 2G\frac{\partial u_z^{(I)}}{\partial z} + \frac{2Gv}{1-2v}e_v^{(I)} - \frac{3(v_u - v)}{B(1-2v)(1+v_u)}p^{(I)}, \tag{18}$$

$$\sigma_{\theta\theta}^{(I)} = 2G\frac{u_r^{(I)}}{r} + \frac{2Gv}{1-2v}e_v^{(I)} - \frac{3(v_u - v)}{B(1-2v)(1+v_u)}p^{(I)}, \tag{19}$$

$$\sigma_{rz}^{(I)} = G\left[\frac{\partial u_r^{(I)}}{\partial z} + \frac{\partial u_z^{(I)}}{\partial r}\right], \tag{20}$$

$$u_\theta^{(I)} = \sigma_{r\theta}^{(I)} = \sigma_{\theta z}^{(I)} = 0, \tag{21}$$

where the superscript (I) is added to distinguish the displacement and stress components for the first problem (fluid discharge) from those corresponding to problem II (stress boundary).

Introduce the Laplace and Fourier integral transforms with respect to t and z coordinates

$$\tilde{f}(r, z, s) = \int_0^\infty f(r, z, t)e^{-st}\, dt, \qquad f(r, z, t) = \frac{1}{2\pi i}\int_{\gamma-i\infty}^{\gamma+i\infty} \tilde{f}(r, z, s)e^{st}\, ds, \tag{22}$$

$$\hat{f}(r, \xi, t) = \frac{1}{\sqrt{2\pi}}\int_{-\infty}^\infty f(r, z, t)e^{i\xi z}\, dz, \qquad f(r, z, t) = \frac{1}{\sqrt{2\pi}}\int_{-\infty}^\infty \hat{f}(r, \xi, t)e^{-i\xi z}\, d\xi, \tag{23}$$

where s and ξ are parameters for the Laplace and Fourier transforms, respectively, and γ is greater than the real part of all singularities of $\tilde{f}(r, z, s)$.

Equation (15) becomes, after Laplace and Fourier transformations,

$$\left[\frac{d^2}{dr^2} + \frac{1}{r}\frac{d}{dr} - \left(\xi^2 + \frac{s}{c}\right)\right]\hat{\tilde{\varepsilon}}_v^{(I)} = 0, \tag{24}$$

which has the solution

$$\hat{\tilde{\varepsilon}}_v^{(I)} = A(\xi, s)K_0(\eta r), \tag{25}$$

where $\eta = +\sqrt{\xi^2 + s/c}$ and $A(\xi, s)$ is an arbitrary function of ξ and s.

Application of the transforms to (13) and (14) results in

$$\left(\frac{d^2}{dr^2} + \frac{1}{r}\frac{d}{dr} - \xi^2\right)\hat{\tilde{e}}_v^{(I)} = \frac{B(1+v_u)}{3(1-v_u)}\left(\frac{d^2}{dr^2} + \frac{1}{r}\frac{d}{dr} - \xi^2\right)\hat{\tilde{\varepsilon}}_v^{(I)}. \tag{26}$$

It then follows from (25) and (26) that

$$\hat{\tilde{e}}_v^{(I)} = C(\xi, s)|\xi|K_0(\rho) + \frac{B(1+v_u)}{3(1-v_u)}A(\xi, s)K_0(\eta r), \tag{27}$$

where $\rho = |\xi|r$ and $C(\xi, s)$ is another arbitrary function of ξ and s. The pore pressure can thus be obtained by back substitution of (25) and (27) into the Laplace and Fourier transforms of (16), yielding

$$\hat{\tilde{p}}^{(I)} = -\frac{2GB^2(1-v)(1+v_u)^2}{9(v-v_u)(1-v_u)}K_0(\eta r)A(\xi, s) - \frac{2GB(1+v_u)}{3(1-2v_u)}|\xi|K_0(\rho)C(\xi, s) \tag{28}$$

and hence

$$\hat{\tilde{q}}^{(I)} = -\kappa\frac{d\hat{\tilde{p}}^{(I)}}{dr} = -\frac{2GB^2(1-v)(1+v_u)^2}{9(v-v_u)(1-v_u)}\eta K_1(\eta r)A(\xi, s) - \frac{2G\kappa B(1+v_u)}{3(1-2v_u)}\xi^2 K_1(\rho)C(\xi, s). \tag{29}$$

Similarly, by substituting (25) and (27) into (13) and (14), one has for the displacement components

$$
\left(\frac{d^2}{dr^2} + \frac{1}{r}\frac{d}{dr} - \frac{1}{r^2} - \xi^2\right)\hat{\tilde{u}}_r^{(I)} = -\frac{B(1+\nu_u)}{3(1-\nu_u)}\eta K_1(\eta r)A(\xi,s) + \frac{\xi^2 K_1(\rho)}{1-2\nu_u}C(\xi,s), \tag{30}
$$

$$
\left(\frac{d^2}{dr^2} + \frac{1}{r}\frac{d}{dr} - \xi^2\right)\hat{\tilde{u}}_z^{(I)} = -\frac{i\xi B(1+\nu_u)}{3(1-\nu_u)}K_0(\eta r)A(\xi,s) + \frac{i\xi|\xi|K_0(\rho)}{1-2\nu_u}C(\xi,s), \tag{31}
$$

and the resulting solutions are

$$
\hat{\tilde{u}}_r^{(I)} = -\frac{B(1+\nu_u)\eta c}{3(1-\nu_u)s}K_1(\eta r)A(\xi,s) - \left(K_1(\rho) + \frac{\rho K_2(\rho)}{2(1-2\nu_u)}\right)C(\xi,s) - i\xi K_1(\rho)D(\xi,s), \tag{32}
$$

$$
\hat{\tilde{u}}_z^{(I)} = -\frac{i\xi B(1+\nu_u)c}{3(1-\nu_u)s}K_0(\eta r)A(\xi,s) - \frac{i\xi r}{2(1-2\nu_u)}K_1(\rho)C(\xi,s) + |\xi|K_0(\rho)D(\xi,s), \tag{33}
$$

where $D(\xi,s)$ is again an arbitrary function of ξ and s.

Finally, it is not difficult to derive the stress expressions from (17)–(20) as follows:

$$
\frac{\hat{\tilde{\sigma}}_{rr}^{(I)}}{2G} = \frac{B(1+\nu_u)}{3(1-\nu_u)}\left\{\left(\frac{c\eta^2}{s}-1\right)K_0(\eta r) + \frac{c\eta}{sr}K_1(\eta r)\right\}A(\xi,s) + i\xi\left\{|\xi|K_0(\rho) + \frac{K_1(\rho)}{r}\right\}D(\xi,s)
$$
$$
+ \left\{\frac{1-\nu_u}{1-2\nu_u}|\xi|K_0(\rho) + \left(\frac{1}{r} + \frac{\rho|\xi|}{2(1-2\nu_u)}\right)K_1(\rho) + \frac{|\xi|}{2(1-2\nu_u)}K_2(\rho)\right\}C(\xi,s), \tag{34}
$$

$$
\frac{\hat{\tilde{\sigma}}_{zz}^{(I)}}{2G} = \frac{B(1+\nu_u)}{3(1-\nu_u)}\left(-\frac{c\xi^2}{s}-1\right)K_0(\eta r)A(\xi,s)
$$
$$
+ \left\{\frac{\nu_u}{1-2\nu_u}|\xi|K_0(\rho) - \frac{\xi^2 r}{2(1-2\nu_u)}K_1(\rho)\right\}C(\xi,s) - i\xi|\xi|K_0(\rho)D(\xi,s), \tag{35}
$$

$$
\frac{\hat{\tilde{\sigma}}_{\theta\theta}^{(I)}}{2G} = \frac{B(1+\nu_u)}{3(1-\nu_u)}\left(-K_0(\eta r) - \frac{c\eta}{sr}K_1(\eta r)\right)A(\xi,s)
$$
$$
+ \left\{\frac{\nu_u}{1-2\nu_u}|\xi|K_0(\rho) - \frac{K_1(\rho)}{r} - \frac{|\xi|}{2(1-2\nu_u)}K_2(\rho)\right\}C(\xi,s) - i\frac{\xi}{r}K_1(\rho)D(\xi,s), \tag{36}
$$

$$
\frac{\hat{\tilde{\sigma}}_{rz}^{(I)}}{2G} = \frac{i\xi B(1+\nu_u)c}{3(1-\nu_u)s}\eta K_1(\eta r)A(\xi,s)
$$
$$
+ \left\{\frac{i\xi\rho}{4(1-2\nu_u)}\left(K_0(\rho) + K_2(\rho)\right) + \frac{i\xi}{2}K_1(\rho)\right\}C(\xi,s) - \xi^2 K_1(\rho)D(\xi,s). \tag{37}
$$

In deriving these displacement and stress solutions, the far field boundary condition (9) has been already taken into account. The three unknown functions $A(\xi,s)$, $C(\xi,s)$, and $D(\xi,s)$ should be determined from the transformed versions of the boundary conditions (10), that is,

$$
\hat{\tilde{\sigma}}_{rz}^{(I)}(R,\xi,s) = 0, \tag{38}
$$

$$\frac{1}{\sqrt{2\pi}} \int_{-\infty}^{\infty} [\hat{\bar{\sigma}}_{rr}^{(I)}(R,\xi,s) + \hat{\bar{p}}^{(I)}(R,\xi,s)] e^{-i\xi z} \, d\xi = 0, \quad 0 \le |z| \le b,$$

$$\frac{1}{\sqrt{2\pi}} \int_{-\infty}^{\infty} \hat{\bar{\sigma}}_{rr}^{(I)}(R,\xi,s) e^{-i\xi z} \, d\xi = 0, \qquad\qquad b \le |z| \le \infty, \tag{39}$$

$$\hat{\bar{q}}^{(I)}(R,\xi,s) = \frac{\sin(\xi b)}{\sqrt{2\pi}\,\xi s} \frac{Q_0}{2\pi\,Rb} = \frac{2q_0 \sin(\xi b)}{\sqrt{2\pi}\,\xi s} = -\Omega(\xi,s), \tag{40}$$

where

$$q_0 = \frac{Q_0}{4\pi\,Rb} \quad \text{and} \quad \Omega(\xi,s) = -\frac{\sin(\xi b)}{\sqrt{2\pi}\,\xi s} \frac{Q_0}{2\pi\,Rb}.$$

On incorporating (29), (34), and (37) into (38) and (40), one can easily determine the three unknown functions in terms of $\hat{\bar{\sigma}}_{rr}^{(I)}(R,\xi,s)$ as follows:

$$A(\xi,s) = \frac{1}{\Delta}\big(-\alpha_{23}\alpha_{32}\hat{\bar{\sigma}}_{rr}^{(I)}(R,\xi,s) + (\alpha_{12}\alpha_{23} - \alpha_{22}\alpha_{13})\Omega(\xi,s)\big), \tag{41}$$

$$C(\xi,s) = \frac{1}{\Delta}\big(\alpha_{23}\alpha_{31}\hat{\bar{\sigma}}_{rr}^{(I)}(R,\xi,s) + (\alpha_{21}\alpha_{13} - \alpha_{11}\alpha_{23})\Omega(\xi,s)\big), \tag{42}$$

$$D(\xi,s) = \frac{1}{\Delta}\big((\alpha_{21}\alpha_{32} - \alpha_{31}\alpha_{22})\hat{\bar{\sigma}}_{rr}^{(I)}(R,\xi,s) + (\alpha_{11}\alpha_{22} - \alpha_{21}\alpha_{12})\Omega(\xi,s)\big), \tag{43}$$

where $\Delta = \alpha_{12}\alpha_{23}\alpha_{31} + \alpha_{13}\alpha_{21}\alpha_{32} - \alpha_{11}\alpha_{23}\alpha_{32} - \alpha_{13}\alpha_{22}\alpha_{31}$ and

$$\alpha_{11} = 2G\frac{B(1+\nu_u)}{3(1-\nu_u)}\left\{\left(\frac{c\eta^2}{s} - 1\right)K_0(\eta R) + \frac{c\eta}{sR}K_1(\eta R)\right\},$$

$$\alpha_{12} = 2G\left\{\frac{1-\nu_u}{1-2\nu_u}|\xi|K_0(|\xi|R) + \left[\frac{1}{R} + \frac{\xi^2 R}{2(1-2\nu_u)}\right]K_1(|\xi|R) + \frac{|\xi|}{2(1-2\nu_u)}K_2(|\xi|R)\right\},$$

$$\alpha_{13} = 2Gi\xi\left\{|\xi|K_0(|\xi|R) + \frac{K_1(|\xi|R)}{R}\right\}, \qquad \alpha_{21} = 2G\frac{i\xi B(1+\nu_u)c}{3(1-\nu_u)s}\eta K_1(\eta R),$$

$$\alpha_{22} = 2G\left\{\frac{i\xi|\xi|R}{4(1-2\nu_u)}[K_0(|\xi|R) + K_2(|\xi|R)] + \frac{i\xi}{2}K_1(|\xi|R)\right\}, \qquad \alpha_{23} = -2G\xi^2 K_1(|\xi|R),$$

$$\alpha_{31} = \frac{2G\kappa B^2(1-\nu)(1+\nu_u)^2}{9(\nu-\nu_u)(1-2\nu_u)}\eta K_1(\eta R), \qquad \alpha_{32} = \frac{2G\kappa B(1+\nu_u)}{3(1-2\nu_u)}\xi^2 K_1(|\xi|R).$$

It is obvious that if $\hat{\bar{\sigma}}_{rr}^{(I)}(R,\xi,s) = 0$, which is the case in [Rajapakse 1993], $A(\xi,s)$, $C(\xi,s)$, and $D(\xi,s)$ can be expressed in explicit form with $\Omega(\xi,s)$. However, for the current boundary conditions where $\hat{\bar{\sigma}}_{rr}^{(I)}(R,\xi,s) \ne 0$, one has to seek the numerical solutions of these three unknown functions, as discussed below.

Substituting (41) and (42) into (28), one has

$$\hat{\bar{p}}^{(I)}(R,\xi,s) = f_1(\xi,s)\hat{\bar{\sigma}}_{rr}^{(I)}(R,\xi,s) + f_2(\xi,s)\Omega(\xi,s), \tag{44}$$

where

$$f_1(\xi, s) = \frac{1}{\Delta}(-\alpha_{23}\alpha_{32}\alpha_{31p} + \alpha_{23}\alpha_{31}\alpha_{32p}),$$

$$f_2(\xi, s) = \frac{1}{\Delta}\big((\alpha_{21}\alpha_{13} - \alpha_{11}\alpha_{23})\alpha_{32p} + (\alpha_{12}\alpha_{23} - \alpha_{22}\alpha_{13})\alpha_{31p}\big)$$

with

$$\alpha_{31p} = -\frac{2GB^2(1-\nu)(1+\nu_u)^2}{9(\nu - \nu_u)(1-\nu_u)}K_0(\eta R), \qquad \alpha_{32p} = -\frac{2GB(1+\nu_u)}{3(1-2\nu_u)}|\xi|K_0(|\xi|R).$$

Now the boundary condition (39), combined with (44), can be transformed into the following dual integral equations

$$\int_{-\infty}^{\infty}[1 + f_1(\xi, s)]\hat{\bar{\sigma}}_{rr}^{(I)}(R, \xi, s)e^{-i\xi z}d\xi = -\int_{-\infty}^{\infty}f_2(\xi, s)\Omega(\xi, s)e^{-i\xi z}\,d\xi, \quad 0 \le |z| \le b,$$

$$\int_{-\infty}^{\infty}\hat{\bar{\sigma}}_{rr}^{(I)}(R, \xi, s)e^{-i\xi z}\,d\xi = 0, \qquad\qquad\qquad\qquad b < |z| < \infty. \tag{45}$$

It is found that $f_1(\xi, s)$, $f_2(\xi, s)$, and $\hat{\bar{\sigma}}_{rr}^{(I)}(R, \xi, s)$ are all real even functions of ξ, so the above dual integral equations can be further simplified as

$$\int_0^{\infty}\xi^{1/2}[1 + f_1(\xi, s)]\,\hat{\bar{\sigma}}_{rr}^{(I)}(R, \xi, s)J_{-1/2}(\xi z)\,d\xi = \sqrt{\frac{2}{\pi z}}g(z, s), \qquad 0 \le z \le b,$$

$$\int_0^{\infty}\xi^{1/2}\hat{\bar{\sigma}}_{rr}^{(I)}(R, \xi, s)J_{-1/2}(\xi z)\,d\xi = 0, \qquad\qquad b < z < \infty, \tag{46}$$

where

$$g(z, s) = -\int_0^{\infty}f_2(\xi, s)\Omega(\xi, s)\cos(\xi z)\,d\xi \tag{47}$$

and $\lim_{\xi \to \infty}f_1(\xi, s) = 0$. Introducing the function $\theta(x, s)$ by [Noble 1963]

$$\hat{\bar{\sigma}}_{rr}^{(I)}(R, \xi, s) = \frac{2}{\pi}\int_0^b\theta(x, s)\cos(x\xi)\,dx; \tag{48}$$

equations (46) are equivalent to the following Fredholm integral equation of the second kind

$$\theta(x, s) + \frac{2}{\pi}\int_0^b M(x, y, s)\theta(y, s)\,dy = g(x, s), \tag{49}$$

where

$$M(x, y, s) = \int_0^{\infty}f_1(\xi, s)\cos(x\xi)\cos(y\xi)d\xi. \tag{50}$$

Equations (48)–(50) determine $\hat{\bar{\sigma}}_{rr}^{(I)}(R, \xi, s)$ in the Laplace–Fourier transformed domain, and the three unknown functions $A(\xi, s)$, $C(\xi, s)$, and $D(\xi, s)$ can thus be numerically obtained from (41)–(43). Once $A(\xi, s)$, $C(\xi, s)$, and $D(\xi, s)$ are known, one can obtain the final solutions for the physical quantities such as displacement and stress components of the solid matrix, pore water pressure, and fluid discharge through the inversion of Laplace and Fourier transforms. It is important to note that $A(\xi, s)$, $C(\xi, s)$, and Δ are real even functions of ξ while $D(\xi, s)$ a pure imaginary odd function of ξ, the infinite integrals for the inverse Fourier transforms are thus reduced to the evaluation of a semiinfinite integral.

Note that the plane strain problem can be obtained by keeping the fluid flow rate $q_0 = Q_0/(4\pi R b)$ constant but allowing $b \to \infty$. As b approaches infinity, all the quantities with respect to z vanish. The fluid discharge problem for the borehole is thus governed only by (13) and (15). In this case the Fourier transform become redundant and it is found that the solutions can be solved directly in the Laplace domain as follows, where we have introduced $\tau = \sqrt{s/c}$:

$$\tilde{p}^{(I)} = \frac{K_0(r\tau)q_0}{s\kappa\tau K_1(R\tau)}, \tag{51}$$

$$\tilde{u}_r^{(I)} = \frac{q_0}{2G\kappa\tau K_1(R\tau)r}\left(R^2 K_0(R\tau) + \frac{\alpha(1-2\nu)}{1-\nu}\frac{RK_1(R\tau) - rK_1(r\tau)}{\tau}\right), \tag{52}$$

$$\tilde{\sigma}_{rr}^{(I)} = -\frac{q_0}{s\kappa\tau K_1(R\tau)r^2}\left(R^2 K_0(R\tau) + \frac{\alpha(1-2\nu)}{1-\nu}\frac{RK_1(R\tau) - rK_1(r\tau)}{\tau}\right), \tag{53}$$

$$\tilde{\sigma}_{\theta\theta}^{(I)} = \frac{q_0}{s\kappa\tau K_1(R\tau)}\left\{\frac{R^2}{r^2}K_0(R\tau) + \frac{\alpha(1-2\nu)}{1-\nu}\left(\frac{RK_1(R\tau)}{r^2\tau} - \frac{K_1(r\tau)}{r\tau} - K_0(r\tau)\right)\right\}. \tag{54}$$

II: Stress boundary problem. Since the pore pressure due to borehole drilling in case of an impermeable wall is much less than the pressure generated by the flux loading, the boundary condition for σ_{rr} can be modified to $\sigma_{rr} = 0$, without causing appreciable mathematical or applications errors. The modified boundary conditions at the borehole wall now correspond to a generalized plane stain problem. As first noted by Cui et al. [1997; 1998], such a problem can be subdivided further into three cases and the stress and pore pressure solutions, $\sigma_{rr}^{(II)}, \sigma_{\theta\theta}^{(II)}, \sigma_{zz}^{(II)}, \sigma_{r\theta}^{(II)}, \sigma_{rz}^{(II)}, \sigma_{\theta z}^{(II)}$, and $p^{(II)}$, may again be obtained using the principle of superposition. These solutions will not be repeated herein and the interested readers should refer to [Cui et al. 1997; 1998] for details.

5. Superposition

Once the stress solutions have been found for the two fundamental problems, the final solutions can be obtained by superposition based on these results, as formally shown below

$$\begin{gathered}
\sigma_{rr} = \sigma_{rr}^{(I)} + \sigma_{rr}^{(II)}, \quad \sigma_{\theta\theta} = \sigma_{\theta\theta}^{(I)} + \sigma_{\theta\theta}^{(II)}, \quad \sigma_{zz} = \sigma_{zz}^{(I)} + \sigma_{zz}^{(II)}, \\
\sigma_{r\theta} = \sigma_{r\theta}^{(II)}, \quad \sigma_{rz} = \sigma_{rz}^{(I)} + \sigma_{rz}^{(II)}, \quad \sigma_{\theta z} = \sigma_{\theta z}^{(II)}, \quad p = p^{(I)} + p^{(II)},
\end{gathered} \tag{55}$$

in which the trivial stress components are dropped.

6. Numerical schemes and comparisons

Due to the complexity of the integrands involved in conducting the Fourier and Laplace inversions, the stress components in the time domain corresponding to problems I and II have to be obtained numerically by applying approximate numerical schemes. As mentioned in the preceding section, the inverse Fourier transform arising from problem I turns to a semiinfinite integral which can be numerically integrated very accurately with Wolfram Mathematica 6.0, provided the upper limit of the integral is sufficiently large. In the ensuing numerical analyses, only the effective tangential stress and pore pressure will be
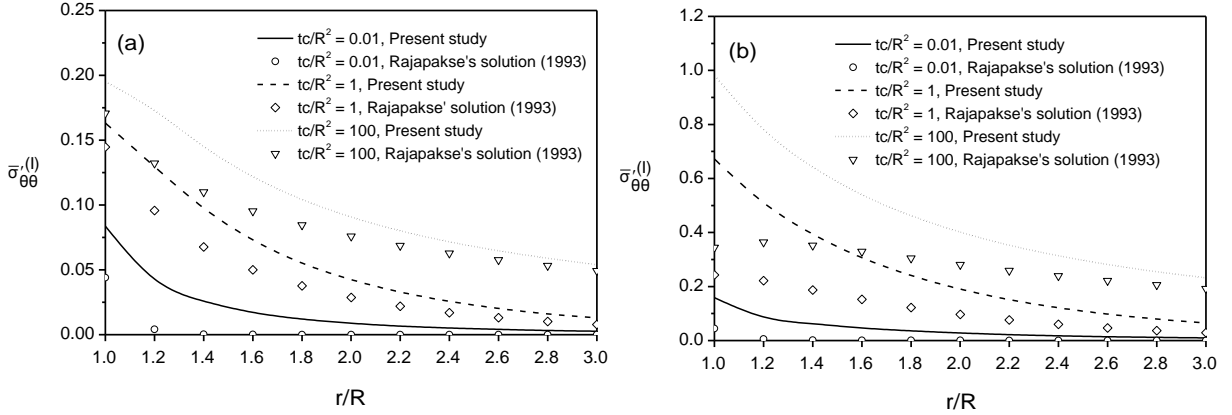
Figure 2. Comparison of effective tangential stress due to fluid injection over segment of length (a) $b/R = 0.25$; (b) $b/R = 1$.

considered as these are of critical importance to the study of borehole stability and fracturing, and the method of [Stehfest 1970] will be adopted in inverting the Laplace transform.

The Stehfest formula is

$$f(t) = \frac{\ln 2}{t} \sum_{n=1}^{N} X_n \tilde{f}\left(n\frac{\ln 2}{t}\right),\tag{56}$$

with the coefficient X_n given by

$$X_n = (-1)^{n+N/2} \sum_{j=\lfloor(n+1)/2\rfloor}^{\min(n,N/2)} \frac{j^{N/2}(2j)!}{(N/2-j)!j!(j-1)!(n-j)!(2j-n)!}.\tag{57}$$

The number of terms N in the series is even and a selection of $N = 8$ generally gives satisfactory results.

The errors caused by assuming a zero radial total stress at the borehole wall — that is, $\tilde{\sigma}_{rr}^{(I)}(R, z, t) = 0$ for $|z| \leq \infty$ — are tested by revisiting the fluid discharge problem of a borehole drilled in an infinite porous medium having incompressible constituents [Rajapakse 1993]. To make the comparison, the parameters $B = 0.999$, $\nu_u = 0.499$, $\nu = 0.3$ are adopted. Figure 2 shows the normalized effective tangential stress

$$\bar{\sigma}_{\theta\theta}^{\prime(I)} = \frac{\kappa\left[\sigma_{\theta\theta}^{(I)}(r, 0, tc/R^2) + p^{(I)}(r, 0, tc/R^2)\right]}{Rq_0}$$

versus the radial distance r/R for tc/R^2 ranging from 0.01 to 100 and for two values of b/R: 0.25 and 1. Although the two results exhibit a similar trend and the effective tangential stress is tensile along the radial distance, it is obvious that Rajapakse's solutions [1993] considerably underestimate the effective tangential stress near the borehole. This will accordingly lead to an overestimation of the fluid discharge needed to perform hydraulic fracturing.

7. Numerical results and discussions

We conducted some detailed parametric studies to examine the influence of permeability, borehole inclination, and the length of discharge loading on the stress distribution surrounding the borehole. To cover a wide range of permeabilities, three typical rocks, Ruhr sandstone, Danian chalk, and Gulf of

Rock type	G (MPa)	ν	ν_u	B	α	c (m^2/day)	k (mD)
Ruhr sandstone	13000	0.12	0.3	0.849	0.645	424	0.2
Danian chalk	2200	0.227	0.354	0.709	0.725	3.67	0.01
Gulf of Mexico shale	760	0.219	0.447	0.868	0.968	0.0143	0.0001

Table 1. Poromechanics constants for various rocks.

Mexico shale [Abousleiman et al. 1996], are considered with their poromechanics properties listed in Table 1. In addition, the following parameters are adopted in the analysis: far field in-situ stress and pore pressure $S_{x'} = 20$ MPa, $S_{y'} = 18$ MPa, $S_{z'} = 25$ MPa, $p_0 = 9.8$ MPa, borehole radius $R = 0.1$ m, borehole rotation $\varphi_{z'} = 30°$, borehole inclination $\varphi_y = 60°$ (varying from $0°$ to $90°$ in investigating the influence of inclination), and unless otherwise stated, the fluid flow rate $Q_0 = 1.4$ l/min.

Figure 3 presents isochrones of the maximum effective tangential stress around the borehole (here $\max_{0 \le \theta \le 2\pi} \sigma'_{\theta\theta} = \sigma_{\theta\theta} + \alpha p$ occurs at the $\theta = -4.8°$ direction for the current in-situ stresses and borehole geometries involved) and the corresponding pore pressure against the radial distance at position $z = 0$, for the case of Ruhr sandstone. It is found that both the effective tangential stress and the pore pressure
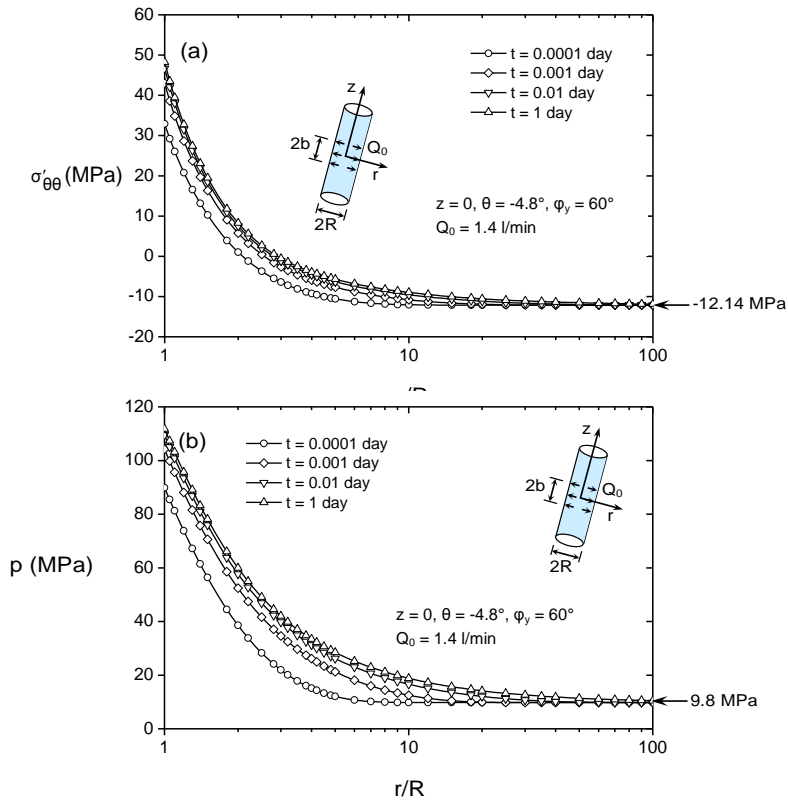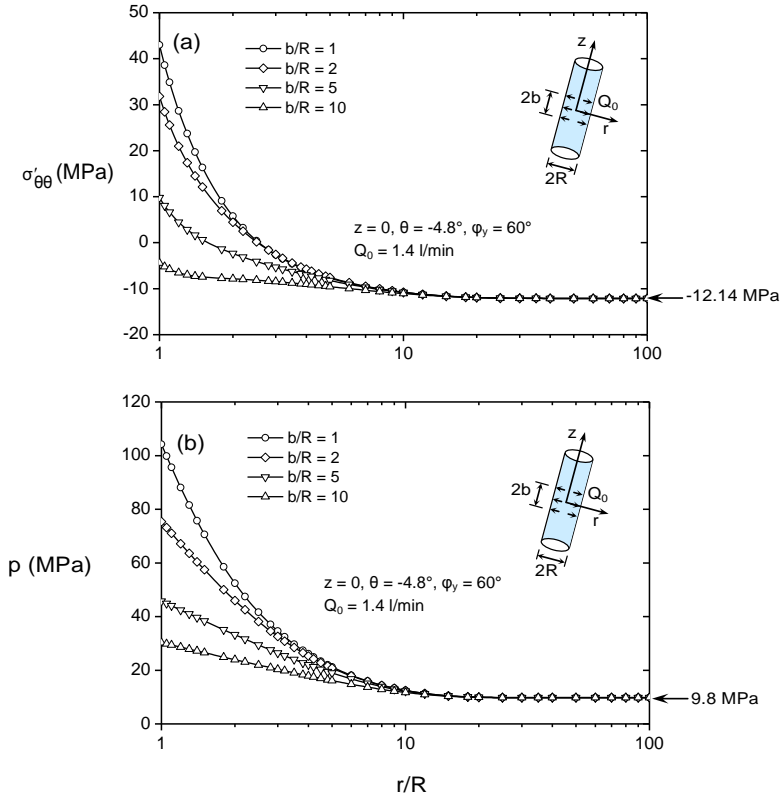

Figure 3. Isochrones of (top) maximum effective tangential stress and (bottom) pore pressure for Ruhr sandstone ($b/R = 1$).

generally increase as time progresses, deviating gradually from their in-situ values (It is recalled that positive values correspond to tension stress and compressive pore pressure, respectively). For all the time intervals considered, the induced pore pressures decrease monotonically as the radial distance increased, and fall uniformly to the virgin pore pressure $p_0 = 9.8$ MPa. Notice that all the four pore pressure curves exhibit the same slope at the borehole wall as a direct consequence of the constant flux (q_0) boundary condition. It is also observed that the effective tangential stresses achieve their maximum values at the borehole wall and then gradually reduce to the in-situ compression stress of

$$\sigma'_{\theta\theta} = \tfrac{1}{2}(S_x + S_y) - \sqrt{S_{xy}^2 + \tfrac{1}{4}(S_x - S_y)^2} - \alpha p_0 = -12.14 \, \text{MPa}$$

as r/R approaches infinity. This indicates that under the combined effects of borehole drilling and fluid flowing into the formation (The effective tangential stress attributed to the drilling of the borehole is compressive, while the fluid flowing into the borehole generates a tensile effective tangential stress), the tensile fracturing would most likely occur at the borehole wall and at a delayed time. This is not the case encountered in a purely drilling problem where the highest failure potential is usually located at some distance from the wellbore [Cui et al. 1997].

Figure 4 shows the influences of the discharge length b on the maximum effective tangential stress

Figure 4. Influences of discharge length on (top) maximum effective tangential stress and (bottom) pore pressure for Ruhr sandstone ($t = 0.001$ day).
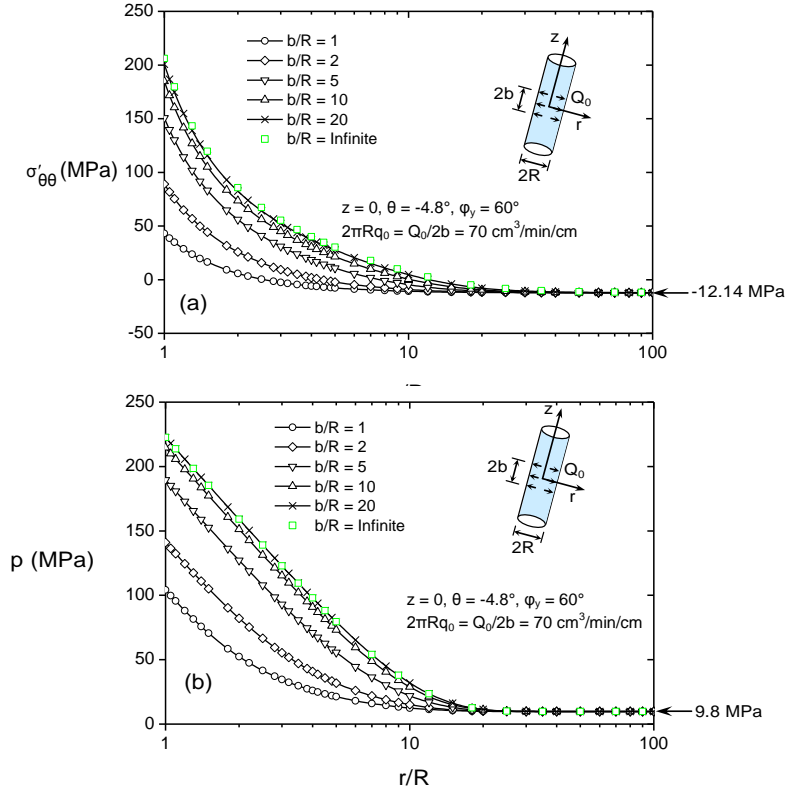
Figure 5. Variations of (top) maximum effective tangential stress and (bottom) pore pressure with discharge length for Ruhr sandstone in case of constant flow rate per unit length ($2\pi R q_0 = Q_0/2b = 70\,\text{cm}^3/\text{min/cm}$, $t = 0.001$ day).

and the pore pressure at $\theta = -4.8°$ direction for a specified time $t = 0.001$ day. It can be observed that both the effective tangential stress and the pore pressure generally decrease with the increasing discharge length. This is expected, because the fluid flow rate $q_0 = Q_0/(4\pi R b)$ is inversely proportional to b which will lead to a reduced contribution of the tensile stress at $z = 0$ as b becomes larger, while the compressive effective tangential stress induced by the borehole opening, on the other hand, is independent of b. Indeed, the decrease in the flow rate q_0 due to increasing b has been clearly linked to the gradual slope drop of the pore pressure curves at $r/R = 1$. Figure 5 shows similar results for the maximum effective tangential stress and the pore pressure distributions at $\theta = -4.8°$ direction with varying discharge length b/R yet constant flow rate per unit length of $2\pi R q_0 = Q_0/2b = 70\,\text{cm}^3/\text{min/cm}$ (Q_0 in this case however becomes proportional to b/R). Also shown in this figure are the limiting plane strain solutions as $b \to \infty$ calculated directly from (51) and (54). It can be concluded from Figure 5 that the flux discharge length of $b/R = 10$ is sufficient large to approximate the planar flow conditions at the mid-section of the borehole.

To visualize variations of the effective tangential stress versus the whole range of the directional angle θ near the borehole drilled in Ruhr sandstone, Figures 6 and 7 present the contours of effective tangential stress at various inclination angles $\varphi_y = 0°$, $30°$, $60°$, and $90°$ and time intervals $t = 0.0001$, 0.001, 0.01, and 1 day, for $z = 0$ position and for the region of $1 \le r/R \le 5$. In these two figures the

x''-axis coincides with the direction of the minimum compressive principal in-situ stress in x-y plane and y'' with the maximum in-situ stress direction. Note that the angle between the x and the x'' axes, θ_r ($\theta_r = \frac{\pi}{2} + \arctan \frac{2S_{xy}}{S_x - S_y}$), varies with the inclination angle φ_y via S_{xy}, S_x, and S_y. For the four inclination angles changing from $0°$ to $90°$ (Figure 6), the resulting values of θ_r are found to be $60°$, $73.9°$, $85.2°$, and $90°$, respectively. As displayed in Figures 6 and 7, the stress distributions are symmetric with respect to the two principal in-situ stress directions, the highest value occurring along the y''-axis direction. When the inclination angle increases, the stress contours tend to rotate counterclockwise with the maximum effective tangential stress slightly increased from 40.7 MPa (Figure 6a) to 44.2 MPa (Figure 6d). For the four different times considered, however, the stress contours will retain almost the same shape, although from Figure 7a to 7d a steady increase in the maximum stress magnitude is clearly seen as time increases.
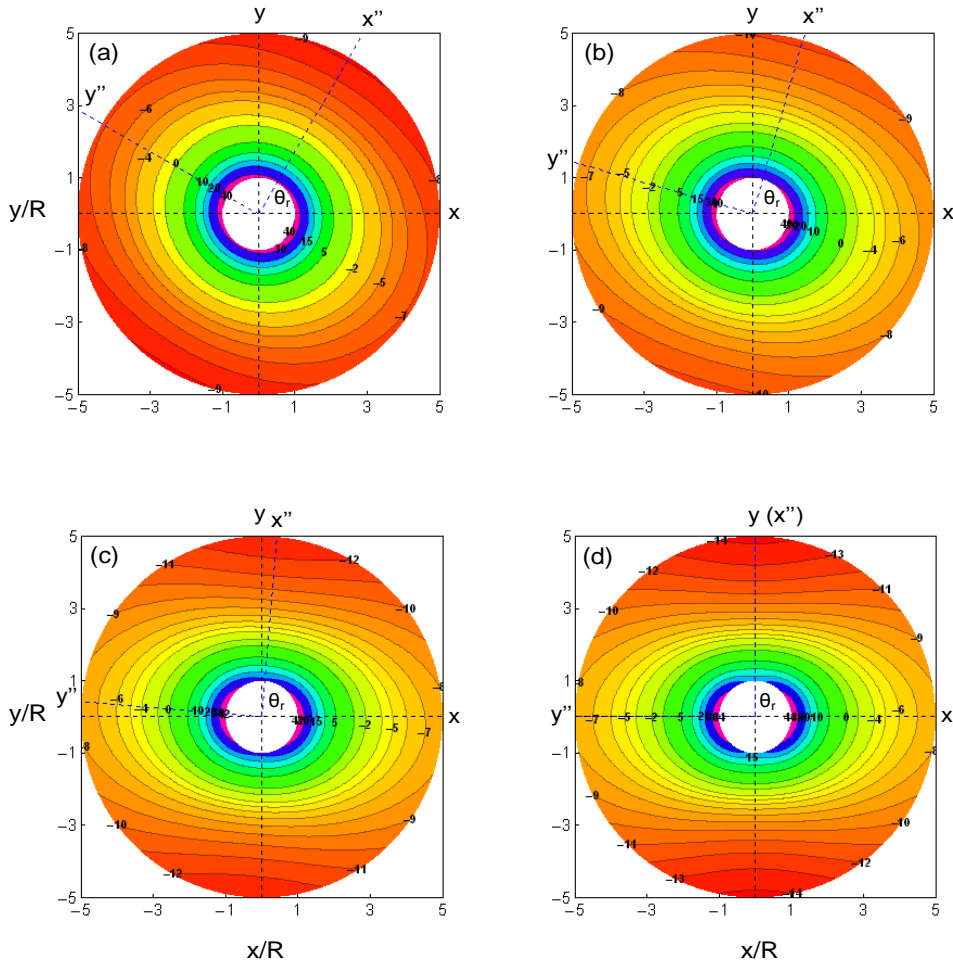
Figure 6. Effective tangential stress contours around the wellbore drilled in Ruhr sandstone with different inclination angles ($b/R = 1$, $t = 0.001$ day, $z = 0$, $1 \leq r/R \leq 5$): (a) $\varphi_y = 0°$, $\theta_r = 60°$; (b) $\varphi_y = 30°$, $\theta_r = 73.9°$; (c) $\varphi_y = 60°$, $\theta_r = 85.2°$; (d) $\varphi_y = 90°$, $\theta_r = 90°$.
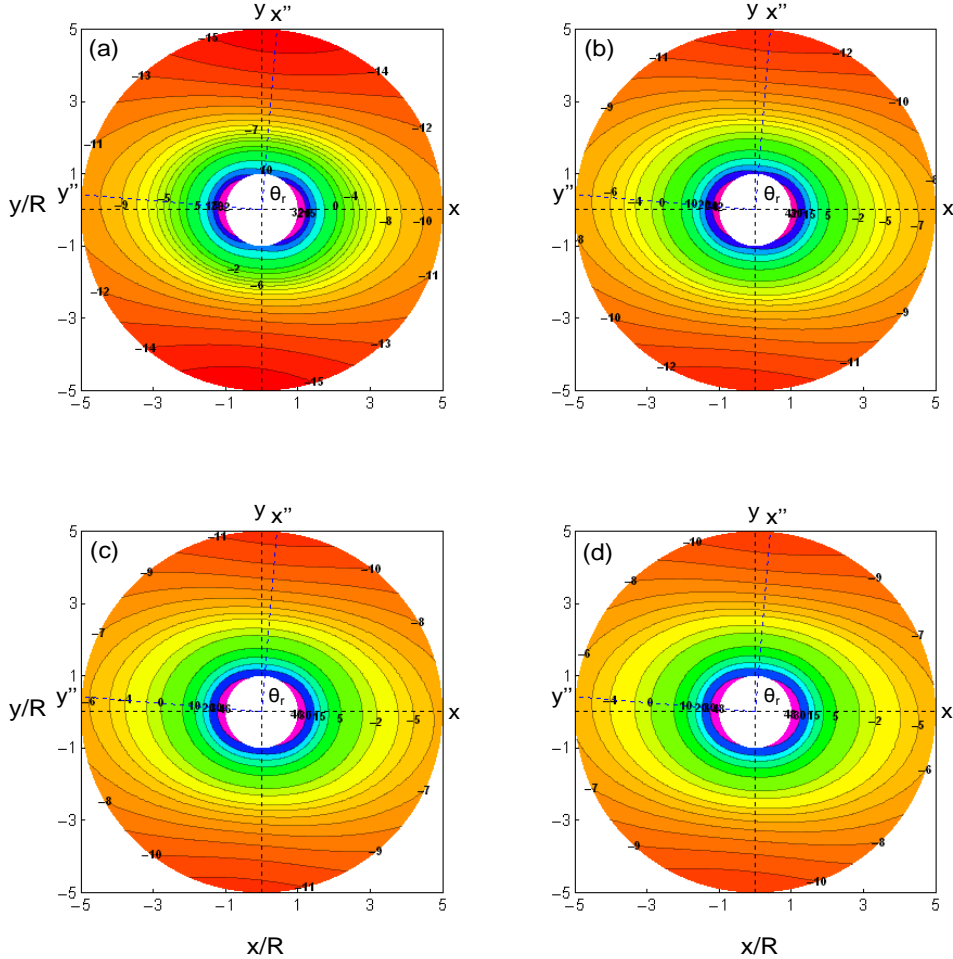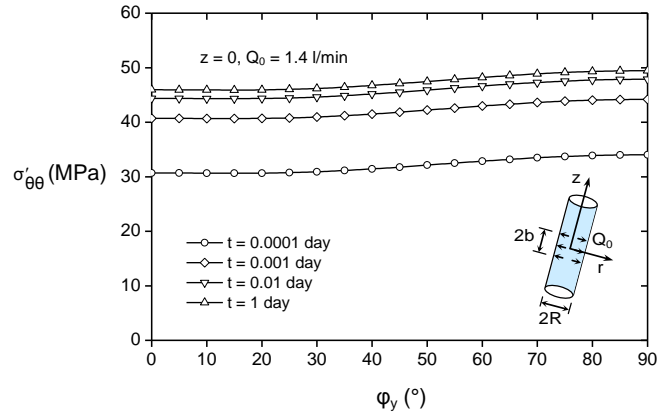
Figure 7. Effective tangential stress contours around the wellbore drilled in Ruhr sandstone at various times ($b/R = 1$, $\varphi_y = 60°$, $\theta_r = 85.2°$, $z = 0$, $1 \leq r/R \leq 5$): (a) $t = 0.0001$ day; (b) $t = 0.001$ day; (c) $t = 0.01$ day; (d) $t = 1$ day.

It is noteworthy that the flux induced effective tangential stress is independent with both φ_y and θ, thus the influences of these two parameters on the combined effective tangential stress are entered only through the stress term corresponding to the borehole drilling.

In Figure 8 the influence of the borehole inclination on the maximum effective tangential stress $\max_{0 \leq \theta \leq 2\pi} \sigma'_{\theta\theta}$, at the borehole wall and $z = 0$ position, are further illustrated for the Ruhr sandstone case. It is found that for all the time intervals, the variation of the maximum effective tangential stress with the inclination is somewhat complex and no longer monotonic. For small values of φ_y, an increase in the inclination angle is accompanied by a nearly indistinguishable reduction in the maximum effective tangential stress. As inclination reaches $\varphi_y = 20°$, however, the influence of the inclination becomes more noticeable and there is a tendency for the effective tangential stress to increase gradually with the inclination angle.
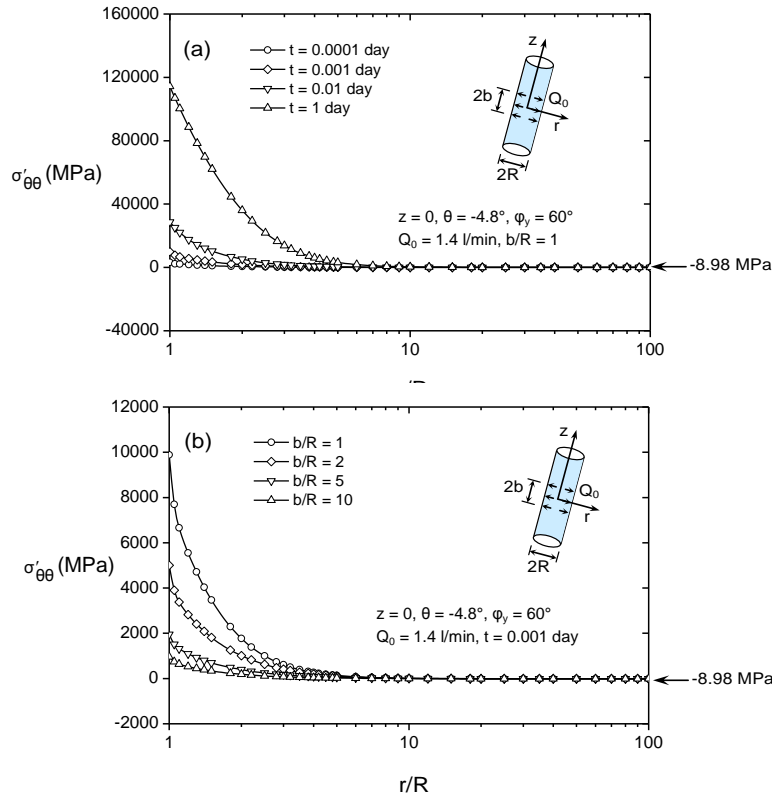
Figure 8. Variation of maximum effective tangential stress with borehole inclination for Ruhr sandstone ($b/R = 1, r/R = 1$).

Additionally, to see how the permeability of the saturated rock affects the stress behavior around the borehole, the solutions for Danian chalk and Gulf of Mexico shale are provided for $t = 0.0001$, 0.001, 0.01, and 1 day and $b/R = 1, 2, 5$, and 10, as plotted in Figures 9 and 10. In general, the influences of
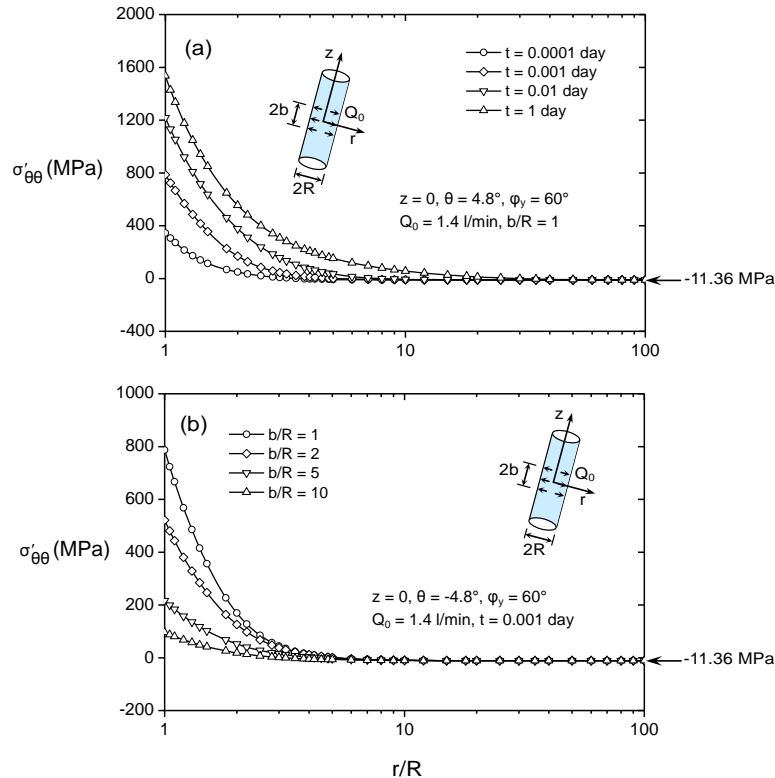
Figure 9. Variations of maximum effective tangential stress with radial distance at (top) various times and (bottom) various discharge length for Danian chalk.

Figure 10. Variations of maximum effective tangential stress with radial distance at (top) various times and (bottom) various discharge lengths for Gulf of Mexico shale.

the fluid discharge length and the time duration on the maximum effective tangential stress, which still occurs at $\theta = -4.8°$ direction for Danian chalk and Gulf of Mexico shale, are similar for the three rock formations with different permeabilities. However, when the permeability becomes smaller, say Danian chalk and Gulf of Mexico shale, the produced effective tangential stress under fixed fluid flow rate $Q_0 = 1.4$ l/min could be much greater and tend to level off much faster than in the relatively permeable formation like Ruhr sandstone. For example, in Figure 10 for Gulf of Mexico shale the predicted effective tangential stress may be as high as 120000 MPa. As in this case the effective tangential stress caused by the borehole drilling is maintained at a low level of around 20 MPa, very high effective tangential stress must be induced as a result of the fluid penetrating into the shale. This indicates that for low-permeable formations, the effective tangential stress is actually dominated by the flux loading. In reality, however, such large an effective tangential stress will never be reached since the tensile strength of a typical shale is less than 10 MPa.

Finally, it should be remarked that having known the stress distribution around a borehole, the analyses of the borehole fracturing will then become a simple matter. Moreover, the current solution can be employed to estimate the fluid flow rate that is required to trigger hydraulic fracturing, which will provide important guidance in the drilling practice.

8. Conclusions

An analytical method has been presented for the stress and pore pressure solutions of an inclined borehole subjected to the far-field three-dimensional in-situ stresses and to a fluid discharge applied over a finite segment of its surface. With the concept of superposition, the problem is decomposed into two fundamental parts whose solutions are simpler to handle. Comprehensive numerical analyses are also presented to examine the effects of some mechanical and geometrical parameters on the effective tangential stress and pore pressure distributions. The following conclusions are drawn:

(a) The existing solution for the limiting case of incompressible constituents which assumes a zero radial total stress along the whole wellbore surface tends to considerably underestimate the effective tangential stress near the borehole, which thus will lead to an overestimation of the fluid discharge needed to perform hydraulic fracturing.

(b) The effective tangential stress around a borehole subjected to a constant fluid flow rate generally increases with the time duration and with the decreasing loading length. The maximum effective tangential stress takes place at the borehole wall, which is not the case encountered in a purely drilling problem where the highest failure potential is usually located at some distance from the wellbore.

(c) The permeability has a pronounced influence on the predicted stress behavior. For a fixed fluid flow rate, the generated effective tangential stresses corresponding to highly impermeable Gulf of Mexico shale would be much greater and degrade much faster than those for Ruhr sandstone.

(d) In the particular case for Ruhr sandstone, the effective tangential stress distributions around the borehole are symmetric with respect to the two principal in-situ stress directions, the highest value occurring along the direction of the maximum compressive principal stress. An increase in the inclination angle φ_y has little influence on the estimated maximum effective tangential stress at the borehole wall for small values of φ_y, but will increase the maximum effective tangential stress and hence the possibility of a fracturing failure when φ_y exceeds 20°.

(e) The present analysis can also be used to backfigure the fluid flow rate that is required to initiate a fracture around the borehole. This will provide important guidance in the drilling practice.

References

[Abousleiman and Ekbote 2005] Y. Abousleiman and S. Ekbote, "Solutions for the inclined borehole in a porothermoelastic transversely isotropic medium", *J. Appl. Mech. (ASME)* **72**:1 (2005), 102–114.

[Abousleiman and Nguyen 2005] Y. Abousleiman and V. Nguyen, "Poromechnanics response of inclined wellbore geometry in fractured porous media", *J. Eng. Mech. (ASCE)* **131**:11 (2005), 1170–1183.

[Abousleiman et al. 1996] Y. Abousleiman, A. H.-D. Cheng, C. Jiang, and J.-C. Roegiers, "Poroviscoelastic analysis of borehole and cylinder problems", *Acta Mech.* **119**:1–4 (1996), 199–219.

[Abousleiman et al. 1999] Y. Abousleiman, S. Ekbote, L. Cui, F. Mody, J.-C. Roegiers, and M. Zaman, "Time-dependent coupled processes in wellbore design and stability: PBORE-3D", in *SPE Annual Technical Conference and Exhibition* (Houston, TX, 1999), Society of Petroleum Engineers, Richardson, TX, 1999. Paper #56759-MS.

[Biot 1941] M. A. Biot, "General theory of three-dimensional consolidation", *J. Appl. Phys.* **12**:2 (1941), 155–164.

[Bowen 1982] R. M. Bowen, "Compressible porous media models by use of the theory of mixtures", *Int. J. Eng. Sci.* **20**:6 (1982), 697–735.

[Carter and Booker 1982] J. P. Carter and J. R. Booker, "Elastic consolidation around a deep circular tunnel", *Int. J. Solids Struct.* **18**:12 (1982), 1059–1074.

[Cui et al. 1997] L. Cui, A. H.-D. Cheng, and Y. Abousleiman, "Poroelastic solution for an inclined borehole", *J. Appl. Mech.* (*ASME*) **64**:1 (1997), 32–38.

[Cui et al. 1998] L. Cui, S. Ekbote, Y. Abousleiman, M. M. Zaman, and J.-C. Roegiers, "Borehole stability analyses in fluid saturated formations with impermeable walls", *Int. J. Rock Mech. Min. Sci.* **35**:4-5 (1998), 582–583.

[Cui et al. 1999] L. Cui, Y. Abouleiman, A. H.-D. Cheng, and J.-C. Roegiers, "Time-dependent failure analysis of inclined boreholes in fluid-saturated formations", *J. Energy Resour. Technol.* (*ASME*) **121**:1 (1999), 31–39.

[Detournay and Cheng 1988] E. Detournay and A. H.-D. Cheng, "Poroelastic response of a borehole in a non-hydrostatic stress field", *Int. J. Rock Mech. Min.* **25**:3 (1988), 171–182.

[Ekbote and Abousleiman 2005] S. Ekbote and Y. Abousleiman, "Porochemothermoelastic solution for an inclined borehole in a transversely isotropic formation", *J. Eng. Mech.* (*ASCE*) **131**:5 (2005), 522–533.

[Ekbote and Abousleiman 2006] S. Ekbote and Y. Abousleiman, "Porochemoelastic solution for an inclined borehole in a transversely isotropic formation", *J. Eng. Mech.* (*ASCE*) **132**:7 (2006), 754–763.

[Jaeger and Cook 1969] J. S. Jaeger and N. G. W. Cook, *Fundamentals of rock mechanics*, Chapman and Hall, New York, 1969.

[Noble 1963] B. Noble, "The solution of Bessel function dual integral equations by a multiplying-factor method", *Math. Proc. Cambridge Philos. Soc.* **59**:2 (1963), 351–362.

[Rajapakse 1993] R. K. N. D. Rajapakse, "Stress analysis of borehole in poroelastic medium", *J. Eng. Mech.* (*ASCE*) **119**:6 (1993), 1205–1227.

[Rice and Cleary 1976] J. R. Rice and M. P. Cleary, "Some basic stress diffusion solutions for fluid-saturated elastic porous media with compressible constituents", *Rev. Geophys.* **14**:2 (1976), 227–241.

[Stehfest 1970] H. Stehfest, "Algorithm 368: numerical inversion of Laplace transforms [D5]", *Commun. ACM* **13**:1 (1970), 47–49.

[Wang 2000] H. Wang, *Theory of poroelasticity with applications to geomechanics and hydrology*, Princeton University Press, Princeton, NJ, 2000.

YOUNANE N. ABOUSLEIMAN: yabousle@ou.edu
The University of Oklahoma, Poromechanics Institute, Mewbourne School of Petroleum & Geological Engineering, 100 East Boyd Street, Norman, OK 73019-1014, United States

SHENGLI CHEN: Shengli.Chen-1@ou.edu
The University of Oklahoma, Poromechanics Institute, Mewbourne School of Petroleum & Geological Engineering, 100 East Boyd Street, Norman, OK 73019-1014, United States

ELASTIC SH WAVE PROPAGATION IN A LAYERED ANISOTROPIC PLATE WITH PERIODIC INTERFACE CRACKS: EXACT VERSUS SPRING BOUNDARY CONDITIONS

ANDERS BOSTRÖM AND OLEG V. KVASHA

The propagating antiplane (SH) modes in a symmetrically three-layered, anisotropic, thick plate with a periodic array of interface cracks are investigated. The exact dispersion relation can be derived with the help of a hypersingular integral equation approach and Floquet's theorem. The interface cracks can be a model for interface damage, but a much simpler model is a recently developed spring boundary condition. This boundary condition is used both for the thick plate and in the derivation of plate equations with the help of power series expansions in the thickness coordinate. For low frequencies (cracks small compared to the wavelength) the three models are shown to give the same results and this is a confirmation that the spring boundary condition is a valid approximation at low frequencies.

1. Introduction

A common failure mode in laminated composite plates is the occurrence of damage at the interface between the plies. This damage is more or less in the form of microcracks at the interface, and affects the propagation of ultrasound in the composite. Thus, ultrasonic nondestructive testing can be used to detect the damage, and in this connection it is very valuable to have a good model of the ultrasonic wave propagation in the damaged plate; see [Datta and Shah 2009] for elastic wave propagation in composite media in general. Recently, Boström and Golub [2009] proposed a (distributed) spring boundary condition to model a distribution of interface microcracks and derived a plate equation including this spring boundary condition. Another way to treat the interface microcracks is to model them as a periodic array of interface cracks; this model is expected to be good at low frequencies (cracks much smaller than the wavelength). As a model case the two-dimensional antiplane (SH) modes in a symmetrically layered, anisotropic, thick plate with a periodic array of interface cracks are investigated in this paper, and the results are compared to the case when the interface cracks are replaced by the spring boundary condition and also to the case when plate theory with the spring boundary condition is used. At low frequencies all three theories give the same result for the solution of the dispersion relation.

Zhang and Gross [1998] consider the elastic wave propagation and scattering in the presence of cracks, and investigate, in particular, the scattering by a periodic array of cracks, also for the two-dimensional SH anisotropic case. The SH wave propagation in isotropic space with a periodic array of interface cracks is considered by Angel and Achenbach [1985].

The plan of the paper is as follows. In Section 2 the exact dispersion relation is derived for the SH modes in a symmetrically three-layered, thick plate with periodic arrays of interface cracks. In Section 3 the spring boundary condition from [Boström and Golub 2009] is stated, and the derivation of symmetric and antisymmetric plate equations is sketched. The antisymmetric plate equation was not given in [Boström and Golub 2009], and the two plate equations are, furthermore, given to higher order in the plate thickness. Section 4 contains a few numerical result comparing the different theories and Section 5 offers a few concluding remarks.

2. Formulation of the problem

Consider a symmetrically three-layered, thick plate according to Figure 1, which also shows the xz coordinate system used. The middle layer has thickness d_1 and the two outer layers have thickness $d_2 - d_1$ each. The material parameters in the layers are denoted by an upper index $j = 1, 2$ for the middle and outer layers, respectively; see Figure 1. Thus the densities are ρ^1 and ρ^2 in the middle and outer layers, respectively. The principal axes of the anisotropic materials are assumed to be parallel with the coordinate axes. The only relevant stiffness constants are thus c_{44}^j and c_{66}^j. All the cracks are of equal width $2l$ and are periodically located with centers at $x = ma$, $z = \pm d_1$, $m = 0, \pm 1, \pm 2, \ldots$.

Only shear horizontal (SH) waves with the polarization vector perpendicular to the plane of propagation are considered. Time harmonic waves are assumed, with the time factor $e^{-i\omega t}$ suppressed throughout. The displacement has only a y component u_y^j, which obeys the equation
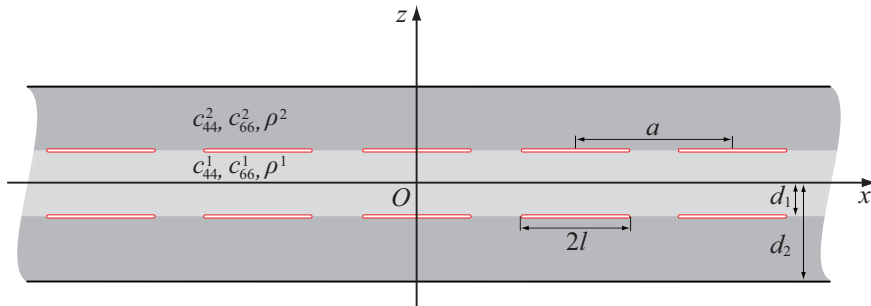
$$c_{66}^j \frac{\partial^2 u_y^j}{\partial x^2} + c_{44}^j \frac{\partial^2 u_y^j}{\partial z^2} + \rho^j \omega^2 u_y^j = 0, \qquad j = 1, 2. \tag{2-1}$$

The two relevant stress components are

$$\sigma_{yx}^j = c_{66}^j \frac{\partial u_y^j}{\partial x}, \qquad \sigma_{yz}^j = c_{44}^j \frac{\partial u_y^j}{\partial z}, \qquad j = 1, 2. \tag{2-2}$$

From the symmetry of the problem it follows that only one half of the plate $(-d_2 < z < 0)$ needs to be considered. The boundary conditions are then

$$u_y^1\big|_{z=0} = 0, \quad \sigma_{yz}^2\big|_{z=-d_2} = 0, \qquad \text{or} \qquad \sigma_{yz}^1\big|_{z=0} = 0, \quad \sigma_{yz}^2\big|_{z=-d_2} = 0, \tag{2-3}$$

Figure 1. Elastic plate with periodic arrays of cracks.

depending on whether the antisymmetric or the symmetric waves in the plate are considered. On the interface $z = -d_1$ the displacement and traction are continuous except on the cracks where the boundary conditions are

$$\sigma_{yz}^1\big|_{z=-d_1} = \sigma_{yz}^2\big|_{z=-d_1} = 0, \qquad |x - ma| < l, \quad m = 0, \pm 1, \pm 2, \dots, \tag{2-4}$$

and this gives rise to a displacement discontinuity on the cracks. The crack-opening displacement on a crack is defined as

$$v_m(x) = u_y^1(x, -d_1) - u_y^2(x, -d_1), \qquad |x - ma| < l, \quad m = 0, \pm 1, \pm 2, \dots. \tag{2-5}$$

As the plate with the cracks is a periodic system Floquet's (or Bloch's) theorem [Yariv and Yeh 1984] states that the modes in the plate have the property

$$u_y^j(x, z) = e^{ikx} w^j(x, z), \qquad j = 1, 2, \tag{2-6}$$

where $w^j(x, z)$ are periodic functions with period a:

$$w^j(x + ma, z) = w^j(x, z), \qquad m = 0, \pm 1, \pm 2, \dots, \quad j = 1, 2. \tag{2-7}$$

The main goal here is to find the dispersion relation $k = k(\omega)$.

3. Exact solution

The wave fields u_y^j can be represented in the form of the inverse Fourier transform:

$$u_y^j(x, z) = \frac{1}{2\pi} \int_\Gamma U_y^j(\alpha, z) e^{-i\alpha x} \, d\alpha, \qquad j = 1, 2, \tag{3-1}$$

where the integration paths are going in the complex α plane along the real axis $\mathrm{Im}\, \alpha = 0$, deviating from it only for bypassing the real singularities of the integrands in accordance with the principle of limiting absorption [Babeshko et al. 1989]. The Fourier transforms of the wave fields $U_y^j(\alpha)$ are expressed as the products of the Fourier transforms $K^1(\alpha, z)$ and $K^2(\alpha, z)$ of the Green's functions $k^1(x, z)$ and $k^2(x, z)$ of the layers $-d_1 < z < 0$ and $-d_2 < z < -d_1$, and the Fourier transform $Q(\alpha)$ of the unknown stress $q(x)$ arising on the contact interface:

$$U_y^j(\alpha, z) = K^j(\alpha, z) Q(\alpha), \qquad j = 1, 2. \tag{3-2}$$

Mathematically, the function $k^1(x, z)$ is the solution to (2-1) with $j = 1$ obeying the boundary conditions

$$u_y^1\big|_{z=0} = 0, \quad \sigma_{yz}^1\big|_{z=-d_1} = \delta(x), \qquad \text{or} \qquad \sigma_{yz}^1\big|_{z=0} = 0, \quad \sigma_{yz}^1\big|_{z=-d_1} = \delta(x), \tag{3-3}$$

where $\delta(x)$ is the delta function. As in (2-3), the choice of the boundary conditions depends on whether the antisymmetric or the symmetric waves in the plate are considered. Analogously, the function $k^2(x, z)$ obeys (2-1) with $j = 2$ and the boundary conditions

$$\sigma_{yz}^2\big|_{z=-d_1} = \delta(x), \qquad \sigma_{yz}^2\big|_{z=-d_2} = 0. \tag{3-4}$$

The Fourier transform of both functions is easily calculated analytically:

$$K^1(\alpha, z) = \frac{\sinh \sigma^1 z}{c_{44}^1 \sigma^1 \cosh \sigma^1 d_1}, \qquad \text{or} \qquad K^1(\alpha, z) = -\frac{\cosh \sigma^1 z}{c_{44}^1 \sigma^1 \sinh \sigma^1 d_1}, \tag{3-5}$$

and

$$K^2(\alpha, z) = \frac{\cosh \sigma^2 (z + d_2)}{c_{44}^2 \sigma^2 \sinh \sigma^2 (d_2 - d_1)}, \tag{3-6}$$

where

$$\sigma^j = \left(\frac{c_{66}^j}{c_{44}^j \alpha^2} - (\kappa_{44}^j)^2 \right)^{1/2}, \qquad \kappa_{44}^j = \sqrt{\frac{\rho^j \omega^2}{c_{44}^j}}, \qquad j = 1, 2. \tag{3-7}$$

($K^2(\alpha, z)$ is the same for the symmetric and antisymmetric problems.)

To solve for $Q(\alpha)$, take the difference between the two equations Equation (3-2), which introduces the sum of all the Fourier transforms $V_m(\alpha)$ of the crack-opening displacements $v_m(x)$:

$$Q(\alpha) = L(\alpha) \sum_{m=-\infty}^{\infty} V_m(\alpha), \qquad L(\alpha) = \left(K^1(\alpha, -d_1) - K^2(\alpha, -d_1) \right)^{-1}. \tag{3-8}$$

Substitution of this expression into (3-2) implies analogous representations of the Fourier transforms of the displacements fields

$$U_y^j(\alpha, z) = N^j(\alpha, z) \sum_{m=-\infty}^{\infty} V_m(\alpha), \qquad N^j(\alpha, z) = K^j(\alpha, z) L(\alpha), \qquad j = 1, 2, \tag{3-9}$$

which leads to the integral representations

$$u_y^j(x, z) = \frac{1}{2\pi} \int_{\Gamma} N^j(\alpha, z) \sum_{m=-\infty}^{\infty} V_m(\alpha) e^{-i\alpha x} d\alpha, \qquad j = 1, 2. \tag{3-10}$$

Due to the periodicity property of the displacements fields (2-6), the Fourier transforms of the unknown crack-opening displacements are connected by

$$V_m(\alpha) = \int_{ma-l}^{ma+l} v_m(x) e^{i\alpha x} dx = \int_{-l}^{l} v_0(x) e^{i(\alpha x + (\alpha + k)ma)} dx = V_0(\alpha) e^{i(\alpha + k)ma}, \tag{3-11}$$

where $m = 0, \pm 1, \pm 2, \ldots$. Substitution of the functions $V_m(\alpha)$ in this form into the representation (3-10) and use of the formula

$$\sum_{m=-\infty}^{\infty} e^{i(\alpha + k)ma} = \sum_{m=-\infty}^{\infty} \delta\left(\frac{\alpha a + ka}{2\pi} - m \right) \tag{3-12}$$

lead to the representation of the wave fields in series form:

$$u_y^j(x, y) = \frac{1}{a} \sum_{m=-\infty}^{\infty} N^j(\alpha_m, z) V_0(\alpha_m) e^{-i\alpha_m x}, \qquad j = 1, 2, \tag{3-13}$$

where $\alpha_m = 2\pi m/a - k$.

Use of the displacements in the form Equation (3-13) to compute the stress and insertion into the stress-free boundary condition (2-4) gives the integral equation for the crack-opening displacement $v_0(x)$:

$$\frac{1}{a} \sum_{m=-\infty}^{\infty} L(\alpha_m) V_0(\alpha_m) e^{-i\alpha_m x} = 0, \qquad |x| < l, \tag{3-14}$$

where the Fourier transform of the crack-opening displacement is

$$V_0(\alpha) = \int_{-l}^{l} v_0(x) e^{i\alpha x} \, dx. \tag{3-15}$$

Note that every solution to (3-14) obtained for $|x| < l$ obeys it also for $|x - ma| < l$, $m = 0, \pm 1, \pm 2, \ldots$ due to the periodicity of the left-hand side of the equation. The values of k, for which nontrivial solutions to (3-14) exist, are exactly the wave numbers of the modes propagating in the plate at the given frequency ω.

To obtain solutions to (3-14), the crack-opening displacement is expanded into a series:

$$v_0(x) = \sum_{n=0}^{\infty} c_n p_n(x), \qquad p_n(x) = U_n\left(\frac{x}{l}\right)\sqrt{1 - \left(\frac{x}{l}\right)^2}, \tag{3-16}$$

where $U_n(x)$, $n = 0, 1, \ldots$ are Chebyshev polynomials of the second kind. Note the important fact that this expansion takes care of the stress singularity at the crack tips. Substitution into (3-14) yields

$$\sum_{n=0}^{\infty} c_n \left[\frac{1}{a} \sum_{m=-\infty}^{\infty} L(\alpha_m) P_n(\alpha_m) e^{-i\alpha_m x} \right] = 0, \qquad |x| < l, \tag{3-17}$$

where

$$P_n(\alpha) = \int_{-l}^{l} p_n(x) e^{i\alpha x} \, dx = \pi l i^n (n + 1) \frac{J_{n+1}(\alpha l)}{\alpha}, \tag{3-18}$$

where $J_{n+1}(\alpha l)$ is a Bessel function. Following the Galerkin scheme, (3-17) is multiplied by $p_j(x)$ for $j = 0, 1, 2, \ldots$ and then integrated over $-l < x < l$ to obtain the homogeneous system of linear algebraic equations

$$\sum_{n=0}^{\infty} A_{jn}(k, \omega) c_n = 0, \qquad j = 0, 1, 2, \ldots, \tag{3-19}$$

where the matrix

$$A_{jn}(k, \omega) = \frac{1}{a} \sum_{m=-\infty}^{\infty} L(\alpha_m) P_n(\alpha_m) P_j(-\alpha_m). \tag{3-20}$$

Nontrivial solutions to this system exist when the matrix $A_{jn}(k, \omega)$ becomes singular, that is

$$\det\left(A_{jn}(k, \omega) \right) = 0. \tag{3-21}$$

This is the desired dispersion relation. It implicitly relates the wave numbers k to the given frequency ω.

4. Approximate plate equations

If the cracks are small as compared to the characteristic wavelengths in the plate, it is possible to consider the system in a simple fashion using an approximate spring boundary condition. First it is noted that the exact distribution of the cracks is expected to be unimportant for small cracks. In [Boström and Golub 2009] an approximate spring boundary condition was derived to model an interface with a random distribution of small cracks of the same size, and this boundary condition should therefore also be applicable to a periodic distribution of interface cracks. Thus, the exact periodic boundary condition at the interface $z = -d_1$ is replaced by the simplified spring boundary condition (*ibid.*):

$$\sigma_{yz}^1 = \sigma_{yz}^2 = \kappa(u^1 - u^2), \qquad z = -d_1, \tag{4-1}$$

where the spring constant is

$$\kappa = \frac{1}{Cl\pi} \cdot \frac{4c_{44}^1 c_{44}^2 k_{44}^1 k_{44}^2}{c_{44}^1 k_{44}^1 k_{66}^2 + c_{44}^2 k_{44}^2 k_{66}^1}. \tag{4-2}$$

Here $k_{mm}^j = \omega / v_{mm}^j$ are the wave numbers and $v_{mm}^j = \sqrt{c_{mm}^j / \rho^j}$ are SH-wave velocities along the z and x axes (for $m = 4, 6$, respectively) in the middle and outer layers ($j = 1, 2$), and $C = 2l/a$ is the relative density of cracks. It is noted that the spring constant κ must be large for the approximations in deriving the spring boundary condition to be valid [Boström and Golub 2009]. The dispersion relation for the plate with this boundary condition is easily derived and is not given here.

If also the thickness of the plate, as well as the cracks, is small as compared to the characteristic wavelengths in the plate, the problem can be further simplified by using plate theory. Here the approach of Boström et al. [2001] and Boström and Golub [2009] is followed. Thus, the assumption of time harmonic waves is lifted, and it is noted that the spring constant in (4-2) is frequency independent. The displacement fields are expanded as

$$u_y^1(x, z) = \sum_{n=0}^{\infty} u_n^1(x) z^n, \qquad u_y^2(x, z) = \sum_{n=0}^{\infty} u_n^2(x)(z + d_1)^n, \tag{4-3}$$

using Taylor power series expansions. Substitution of these formulas into (2-1) leads to the recurrence relations

$$u_n^j = \frac{1}{n!} \cdot \frac{1}{(c_{44}^j)^{n/2}} \cdot D_j^{n/2} u_0^j, \quad n = 2, 4, \ldots, \qquad u_n^j = \frac{1}{n!} \cdot \frac{1}{(c_{44}^j)^{(n-1)/2}} \cdot D_j^{(n-1)/2} u_1^j, \quad n = 3, 5, \ldots, \tag{4-4}$$

where the wave operator is

$$D_j u_n^j = \left(\rho^j \frac{\partial^2 u_n^j}{\partial t^2} - c_{66}^j \frac{\partial^2 u_n^j}{\partial x^2} \right), \qquad j = 1, 2. \tag{4-5}$$

The recurrence relations can be used to eliminate all the expansion functions except u_0^1 and u_1^1; and u_0^2 and u_1^2. Substitution into the boundary conditions (2-3) and (4-1) and keeping terms up to a certain order in thickness lead to the equations of motion of the plate. In the case of symmetric waves in the plate the

equation becomes

$$\left[d_1 D_1 + (d_2 - d_1)D_2 + \frac{d_1(d_2 - d_1)}{\kappa}D_1 D_2 + + \frac{d_1(d_2 - d_1)^2}{2c_{44}^2}D_1 D_2 + \frac{d_1^2(d_2 - d_1)}{2c_{44}^1}D_1 D_2 \right]u_0^1 = 0, \quad (4\text{-}6)$$

while in the antisymmetric case it becomes

$$\left[1 + \frac{(d_2 - d_1)}{\kappa}D_2 + \frac{d_1^2}{2c_{44}^1}D_1 + \frac{d_1(d_2 - d_1)}{c_{44}^1}D_2 + \frac{(d_2 - d_1)^2}{2c_{44}^2}D_2 \right]u_1^1 = 0. \quad (4\text{-}7)$$

The first equation is written to third order in thickness, the second to second order (but it also contains a zero order term), but it is straightforward to go to higher orders.

The effects of the spring boundary conditions, manifesting themselves in terms that depend on the spring constant κ, enter the two plate equations in a slightly different manner. In the symmetric equation the effects enter to second order in plate thickness, without any effects to the lowest order (where the equation just becomes a thickness weighted wave equation). The antisymmetric equation is a little strange in that the spring term is of linear order, while the lowest meaningful order without the springs ($\kappa \to \infty$) is of second order. This might have something to do with the fact that the antisymmetric equation has no low frequency mode, see the numerical results in Section 5.

5. Numerical examples

In this section some numerical results are given to compare the different approximations for a layered plate with interface damage. The first approximation is the thick plate with a periodic array of interface cracks as treated in Section 2. The second is the thick plate with the spring boundary condition (4-1). The corresponding dispersion relation is very easily derived and is not given. The third approach is to use the spring boundary condition together with the plate equations (4-6) or (4-7) (taken to the order given), with the dispersion relations following directly from the plate equations. In this way both the spring boundary condition and the plate equations are checked. Another matter, which can only be checked against experiments, is how well these theories really model a real plate with interface damage.

A fiber-reinforced graphite-epoxy composite which has density $\rho = 1578\,\text{kg/m}^3$ and stiffness constants $c_{44}^1 = 3.50\,\text{GPa}$ and $c_{66}^1 = 7.07\,\text{GPa}$ is considered. The lay-up is assumed to be $0°\backslash90°\backslash0°$, which means that the material in the middle layer is rotated $90°$ relative to the top and bottom layers and the stiffness constants are connected by the relations $c_{44}^2 = c_{66}^1$ and $c_{66}^2 = c_{44}^1$. The thicknesses of the layers are assumed to be equal for all examples, so $2d_1 = (d_2 - d_1) = d/3$, where $d = 2d_2$ is the total thickness of the plate.

Figures 2–7 show the dispersion curves, that is, dimensionless frequency $\omega d\sqrt{\rho/c_{44}^1}$ as a function of dimensionless wave number kd. Figures 2, 4, and 6 show results for symmetric modes and Figures 3, 5, and 7 show results for antisymmetric modes. Figures 2 and 3 show the modes for $l/d = 0.05$ and $a/d = 0.5$, so the cracks are small and the damage parameter is $C = 2l/a = 0.2$, that is, the cracks occupy 20% of the interface. In Figures 4 and 5 the crack size and the spacing is doubled, that is, $l/d = 0.1$ and $a/d = 1$. Finally, in Figures 6 and 7 the values are $l/d = 0.5$ and $a/d = 2$. The solid lines show results for the thick plate with periodic interface cracks, the dashed lines results for the thick plate with spring boundary conditions, and the dash-dotted lines results for the plate equations. Note that the plate
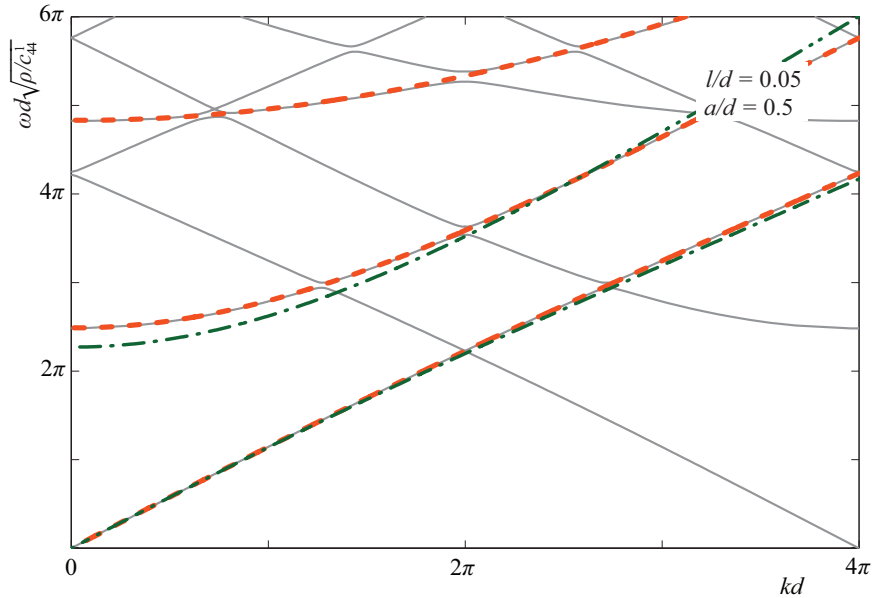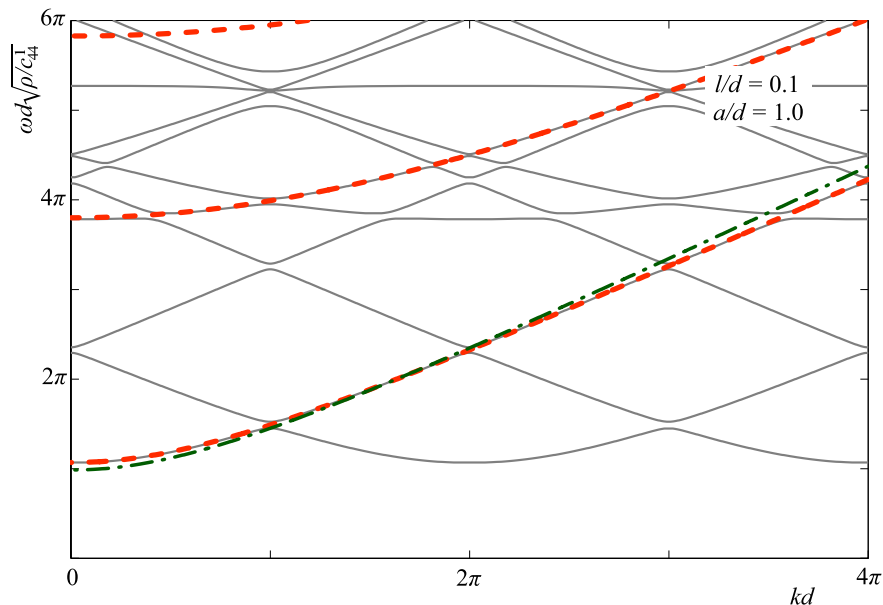
Figure 2. Dispersion curves in the wave number kd-frequency $\omega d\sqrt{\rho/c_{44}^1}$ plane for the symmetric modes and $l/d = 0.05$ and $a/d = 0.5$; solid lines: thick plate with periodic cracks; dotted lines: thick plate with spring boundary conditions; dash-dotted lines: plate equation with spring boundary conditions.
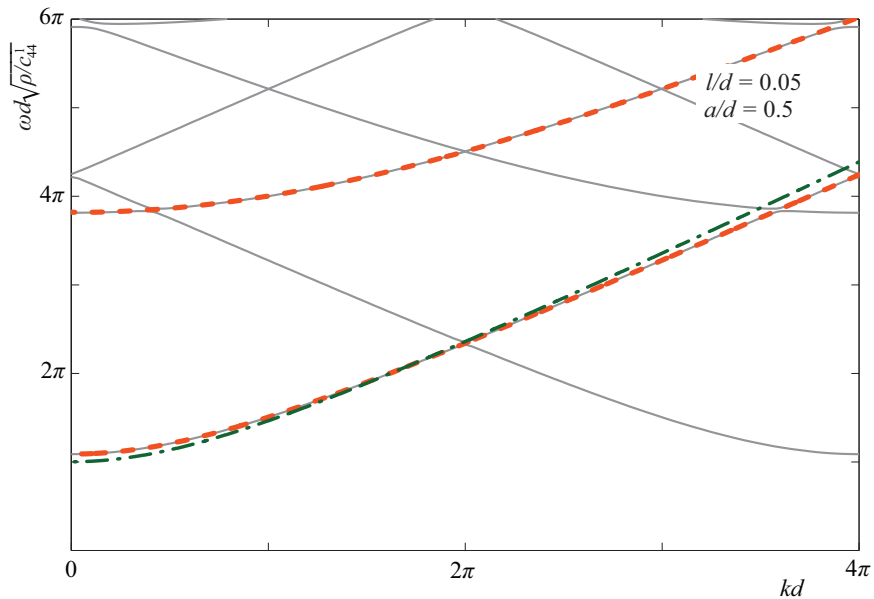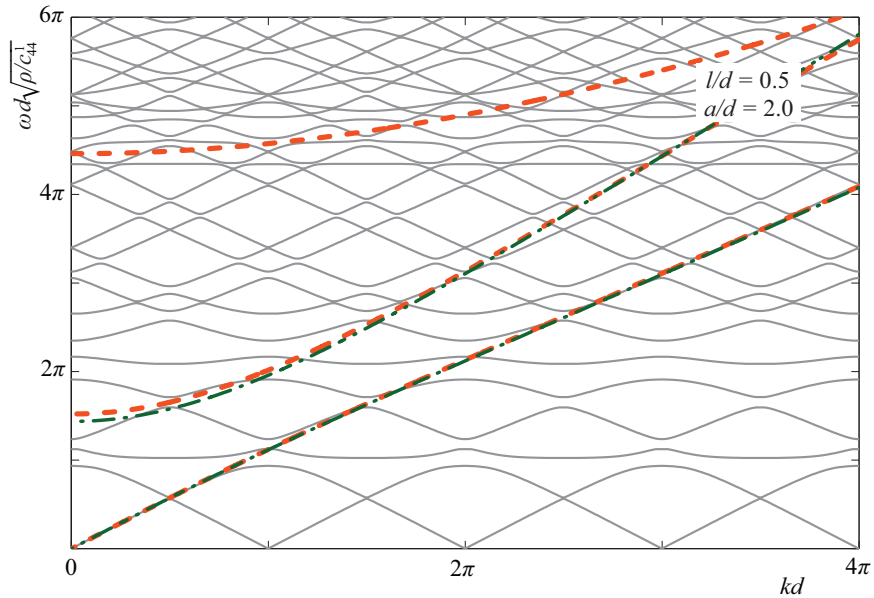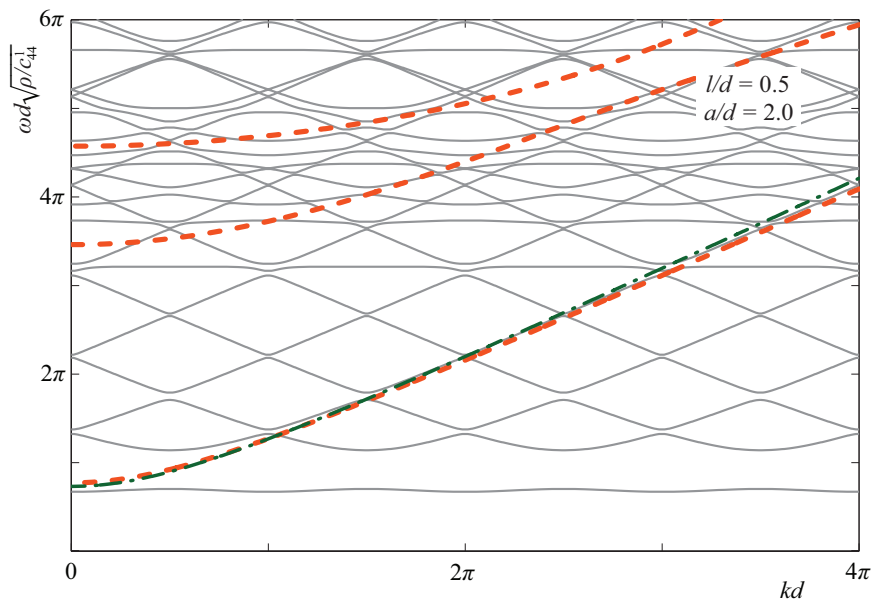

Figure 3. Dispersion curves in the wave number kd-frequency $\omega d\sqrt{\rho/c_{44}^1}$ plane for the antisymmetric modes and $l/d = 0.05$ and $a/d = 0.5$; solid lines: thick plate with periodic cracks; dotted lines: thick plate with spring boundary conditions; dash-dotted lines: plate equation with spring boundary conditions.
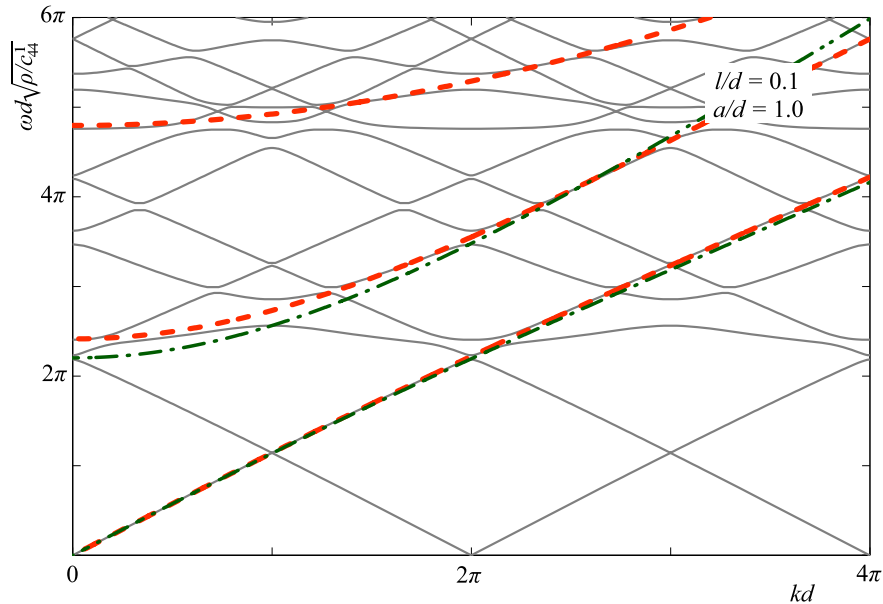
Figure 4. Dispersion curves in the wave number kd-frequency $\omega d \sqrt{\rho/c_{44}^1}$ plane for the symmetric modes and $l/d = 0.1$ and $a/d = 1.0$; solid lines: thick plate with periodic cracks; dotted lines: thick plate with spring boundary conditions; dash-dotted lines: plate equation with spring boundary conditions.

Figure 5. Dispersion curves in the wave number kd-frequency $\omega d \sqrt{\rho/c_{44}^1}$ plane for the antisymmetric modes and $l/d = 0.1$ and $a/d = 1.0$; solid lines: thick plate with periodic cracks; dotted lines: thick plate with spring boundary conditions; dash-dotted lines: plate equation with spring boundary conditions.

Figure 6. Dispersion curves in the wave number kd-frequency $\omega d\sqrt{\rho/c_{44}^1}$ plane for the symmetric modes and $l/d = 0.5$ and $a/d = 2.0$; solid lines: thick plate with periodic cracks; dotted lines: thick plate with spring boundary conditions; dash-dotted lines: plate equation with spring boundary conditions.

Figure 7. Dispersion curves in the wave number kd-frequency $\omega d\sqrt{\rho/c_{44}^1}$ plane for the antisymmetric modes and $l/d = 0.5$ and $a/d = 2.0$; solid lines: thick plate with periodic cracks; dotted lines: thick plate with spring boundary conditions; dash-dotted lines: plate equation with spring boundary conditions.

equations only give two and one solution to the dispersion relation for the symmetric and antisymmetric plate equations, respectively. In many cases the dashed and dash-dotted lines are on top of the solid lines; the dashed line is, in particular, exactly on top of the solid line for the first mode at low frequencies. As the interface cracks form a periodic system, this gives the usual system of Bloch modes with periodicity in the kd direction.

For the first symmetric mode at low frequencies all three theories agree very well. However, the antisymmetric problem has no mode at low frequencies, and the first antisymmetric mode, as well as the second symmetric mode, agree more or less depending on the parameters. It is seen that the thick plate with the spring boundary condition performs better than the plate theory. This indicates that the spring boundary condition can be used for higher frequencies than the plate theories.

6. Concluding remarks

The SH modes in a layered, anisotropic, thick plate with a periodic distribution of interface cracks have been investigated. The dispersion relation is compared to the case when the distribution of cracks is replaced by an equivalent spring boundary condition, and also to a plate equation with this spring boundary condition. For low frequencies the agreement is excellent between all three theories; this shows that the equivalent spring boundary condition can be used instead of the distribution of cracks. A periodic or random distribution of small cracks is a plausible model for interface damage, and the main result of the present investigations is thus a verification that the spring boundary condition should be a useful model for such damage. The great advantage with the spring boundary condition is its simplicity and that it only depends on the physical parameters of crack size and relative density of cracks (and the material parameters). Here only dispersion relations are studied but the spring boundary condition should also be applicable to more general situations, for example, for a plate with interface damage on only a part. The results presented here for periodic cracks may also have an intrinsic interest with possible applications of the passband-stopband structure.

The two-dimensional SH waves considered here can be regarded as a model case of limited interest. It is of course worthwhile to go further and investigate the more realistic two-dimensional in-plane problem and three-dimensional problems. It should be possible to follow a similar procedure in most cases. For three-dimensional problems there are a number of possibilities: isotropic or anisotropic media, and different shapes of interface cracks, most easily rectangular or (for isotropic media) circular cracks.

Acknowledgment

References

[Angel and Achenbach 1985] Y. C. Angel and J. D. Achenbach, "Reflection and transmission of elastic waves by a periodic array of cracks: oblique incidence", *Wave Motion* **7**:4 (1985), 375–397.

[Babeshko et al. 1989] V. A. Babeshko, E. V. Glushkov, and J. F. Zinchenko, Динамика неоднородных линейно-упругих сред, Nauka, Moscow, 1989.

[Boström and Golub 2009] A. Boström and M. Golub, "Elastic SH wave propagation in a layered anisotropic plate with interface damage modelled by spring boundary conditions", *Q. J. Mech. Appl. Math.* **62**:1 (2009), 39–52.

[Boström et al. 2001] A. Boström, G. Johansson, and P. Olsson, "On the rational derivation of a hierarchy of dynamic equations for a homogeneous, isotropic, elastic plate", *Int. J. Solids Struct.* **38**:15 (2001), 2487–2501.

[Datta and Shah 2009] S. K. Datta and A. H. Shah, *Elastic waves in composite media and structures: with applications to ultrasonic nondestructive evaluation*, CRC Press, Boca Raton, FL, 2009.

[Yariv and Yeh 1984] A. Yariv and P. Yeh, *Optical waves in crystals: propagation and control of laser radiation*, Wiley, New York, 1984.

[Zhang and Gross 1998] C. Zhang and D. Gross, *On wave propagation in elastic solids with cracks*, vol. 2, International Series on Advances in Fracture Mechanics, Computational Mechanics Publications, Southampton, 1998.

ANDERS BOSTRÖM: anders.bostrom@chalmers.se
Department of Applied Mechanics, Chalmers University of Technology, SE-412 96 Göteborg, Sweden

OLEG V. KVASHA: ovk@math.kubsu.ru
Institute for Mathematics, Mechanics and Informatics, Kuban State University, Krasnodar 350080, Russia

EXACT CLOSED-FORM SOLUTION OF THE
DYNAMIC COUPLED THERMOELASTIC RESPONSE
OF A FUNCTIONALLY GRADED TIMOSHENKO BEAM

MOSTAFA ABBASI, MEHDY SABBAGHIAN AND M. REZA ESLAMI

We present the analytical solution for a beam made of a functionally graded material based on first-order shear deformation theory and subjected to lateral thermal shock loads. The beam is assumed to be graded across the thickness direction. The material properties across the thickness direction follow the volume fraction of the constitutive materials in power law form. The solution is obtained under the coupled thermoelastic assumption. The equation of motion and the conventional coupled energy equation are simultaneously solved to obtain the transverse deflection and temperature distribution in the beam. The governing partial differential equations are solved using the finite Fourier transformation method. Using the Laplace transform, the unknown variables are obtained in the Laplace domain. Applying the analytical Laplace inverse method, the solution in the time domain is derived. Results are presented for different power law indices and the coupling coefficients for a beam with simply supported boundary conditions. The results are validated with data reported in the literature.

1. Introduction

Recently developed functionally graded materials (FGM) show promise for their adaptability to high temperature environments, and have thus attracted international attention. Therefore, it is desirable to analyze FGM structures subjected to thermal loadings such as thermal shock, which have a wide range of applications in engineering and science. Very rapid thermal processes, under the action of a thermal shock are interesting from the standpoint of thermoelasticity. Under thermal shock, the characteristic times of structural and thermal disturbances are of comparable magnitudes, the equations of motion of a structure are coupled with the energy equation, and the solution of the coupled system of equations provides the stress and temperature fields.

The equations for a coupled thermoelastic beam, including the effects of the shear deformation and rotatory inertia, are derived in [Jones 1966]. McQuillen and Brull [1970] presented an analytical solution for the dynamic thermoelastic response of cylindrical shells using the variational theorem. The coupled thermally induced vibrations of the Euler–Bernoulli and Timoshenko beams with one-dimensional heat conduction are investigated in [Seibert and Rice 1973]. The coupled thermoelasticity of beams made of homogeneous and isotropic material is discussed in [Massalas and Kalpakidis 1983; 1984]. The analytical solution of the coupled thermoelasticity of beams with the Euler–Bernoulli assumption is given in the first of these papers, that with the Timoshenko assumption in the second. In the treatment of these problems, a linear approximation for temperature variation across the thickness direction of the beam is

considered. Eslami and Vahedi [1988] studied the one-dimensional coupled thermoelasticity problem of rods with the classical coupled thermoelastic assumption using the Galerkin finite element method.

A finite element coupled thermoelastic analysis of composite Timoshenko beams is given in [Maruthi Rao and Sinha 1997], where the temperature variation across the thickness direction is neglected. The coupled thermoelastic behavior of shells of revolution is analyzed in [Eslami et al. 1999]. Manoach and Ribeiro [2004] developed a numerical procedure to study the coupled large amplitude thermoelastic vibrations of the Timoshenko beams subjected to the thermal and mechanical loads using finite difference approximations and modal coordinate transformations. Sankar [2001; Sankar and Tzeng 2002] considered an FGM Euler beam and computed the thermal stresses based on the uncoupled thermoelastic assumption. The coupled thermoelasticity of functionally graded cylindrical shells is investigated in [Bahtui and Eslami 2007] using the Galerkin finite element method with two element types (C^0- and C^1-continuous) under impulsive thermal shock load. Babaei et al. [2008] present the behavior of an FGM Euler–Bernoulli beam under lateral thermal shock with the coupled thermoelastic assumption. The analysis is based on the Galerkin finite element method, using a C^1-continuous shape function, where the temperature change across the thickness direction is assumed to be linear and the axial inertia effect is neglected.

The aim of this paper is to present the analytical solution for the behavior of an FGM beam under lateral thermal shock with the coupled thermoelastic assumption. The analysis is based on first-order shear deformation theory. The mathematical functions of unknown variables such as lateral deflection and temperature are presented using the finite Fourier transformation and analytical Laplace inverse method. The time constants and frequencies of oscillations are presented for different power law indices. The novelty of the analytical solution presented in this work in comparison with prior researches is the absence of the unbalance of the members of matrices appearing in the numerical methods. Random dimensionless parameters are used to overcome this problem in previous studies about coupled thermoelasticity of FGM structures [Bahtui and Eslami 2007; Babaei et al. 2008]. Also, in analytical analysis, the coupled effect is stronger than perceived especially for long time periods, in comparison with the numerical methods.

2. Derivation of the governing equations

Consider a beam of rectangular cross section with length l, height h, and width b, as shown in Figure 1. Using first-order shear deformation theory, the displacement components are

$$u(x, z, t) = u_0 - z\psi_{,x}, \qquad w(x, z, t) = w(x, t), \tag{1}$$

where u is the axial displacement component, u_0 the displacement of a point on the reference plane, w is the lateral deflection, ψ is the rotation angle of the cross section with respect to the longitudinal axis,

Figure 1. The beam and coordinates.

t is the time variable, and z is measured across the thickness direction from the middle plane of the beam at $x = 0$. A comma in subscripts indicates partial differentiation.

The FGM profile across the thickness direction of the beam, made of ceramic and metal constituent materials, may be assumed to follow a power law form as

$$f(z) = f_m + f_{cm}\left(\frac{2z+h}{2h}\right)^n,\tag{2}$$

where f is any material property of the FGM, f_m is the metal property of FGM, $f_{cm} = f_c - f_m$, f_c being the ceramic property of FGM, and n is the power law index. The density, modulus of elasticity, coefficient of specific heat, coefficient of thermal expansion, and conduction coefficient may be assumed to follow the power law form, indicated by Equation (2).

Assuming that the beam material is linear elastic, the stress-strain relations for the FGM beam based on the assumed displacement components, including the shear deformation, are [Manoach and Ribeiro 2004]

$$\sigma_x = E(z)[\epsilon_x - \alpha(z)\theta], \qquad \sigma_{xz} = k_s G(z)\epsilon_{xz},\tag{3}$$

where E is the modulus of elasticity, G is the shear modulus, k_s is the shear correction factor, α is the coefficient of thermal expansion, $\theta = T - T_0$ is the temperature change, and T_0 is the reference temperature.

The bending moment, the shear force, and the in-plane stress resultants are expressed by the stresses as follows:

$$M = \int_z \sigma_x z\, dz, \qquad Q = \int_z \sigma_{xz}\, dz, \qquad N = \int_z \sigma_x\, dz.\tag{4}$$

The temperature change across the thickness direction is assumed to be linear. This assumption is justified considering that the thickness of the beam is small with respect to its length [Massalas and Kalpakidis 1983; 1984] and thus

$$\theta(x, z, t) = \tfrac{1}{2}\big(\theta_1(x, t) + \theta_2(x, t)\big) + \frac{z}{h}\big(\theta_1(x, t) - \theta_2(x, t)\big)\tag{5}$$

where θ_1 and θ_2 are unknowns to be found across the beam's height and are coupled with the displacement components of the beam.

Equation of motion. The equations of motion of a beam based on first-order shear deformation theory are [Manoach and Ribeiro 2004]

$$N_{,x} = I_0 u_{0,tt} - I_1 \psi_{,tt}, \qquad M_{,x} - Q = I_1 u_{0,tt} - I_2 \psi_{,tt}, \qquad Q_{,x} = I_0 w_{,tt} - p(x, t),\tag{6}$$

where p is the applied surface lateral mechanical load, $I_i = \int_z \rho(z) z^i\, dz$ $(i = 0, 1, 2)$ is the mass moment of inertia, and ρ is the mass density of the beam.

Substituting (3), (4), (5) into (6), the equations of motion become

$$A_1 u_{0,xx} + A_2 \psi_{,xx} + A_3 \theta_{1,xx} + A_4 \theta_{2,xx} + A_5 u_{0,tt} + A_6 \psi_{,tt} = 0,$$
$$B_1 u_{0,xx} + B_2 \psi_{,xx} + B_3 \psi + B_4 w_{,x} + B_5 \theta_{1,xx} + B_6 \theta_{2,xx} + B_7 u_{0,tt} + B_8 \psi_{,tt} = 0,\tag{7}$$
$$C_1 \psi_{,x} + C_2 w_{,xx} + C_3 w_{,tt} = 0,$$

where the coefficients are given by

$$A_1 = \int E(z)\,dz, \qquad A_3 = \int \left(-\frac{1}{2} - \frac{z}{h}\right)E(z)\alpha(z)\,dz, \quad A_5 = -I_0, \quad B_1 = \int E(z)z\,dz,$$

$$A_2 = \int -E(z)z\,dz, \qquad A_4 = \int \left(-\frac{1}{2} + \frac{z}{h}\right)E(z)\alpha(z)\,dz, \quad A_6 = I_1, \qquad B_2 = \int -E(z)z^2\,dz,$$

$$B_3 = \int \frac{k_s}{2(1+\nu)}E(z)\,dz, \quad B_5 = \int \left(-\frac{z}{2} - \frac{z^2}{h}\right)E(z)\alpha(z)\,dz, \quad B_7 = -I_1, \quad C_1 = B_3, \quad C_2 = B_4,$$

$$B_4 = \int \frac{k_s}{2(1+\nu)}E(z)\,dz, \quad B_6 = \int \left(-\frac{z}{2} + \frac{z^2}{h}\right)E(z)\alpha(z)\,dz, \quad B_8 = I_2, \qquad C_3 = -I_0.$$

Considering a beam with simply supported boundary conditions with initial zero deflection and zero velocity, the boundary and initial conditions may be assumed to be

$$\begin{aligned}
u_{0,x}(0,t) = u_{0,x}(l,t) &= 0, & t &> 0, \\
\psi_{,x}(0,t) = \psi_{,x}(l,t) &= 0, & t &> 0, \\
w(0,t) = w(l,t) &= 0, & t &> 0, \\
u_0(x,0) = \psi(x,0) = w(x,0) &= 0, & 0 &\le x \le l.
\end{aligned} \tag{8}$$

Energy equations. The first law of thermodynamics for heat conduction in the beam in coupled form is [Hetnarski and Eslami 2009]

$$(k\theta_{,i})_{,i} - \rho c_v \theta_{,t} - \alpha(3\lambda + 2\mu)T_0(\epsilon_{ii})_{,t} = 0, \quad i = 1, 2, 3, \tag{9}$$

where k, c_v, α, and ϵ_{ii} are the thermal conductivity, specific heat, coefficient of linear thermal expansion, and normal strain tensor, respectively, and λ and μ are the Lamé constants. The energy equation for the beam based on first-order shear deformation theory is reduced to

$$\text{Res.} = k(z)\theta_{,xx} + (k(z)\theta_{,z})_{,z} - \rho(z)c_v(z)\theta_{,t} - \alpha(z)E(z)T_0[u_{0,xt} - z\psi_{,xt}] = 0. \tag{10}$$

The thermal boundary conditions may be assumed in form of an applied heat flux q, convection h_c, or specified temperature shock on the upper or lower surfaces of the beam. The energy equation is obtained assuming that the upper surface of the beam is exposed to a known heat flux $q(x,t)$ and the lower surface is under convection to the ambient with coefficient h_c.

The beam is initially assumed to be at ambient temperature and the thermal boundary and initial conditions are assumed as

$$\theta(0,t) = \theta(l,t) = 0, \quad t > 0, \qquad \theta(x,0) = 0, \quad 0 \le x \le l. \tag{11}$$

Using (10), the residue, Res., of the energy equation may be made orthogonal with respect to dz and $z\,dz$ to provide two independent equations for two independent functions θ_1 and θ_2 as [McQuillen and Brull 1970]

$$\begin{aligned}
D_1\theta_{1,xx} + D_2\theta_{2,xx} + D_3\theta_{1,t} + D_4\theta_{2,t} + D_5 u_{0,xt} + D_6\psi_{,xt} + D_7\theta_2 + D_8 q(x,t) = 0, \\
E_1\theta_{1,xx} + E_2\theta_{2,xx} + E_3\theta_1 + E_4\theta_2 + E_5\theta_{1,t} + E_6\theta_{2,t} + E_7 u_{0,xt} + E_8\psi_{,xt} + E_9\theta_2 + E_{10}q(x,t) = 0,
\end{aligned} \tag{12}$$

where the coefficients are given by

$$D_1 = \int \left(\frac{1}{2} + \frac{z}{h} \right) K(z)\, dz, \qquad D_3 = \int \left(-\frac{1}{2} - \frac{z}{h} \right) \rho(z) c_v(z)\, dz, \quad D_5 = \int -E(z)\alpha(z) T_0\, dz,$$

$$D_2 = \int \left(\frac{1}{2} - \frac{z}{h} \right) K(z)\, dz, \qquad D_4 = \int \left(-\frac{1}{2} + \frac{z}{h} \right) \rho(z) c_v(z)\, dz, \quad D_6 = \int E(z)\alpha(z) T_0 z\, dz,$$

$$E_1 = \int \left(\frac{z}{2} + \frac{z^2}{h} \right) K(z)\, dz, \qquad E_3 = \int -\frac{K(z)}{h}\, dz, \qquad D_7 = -h_c,$$

$$E_2 = \int \left(\frac{z}{2} - \frac{z^2}{h} \right) K(z)\, dz, \qquad E_4 = \int \frac{K(z)}{h}\, dz, \qquad D_8 = 1,$$

$$E_5 = \int \left(-\frac{z}{2} - \frac{z^2}{h} \right) \rho(z) c_v(z)\, dz, \quad E_7 = \int -E(z)\alpha(z) z T_0\, dz, \qquad E_9 = -\frac{h}{2} h_c,$$

$$E_6 = \int \left(-\frac{z}{2} + \frac{z^2}{h} \right) \rho(z) c_v(z)\, dz, \quad E_8 = \int E(z)\alpha(z) T_0 z^2\, dz, \qquad E_{10} = \frac{h}{2}.$$

3. Solution procedure

To solve the simultaneous governing equations, dimensionless values are defined as

$$\bar{u}_0 = \frac{k_c}{q_{\text{avg}} \alpha_c l^2} u_0, \quad \bar{\psi} = \frac{k_c}{q_{\text{avg}} \alpha_c l} \psi, \quad \bar{w} = \frac{k_c}{q_{\text{avg}} \alpha_c l^2} w, \quad \bar{x} = \frac{x}{l}, \quad \bar{t} = \frac{\kappa_c}{h^2} t, \quad \bar{\theta} = \frac{k_c}{q_{\text{avg}} \alpha_c l T_0} \theta, \quad (13)$$

where q_{avg} and κ_c are, respectively, the average heat flux at the top of the beam and the thermal diffusivity. The bar indicates dimensionless parameters.

Using the dimensionless parameters, the five coupled governing equations are

$$a_1 \bar{u}_{0,\bar{x}\bar{x}} + a_2 \bar{\psi}_{,\bar{x}\bar{x}} + a_3 \bar{\theta}_{1,\bar{x}\bar{x}} + a_4 \bar{\theta}_{2,\bar{x}\bar{x}} + a_5 \bar{u}_{0,\bar{t}\bar{t}} + a_6 \bar{\psi}_{,\bar{t}\bar{t}} = 0,$$

$$b_1 \bar{u}_{0,\bar{x}\bar{x}} + b_2 \bar{\psi}_{,\bar{x}\bar{x}} + b_3 \bar{\psi} + b_4 \bar{w}_{,\bar{x}} + b_5 \bar{\theta}_{1,\bar{x}\bar{x}} + b_6 \bar{\theta}_{2,\bar{x}\bar{x}} + b_7 \bar{u}_{0,\bar{t}\bar{t}} + b_8 \bar{\psi}_{,\bar{t}\bar{t}} = 0,$$

$$c_1 \bar{\psi}_{,\bar{x}} + c_2 \bar{w}_{,\bar{x}\bar{x}} + c_3 \bar{w}_{,\bar{t}\bar{t}} = 0, \qquad (14)$$

$$d_1 \bar{\theta}_{1,\bar{x}\bar{x}} + d_2 \bar{\theta}_{2,\bar{x}\bar{x}} + d_3 \bar{\theta}_{1,\bar{t}} + d_4 \bar{\theta}_{2,\bar{t}} + d_5 \bar{u}_{0,\bar{x}\bar{t}} + d_6 \bar{\psi}_{,\bar{x}\bar{t}} + d_7 \bar{\theta}_2 + d_8 q(\bar{x}, \bar{t}) = 0,$$

$$e_1 \bar{\theta}_{1,\bar{x}\bar{x}} + e_2 \bar{\theta}_{2,\bar{x}\bar{x}} + e_3 \bar{\theta}_1 + e_4 \bar{\theta}_2 + e_5 \bar{\theta}_{1,\bar{t}} + e_6 \bar{\theta}_{2,\bar{t}} + e_7 \bar{u}_{0,\bar{x}\bar{t}} + e_8 \bar{\psi}_{,\bar{x}\bar{t}} + e_9 \bar{\theta}_2 + e_{10} q(\bar{x}, \bar{t}) = 0,$$

where the as, bs, cs, ds, and es are dimensionless constants of the coupled equations. Simultaneous solution of these equations provides the distribution of the displacement components of the beam and the temperature variables θ_1 and θ_2.

Regarding the boundary conditions given by (8) and (11), to solve (14), the finite Fourier transformation can be used to obtain

$$\bar{u}_{0m}(\bar{t}) = \int_0^1 \bar{u}_0(\bar{x}, \bar{t}) \cos(m\pi \bar{x})\, d\bar{x}, \quad \bar{\psi}_m(\bar{t}) = \int_0^1 \bar{\psi}(\bar{x}, \bar{t}) \cos(m\pi \bar{x})\, d\bar{x}, \quad \bar{w}_m(\bar{t}) = \int_0^1 \bar{w}(\bar{x}, \bar{t}) \sin(m\pi \bar{x})\, d\bar{x},$$

$$\bar{\theta}_{1m}(\bar{t}) = \int_0^1 \bar{\theta}_1(\bar{x}, \bar{t}) \sin(m\pi \bar{x})\, d\bar{x}, \quad \bar{\theta}_{2m}(\bar{t}) = \int_0^1 \bar{\theta}_2(\bar{x}, \bar{t}) \sin(m\pi \bar{x})\, d\bar{x}, \qquad (15)$$

where $m = 1, 3, 5, \ldots$.

The solutions given by (15) automatically satisfy the boundary conditions, (8) and (11). Based on Fourier series theory, the inverse transformation can be expressed by

$$\bar{u}_0(\bar{x}, \bar{t}) = 2 \sum_m \bar{u}_{0m}(\bar{t}) \cos(m\pi\bar{x}), \quad \bar{\psi}(\bar{x}, \bar{t}) = 2 \sum_m \bar{\psi}_m(\bar{t}) \cos(m\pi\bar{x}), \quad \bar{w}(\bar{x}, \bar{t}) = 2 \sum_m \bar{w}_m(\bar{t}) \sin(m\pi\bar{x}),$$

$$\bar{\theta}_1(\bar{x}, \bar{t}) = 2 \sum_m \bar{\theta}_{1m}(\bar{t}) \sin(m\pi\bar{x}), \quad \bar{\theta}_2(\bar{x}, \bar{t}) = 2 \sum_m \bar{\theta}_{2m}(\bar{t}) \sin(m\pi\bar{x}), \tag{16}$$

where the sum is all over m odd and positive. Applying a step function heat flux of intensity q to the upper beam surface, the Fourier transformation of (14), considering the initial conditions (8) and (11), yields

$$-r^2 a_1 \bar{u}_{0m} - r^2 a_2 \bar{\psi}_m + r a_3 \bar{\theta}_{1m} + r a_4 \bar{\theta}_{2m} + a_5 \bar{u}_{0m,\bar{t}\bar{t}} + a_6 \bar{\psi}_{m,\bar{t}\bar{t}} = 0,$$

$$-r^2 b_1 \bar{u}_{0m} - r^2 b_2 \bar{\psi}_m + + b_3 \bar{\psi}_m + r b_4 \bar{w}_m + r b_5 \bar{\theta}_{1m} + r b_6 \bar{\theta}_{2m} + b_7 \bar{u}_{0m,\bar{t}\bar{t}} + b_8 \bar{\psi}_{m,\bar{t}\bar{t}} = 0,$$

$$-r c_1 \bar{\psi}_m - r^2 c_2 \bar{w}_m + c_3 \bar{w}_{m,\bar{t}\bar{t}} = 0, \tag{17}$$

$$-r^2 d_1 \bar{\theta}_{1m} - r^2 d_2 \bar{\theta}_{2m} + d_3 \bar{\theta}_{1m,\bar{t}} + d_4 \bar{\theta}_{2m,\bar{t}} - r d_5 \bar{u}_{0m,\bar{t}} - r d_6 \bar{\psi}_{m,\bar{t}} + d_7 \bar{\theta}_{2m} + \frac{2d_8}{r} q = 0,$$

$$-r^2 e_1 \bar{\theta}_{1m} - r^2 e_2 \bar{\theta}_{2m} + e_3 \bar{\theta}_{1m} + e_4 \bar{\theta}_{2m} + e_5 \bar{\theta}_{1m,\bar{t}} + e_6 \bar{\theta}_{2m,\bar{t}} - r e_7 \bar{u}_{0m,\bar{t}} - r e_8 \bar{\psi}_{m,\bar{t}} + e_9 \bar{\theta}_{2m} + \frac{2e_{10}}{r} q = 0,$$

where $r = m\pi$.

Laplace transform. The system of coupled equations (17) are functions of the Fourier parameter m and time t. The solution presented in this paper is obtained by the finite Fourier transformation, where time is eliminated using the Laplace transform. Once the solution in the space domain is obtained, an analytical scheme is used for the inverse Laplace transformation to find the final solution in the real time domain. Applying the Laplace transform to (17) gives

$$-r^2 a_1 \bar{U}_{0m} - r^2 a_2 \bar{\Psi}_m + r a_3 \bar{\Theta}_{1m} + r a_4 \bar{\Theta}_{2m} + a_5 s^2 \bar{U}_{0m} + a_6 s^2 \bar{\Psi}_m = 0,$$

$$-r^2 b_1 \bar{U}_{0m} - r^2 b_2 \bar{\Psi}_m + + b_3 \bar{\Psi}_m + r b_4 \bar{W}_m + r b_5 \bar{\Theta}_{1m} + r b_6 \bar{\Theta}_{2m} + b_7 s^2 \bar{U}_{0m} + b_8 s^2 \bar{\Psi}_m = 0,$$

$$-r c_1 \bar{\Psi}_m - r^2 c_2 \bar{W}_m + c_3 s^2 \bar{W}_m = 0,$$

$$-r^2 d_1 \bar{\Theta}_{1m} - r^2 d_2 \bar{\Theta}_{2m} + d_3 s \bar{\Theta}_{1m} + d_4 s \bar{\Theta}_{2m} - r d_5 s \bar{U}_{0m} - r d_6 s \bar{\Psi}_m + d_7 \bar{\Theta}_{2m} + \frac{2d_8}{rs} q = 0, \tag{18}$$

$$-r^2 e_1 \bar{\Theta}_{1m} - r^2 e_2 \bar{\Theta}_{2m} + e_3 \bar{\Theta}_{1m} + e_4 \bar{\Theta}_{2m} + e_5 s \bar{\Theta}_{1m} + e_6 s \bar{\Theta}_{2m}$$
$$- r e_7 s \bar{U}_{0m} - r e_8 s \bar{\Psi}_m + e_9 \bar{\Theta}_{2m} + \frac{2e_{10}}{rs} q = 0,$$

where s is the Laplace transform parameter and $\bar{U}_{0m} = L[\bar{u}_{0m}]$, $\bar{\Psi}_m = L[\bar{\psi}_m]$, $\bar{W}_m = L[\bar{w}_m]$, and $\bar{\Theta}_{im} = L[\bar{\theta}_{im}]$ for $i = 1, 2$, where L stands for the Laplace operator. Denoting by

$$\langle F_{m_j} \rangle = \langle \bar{U}_{0m} \quad \bar{\Psi}_m \quad \bar{W}_m \quad \bar{\Theta}_{1m} \quad \bar{\Theta}_{2m} \rangle \tag{19}$$

the solution for the unknown variables in (18), in the Laplace transformation domain we obtain

$$F_{m_j}(s) = \frac{Q_{m_j}(s)}{P_{m_j}(s)}, \tag{20}$$

where $Q_{m_j}(s)$ and $P_{m_j}(s)$ are polynomial functions of s. As an example, the lateral deflection of the beam in the Laplace domain for the coupled assumption (d_5, d_6, e_7, $e_8 \neq 0$) can be given as

$$\bar{W}_m = \frac{q_0 + q_1 s + q_2 s^2 + q_3 s^3}{s(p_0 + p_1 s + p_2 s^2 + p_3 s^3 + p_4 s^4 + p_5 s^5 + p_6 s^6 + p_7 s^7 + p_8 s^8)}, \tag{21}$$

where the qs and ps are coefficients obtained by solving the system of (18).

Carrying out analytically the inverse Laplace transform of (20) [Massalas and Kalpakidis 1983; 1984], we obtain solutions for the unknown variables in the real physical time domain:

$$f_{m_j}(m, \bar{t}) = \sum_{\gamma=1}^{n_p} \frac{Q_{m_j}(s_{p_\gamma})}{P'_{m_j}(s_{p_\gamma})} e^{s_{p_\gamma} \bar{t}}, \tag{22}$$

where

$$\langle f_{m_j} \rangle = \langle u_{0m} \quad \psi_m \quad w_m \quad \theta_{1m} \quad \theta_{2m} \rangle,$$

the s_{p_γ} are the roots of $P_{m_j}(s)$, and n_p is the number of roots. A prime indicates a derivative with respect to s.

Using (16) and (22), the unknown variable functions are obtained in the space variable x and time t. As an example, the lateral deflection function is computed as

$$\bar{w}(\bar{x}, \bar{t}) = 2 \sum_{m=1,3,\ldots}^{\infty} \bar{w}_m(m, \bar{t}) \sin(m\pi\bar{x}) = 2 \sum_{m=1,3,\ldots}^{\infty} \sum_{\gamma=1}^{n_p} \frac{q_0 + q_1 s_{p_\gamma} + q_2 s_{p_\gamma}^2 + q_3 s_{p_\gamma}^3}{P_{\bar{w}}(s_{p_\gamma})} e^{s_{p_\gamma} \bar{t}} \sin(m\pi\bar{x}),$$
$$P_{\bar{w}} = p_0 + 2p_1 s_{p_\gamma} + 3p_2 s_{p_\gamma}^2 + 4p_3 s_{p_\gamma}^3 + 5p_4 s_{p_\gamma}^4 + 6p_5 s_{p_\gamma}^5 + 7p_6 s_{p_\gamma}^6 + 8p_7 s_{p_\gamma}^7 + 9p_8 s_{p_\gamma}^8. \tag{23}$$

Using (16) and (22), and considering $m = 1$, the dimensionless functions for the midlength lateral deflection w, upper side temperature θ_1 at the midpoint of the beam, maximum u_0, and rotation angle ψ at $\bar{x} = 0$ are obtained for the coupled and uncoupled assumptions. For the uncoupled assumption, where d_5, d_6, e_7, $e_8 = 0$, we obtain

$$\bar{w}_{uc}(0.5, \bar{t}) = \acute{A}_1 + \acute{A}_2 e^{\tau_{uc_1} \bar{t}} + \acute{A}_3 e^{\tau_{uc_2} \bar{t}} + \acute{A}_4 \cos(\omega_{uc_1} \bar{t}) + \acute{A}_5 \sin(\omega_{uc_1} \bar{t})$$
$$+ \acute{A}_6 \cos(\omega_{uc_2} \bar{t}) + \acute{A}_7 \sin(\omega_{uc_2} \bar{t}) + \acute{A}_8 \cos(\omega_{uc_3} \bar{t}) + \acute{A}_9 \sin(\omega_{uc_3} \bar{t}),$$
$$\bar{\theta}_{1uc}(0.5, \bar{t}) = \acute{B}_1 + \acute{B}_2 e^{\tau_{uc_1} \bar{t}} + \acute{B} e^{\tau_{uc_2} \bar{t}},$$
$$\bar{u}_{0uc}(0, \bar{t}) = \acute{C}_1 + \acute{C}_2 e^{\tau_{uc_1} \bar{t}} + \acute{C}_3 e^{\tau_{uc_2} \bar{t}} + \acute{C}_4 \cos(\omega_{uc_1} \bar{t}) + \acute{C}_5 \sin(\omega_{uc_1} \bar{t}) + \acute{C}_6 \cos(\omega_{uc_2} \bar{t}) \tag{24}$$
$$+ \acute{C}_7 \sin(\omega_{uc_2} \bar{t}) + \acute{C}_8 \cos(\omega_{uc_3} \bar{t}) + \acute{C}_9 \sin(\omega_{uc_3} \bar{t}),$$
$$\bar{\psi}_{uc}(0, \bar{t}) = \acute{D}_1 + \acute{D}_2 e^{\tau_{uc_1} \bar{t}} + \acute{D}_3 e^{\tau_{uc_2} \bar{t}} + \acute{D}_4 \cos(\omega_{uc_1} \bar{t}) + \acute{D}_5 \sin(\omega_{uc_1} \bar{t}) + \acute{D}_6 \cos(\omega_{uc_2} \bar{t})$$
$$+ \acute{D}_7 \sin(\omega_{uc_2} \bar{t}) + \acute{D}_8 \cos(\omega_{uc_3} \bar{t}) + \acute{D}_9 \sin(\omega_{uc_3} \bar{t}),$$

where the τ_{uc_i} are dimensionless time constants, the ω_{uc_i} are dimensionless oscillation frequencies, and the $\acute{A}$, $\acute{B}$, $\acute{C}$, $\acute{D}$ are dimensionless constants. Similarly, for the coupled assumption,

$$\bar{w}_c(0.5, \bar{t}) = \tilde{A}_1 + \tilde{A}_2 e^{\tau_{c_1}\bar{t}} + \tilde{A}_3 e^{\tau_{c_2}\bar{t}} + e^{\tau_{c_3}\bar{t}}\big(\tilde{A}_4 \cos(\omega_{c_1}\bar{t}) + \tilde{A}_5 \sin(\omega_{c_1}\bar{t})\big)$$
$$+ e^{\tau_{c_4}\bar{t}}\big(\tilde{A}_6 \cos(\omega_{c_2}\bar{t}) + \tilde{A}_7 \sin(\omega_{c_2}\bar{t})\big) + e^{\tau_{c_5}\bar{t}}\big(\tilde{A}_8 \cos(\omega_{c_3}\bar{t}) + \tilde{A}_9 \sin(\omega_{c_3}\bar{t})\big),$$

$$\bar{\theta}_{1c}(0.5, \bar{t}) = \tilde{B}_1 + \tilde{B}_2 e^{\tau_{c_1}\bar{t}} + \tilde{B}_3 e^{\tau_{c_2}\bar{t}} + e^{\tau_{c_3}\bar{t}}\big(\tilde{B}_4 \cos(\omega_{c_1}\bar{t}) + \tilde{B}_5 \sin(\omega_{c_1}\bar{t})\big)$$
$$+ e^{\tau_{c_4}\bar{t}}\big(\tilde{B}_6 \cos(\omega_{c_2}\bar{t}) + \tilde{B}_7 \sin(\omega_{c_2}\bar{t})\big) + e^{\tau_{c_5}\bar{t}}\big(\tilde{B}_8 \cos(\omega_{c_3}\bar{t}) + \tilde{B}_9 \sin(\omega_{c_3}\bar{t})\big),$$

$$\bar{u}_{0c}(0, \bar{t}) = \tilde{C}_1 + \tilde{C}_2 e^{\tau_{c_1}\bar{t}} + \tilde{C}_3 e^{\tau_{c_2}\bar{t}} + e^{\tau_{c_3}\bar{t}}\big(\tilde{C}_4 \cos(\omega_{c_1}\bar{t}) + \tilde{C}_5 \sin(\omega_{c_1}\bar{t})\big) \qquad (25)$$
$$+ e^{\tau_{c_4}\bar{t}}\big(\tilde{C}_6 \cos(\omega_{c_2}\bar{t}) + \tilde{C}_7 \sin(\omega_{c_2}\bar{t})\big) + e^{\tau_{c_5}\bar{t}}\big(\tilde{C}_8 \cos(\omega_{c_3}\bar{t}) + \tilde{C}_9 \sin(\omega_{c_3}\bar{t})\big),$$

$$\bar{\psi}_c(0, \bar{t}) = \tilde{D}_1 + \tilde{D}_2 e^{\tau_{c_1}\bar{t}} + \tilde{D}_3 e^{\tau_{c_2}\bar{t}} + e^{\tau_{c_3}\bar{t}}\big(\tilde{D}_4 \cos(\omega_{c_1}\bar{t}) + \tilde{D}_5 \sin(\omega_{c_1}\bar{t})\big)$$
$$+ e^{\tau_{c_4}\bar{t}}\big(\tilde{D}_6 \cos(\omega_{c_2}\bar{t}) + \tilde{D}_7 \sin(\omega_{c_2}\bar{t})\big) + e^{\tau_{c_5}\bar{t}}\big(\tilde{D}_8 \cos(\omega_{c_3}\bar{t}) + \tilde{D}_9 \sin(\omega_{c_3}\bar{t})\big),$$

where the symbols have a similar meaning as in the uncoupled case. Therefore, it can be found from (24) and (25) that the coupling between the strain and temperature fields causes the damping effect on the dimensionless lateral deflection, w.
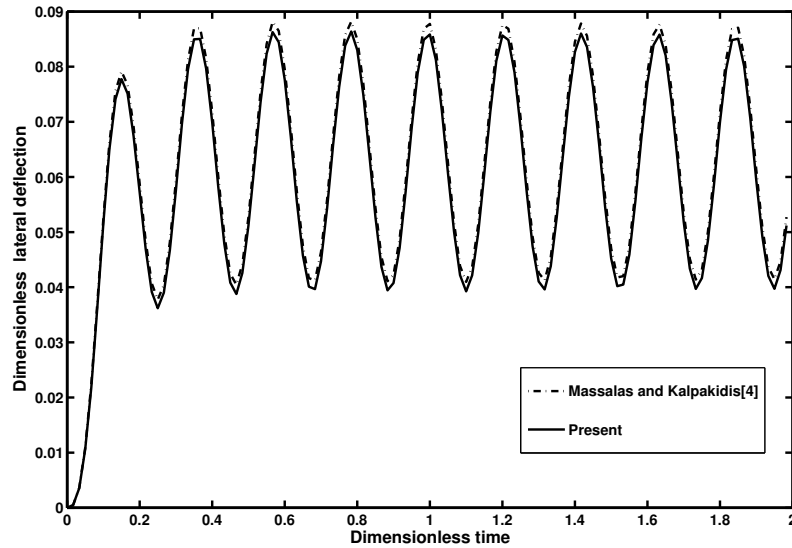
4. Results

To validate the formulations, the results of this paper are compared with the analytical solution of a homogeneous beam reported in [Massalas and Kalpakidis 1983]. An aluminum beam of length 0.25 m and height 0.0022 m with simply supported boundary conditions is assumed. The ends of the beam are assumed to be at ambient temperature $T_0 = 293$ K. The upper surface of the beam is exposed to a step function heat flux, while the lower surface is assumed to be thermally insulated. Figure 2 shows the midpoint lateral deflection history of the heated beam for the coupled thermoelasticity assumptions reported in [Massalas and Kalpakidis 1983] and the present study. Close agreements are observed between the two studies.

Consider an FGM beam with ceramic upper surface and metal lower surface. The material properties of metal and ceramic are given in Table 1. The mechanical boundary conditions at the ends of the beam are assumed to be simply supported. The thermal boundary conditions at the ends of the beam are assumed to be at ambient temperature at $T_0 = 293$ K. The upper side of the beam is subjected to a step function thermal shock while the lower side is subjected to convection to the surrounding ambient with coefficient $h_c = 10000$ W/m^{2}K.

| Metal: Ti-6Al-4V	Ceramic: ZrO$_2$
$E_m = 66.2$ GPa	$E_c = 117.0$ GPa
$\nu\ \ = 0.322$	$\nu\ \ = 0.322$
$\alpha_m = 10.3 \times 10^{-6}$/K	$\alpha_c = 7.11 \times 10^{-6}$/K
$\rho_m = 4.41 \times 10^3$ kg/m^3	$\rho_c = 5.6 \times 10^3$ kg/m^3
$k_m\ = 18.1$ W/(m·K)	$k_c\ = 2.036$ W/(m·K)
$c_m\ = 808.3$ J/(kg·K)	$c_c\ = 615.6$ J/(kg·K)

**Table 1.** Material properties of metal and ceramic constituents.

Figure 2. Lateral deflection history of an aluminum beam at midpoint with the coupled thermoelasticity assumption.

To compare the results with the numerical solutions presented by Babaei et al. [2008] for the FGM beam when $n = 0$, and $h/l = 0.001$, Figure 3 is plotted for the midpoint lateral deflection history for the uncoupled thermoelasticity case. It can be observed that the numerical solution had reasonable agreement with the present exact solution. The analytical solution presented in this work doesn't have the difficulties of numerical methods such as the unbalance of the members of matrices due to coupling between the strain and temperature fields and a time-consuming process.
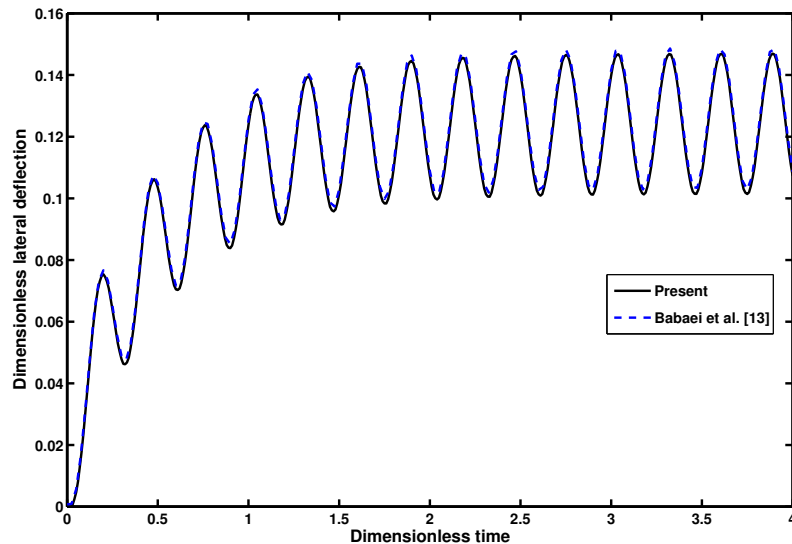
Figure 3. Comparison of the lateral deflection history at the midpoint of the FGM beam for $n = 0$ and $h/l = 0.001$.
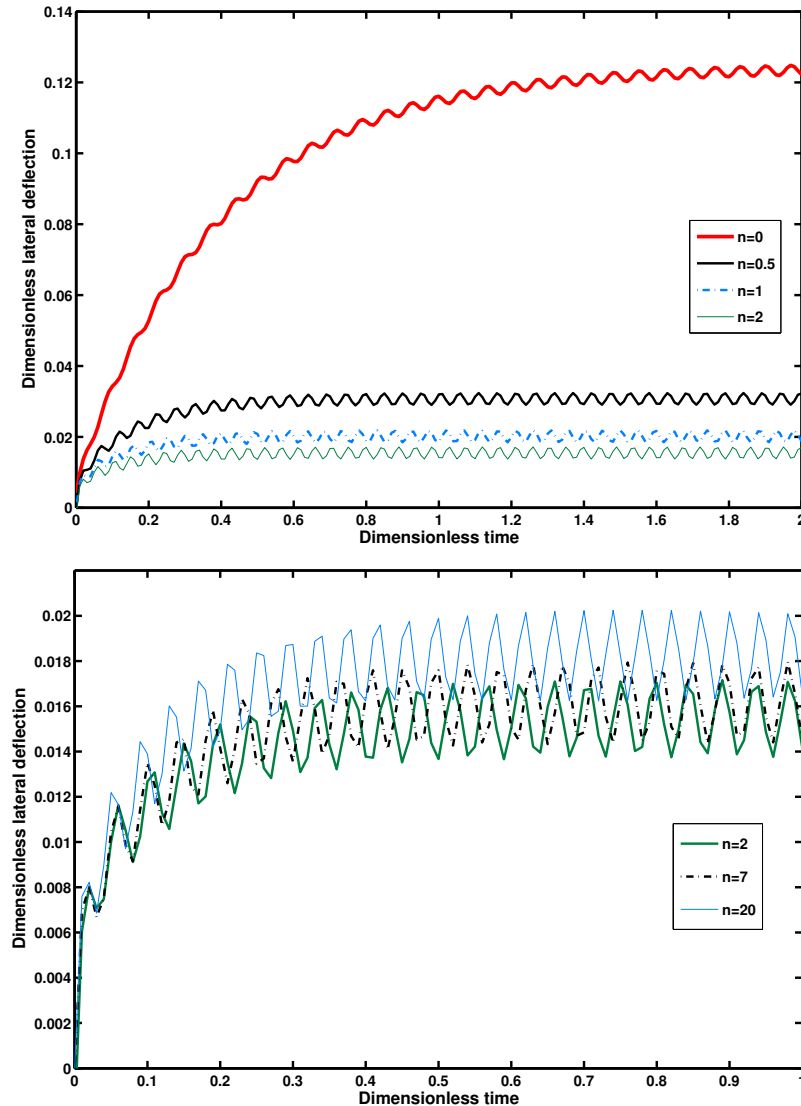
Figure 4. Lateral deflection history at the midpoint of the beam for different power law indices.

The next few figures show the effect of the power law index of the functionally graded beam in the uncoupled case. The maximum lateral deflection, frequency, and lateral amplitude of the FGM beam vibration due to the thermal shock depend on the mechanical and thermal properties of the beam. Thus, when n changes, the FGM beam shows different behaviors. Figure 4 plots the lateral deflection at midlength versus time for different values of the power law index n. The value $n = 0$ corresponds to a pure ceramic beam. We see in Figure 4, top, that as n increases, the midpoint lateral deflection of the FGM beam decreases due to the decline of the temperature gradient in the beam. However, this condition does not always continue. As shown in Figure 4, bottom, when $n > 1$, the difference in lateral deflection for different values of n becomes smaller with smaller amplitudes. Ceramic has a larger modulus of

n	τ_{uc_1}	τ_{uc_2}	ω_{uc_1}	ω_{uc_2}	ω_{uc_3}
0	-58.6014	-2.5144	538.2486		3.6757×10^7
0.5	-84.3941	-6.0998	507.8697	1.8224×10^5	3.5470×10^7
1	-98.4801	-7.0313	497.3527	1.7778×10^5	3.4484×10^7
2	-113.3725	-7.7118	492.1442	1.7282×10^5	3.3254×10^7
7	-131.8458	-8.3314	485.4957	1.6578×10^5	3.1632×10^7
20	-138.3074	-8.5187	472.9925	1.6288×10^5	3.1229×10^7

Table 2. Values of the dimensionless time constants and the dimensionless frequencies of oscillations for different power law indices in the uncoupled solution.

elasticity than metal, but a smaller coefficient of thermal expansion. This causes noncontinuous behavior in the maximum lateral deflection for FGM beams subjected to thermal shock. Furthermore, for larger power law indices which provide most metal rich FGM, the lateral deflection and oscillation frequency begin to slightly increase. In general, the lateral amplitude of vibration of the FGM beam due to the applied thermal shock is increased when the beam constituent materials change from the ceramic-rich to the metal-rich condition. Using (24), the dimensionless time constants and the dimensionless frequencies of oscillations are presented for different power law indices in Table 2.

From Table 2 we see that the frequency of the FGM beam vibration drops when the power law index n increases. Also, the diffusivity effect of the FGM beam is increased when the beam constituent materials change from the ceramic-rich to the metal-rich condition, that is when n is increased.

Figure 5 shows the temperature history at the upper side and the midlength of the beam. Due to the applied step function thermal shock, the beam temperature peaks to a maximum value, and then diffuses during the time. The figure shows that for the most metal rich FGM beams (higher values of n), the
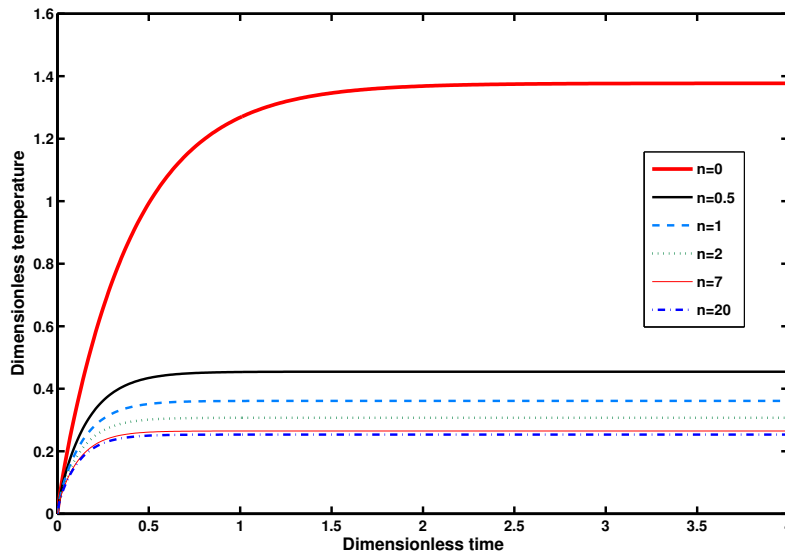
Figure 5. Temperature change history at the midpoint of the beam at the upper side for different power law indices.
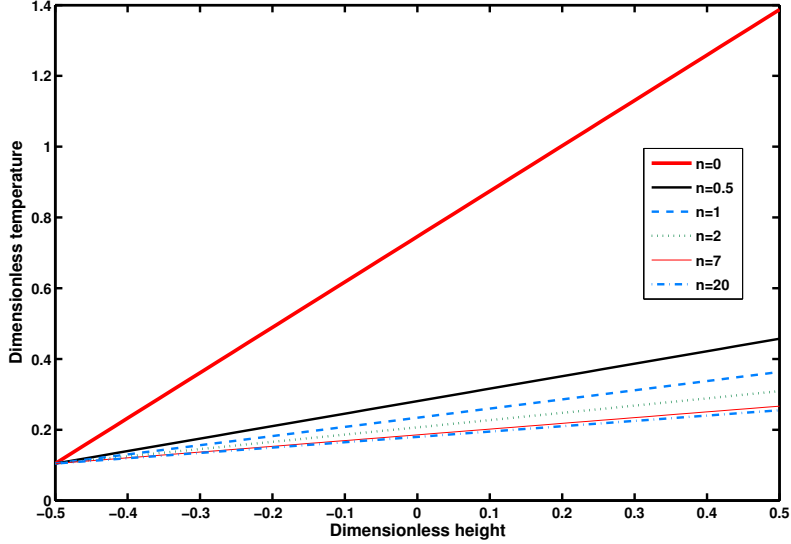
Figure 6. Temperature change distribution at the midpoint of the beam across the thickness direction at $\bar{t} = 3$ for different power law indices.

temperature distribution decreases in value due to the higher thermal conductivity of metal. Figure 6 shows the distribution of the temperature changes across the thickness direction at the midpoint of the beam at $\bar{t} = 3$. It is concluded that for higher values of n, the temperature distribution is changed slightly across the thickness of the FGM beam. By increasing the ceramic share of the beam, the gradient of temperature increases in value due to the lower thermal conductivity of ceramic.

Using (16) and (22), the expressions for the lateral deflection w and the upper surface temperature θ_1 at the midpoint of the beam can be obtained. In terms of the dimensionless quantities, and when $m = 1$, $n = 0$, and $h/l = 0.001$, the lateral deflection and the upper surface temperature at the midpoint of the beam for the coupled and coupled assumptions are

$$
\begin{aligned}
\bar{w}_{uc}(0.5, \bar{t}) = {} & 0.1290 - 6.6592 \cdot 10^{-3} e^{-29.6594\bar{t}} - 0.1094 e^{-1.9872\bar{t}} \\
& - 1.2936 \cdot 10^{-2} \cos(22.0503\bar{t}) - 1.8817 \cdot 10^{-2} \sin(22.0503\bar{t}) \\
& + 1.7574 \cdot 10^{-24} \cos(1.4703 \cdot 10^7 \bar{t}) + 1.1840 \cdot 10^{-19} \sin(1.4703 \cdot 10^7 \bar{t}),
\end{aligned}
$$

$$
\begin{aligned}
\bar{w}_{c}(0.5, \bar{t}) = {} & 0.1290 - 6.6635 \cdot 10^{-3} e^{-29.6531\bar{t}} - 0.1094 e^{-1.9862\bar{t}} \\
& + e^{-2.4257 \cdot 10^{-3}\bar{t}} \left(-1.2931 \cdot 10^{-2} \cos(22.0526\bar{t}) - 1.8816 \cdot 10^{-2} \sin(22.0526\bar{t}) \right) \\
& + e^{-1.2339 \cdot 10^{-3}\bar{t}} \left(2.6551 \cdot 10^{-18} \cos(2.432 \cdot 10^4 \bar{t}) + 1.1878 \cdot 10^{-20} \sin(2.432 \cdot 10^4 \bar{t}) \right) \\
& + e^{-2.0487 \cdot 10^{-8}\bar{t}} \left(1.7574 \cdot 10^{-25} \cos(1.4703 \cdot 10^7 \bar{t}) + 1.1840 \cdot 10^{-19} \sin(1.4703 \cdot 10^7 \bar{t}) \right),
\end{aligned} \tag{26}
$$

$$
\bar{\theta}_{1uc}(0.5, \bar{t}) = 0.7356 - 0.0355 e^{-29.6594\bar{t}} - 0.7001 e^{-1.9872\bar{t}},
$$

$$
\begin{aligned}
\bar{\theta}_{1c}(0.5, \bar{t}) = {} & 0.7356 - 0.0355^{-29.6531\bar{t}} - 0.7001 e^{-1.9862\bar{t}} \\
& + e^{-2.4257 \cdot 10^{-3}\bar{t}} \left(1.6513 \cdot 10^{-5} \cos(22.0526\bar{t}) + 6.3336 \cdot 10^{-6} \sin(22.0526\bar{t}) \right) \\
& + e^{-1.2339 \cdot 10^{-3}\bar{t}} \left(-1.0203 \cdot 10^{-11} \cos(2.432 \cdot 10^4 \bar{t}) + 1.2627 \cdot 10^{-8} \sin(2.432 \cdot 10^4 \bar{t}) \right) \\
& + e^{-2.0487 \cdot 10^{-8}\bar{t}} \left(3.7231 \cdot 10^{-22} \cos(1.4703 \cdot 10^7 \bar{t}) + 1.7298 \cdot 10^{-16} \sin(1.4703 \cdot 10^7 \bar{t}) \right).
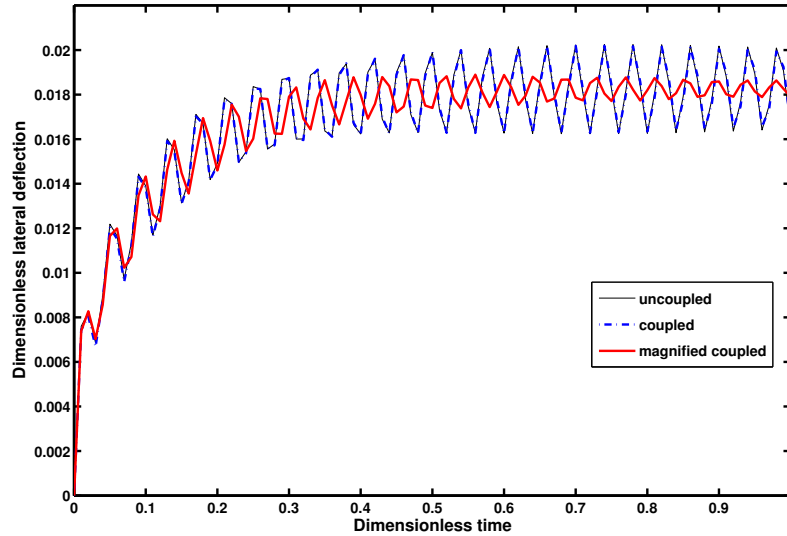\end{aligned}
$$
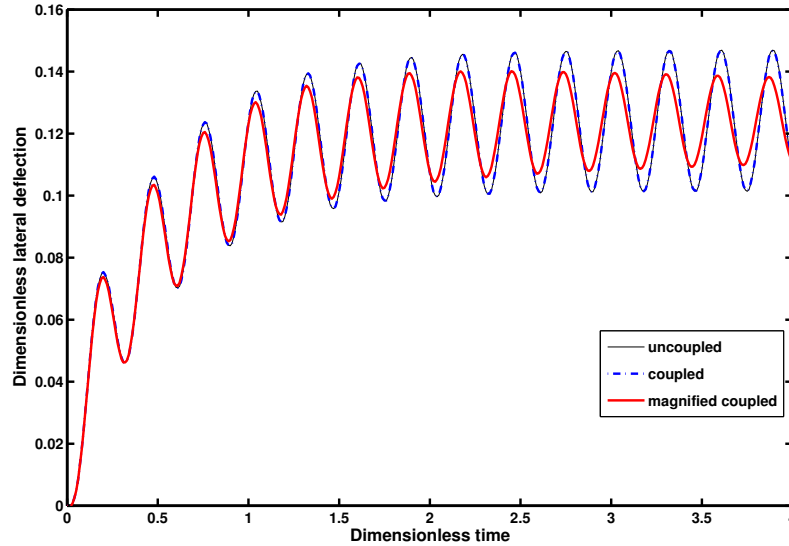
Figure 7. Lateral deflection history at the midpoint of the FGM beam for $n = 0$ and $h/l = 0.001$, showing the effects of coupling.

Investigating (26), one sees that the coupling between the strain and temperature fields has a damping effect on the dimensionless lateral deflection w. The plot of (26) for the lateral deflection history at the midpoint of a beam when $n = 0$, $h/l = 0.001$, and the coupling factors are $d_5 = -0.5027$, $d_6 = 0$, $e_7 = 0$, and $e_8 = 4.1891 \times 10^{-5}$, is shown in Figure 7. As shown in this figure the difference between the coupled and uncoupled solutions for the lateral deflection is negligible. For the magnified coupled solution, where the coupling coefficient is made 50 times larger, the amplitude of vibration increases and the frequency of vibration decreases, compared to the uncoupled solution, as time advances.

Figure 8 shows the lateral deflection history at the midpoint of an FGM beam ($n = 20$) with $h/l = 0.003125$, where the coupling factors are $d_5 = -0.1339$, $d_6 = 2.9444 \times 10^{-6}$, $e_7 = 9.4221 \times 10^{-4}$, and $e_8 = 3.5667 \times 10^{-5}$. Figure 9 shows the temperature history on the upper side of the FGM beam ($n = 20$) with $h/l = 0.003125$ for the coupled and uncoupled solutions, where no distinguishable difference is observed.

In general, the coupled and uncoupled thermoelasticity solutions of the structural problems do not have significant differences in the distribution of displacement and stress, except that for the coupled problems local stress and temperature wave fronts appear, which may cause structural damage. In addition, the coupled solution for the major part of the stress distribution (except around the wave front) is lower than that of the uncoupled solution. Now, the magnitudes of the stress and temperature wave fronts depend upon how short a time the thermal shock is applied. The shorter duration of the applied thermal shock, the higher the magnitude of the stress wave front becomes.

In Figures 7–9, however, wave fronts for the displacement and temperature do not appear. The reason is that the stress and temperature wave fronts appear in any structure under thermal shock. But, they are only detected when the solution is based on the generalized thermoelasticity equations. That is, when the flexural model is used, such as the beams, plates, and shells, the wave fronts do not appear in the

Figure 8. Lateral deflection history at the midpoint of the FGM beam for $n = 20$ and $h/l = 0.003125$, showing the effects of coupling.
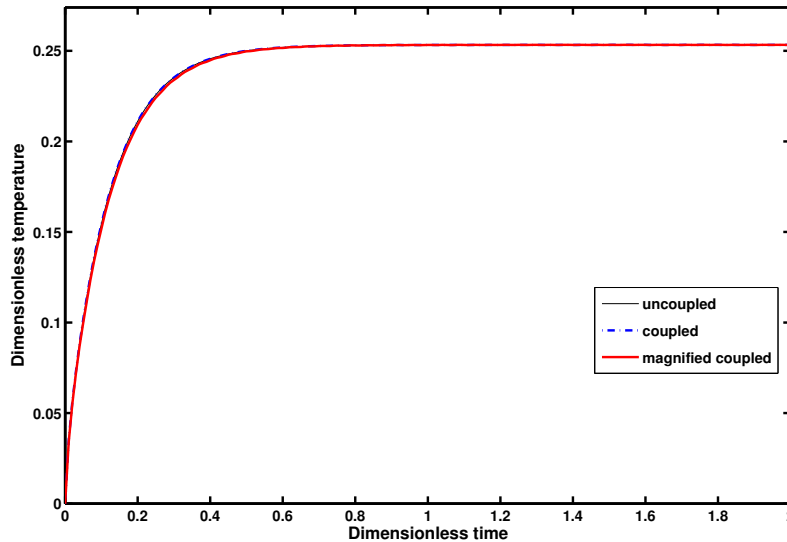
Figure 9. Temperature change history at the midpoint of the FGM beam at the upper side for $n = 20$ and $h/l = 0.003125$, showing the effects of coupling.

solution. The reason is simple, as we have lumped the stress through the thickness. Figure 9 for the temperature distribution does not show a wave front, as the classical coupled thermoelasticity theory is used in this paper, where the temperature equation is of parabolic type and the speed of propagation of the temperature

5. Conclusions

In the present paper, the coupled thermoelasticity of a beam based on first-order shear deformation theory with functionally graded material is investigated. The beam is subjected to a thermal shock of step function type on the upper side. The lower side of the beam is assumed to have convection to the surrounding ambient. Boundary conditions of the beam are taken to be simply supported, with ambient temperature at the ends of the beam. To solve the problem, the finite Fourier transformation is used. Moreover, to treat the time dependency, the Laplace transform technique is applied. The inverse Laplace transform is carried out analytically.

Results show that for larger values of power law indices, which provide the most metal rich FGM, the lateral deflection of an FGM beam due to a applied thermal shock does not decrease proportionally. There is an optimum value for the FGM parameter at which the beam's lateral deflection is minimum. By increasing the metal share of the FGM beam, the distribution of temperature changes slightly across the thickness of the beam. The amplitude of lateral vibration considerably increases as the aspect ratios of the beam decrease. Moreover, generally it can be said that there is no significant difference between the coupled and uncoupled solutions. However, the effect of coupling is in the form of damping. It decreases the amplitude of vibration and increase the frequency of the vibrations with the increase of time.

Acknowledgement

References

[Babaei et al. 2008] M. H. Babaei, M. Abbasi, and M. R. Eslami, "Coupled thermoelasticity of functionally graded beams", *J. Therm. Stresses* **31**:8 (2008), 680–697.

[Bahtui and Eslami 2007] A. Bahtui and M. R. Eslami, "Coupled thermoelasticity of functionally graded cylindrical shells", *Mech. Res. Commun.* **34**:1 (2007), 1–18.

[Eslami and Vahedi 1988] M. R. Eslami and H. Vahedi, "Coupled thermoelasticity beam problems", *AIAA J.* **27**:5 (1988), 662–665.

[Eslami et al. 1999] M. R. Eslami, M. Shakeri, A. R. Ohadi, and B. Shiari, "Coupled thermoelasticity of shells of revolution: effect of normal stress and coupling", *AIAA J.* **37**:4 (1999), 496–504.

[Hetnarski and Eslami 2009] R. B. Hetnarski and M. R. Eslami, *Thermal stresses: advanced theory and applications*, Solid Mechanics and its Applications **158**, Springer, Dordrecht, 2009.

[Jones 1966] P. J. Jones, "Thermoelastic vibrations of a beam", *J. Acoust. Soc. Am.* **39**:3 (1966), 542–548.

[Manoach and Ribeiro 2004] E. Manoach and P. Ribeiro, "Coupled, thermoelastic, large amplitude vibrations of Timoshenko beams", *Int. J. Mech. Sci.* **46**:11 (2004), 1589–1606.

[Maruthi Rao and Sinha 1997] D. Maruthi Rao and P. K. Sinha, "Finite element coupled thermostructural analysis of composite beams", *Comput. Struct.* **63**:3 (1997), 539–549.

[Massalas and Kalpakidis 1983] C. V. Massalas and V. K. Kalpakidis, "Coupled thermoelastic vibrations of a simply supported beam", *J. Sound Vib.* **88**:3 (1983), 425–429.

[Massalas and Kalpakidis 1984] C. V. Massalas and V. K. Kalpakidis, "Coupled thermoelastic vibrations of a Timoshenko beam", *Int. J. Eng. Sci.* **22**:4 (1984), 459–465.

[McQuillen and Brull 1970] E. J. McQuillen and M. A. Brull, "Dynamic thermoelastic response of cylindrical shell", *J. Appl. Mech.* (*ASME*) **37**:3 (1970), 661–670.

[Sankar 2001] B. V. Sankar, "An elasticity solution for functionally graded beams", *Compos. Sci. Technol.* **61**:5 (2001), 689–696.

[Sankar and Tzeng 2002] B. V. Sankar and J. T. Tzeng, "Thermal stresses in functionally graded beams", *AIAA J.* **40**:6 (2002), 1228–1232.

[Seibert and Rice 1973] A. G. Seibert and J. S. Rice, "Coupled thermally induced vibrations of beams", *AIAA J.* **11**:7 (1973), 1033–1035.

MOSTAFA ABBASI: musan.abbasi@gmail.com
Mechanical Engineering Department, Amirkabir University of Technology, 424 Hafez Avenue, Tehran 15914, Iran
http://www.mostafabbasi.ir

MEHDY SABBAGHIAN: mehdys@bellsouth.net
Mechanical Engineering Department, Louisiana State University, Baton Rouge, LA 70803, United States

M. REZA ESLAMI: eslami@aut.ac.ir
Mechanical Engineering Department, Amirkabir University of Technology, 424 Hafez Avenue, Tehran 15914, Iran
http://me.aut.ac.ir/M.Eslami.htm

A NEW METHOD FOR CALCULATING THE PEAK TEMPERATURE EVOLUTION IN THE ADIABATIC SHEAR BAND OF STEEL

XUE-BIN WANG

A new method for predicting the peak temperature evolution in the adiabatic shear band (ASB) of steel is proposed to overcome the drawback of the traditional method's underestimation of the peak temperature in the ASB. The average shear strain of a thin-walled tube in torsion is divided into three parts: the elastic shear strain, the average plastic shear strain outside the ASB, and the average plastic shear strain of the ASB. The relation between the shear stress acting on the tube and the average shear strain of the tube is established. The postpeak shear stress-average shear strain curve of the ASB is found to be dependent on the gage length. As an example, the shear stress-average plastic shear strain curve of the ASB is back-calculated from the measured shear stress-average shear strain curve of an AISI 1018 cold rolled steel tube. The peak temperature and average temperature in the ASB are calculated and compared with the experimental result. It is found that the calculated peak temperature is closer to or slightly higher than the experimental result. The latter is a satisfactory result due to the underestimated peak temperature in the ASB in experiments.

1. Introduction

At high strain rates, metals and alloys frequently show narrow bands of highly localised shear deformation, referred to as adiabatic shear bands (ASBs). ASBs can be generally observed in applications such as metal forming, perforation, impact on structures, ballistic impact, machining, torsion, explosive fragmentation, grinding, interfacial friction, powder compaction, and granular flow.

The localised shear deformation in ASBs is accompanied by a rapid temperature rise of a very short duration, softening the material and reducing its resistance to further plastic deformation. The accurate assessment of the peak temperature in ASBs is especially important in identifying whether the dynamic recovery, recrystallisation, or phase transformation occurs and in determining the extent of softening of the material and its load-carrying capacity. The temperature in ASBs is usually assessed by the plastic work determined by the area below the measured stress-strain curve of a specimen [Xu et al. 2001; 2008; Wei et al. 2004]. However, using the traditional method, only the average temperature in the specimen is assessed, rather than the peak temperature in the ASBs. Undoubtedly, the traditional method will underestimate the peak temperature in the ASBs.

Some researchers have measured the temperature distribution and evolution in ASBs using infrared detectors and infrared high-speed microscopic cameras. Hartley et al. [1987] observed ASBs in two kinds of steels and measured the temperature in the ASBs by determining the infrared radiation emitted at the metal surface. It was found that the maximum temperature rise in the ASBs was about 450°C and that the temperature distribution across the ASBs was consistent with results of stability analyses. A series of

experiments was performed by Duffy and Chi [1992] to study the process of ASB initiation and formation in steels. The local temperature in the ASB was measured by employing an array of small high-speed infrared detectors that provided a plot of temperature as a function of time and position. Within the ASB region, temperatures of 600°C were measured. Dynamic torsion experiments were conducted by Cho et al. [1993] and local temperature increases of up to 600°C were measured. Zhou et al. [1996] studied the initiation and propagation of ASBs by subjecting prenotched plates to asymmetric impact loading. The highest temperature measured was in excess of 1400°C. The results showed that the peak temperatures inside the propagating ASBs increased with impact velocity. Liao and Duffy [1998] investigated the process of initiation and formation of ASBs in Ti-6Al-4V. An array of infrared detectors was employed to measure the local temperature rise in ASBs during the deformation process. A peak temperature of 440–550°C was found in their tests. Guduru et al. [2001] investigated the initiation and propagation characteristics of ASBs in a type of steel. A developed two-dimensional high speed infrared camera was employed to observe the temperature field evolution during the initiation and propagation of ASBs. The results support the notion of a diffuse ASB tip and reveal "hot spots" distributed along the length of a well-developed ASB. ASBs in pure shear were studied in a type of steel and the temperature in the ASBs was obtained by Giovanola [1988]. It was found that temperature elevation was in excess of 1000°C.

As is known, the thinness of ASBs (about ten to hundreds of microns) and the complex geometry of the thin-walled tube specimen render peak temperature measurement difficult. Actually, the highest temperatures measured in ASBs are usually lower than the phase transformation temperatures of steels or titanium alloys [Xu et al. 2008]. ASBs can be rapidly cooled by the surrounding bulk material in the deformational process. Besides this, the other reasons for the underestimated peak temperature in ASBs in experiments are:

- Only the temperature on the surface of a specimen is measured. Hence, the measured peak temperature perhaps will be underestimated since the material on the external surface of the specimen is readily cooled.

- In tests, the viewing area of one detector element can cover a portion of cooler adjacent material outside an ASB. Hence, the detector output undoubtedly underestimates the peak temperature in the ASB to some extent.

Recently, Wang introduced the gradient-dependent plasticity (GDP) where an internal length parameter was included in the yield function to describe the interactions and interplay among microstructures (the so-called microstructural effect) of heterogeneous metal materials [De Borst and Mühlhaus 1992] into the Johnson–Cook (J–C) and Zerilli–Armstrong (Z–A) models to investigate the temperature distribution and evolution in ASBs of Ti-6Al-4V and aluminium-lithium alloy [Wang 2006a; 2006b; 2006c], the strain and deformation distribution in ASBs of steels [Wang 2007], and the evolution of the transformed ASB thickness, local strain, and deformation at interfaces between the deformed and transformed ASBs [Wang 2008].

In the present paper, the J–C and Z–A models are abandoned and a new method for calculating the peak temperature evolution in the ASB is proposed. In the method, the measured shear stress-shear strain curve of a thin-walled tube in torsion is adopted. Using the measured curve, the shear stress-average plastic shear strain curve of the ASB can be back-calculated. Then, the peak temperature evolution in the ASB can be obtained. To this end, the relation between the shear stress acting on the tube and the average

shear strain of the tube must be established. The postpeak shear stress-average shear strain curve of the ASB is found to be dependent on the gage length. The predicted peak temperature evolution in the ASB is compared with the experimental result and the predicted value is closer to or slightly higher than the measured one. The latter is very reasonable since the peak temperature measured in tests is inevitably underestimated. The proposed method has a wide applicability for ductile metals and alloys.

2. Theoretical analysis

Derivation of the peak temperature in the ASB. The occurrence of ASBs is usually attributed to the thermal softening effect overcoming the strain-hardening effect. In this paper, for the sake of simplicity, an ASB is assumed to initiate just at peak shear stress τ_c (the maximum shear stress criterion).

Using three assumptions (the first is that the local plastic shear strain $\gamma_p(y)$ in the ASB is symmetrical with respect to the center of the ASB, the second is that the local plastic shear strain at the edges of the ASB is equal to the critical plastic shear strain, that is, the plastic shear strain corresponding to the maximum shear stress, and the third is that the actual thickness of the ASB corresponds to the maximum value of $\gamma_p(y)$), Wang has derived the expressions for $\gamma_p(y)$ and w (the thickness of the ASB) according to the GDP [Wang 2006a; 2006b; 2006c; 2007; 2008]:

$$\gamma_p(y) = \gamma_c + (\bar{\gamma}_p - \gamma_c) \cdot \left(1 + \cos\frac{y}{l}\right), \qquad w = 2\pi l, \tag{1}$$

where l is the internal length parameter describing the heterogeneity of the material, $\bar{\gamma}_p$ is the average plastic shear strain of the ASB, γ_c is the critical plastic shear strain, y is the coordinate whose origin O is set at the center of the ASB (see Figure 1), and τ is the shear stress acting on the top and base of the ASB (see Figure 1).
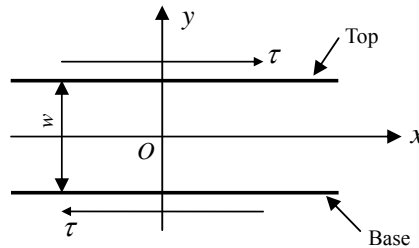
The uniform temperature rise T_1 at prepeak is calculated as [Wang 2006a; 2006b; 2006c; 2007]

$$T_1 = \frac{\beta}{\rho C_p} \int_0^{\gamma_c} \tau \, d\bar{\gamma}_p, \tag{2}$$

where β is the work to heat conversion factor, C_p is the heat capacity, and ρ is the density.

Beyond the initiation of the ASB, the local plastic work $W_p(y)$ due to the microstructural effect done by the shear stress τ is [Wang 2006a; 2006b; 2006c; 2007]

$$W_p(y) = \int \tau \, d\gamma_p(y). \tag{3}$$

Figure 1. A narrow ASB in shear.

Using Equation (1)$_1$, (3) can be expressed as [Wang 2006a; 2006b; 2006c; 2007]

$$W_p(y) = \left(1 + \cos \frac{y}{l}\right) \int_{\gamma_c}^{\bar{\dot{\gamma}}_p} \tau \, d\bar{\gamma}_p. \tag{4}$$

Thus, the local temperature distribution $T_m(y)$ in the ASB due to the microstructural effect is [Wang 2006a; 2006b; 2006c; 2007]

$$T_m(y) = \frac{\beta}{\rho C_p} \int \tau \, d\gamma_p(y) = \frac{\beta}{\rho C_p} \cdot \left(1 + \cos \frac{y}{l}\right) \int_{\gamma_c}^{\bar{\dot{\gamma}}_p} \tau \, d\bar{\gamma}_p. \tag{5}$$

The peak temperature $T_m(0)$ in the ASB due to the microstructural effect is

$$T_m(0) = \frac{2\beta}{\rho C_p} \int_{\gamma_c}^{\bar{\dot{\gamma}}_p} \tau \, d\bar{\gamma}_p. \tag{6}$$

The peak temperature $T(0)$ in the ASB is the sum of the initial temperature T_0, the temperature rise T_1 at prepeak, and the peak temperature rise $T_m(0)$ at postpeak:

$$T(0) = T_0 + T_1 + T_m(0) = T_0 + \frac{\beta}{\rho C_p} \int_0^{\gamma_c} \tau \, d\bar{\gamma}_p + \frac{2\beta}{\rho C_p} \int_{\gamma_c}^{\bar{\dot{\gamma}}_p} \tau \, d\bar{\gamma}_p. \tag{7}$$

The average temperature T_a in the ASB can be calculated as

$$T_a = T_0 + \frac{\beta}{\rho C_p} \int_0^{\bar{\dot{\gamma}}_p} \tau \, d\bar{\gamma}_p. \tag{8}$$

Considering (8), (7) can be rewritten as

$$\begin{aligned} T(0) &= T_0 + \frac{\beta}{\rho C_p} \int_0^{\gamma_c} \tau \, d\bar{\gamma}_p + \frac{\beta}{\rho C_p} \int_{\gamma_c}^{\bar{\dot{\gamma}}_p} \tau \, d\bar{\gamma}_p + \frac{\beta}{\rho C_p} \int_{\gamma_c}^{\bar{\dot{\gamma}}_p} \tau \, d\bar{\gamma}_p \\ &= T_0 + \frac{\beta}{\rho C_p} \int_0^{\bar{\dot{\gamma}}_p} \tau \, d\bar{\gamma}_p + \frac{\beta}{\rho C_p} \int_{\gamma_c}^{\bar{\dot{\gamma}}_p} \tau \, d\bar{\gamma}_p = T_a + \frac{\beta}{\rho C_p} \int_{\gamma_c}^{\bar{\dot{\gamma}}_p} \tau \, d\bar{\gamma}_p. \end{aligned} \tag{9}$$

Using (6), $T(0)$ is written as

$$T(0) = T_a + \frac{T_m(0)}{2}. \tag{10}$$

It is found from (9) and (10) that the peak temperature $T(0)$ in the ASB is always higher than the average value T_a beyond the occurrence of the ASB. The difference between the two kinds of temperatures is greater when the plastic work done by the shear stress is higher. Moreover, when β is higher, or ρ and C_p are lower, $T(0)$ will be greatly higher than T_a.

The peak temperature $T(0)$ in the ASB is dependent on the average temperature T_a and the shear stress-average plastic shear strain curve (τ-$\bar{\gamma}_p$ curve) of the ASB. This curve cannot be measured experimentally. Only the shear stress-average shear strain curve (τ-γ curve) of a specimen can be measured. When the tested specimen is subjected to localised failure in a form of an ASB beyond the peak shear stress, the size of the ASB will be smaller than the gage length of the specimen.

Derivation of the shear stress-average shear strain curve of a tube specimen. We will now establish the theoretical expression for the τ-γ curve of a tube specimen. Using this expression, the τ-$\bar{\gamma}_p$ curve of the ASB can be back-calculated from the measured τ-γ curve. Thus, the peak temperature $T(0)$ in the ASB can be assessed.

Figure 2 shows a thin-walled tube in torsion. We have drawn a straight line fg on the outer surface of the tube, which is parallel to the symmetric axis of the tube (see Figure 2a). In the elastically deformational stage and the strain-hardening stage, the deformation within the tube is considered to be uniform. Thus, the straight line fg will change to an inclined straight line $f'g$ (see Figure 2b). After an ASB is initiated at a position on the tube, the material outside the ASB will be unloaded elastically, while the material in the ASB will be subjected to a severe plastic shear deformation in the strain-softening process. Thus, the initial straight line fg will change to a complex pattern (see Figure 2c). In the ASB, $g'g''$ (also called a flow line) will be a curve. Outside the ASB, gg' and $f''g''$ are still two straight lines.

The size of the ASB is assumed to be w. Outside the ASB, the size of the uniformly deformational part is assumed to be L'. Thus, the gage length L of the tube is

$$L = L' + w. \tag{11}$$

The elastic shear strain γ^e within the tube is always seen as uniform. Thus, beyond the occurrence of the ASB, we have

$$\gamma^e = \frac{\tau}{G}, \tag{12}$$

where G is the shear elastic modulus.

The localised plastic shear deformation only exists in the ASB. Thus, the average value $\bar{\gamma}_a^p$ of the average plastic shear strain $\bar{\gamma}_p$ of the ASB over the entire tube is

$$\bar{\gamma}_a^p = \frac{\bar{\gamma}_p w}{L}. \tag{13}$$

The average value γ of the total shear strain of the tube will be composed of three parts beyond the occurrence of the ASB: the elastic shear strain γ^e, the average plastic shear strain $\gamma_c L'/L$ due to the uniformly plastic shear deformation outside the ASB, and the average plastic shear strain $\bar{\gamma}_a^p$ due to the
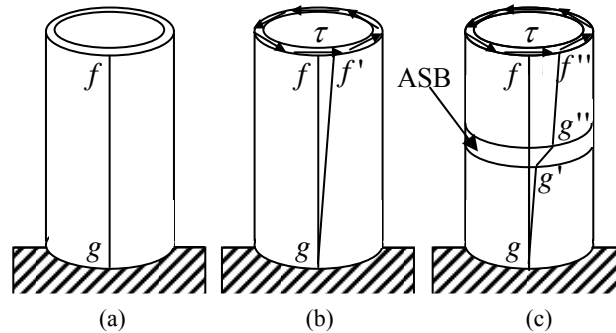
Figure 2. A thin-walled tube specimen without deformation (a), the uniform shear deformation in the elastic and strain-softening stages (b), and the localised shear deformation in the ASB and uniform shear deformation outside the ASB (c).

localised shear deformation in the ASB. Thus, we have

$$\gamma = \gamma_c \frac{L'}{L} + \gamma^e + \bar{\gamma}_a^p. \tag{14}$$

Using Equations (11)–(14), we have

$$\gamma = \frac{\gamma_c L'}{L' + w} + \frac{\tau}{G} + \frac{\bar{\gamma}_p w}{L' + w}. \tag{15}$$

The shear stress-average shear strain curve (τ-γ curve) of a thin-walled tube can be measured in the torsional Kolsky bar experiment. It is found from (15) that after the ASB initiates, the measured postpeak τ-γ curve depends on the size of the gage length (L).

For a given thin-walled tube tested in torsion, one can determine the shear elastic modulus G and the critical plastic shear strain γ_c from the measured τ-γ curve. Once the thickness of the ASB is measured, the postpeak shear stress-average plastic shear strain curve (τ-$\bar{\gamma}_p$ curve) of the ASB can be back-calculated from the measured τ-γ curve. Thus, $T(0)$ can be calculated, see (9) and (10).

Calculation of the peak temperature in the ASB using the back-calculated shear stress-average plastic shear strain curve of the ASB. Herein, the back-calculated postpeak τ-$\bar{\gamma}_p$ curve of the ASB is approximated by n' linear segments (see Figure 3). When the shear stress τ decreases to τ_{i+1} from τ_i, the increment of the average plastic shear strain of the ASB is $\bar{\gamma}_p^{i+1} - \bar{\gamma}_p^i$. Therefore, (6) can be written as

$$T_m(0) = \frac{\beta}{\rho C_p} \sum_{i=1}^{n'} (\tau_i + \tau_{i+1}) \cdot (\bar{\gamma}_p^{i+1} - \bar{\gamma}_p^i). \tag{16}$$

Similarly, the prepeak τ-$\bar{\gamma}_p$ curve is approximated by m' linear segments. When the shear stress τ decreases or increases to τ_{j+1} from τ_j, the increment of the plastic shear strain is $\bar{\gamma}_p^{j+1} - \bar{\gamma}_p^j$. Therefore, Equation (2) can be written as

$$T_1 = \frac{\beta}{2\rho C_p} \sum_{j=1}^{m'} (\tau_j + \tau_{j+1}) \cdot (\bar{\gamma}_p^{j+1} - \bar{\gamma}_p^j). \tag{17}$$
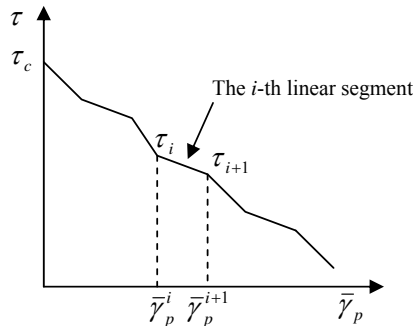
Figure 3. A schematic of the postpeak shear stress-average plastic shear strain relation of the ASB.

Thus, the peak temperature $T(0)$ in the ASB is

$$
\begin{aligned}
T(0) = T_0 + T_1 + T_m(0) &= T_0 + \frac{\beta}{2\rho C_p} \sum_{j=1}^{m'} (\tau_j + \tau_{j+1}) \cdot (\bar{\gamma}_p^{j+1} - \bar{\gamma}_p^j) + \frac{\beta}{\rho C_p} \sum_{i=1}^{n'} (\tau_i + \tau_{i+1}) \cdot (\bar{\gamma}_p^{i+1} - \bar{\gamma}_p^i) \\
&= T_0 + \frac{\beta}{2\rho C_p} \sum_{j=1}^{m'} (\tau_j + \tau_{j+1}) \cdot (\bar{\gamma}_p^{j+1} - \bar{\gamma}_p^j) + \frac{\beta}{2\rho C_p} \sum_{i=1}^{n'} (\tau_i + \tau_{i+1}) \cdot (\bar{\gamma}_p^{i+1} - \bar{\gamma}_p^i) \\
&\qquad\qquad\qquad\qquad\qquad\qquad + \frac{\beta}{2\rho C_p} \sum_{i=1}^{n'} (\tau_i + \tau_{i+1}) \cdot (\bar{\gamma}_p^{i+1} - \bar{\gamma}_p^i) \\
&= T_0 + \frac{\beta}{2\rho C_p} \sum_{k=1}^{n'+m'} (\tau_k + \tau_{k+1}) \cdot (\bar{\gamma}_p^{k+1} - \bar{\gamma}_p^k) + \frac{\beta}{2\rho C_p} \sum_{i=1}^{n'} (\tau_i + \tau_{i+1}) \cdot (\bar{\gamma}_p^{i+1} - \bar{\gamma}_p^i) \\
&= T_a + \frac{\beta}{2\rho C_p} \sum_{i=1}^{n'} (\tau_i + \tau_{i+1}) \cdot (\bar{\gamma}_p^{i+1} - \bar{\gamma}_p^i).
\end{aligned}
\tag{18}
$$

3. Examples and discussion

Calculation of the shear stress-average plastic shear strain curve of the ASB. For AISI 1018 cold rolled steel, Hartley et al. [1987] measured the shear stress-time curves of nine thin-walled tubes in torsion and the peak temperature evolution in ASBs. In their experiments, in order to determine the temperature profile within ASBs, each detector element was focused on a 20 micro spot size on the specimen. The maximum temperature rise recorded in their tests was about 420°C, significantly higher than the average temperature (240°C) measured with a 250 micro spot size.

The typical behaviour of shear stress and ASB peak temperature as functions of time are shown in Figure 4, left, taken from[Hartley et al. 1987]. In each experiment, the duration was 650 microseconds. The measured maximum average shear strain of the tube was 0.45. For the constant strain rate test, we can translate the shear stress-time curve into a τ-γ curve for the tube (Figure 4, right).
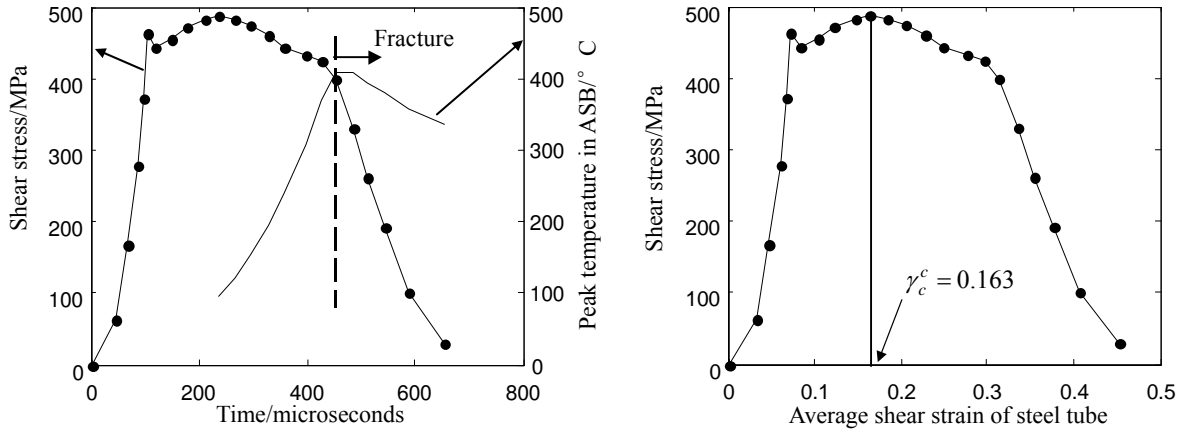
Figure 4. Left: Experimentally observed curves of shear stress and ASB peak temperature versus time. From [Hartley et al. 1987]. Right: Shear stress versus average shear strain curve for a steel tube, based on values on the left.

It can be seen in Figure 4 that the peak temperature in the ASB increases with decreasing shear stress beyond the peak shear stress. When fracture just occurs, the peak temperature reaches its maximum (about 680 K) and then drops slowly.

Prior to the peak stress, the elastic and plastic shear deformations within the tube can be considered to be uniform. After subtracting the elastic shear strain γ^e from the total shear strain γ, we can determine the prepeak τ-$\bar{\gamma}_p$ curve. To back-calculate the τ-$\bar{\gamma}_p$ curve of the ASB from the τ-γ curve, one needs to determine the values of G, L, w, and γ_c.

In the initial loading stage, the measured shear stress-time curve exhibits nonlinearity (see Figure 4, right). The adopted value of the shear elastic modulus of AISI 1018 cold rolled steel is equal to the slope of the shear stress-shear strain curve in the linearly elastic stage, that is, $G = 10.328$ GPa.

The value of the gage length of the tube in the present calculation is assumed to be the gage length of the tube in the experiment (2.5 mm) of Hartley et al. [1987], that is, $L = 2.5$ mm.

The critical plastic shear strain γ_c is calculated as

$$\gamma_c = \gamma_c^c - \frac{\tau_c}{G}, \tag{19}$$

where γ_c^c is the shear strain corresponding to the peak shear stress τ_c. According to Figure 4, right, γ_c^c and τ_c are 0.163 and 486 MPa, respectively. Thus, using Equation (19), we have $\gamma_c = 0.116$.

The reported thickness of the ASBs was about 0.3 mm [Hartley et al. 1987]. Considering the strain rate, plastic work, and thermal conductivity [Dodd and Bai 1985], the value calculated was 0.2 mm [Dodd and Bai 1985; Hartley et al. 1987]. In this paper, the adopted values of the thickness of the ASB are 0.3 mm and 0.25 mm, respectively.

The calculated prepeak shear stress-plastic shear strain curve of the specimen and shear stress-average plastic shear strain curve of the ASB is shown in Figure 5, left, with $G = 10.328$ GPa, $L = 2.5$ mm, $\gamma_c = 0.116$, and $w = 0.3$ mm. The calculated prepeak shear stress-plastic shear strain curve of the specimen and shear stress-average plastic shear strain curve of the ASB are shown in Figure 5, right, with $G = 10.328$ GPa, $L = 2.5$ mm, $\gamma_c = 0.116$, and $w = 0.25$ mm. Five and seven linear segments are
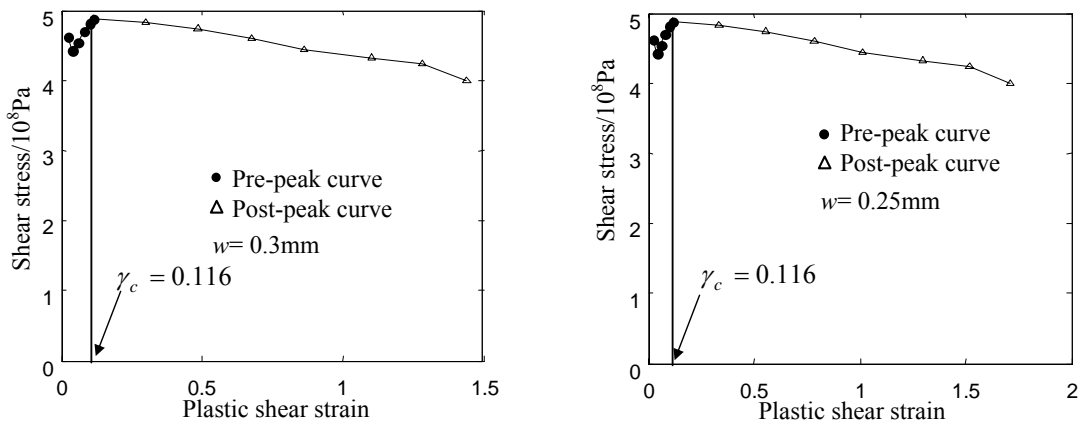
Figure 5. Calculated prepeak shear stress-plastic shear strain curve of the specimen and shear stress-average plastic shear strain curve of the ASB.

used to approximate the prepeak and postpeak parts of the τ-$\bar{\gamma}_p$ curve, respectively, that is, $m' = 5$ and $n' = 7$.

In two graphs of Figure 5, the predicted maximum values of $\bar{\gamma}_p$ are 1.44 and 1.71, respectively. Therefore, the wider the ASB is, the lower the maximum value of the average plastic shear strain of the ASB is. In the left graph, the calculated maximum value of the average plastic shear strain of the ASB is about $1.44/0.116 = 12.4$ times the critical plastic shear strain corresponding to the initiation of the ASB. In the right graph, the maximum value is about $1.71/0.116 = 14.7$ times the initial value.

Comparison of the calculated peak and average temperatures in the ASB and the experimental result.
The top row of Figure 6 shows the evolution of $T(0)$ and T_a with decreasing shear stress, with parameters $w = 0.30$ mm,

$$C_p = 473 \text{ J/(kg·K)}, \quad \rho = 7800 \text{ kg·m}^{-3}, \quad T_0 + T_1 = 367 \text{ K}, \quad \beta = 0.95 \text{ (left) or } 0.85 \text{ (right)}. \quad (20)$$
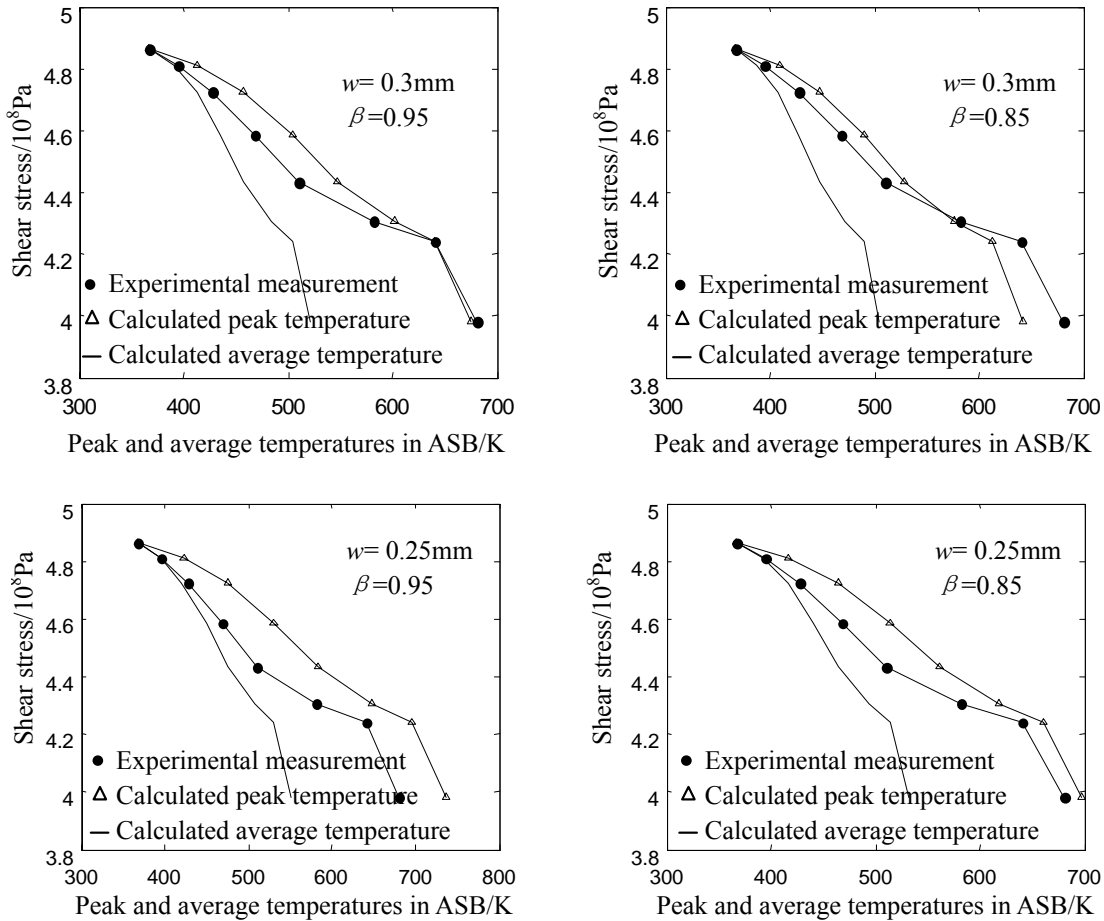
Figure 6. Predicted peak and average temperature evolution in the ASB with decreasing shear stress. For comparison we include experimental results from [Hartley et al. 1987].
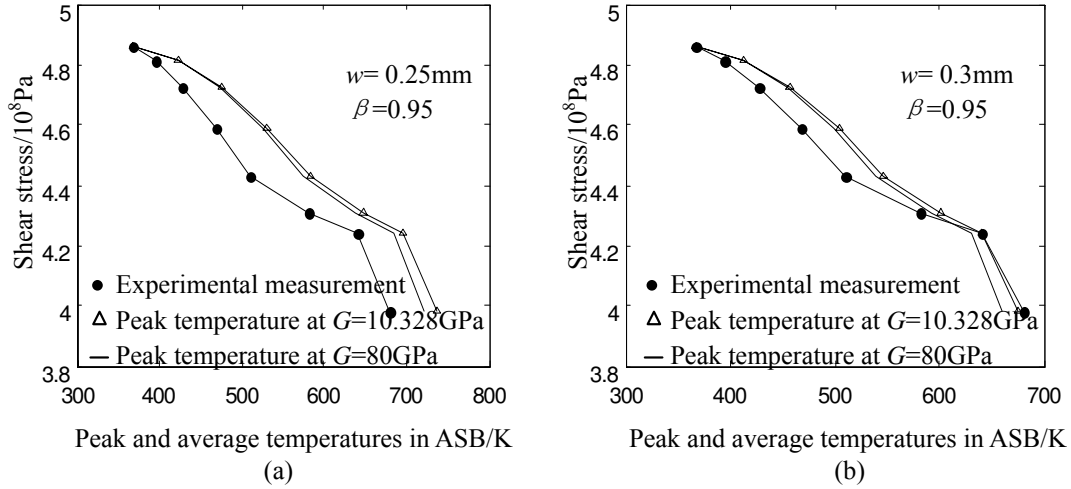
Figure 7. Effect of shear elastic modulus on the predicted peak temperature evolution in the ASB. For comparison we include experimental results from [Hartley et al. 1987].

together with the experimental measurements from [Hartley et al. 1987].

It is found from these graphs that both $T(0)$ and T_a increase with decreasing shear stress. The predicted value of $T(0)$ is even closer to the experimental result. The predicted maximum values of $T(0)$ are 675 K and 642 K, respectively, for the situations in these two graphs. The calculated peak temperature (675 K) in the ASB at $\beta = 0.95$ is slightly lower than the measured peak temperature in the ASB (680 K). When β decreases, $T(0)$ and T_a decrease.

The bottom row of Figure 6 shows the evolution of $T(0)$ and T_a with decreasing shear stress, $w = 0.25$ mm and other parameters as in (20). Again we show the experimental measurements from [Hartley et al. 1987] for comparison.

It is found from these two graphs that the evolution of $T(0)$ with decreasing shear stress is still closer to the experimental result. The calculated value of the peak temperature in the ASB is always higher than the experimental measurement. The predicted maximum values of $T(0)$ are 737 K and 698 K, respectively, for the situations in these two graphs. The calculated peak temperature (698 K) in the ASB at $\beta = 0.85$ is slightly higher than the measured peak temperature in the ASB (680 K) — a very reasonable prediction given the underestimate of the peak temperature in the ASB in tests.

Effect of shear elastic modulus. As is known, the measured shear elastic modulus of any steel is about 80 GPa, while the value of the shear elastic modulus used in the situation depicted in Figures 5 and 6 is about 10 GPa, which is lower and is directly derived from the shear stress-average shear strain curve of a steel tube according to Figure 4. Herein, the shear elastic modulus of 80 GPa is used to calculate the peak temperature evolution in the ASB. In Figure 7, the calculated result with $G = 80$ GPa is compared with the experimental results of [Hartley et al. 1987]; the other parameters are identical to those in 6, left column. The calculated results with $G = 10.328$ GPa are also given in Figure 7. It is found that if the frequently cited shear elastic modulus of about 80 GPa is used, then the calculated peak temperatures are slightly lower than the results at $G = 10.328$ GPa. Moreover, the maximum temperature difference calculated

is only 17 K and 14 K, respectively, in the two parts of Figure 7. This suggests that the influence of the shear elastic modulus may be negligible.

4. Conclusions

The relation between the shear stress acting on a thin-walled tube in torsion and the average shear strain of the tube is established to back-calculate the shear stress-average plastic shear strain curve of the adiabatic shear band (ASB) from the shear stress-shear strain curve of the tube and then to calculate the peak temperature evolution in the ASB in the strain-softening process.

The peak and average temperatures in the ASB are calculated and compared with the experimental results of a AISI 1018 cold rolled steel tube. In a wider ASB, a lower maximum average plastic shear strain of the ASB is expected. A lower work to heat conversion factor leads to lower peak and average temperatures in the ASB. The maximum average plastic shear strain of the ASB is over ten times larger than the critical plastic shear strain corresponding to the initiation of the ASB.

The calculated peak temperature is very close to the experimental measurement. If the value (0.25 mm) of the ASB thickness used is slightly lower than the value (0.3 mm) reported by Hartley et al. [1987], then a reasonable prediction of the peak temperature in the ASB is obtained and the predicted value is slightly higher than the experimental result, which is reasonable since the ASB peak temperature is underestimated in experimental tests to some extent.

References

[Cho et al. 1993] K. M. Cho, S. Lee, S. R. Nutt, and J. Duffy, "Adiabatic shear band formation during dynamic torsional deformation of an HY-100 steel", *Acta Metall. Mater.* **41** (1993), 923–932.

[De Borst and Mühlhaus 1992] R. De Borst and H. B. Mühlhaus, "Gradient-dependent plasticity: formulation and algorithmic aspects", *Int. J. Numer. Meth. Eng.* **35** (1992), 521–539.

[Dodd and Bai 1985] B. Dodd and Y. Bai, "Width of adiabatic shear bands.", *Mater. Sci. Tech.* **1** (1985), 38–40.

[Duffy and Chi 1992] J. Duffy and Y. C. Chi, "On the measurement of local strain and temperature during the formation of adiabatic shear bands", *Mater. Sci. Eng. A* **157** (1992), 195–210.

[Giovanola 1988] J. H. Giovanola, "Adiabatic shear banding under pure shear loading, I: Direction observation of strain localization at energy dissention measurement", *Mech. Mater.* **7** (1988), 59–71.

[Guduru et al. 2001] P. R. Guduru, A. J. Rosakis, and G. Ravichandran, "Dynamic shear bands: An investigation using high speed optical and infrared diagnostics", *Mech. Mater.* **33** (2001), 371–402.

[Hartley et al. 1987] K. A. Hartley, J. Duffy, and R. H. Hawley, "Measurement of the temperature profile during shear band formation in steels deforming at high strain rates", *J. Mech. Phys. Solids* **35** (1987), 283–301.

[Liao and Duffy 1998] S. C. Liao and J. Duffy, "Adiabatic shear bands in a Ti-6Al-4V Titanium alloy", *J. Mech. Phys. Solids* **46** (1998), 2201–2231.

[Wang 2006a] X. B. Wang, "Effects of constitutive parameters on adiabatic shear localization for ductile metal based on Johnson-Cook and gradient plasticity models", *Trans. Nonferrous Met. Soc. China* **16** (2006a), 1362–1369.

[Wang 2006b] X. B. Wang, "Temperature-dependent shear strain localization of aluminum-lithium alloy in uniaxial compression using Zerilli-Armstrong and gradient plasticity models", *Mater. Sci. Forum* **519–521** (2006b), 789–794.

[Wang 2006c] X. B. Wang, "Temperature distribution in adiabatic shear band for ductile metal based on Johnson-Cook and gradient plasticity models", *Trans. Nonferrous Met. Soc. China* **16** (2006c), 333–338.

[Wang 2007] X. B. Wang, "Adiabatic shear localization for steels based on Johnson-Cook model and second- and fourth-order gradient plasticity models", *J. Iron Steel Res., Int.* **14** (2007), 56–61.

[Wang 2008] X. B. Wang, "Effects of temperature and strain rate on the evolution of thickness of transformed adiabatic shear band", *Solid State Phenom.* **138** (2008), 385–392.

[Wei et al. 2004] Q. Wei, L. Kecskes, T. Jiao, K. T. Hartwig, K. T. R. , and E. Ma, "Adiabatic shear banding in ultrafine-grained Fe processed by severe plastic deformation", *Acta Mater.* **52** (2004), 1859–1869.

[Xu et al. 2001] Y. B. Xu, W. L. Zhong, Y. J. Chen, L. T. Shen, Q. Liu, Y. L. Bai, and M. A. Meyers, "Shear localization and recrystallization in dynamic deformation of 8090 Al-Li alloy", *Mater. Sci. Eng. A* **299** (2001), 287–295.

[Xu et al. 2008] Y. B. Xu, J. H. Zhang, Y. L. Bai, and M. A. Meyers, "Shear localization in dynamic deformation: Microstructural evolution", *Metall. Mater. Trans. A* **39** (2008), 811–843.

[Zhou et al. 1996] M. Zhou, A. J. Rosakis, and G. Ravichandran, "Dynamically propagating shear bands in impact-loaded prenotched plates, I: Experimental investigations of temperature signatures and propagation speed", *J. Mech. Phys. Solids* **44** (1996), 981–1006.

XUE-BIN WANG: wxbbb@263.net
Department of Mechanics and Engineering Sciences, Liaoning Technical University, Fuxin 123000, China

CREEP BUCKLING OF IMPERFECT THIN-WALLED
SHALLOW CONCRETE DOMES

EHAB HAMED, MARK A. BRADFORD AND R. IAN GILBERT

The sensitivity of the nonlinear long-term creep behaviour of shallow concrete domes to geometric and material imperfections is investigated in this paper. A nonlinear incremental theoretical model is developed, which accounts for the effects of creep and shrinkage, considers the aging of the concrete material and the variation of the internal stresses and geometry in time, and is applicable for different and nonaxisymmetric imperfection scenarios and loading schemes. The model focuses only on shallow concrete domes, but the modelling concepts and solution techniques can be generated for the creep buckling analysis of different types of thin-walled concrete structures. The field equations are derived using the variational principles of virtual work and using integral-history-type constitutive relations that are based on the principle of superposition. A step-by-step procedure is used for the solution of the governing equations in time, while the solution of the incremental partial differential equations in space is achieved by a separation of variables and expansion into truncated Fourier series in the circumferential direction, along with the use of the multiple shooting method in the meridional direction. Numerical and parametric studies, which highlight the capabilities of the model and which provide insight into the nonlinear long-term behaviour of imperfect shallow concrete domes, are presented. The results show that the structural behaviour and the critical time to cause creep buckling are very sensitive to geometric and material imperfections.

1. Introduction

Like all other engineering structures, concrete structures have a finite design life. While strengthening and upgrading techniques have been recognised and highlighted over the past two decades in order to increase the safety and serviceability of existing structures, an understanding of the long-term behaviour of concrete structures and the development of suitable and reliable theoretical models for their analysis and safety assessment are essential before the application of costly strengthening techniques. These aspects become more critical in thin-walled concrete shells and in shallow spherical shells (domes) in particular, as these structures are vulnerable to the effects of creep and shrinkage, and unfortunately characterized by catastrophic and sudden buckling failures [DPW NSW 1978; Takeuchi et al. 2004; Moncarz et al. 2007].

In general, all concrete shells of revolution should be designed for the combined effects of creep and buckling; yet, considering the shape of the shell, its use in civil engineering applications, the thickness requirements, and the level of applied sustained loads (self-weight, periodic snow, water/earth pressure), it can be observed that the vulnerability of vertical cylindrical or conical concrete shells of revolution (as

cooling towers or storage tanks for example) to creep buckling failures is less than the case in shallow concrete domes or other concrete shell roofs, where creep buckling becomes a key-parameter in their design [Zarghamee and Heger 1983; Bockhold and Petryna 2008]. This paper focuses on the influence of creep on the buckling aspects of shallow concrete domes, and particularly, on the sensitivity of the long-term behaviour to structural imperfections. The challenges associated with the modelling, analysis, and quantitative assessment of the creep buckling phenomenon in general concrete structures are also discussed.

Creep effects generally increase the deformations of a concrete structure even at ambient temperatures, and are usually only considered to affect behaviour at the serviceability limit states. However, in thin-walled shallow concrete domes and other structures that may exhibit sudden buckling failures, the deformations caused by creep and other time-dependent effects become more critical and bring the safety of the structure into question. Due to the geometric nonlinearity, creep leads to a reduction of the height of the dome with a consequent increase or modification of the internal stresses. These two effects may interact to produce localised damage, or may lead to a configuration which produces so-called creep buckling, in which the structure loses its stability slowly over time. The dependence of the creep strains on the level of stresses, their interaction with nonmechanical shrinkage and thermal strains, the aging of the concrete material, and the effects of structural imperfections that cannot be avoided in practice, make accurate prediction of the nonlinear behaviour of concrete domes a challenging and difficult task.

The buckling behaviour of elastic domes has been intensively studied; see for example [Reissner 1946; Sheinman 1981; Błachut and Galletly 1990; 1995; Muc 1992; Teng and Lou 1997; Teng and Song 2001; Hong and Teng 2002; Wunderlich and Albertin 2002; Grigolyuk and Lopanitsyn 2003; Teng and Hong 2006; Marcinowski 2007]. These studies revealed the main aspects that characterize the buckling behaviour of domes, which include snap-through behaviour, the sensitivity of the dome to geometric imperfections, the existence of asymmetric bifurcation points even under axisymmetric loads, and the mode switching and mode interaction in the post buckling deformations. These studies also provided the required theoretical models and numerical tools for the nonlinear analysis of general domes under arbitrary loadings. However, all the aforementioned studies focused only on the nonlinear instantaneous behaviour of domes made of an elastic material, while the nonlinear long-term effects which characterize concrete domes were not investigated.

Only a few research works have focused on the buckling behaviour of concrete domes in general, and a much smaller number of these have focused on the influence of creep on their nonlinear behaviour. In terms of experimental findings, which reveal the importance of considering the long-term effects, Litle et al. [1970] investigated the buckling behaviour of two spherical reinforced mortar domes. It was found that the experimental buckling pressures were only approximately 40% of the classical theoretical value, due to cracking, geometric imperfections, and long-term effects. Vandepitte and Lagae [1986] indicated that the buckling analysis of concrete domes must account for long-term effects and that classical buckling formulae provide much higher buckling pressures than was observed in their experimental work. Based on a decade of a comprehensive experimental work, they observed that creep caused a significant reduction (about 67%) in the buckling pressure. Thus, under sustained loading, a dome may collapse over time under only 33% of its buckling pressure.

In terms of theoretical models, Teng and Rotter [1992] developed a general finite element model for the geometrically and materially nonlinear analysis of reinforced concrete shells of revolution. However,

the long-term effects of the concrete were not included. Dulácska and Kollár [1995] indicated that various long-term effects can be assessed as multipliers of the classical buckling pressure, but a detailed theoretical or experimental basis that supports the proposed factored buckling pressure was not found. Zarghamee and Heger [1983] presented a design procedure for determining the buckling pressure of concrete domes, based on a computer program that was developed by Bushnell [1976] and uses the rate-of-creep method (the Dischinger method). However, the rate-of-creep method is more suitable for materials that exhibit almost linear or bilinear creep behaviour in time. The rate of creep of the concrete material approaches zero as time increases. Hence, when this method is applied for the buckling analysis of concrete structures, where creep causes a significant variation of the internal stresses in time or when the structure is gradually loaded, it may lead to erroneous results because of its inability to accurately asses the creep caused by loads that are applied at older ages [Bažant 1988; Gilbert 1988]. Therefore, a model that is able to account for these effects needs to be implemented in the creep buckling analysis of concrete domes.

The effects of creep and shrinkage on the behaviour of concrete structures have been widely studied and reported [Bažant 1988; Gilbert 1988]. However, very little advanced research appears to have been reported on these effects in concrete shell structures, and in shallow concrete domes in particular. On the other hand, the creep buckling phenomenon of shells and columns made of metals and polymeric composite materials has been studied by many researchers [Hoff 1968; Bushnell 1977; Minahen and Knauss 1993]. Special attention to the creep buckling of circular cylindrical shells was made by [Murakami and Tanaka 1976; Arnold et al. 1989; Miyazaki et al. 1991], and many others. However, in all of these studies, the rate-of-creep method was used, which is of questionable accuracy when applied to concrete structures with stress levels that vary significantly with time.

Similar to the above studies and based on the rate-of-creep method, a few research contributions have been reported on the creep buckling of spherical shells made of metals and other materials. Shi et al. [1970] and Kao [1981] focused only on the nonlinear axisymmetric creep behaviour. It was concluded by Kao [1981] that a creep law that is based on the strain-hardening hypotheses (where the creep rate is a function of the accumulated creep strain) provides more accurate results than the time-hardening hypotheses (where the creep rate is a function of time elapsed since creep started) (also see [Arbabi-Kanjoori and Leonard 1979]). Yet, these two models cannot be used separately for the geometrically nonlinear analysis of concrete structures, because they significantly underestimate the additional creep due to stress changes [Bažant 1987]. Xirouchakis and Jones [1980] studied the full nonlinear creep behaviour considering an imperfection shape according to the classical axisymmetric buckling mode only. Miyazaki [1986] developed a finite element procedure for the creep buckling analysis of spherical shells of revolution considering the bifurcation behaviour, but without considering the effects of imperfections. Huang [1965] used the Volterra integral constitutive relation, which is applicable for aging materials, for the analysis of clamped shallow spherical shells. However, the model is limited to the axisymmetric analysis of shells made of polymethyl-methacrylate with uniform thickness and clamped edges.

It can be seen that most of the existing research contributions have focused on domes made of metals and other materials, where the use of the rate-of-creep method (strain hardening or time hardening) is justified. These existing studies are also limited to specific geometry and boundary conditions, and cover only a small range of imperfection scenarios that can exist in concrete domes. The main objective of this paper is to provide insight into the creep buckling behaviour of thin-walled imperfect shallow concrete

domes, in order to enhance their effective design and safe use, and to contribute to the establishment of a foundation of theoretical knowledge required for nonlinear long-term analysis of concrete structures. Another goal of the paper is to present and to study a different aspect of the influence of creep beyond the service limit state of concrete structures. Studying the behaviour of shallow concrete domes can best contribute to this, because along with other roof shells, these structures are more prone to creep buckling failures than other concrete shells of revolution. A general theoretical model that accounts for the nonlinear creep and shrinkage effects using a history integral-type analysis rather than a rate-of-creep analysis, is developed. The model accounts for the aging of the concrete, different geometry configurations and boundary conditions, and different axisymmetric and nonaxisymmetric loading and imperfection shapes. A study of the creep and shrinkage effects on the geometrically linear behaviour of shallow concrete domes under service loads was conducted by the authors [Hamed et al. 2009b]. The effects of creep and shrinkage on the geometrically nonlinear behaviour were also studied [Hamed et al. 2008; 2009a; 2010] but considering axisymmetric behaviour only and without including the effects of imperfections.

The variational principle of virtual work is used to derive the field equations and the boundary conditions for the problem. Due to the use of an implicit integral-type constitutive relation, a time incremental superposition approach is invoked to formulate the time-dependent governing equations, where the creep and shrinkage strains are treated as initial strains and kept constant with each time step interval [Bažant 1988]. The time integration scheme utilises a slightly variable time step, to account for the decrease of the creep rate, and to account for the rapid change of the structural response prior to buckling. It is assumed that the dome behaves quasistatically, that is, the effects of inertia forces are neglected. Finally, as a first step, and in order to focus on and clarify the stability characteristics of the dome, the analysis is conducted in the framework of linear elasticity. Numerical and parametric studies are included, which provide some insight into the nonlinear long-term behaviour of imperfect shallow concrete domes through the examination of three different imperfection scenarios. The results highlight the capabilities of the proposed theoretical model, and reveal some aspects of the creep response of these structures.

2. Mathematical formulation

The sign conventions for the coordinates, deformations, loads, and stress resultants of a spherical shallow concrete dome are shown in Figure 1. The variational principle of virtual work is used to derive the nonlinear long-term incremental equilibrium equations along with the boundary conditions, which requires that

$$\delta U + \delta W = 0, \tag{1}$$

where δU and δW are the virtual works of the internal stresses and external loads respectively, and δ is the variational operator. The virtual work of the internal stresses is

$$\delta U = \int_V \left[(\sigma_{\varphi\varphi} + \Delta\sigma_{\varphi\varphi})\delta\Delta\varepsilon_{\varphi\varphi} + (\sigma_{\theta\theta} + \Delta\sigma_{\theta\theta})\delta\Delta\varepsilon_{\theta\theta} + (\sigma_{\varphi\theta} + \Delta\sigma_{\varphi\theta})\delta\Delta\varepsilon_{\varphi\theta} \right] dV, \tag{2}$$

where $\sigma_{\varphi\varphi}$ and $\sigma_{\theta\theta}$ are the stresses in the radial and circumferential directions respectively, $\sigma_{\varphi\theta}$ is the in-plane shear stress, $\varepsilon_{\varphi\varphi}$, $\varepsilon_{\theta\theta}$ and $\varepsilon_{\varphi\theta}$ are the corresponding strains, Δ is the incremental operator, and
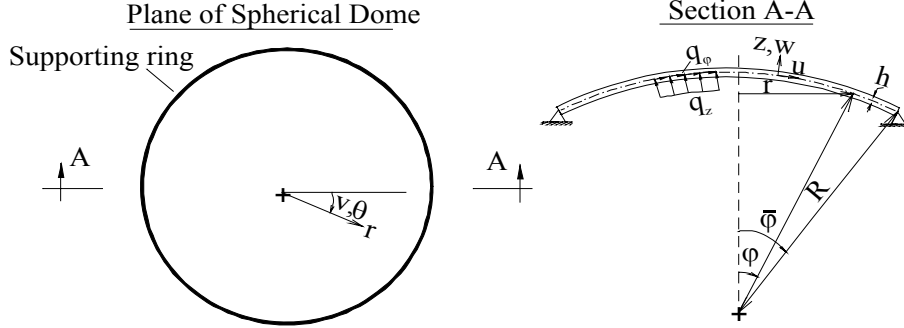
Figure 1. Geometry, loads, and sign conventions.

V is the volume of the dome shell. The virtual work of the external loads is

$$\delta W = -\int_{\theta=0}^{2\pi}\int_{\varphi=0}^{\varphi=\bar{\varphi}}\big[(q_\varphi+\Delta q_\varphi)\delta\Delta u + (q_\theta+\Delta q_\theta)\delta\Delta v + (q_z+\Delta q_z)\delta\Delta w\big]Rr(\varphi)\,d\varphi\,d\theta, \qquad (3)$$

where u, v, and w are the components of the displacement at the reference surface of the dome shell in the φ, θ, and z directions, respectively (see Figure 1); q_φ, q_θ, and q_z are the corresponding load components, R is the radius of curvature of the spherical dome, and $r(\varphi) = R\sin(\varphi)$ is a horizontal coordinate that runs along the radius of the base parallel circle of the dome (see Figure 1).

2.1. *Kinematic relations.* The theoretical model is based on the Kirchhoff–Love hypothesis, for which the strains at any material point (φ, θ, z) are

$$\{\varepsilon(\varphi,\theta,z)\} = \{\bar{\varepsilon}(\varphi,\theta)\} + z\{\kappa(\varphi,\theta)\}, \qquad (4)$$

where $\{\varepsilon\} = \{\varepsilon_{\varphi\varphi}, \varepsilon_{\theta\theta}, \varepsilon_{\varphi\theta}\}^T$ is the strain tensor, and $\{\bar{\varepsilon}\} = \{\bar{\varepsilon}_{\varphi\varphi}, \bar{\varepsilon}_{\theta\theta}, \bar{\varepsilon}_{\varphi\theta}\}^T$ and $\{\kappa\} = \{\kappa_{\varphi\varphi}, \kappa_{\theta\theta}, \kappa_{\varphi\theta}\}^T$ are the nonlinear membrane tensor and the change of curvature tensor of the reference surface, respectively.

Based on Donnell's nonlinear shell theory, the incremental strain-displacement relations which account for initial geometric imperfection ($\hat{w}(\varphi, \theta)$), take the following form (for brevity, the notation of the independent coordinates is omitted):

$$\Delta\bar{\varepsilon}_{\varphi\varphi} = \frac{\Delta u,_\varphi}{R} + \frac{\Delta w}{R} + \frac{1}{2}\left(\frac{\Delta w,_\varphi}{R}\right)^2 + \frac{w,_\varphi\,\Delta w,_\varphi}{R^2} + \frac{\hat{w},_\varphi\,\Delta w,_\varphi}{R^2},$$

$$\Delta\bar{\varepsilon}_{\theta\theta} = \frac{\cos(\varphi)}{r}\Delta u + \frac{\sin(\varphi)}{r}\Delta w + \frac{\Delta v,_\theta}{r} + \frac{1}{2}\left(\frac{\Delta w,_\theta}{r}\right)^2 + \frac{w,_\theta\,\Delta w,_\theta}{r^2} + \frac{\hat{w},_\theta\,\Delta w,_\theta}{r^2},$$

$$\Delta\bar{\varepsilon}_{\varphi\theta} = \frac{\Delta u,_\theta}{r} + \frac{\Delta v,_\varphi}{R} - \frac{\cos(\varphi)}{r}\Delta v + \frac{\Delta w,_\theta\,\Delta w,_\varphi}{rR} + \frac{\Delta w,_\theta\,(w,_\varphi + \hat{w},_\varphi)}{rR} + \frac{\Delta w,_\varphi\,(w,_\theta + \hat{w},_\theta)}{rR}, \qquad (5)$$

$$\Delta\kappa_{\varphi\varphi} = -\frac{\Delta w,_{\varphi\varphi}}{R^2}, \quad \Delta\kappa_{\theta\theta} = -\frac{\cos(\varphi)}{rR}\Delta w,_\varphi - \frac{1}{r^2}\Delta w,_{\theta\theta}, \quad \Delta\kappa_{\varphi\theta} = \frac{2\cos(\varphi)}{r^2}\Delta w,_\theta - \frac{2}{rR}\Delta w,_{\varphi\theta},$$

where ( ),$_\varphi$ and ( ),$_\theta$ denote the derivative with respect to the angular and circumferential coordinates respectively. Note that all the deformations that appear without the Δ operator are actually accumulated known deformations from the previous time step. Also note that the strain-displacement relations presented in Equation (5) are valid only for moderate displacements and rather shallow shells.

2.2. *Equilibrium equations.* The incremental equilibrium equations are formulated using the variational principle of virtual work, (1)–(3), along with the kinematic relations, (4) and (5), and read

$$-(r\,\Delta N_{\varphi\varphi}),_{\varphi} + R\cos(\varphi)\Delta N_{\theta\theta} - (r\,\Delta N_{\varphi\theta}),_{\theta} - rRq_{\varphi} = 0,$$

$$r\,\Delta N_{\varphi\varphi} + R\sin(\varphi)\Delta N_{\theta\theta} - \left(\frac{r}{R}\Delta M_{\varphi\varphi}\right),_{\varphi\varphi} + \left(\cos(\varphi)\Delta M_{\theta\theta}\right),_{\varphi} - \left(\frac{R}{r}\Delta M_{\theta\theta}\right),_{\theta\theta}$$

$$- \left(\frac{2R}{r}\cos(\varphi)\Delta M_{\varphi\theta}\right),_{\theta} - (2\Delta M_{\varphi\theta}),_{\varphi\theta} - \left(\frac{r}{R}(N_{\varphi\varphi}+\Delta N_{\varphi\varphi})\Delta w,_{\varphi}\right),_{\varphi} - \left(\frac{r}{R}\Delta N_{\varphi\varphi}(w,_{\varphi}+\hat{w},_{\varphi})\right),_{\varphi}$$

$$- \left(\frac{R}{r}(N_{\theta\theta}+\Delta N_{\theta\theta})\Delta w,_{\theta}\right),_{\theta} - \left(\frac{R}{r}\Delta N_{\theta\theta}(w,_{\theta}+\hat{w},_{\theta})\right),_{\theta} - \left((N_{\varphi\theta}+\Delta N_{\varphi\theta})\Delta w,_{\theta}\right),_{\varphi}$$

$$- \left(\Delta N_{\varphi\theta}(w,_{\theta}+\hat{w},_{\theta})\right),_{\varphi} - \left((N_{\varphi\theta}+\Delta N_{\varphi\theta})\Delta w,_{\varphi}\right),_{\theta} - \left(\Delta N_{\varphi\theta}(w,_{\varphi}+\hat{w},_{\varphi})\right),_{\theta} - q_{z}rR = 0,$$

$$-(R\,\Delta N_{\theta\theta}),_{\theta} - (r\,\Delta N_{\varphi\theta}),_{\varphi} - R\cos(\varphi)\Delta N_{\varphi\theta} - rRq_{\theta} = 0, \tag{6}$$

with $N_{\varphi\varphi}$, $N_{\theta\theta}$, and $N_{\varphi\theta}$ being the radial, circumferential, and shear forces, respectively; and $M_{\varphi\varphi}$, $M_{\theta\theta}$, and $M_{\varphi\theta}$ are the bending moments.

The boundary conditions, which result from the variational calculus, are

$$krN_{\varphi\varphi} = \bar{N}_{\varphi\varphi} \quad \text{or} \quad u = \bar{u},$$

$$krN_{\varphi\theta} = \bar{N}_{\varphi\theta} \quad \text{or} \quad v = \bar{v},$$

$$k\left[\frac{r}{R}(N_{\varphi\varphi}+\Delta N_{\varphi\varphi})\Delta w,_{\varphi} + \frac{r}{R}\Delta N_{\varphi\varphi}(w,_{\varphi}+\hat{w},_{\varphi}) + \left(\frac{r}{R}M_{\varphi\varphi}\right),_{\varphi}\right.$$

$$\left. - \cos(\varphi)M_{\theta\theta} + (2M_{\theta\theta}),_{\theta} + (N_{\varphi\theta}+\Delta N_{\varphi\theta})\Delta w,_{\theta} + \Delta N_{\varphi\theta}(w,_{\theta}+\hat{w},_{\theta})\right] = \bar{P}_{z} \quad \text{or} \quad w = \bar{w},$$

$$-k\frac{r}{R}M_{\varphi\varphi} = \bar{M}_{\varphi\varphi} \quad \text{or} \quad w,_{\varphi} = \bar{w},_{\varphi}, \tag{7}$$

where $\bar{N}_{\varphi\varphi}$, $\bar{N}_{\varphi\theta}$, $\bar{P}_{z}$, and $\bar{M}_{\varphi\varphi}$ are external loads and bending moments at the boundaries; the over-bar designates prescribed deformations; $k = 1$ where $\varphi = \bar{\varphi}$ and $k = -1$ where $\varphi = 0$.

2.3. *Constitutive relations.* The principle of superposition is adopted here for describing the time-dependent stress-strain relations, which accounts for the aging of the concrete material, as well as, the variation of the internal stresses and the dome's shape in time [Bažant 1988; Gilbert 1988]. Although this approach is more applicable for linear stress-strain relations; in practice, most thin-walled shallow concrete domes are designed to stay in the linear range, and in many cases buckling may occur under this level of stresses where the principle of superposition holds [Zarghamee and Heger 1983]. The study of the creep effects at the materially linear level provides a theoretical basis and a basic understanding for developing more advanced theoretical models that account for the material nonlinearity.

The history integral-type constitutive relations take the form

$$\{\varepsilon(t)\} = \int_{t_o}^{t} J(t,t')[B]\,d\{\sigma(t')\} + \{\varepsilon_{\text{sh}}(t)\} \quad \text{or} \quad \{\sigma(t)\} = \int_{t_o}^{t} \bar{R}(t,t')[B]^{-1}\big(d\{\varepsilon(t')\} - d\{\varepsilon_{\text{sh}}(t')\}\big), \tag{8}$$

where $J(t,t')$ is the compliance or creep function, $\bar{R}(t,t')$ is the relaxation function, ε_{sh} is the shrinkage strain, t_o corresponds to the time at first loading/deforming, and $[B]$ is an elastic matrix that takes the

form

$$[B] = \begin{pmatrix} 1 & -\nu & 0 \\ -\nu & 1 & 0 \\ 0 & 0 & \dfrac{1-\nu}{2} \end{pmatrix}, \tag{9}$$

where ν is Poisson's ratio, which is assumed to be constant with time [Bažant 1988]. It is also assumed that the creep/relaxation function under biaxial loading is similar to the one obtained under uniaxial loading, while the matrix $[B]$ introduces the Poisson's effect [Buyukozturk and Shareef 1985; Bažant 1988].

The governing equations in terms of the unknown deformations (u, v, w) that are based on Equation (8) suffer from the existence of implicit integral expressions, which introduce a major difficulty in their solution. Because of this, an incremental procedure that was first developed by Bažant [1972] for the geometrically linear analysis of concrete structures is adopted and further extended here to the geometrically nonlinear analysis (also see [Bažant 1988]). According to the incremental approach, the time t is subdivided into n_t discrete times with $\Delta t_i = t_i - t_{i-1}$ ($i = 1, 2, \ldots, n_t$). Using the trapezoidal numerical integral rule, the integral constitutive relation presented in (8) is approximated as

$$\{\varepsilon(t_i)\} = J(t_i, t_o)[B]\{\sigma(t_o)\} + \{\varepsilon_{\text{sh}}(t_i)\} + \sum_{s=1}^{i} \left(\frac{J(t_i, t_s) + J(t_i, t_{s-1})}{2} \right)[B]\{\sigma(t_s) - \sigma(t_{s-1})\}. \tag{10}$$

Using the same procedure for the strain at t_{i-1}, the following incremental stress-strain relations are obtained, which present a quasistatic relation with a modulus E'' along with a prescribed incremental strain $\Delta \varepsilon''$ that introduces the effects of the creep and shrinkage into the system

$$\{\Delta \varepsilon(t_i)\} = \frac{1}{E''(t_i)}[B]\{\Delta \sigma(t_i)\} + \{\Delta \varepsilon''(t_i)\} \quad \text{or} \quad \{\Delta \sigma(t_i)\} = E''(t_i)[B]^{-1}\{\Delta \varepsilon(t_i) - \Delta \varepsilon''(t_i)\}, \tag{11}$$

and correspondingly

$$\{\Delta N(t_i)\} = E''(t_i)h[B]^{-1}\{\Delta \bar{\varepsilon}(t_i) - \Delta \tilde{\varepsilon}(t_i)\}, \quad \{\Delta M(t_i)\} = E''(t_i)\frac{h^3}{12}[B]^{-1}\{\Delta \kappa(t_i) - \Delta \tilde{\kappa}(t_i)\}, \tag{12}$$

where $\{\Delta N\} = \{\Delta N_{\varphi\varphi}, \Delta N_{\theta\theta}, \Delta N_{\varphi\theta}\}^T$ and $\{\Delta M\} = \{\Delta M_{\varphi\varphi}, \Delta M_{\theta\theta}, \Delta M_{\varphi\theta}\}^T$, and h is the thickness of the dome shell.

The incremental modulus and incremental strains caused by creep and shrinkage are

$$E''(t_i) = \frac{2}{J(t_i, t_i) + J(t_i, t_{i-1})}, \tag{13}$$

$$\{\Delta \tilde{\varepsilon}(t_i)\} = \left(J(t_i, t_o) - J(t_{i-1}, t_o) \right)[B]\frac{\{N(t_o)\}}{h} + \{\varepsilon_{\text{sh}}(t_i) - \varepsilon_{\text{sh}}(t_{i-1})\}$$

$$+ \sum_{s=1}^{i-1} \left(\frac{J(t_i, t_s) + J(t_i, t_{s-1})}{2} - \frac{J(t_{i-1}, t_s) + J(t_{i-1}, t_{s-1})}{2} \right)[B]\frac{\{N(t_s) - N(t_{s-1})\}}{h}, \tag{14}$$

$$\{\Delta \tilde{\kappa}(t_i)\} = \left(J(t_i, t_o) - J(t_{i-1}, t_o) \right)[B]\frac{\{M(t_o)\}12}{h^3}$$

$$+ \sum_{s=1}^{i-1} \left(\frac{J(t_i, t_s) + J(t_i, t_{s-1})}{2} - \frac{J(t_{i-1}, t_s) + J(t_{i-1}, t_{s-1})}{2} \right)[B]\{M(t_s) - M(t_{s-1})\}\frac{12}{h^3}. \tag{15}$$

2.4. *Governing equations.* The incremental governing equations are formulated by substitution of the incremental constitutive relations, (12)–(15), into the equilibrium equations, (6), noting that terms that include uncoupled functions from the initial state (or previous increment) vanish since they are in equilibrium, and that terms of higher order product of the incremental displacement may be neglected due to the use of sufficiently small increments in time. The incremental governing equations are written in terms of the unknown deformations:

$$\psi_p(\Delta u, \Delta v, \Delta w) = 0, \qquad p = 1, 2, 3, \tag{16}$$

where ψ_p consists of differential operators. For brevity, the explicit form of these equations is not presented here.

This incremental formulation, which is based on the history integral constitutive relation, requires that at each time increment all the preceding values of the stresses and strains that are represented in terms of prescribed strains ($\Delta\tilde{\varepsilon}_{\varphi\varphi}$, $\Delta\tilde{\varepsilon}_{\theta\theta}$, $\Delta\tilde{\kappa}_{\varphi\varphi}$, and $\Delta\tilde{\kappa}_{\theta\theta}$) in (12) must be stored by means of (14) and (15). Despite this, the method is preferred over the incremental differential-type formulation because in the nonlinear case studied here, where the internal stresses may significantly vary with time, the conversion of the constitutive equation of an integral type to one of a differential type using a series expansion (a Dirichlet series for example [Bažant 1988]) is required at each time increment. This procedure is difficult, consuming in computational effort, and in essence only provides an approximation to the compliance function. Moreover, in many cases the use of differential type constitutive relations based on Kelvin or Maxwell chains violate basic thermodynamics laws, where the spring moduli and dashpot viscosities become negative [Bažant and Chern 1984].

2.5. *Time dependent parameters.* In general, the creep and shrinkage characteristics of concrete are highly variable and are never known exactly. There are many theoretical models which aim to predict the time-dependent behaviour of concrete [Bažant 1988; Gilbert 1988]. In this paper, the influences of creep and shrinkage are introduced based on the well-known and commonly used recommendations of [ACI 1982]. The shrinkage strain includes the influences of the drying, autogenous, and carbonation shrinkage. It is assumed here that the shrinkage strain is axisymmetric, and uniform along the meridian of the dome and through its thickness, and takes the following algebraic empirical form:

$$\varepsilon_{\text{sh}}(\varphi, \theta, z, t) = \varepsilon_{\text{sh}}(t) = \frac{t^\beta}{f + t^\beta}\varepsilon_{\text{sh}}^u, \tag{17}$$

where β and f are parameters that control the magnitude of the shrinkage strain, and $\varepsilon_{\text{sh}}^u$ is the final shrinkage strain, at time infinity.

[ACI 1982] recommends the following expression for the creep or compliance function, which includes the effects of basic and drying creep:

$$J(t, t') = \frac{1 + \phi(t, t')}{E(t')}, \tag{18}$$

where $\phi(t, t')$ is the creep coefficient and is evaluated as follows:

$$\phi(t, t') = \left[\frac{(t - t')^\lambda}{d + (t - t')^\lambda}\right]\phi_u(t'). \tag{19}$$

λ and d are wide-range parameters that control the creep coefficient, and the time t and the age of loading t' are measured in days. $\phi_u(t')$, which depends on the age of loading, takes the following form for moist cured concrete:

$$\phi_u(t') = 1.25 \times t'^{(-0.118)} \phi(\infty, 7). \tag{20}$$

$\phi(\infty, 7)$ is the final creep coefficient at time infinity for a load first applied at age 7 days [ACI 1982; AS 3600 2001].

The modulus of elasticity takes the following form [AS 3600 2001]:

$$E(t') = 0.043 \rho^{1.5} \sqrt{f_c(t')} \quad \text{(in MPa)}, \tag{21}$$

where ρ is the concrete mass density (in kg/m^3) and f_c is the time dependent characteristic compressive strength of the concrete (in MPa), which is given by [ACI 1982]

$$f_c(t') = \frac{t'}{\alpha + \gamma\, t'} f_c^{28}, \tag{22}$$

where f_c^{28} is the characteristic compressive strength at 28 days, and α and γ are constants. The above expressions show that the compliance function (18) depends on the age of loading and introduces the effect of aging into the system.

3. Solution procedure

The set of incremental partial differential equations, (16), and their boundary conditions, (7), are reduced to a set of ordinary differential equations by a separation of variables and expansion into truncated Fourier series [Hong and Teng 2002; Sheinman and Jabareen 2005]:

$$\{\Delta u(\varphi, \theta), \Delta v(\varphi, \theta), \Delta w(\varphi, \theta)\} = \sum_{m=0}^{2F} \{\Delta u_m(\varphi), \Delta v_m(\varphi), \Delta w_m(\varphi)\} g_m(\theta), \tag{23}$$

where $F = (F_u, F_v, \text{ or } F_w)$ is the number of terms in the relevant Fourier series. The solution of the initial state (or previous increment), the geometric imperfection, the external load (which can be of any shape and not necessarily axisymmetric), and the incremental initial strains at each time increment that results from creep and shrinkage, take this form:

$$\{u(\varphi, \theta), v(\varphi, \theta), w(\varphi, \theta)\} = \sum_{m=0}^{2F} \{u_m(\varphi), v_m(\varphi), w_m(\varphi)\} g_m(\theta), \tag{24}$$

$$\hat{w}(\varphi, \theta) = \sum_{m=0}^{2F_w} \hat{w}_m(\varphi) g_m(\theta), \tag{25}$$

$$\{q_\varphi(\varphi, \theta), q_\theta(\varphi, \theta), q_z(\varphi, \theta)\} = \sum_{m=0}^{2Fq} \{q_{\varphi m}(\varphi), q_{\theta m}(\varphi), q_{zm}(\varphi)\} g_m(\theta), \tag{26}$$

$$\{\Delta\tilde{\varepsilon}(\varphi, \theta)\} = \sum_{m=0}^{2Fc} \{\Delta\tilde{\varepsilon}_m(\varphi)\} g_m(\theta), \tag{27}$$

$$\{\Delta\tilde{\kappa}(\varphi,\theta)\} = \sum_{m=0}^{2Fc} \{\Delta\tilde{\kappa}_m(\varphi)\}g_m(\theta), \tag{28}$$

where $Fq = (Fq_\varphi, Fq_\theta, \text{ or } Fq_z)$, and $Fc = (Fc_{\varphi\varphi}, Fc_{\varphi\theta}, \text{ or } Fc_{\theta\theta})$ are the number of terms in the relevant Fourier series. The functions $g_m(\theta)$ are

$$g_m(\theta) = \begin{cases} \cos(nm\theta), & m = 0, 1, \dots, F, \\ \sin[n(m-F)\theta], & m = F+1, \dots, 2F, \end{cases} \tag{29}$$

where n is the characteristic circumferential wave number.

Minimization of the errors due to the truncated Fourier series by the Galerkin procedure with trigonometric weighting functions yields the nonlinear ordinary differential equations

$$\Psi_p^m(\varphi) = \oint \psi_p(u,v,w)g_m(\theta)\,d\theta \qquad m = 0, 1, \dots, 2F, \quad p = 1, 2, 3. \tag{30}$$

As $r \to 0$, the solution of the equations becomes singular at the pole (see (6)). In order to prevent this singularity, the strains and change of curvature must remain finite as $r \to 0$. In other words, $\lim_{r\to 0}\{\Delta\bar{\varepsilon}\}$ and $\lim_{r\to 0}\{\Delta\kappa\}$ must be finite. Following Gould [1988], and noting that $n \geq 4$ based on Donnell's theory, these requirements, which are treated by the aid of l'Hospital's rule, yields the following boundary conditions at the pole:

For $m = 0$ (axisymmetric):

$$u = 0, \qquad v = 0, \qquad w,_\varphi = 0, \tag{31}$$

$$\frac{r}{R}(N_{\varphi\varphi} + \Delta N_{\varphi\varphi})\Delta w,_\varphi + \frac{r}{R}\Delta N_{\varphi\varphi}(w,_\varphi + \hat{w},_\varphi) + \left(\frac{r}{R}M_{\varphi\varphi}\right),_\varphi$$
$$- \cos(\varphi)M_{\theta\theta} + (2M_{\theta\theta}),_\theta + (N_{\varphi\theta} + \Delta N_{\varphi\theta})\Delta w,_\theta + \Delta N_{\varphi\theta}(w,_\theta + \hat{w},_\theta) = 0. \tag{32}$$

For $m \geq 1$ (nonaxisymmetric):

$$u = 0, \qquad v = 0, \qquad w = 0, \qquad w,_\varphi = 0. \tag{33}$$

Equations (31)–(33) impose the boundary conditions at the dome's pole only, while the actual boundary conditions at the edge of the dome are defined or generated via (7).

The solution of the coupled governing equations and the boundary conditions in the meridional direction is conducted via the multiple shooting numerical method [Stoer and Bulirsch 2002]. In order to account for the possible bifurcation and mode-switching (secondary bifurcation) behaviours of the dome, the load-disturbance method is used. In this method, very small nonaxisymmetric loads in selected harmonics are added to the axisymmetric loads to guide the structure into the new equilibrium mode (see [Teng and Hong 2006] for more details). The analysis is conducted up to a certain time (the ultimate time) where the rate of deformation of the system begins to increase rapidly and becomes infinite or when the deformations exceed prescribed limits [Murakami and Tanaka 1976; Miyazaki 1986]. The development of bifurcation points through the time response, which may or may not result in instantaneous loss of load carrying capacity [Obrecht 1977], is accounted for as an automatic outcome of the full nonlinear analysis combined with the load disturbance method, rather than by performing a perturbation analysis. In order to account for the rapid increase of the deformations rate at certain points, to consider the fact that the

rate of creep is higher at the early ages of loading, and to account for gradually increasing loadings, the time step was kept relatively small and almost constant through the entire analysis. However, at certain points or time domains, a reduction of the time step is required, and in other cases, an increase is allowed. In this paper, user intervention was used when necessary. The appropriate time step for a given loading is selected so that the difference between the ultimate times based on the selected time step and one-half of this step is of minor significance [Kao 1981].

4. Numerical study

The geometry of the examined dome, which is loaded by an axisymmetric vertical load, is given in Figure 2a. The boundary conditions at the edge are $u = v = w = M_{\varphi\varphi} = 0$, which are derived via (7), while the conditions at the pole are given by (31)–(33). The characteristic compressive strength and modulus of elasticity of the concrete (N32) are taken as 32 MPa and 28.6 GPa respectively [AS 3600 2001], with a Poisson's ratio of 0.15, and a mass density of $\rho = 2400\,\text{kg/m}^3$. Note that the mass density is given for the determination of the time-dependent modulus of elasticity through (21) and for the determination of the dead load, but not for any dynamic effects. Based on the recommendations of [ACI 1982; Gilbert 1988], the following values are adopted for the parameters that control the long-term behaviour: $\beta = 1$, $f = 35$, $\varepsilon_{\text{sh}}^u = -780\,\mu\varepsilon$, $\lambda = 0.6$, $d = 10$ days, $\phi(\infty, 7) = 2.35$, $\alpha = 4$, and $\gamma = 0.85$. Note that the radial and perpendicular components of the vertical load are considered in the analysis, which become nonuniform and depend upon the radial coordinate.

4.1. *Short-term behaviour.* For reference, the short-term behaviour of the perfect shallow dome is studied first in Figure 2b and Figure 2c using the characteristic modulus of elasticity. The governing equations for the short-term analysis can be easily generated from (6) by dropping all the terms that are related to the response at the previous increment, and by dropping the Δ operator. These equations are not incremental ones, in which the solution at each load level can be obtained by a straightforward procedure using the arc-length continuation technique [Sundararajan and Noah 1997]. The normalized equilibrium path, Figure 2b, shows that the shallow dome is characterized by a limit-point type of behaviour with no bifurcation point observed at the examined range of displacements. Yet, examining a wider range of displacements
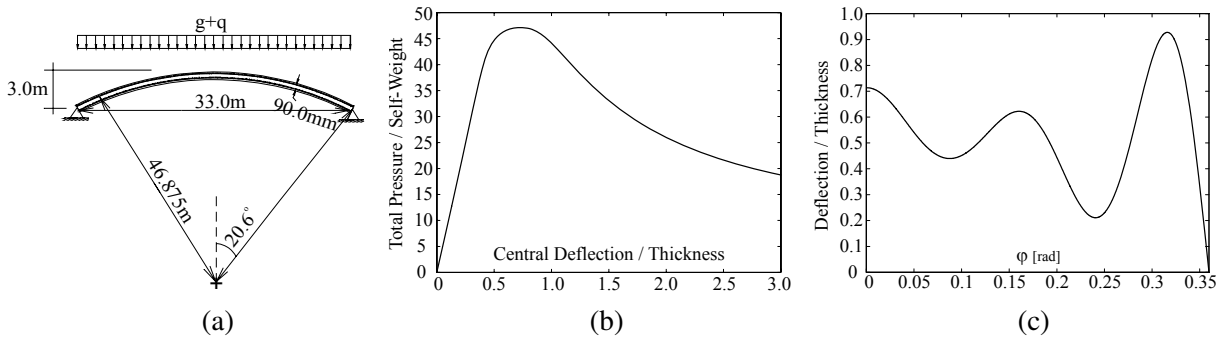
Figure 2. Numerical example: (a) geometry of a shallow dome; (b) short-term loading equilibrium path; (c) axisymmetric buckling mode.

may reveal primary and secondary bifurcation points in the postbuckling range. Nevertheless, the post-buckling behaviour of thin walled concrete structures is of little concern in most practical cases because of the brittleness of the concrete material and its very limited ability to undergo a snap-through behaviour, which is associated with dynamic effects and relatively high tensile and compressive strains [Gioncu 1979]. In general, however, perfect shallow domes under axisymmetric loading may exhibit bifurcation points that may appear before or after the limit point. This depends on many parameters including the radius/thickness ratio, the rise/(base diameter) ratio, the boundary conditions, the loading pattern (radial or vertical), and others. In the case studied here, the buckling mode, which is an axisymmetric one, appears in Figure 2c.

As can be seen in Figure 2b, the vertical buckling pressure of the dome equals 47 times its self-weight and the displacement at this point is approximately 0.72 of the thickness of the dome shell. Though the buckling pressure could be very conservative for design purposes, considering the fact that the buckling pressure of imperfect domes could be 50% that of the perfect one [Zarghamee and Heger 1983], and the fact that many concrete domes are subjected to snow loads of the same level of magnitudes as their self-weight, the actual buckling pressure could be as low as 12 times the actual weight of the dome. When the long-term effects of creep and shrinkage are considered, this value could be even much lower as shown subsequently.

Using the classical theoretical value for the buckling pressure [Billington 1982],

$$q_{cr} = CE\left(\frac{h}{R}\right)^2, \tag{34}$$

where $C = 2/\sqrt{3(1 - \nu^2)}$, the classical buckling pressure of the dome becomes 57 times its self-weight, which is 19% higher than the one obtained in Figure 2b. The differences are because (34) is based on the linear stability approach that does not account for the nonlinear prebuckling deformations, and because it is appropriate for complete spherical shells and not shallow ones. Also, note that (34) is valid for radial loading only; yet, this result provides a level of verification to the proposed model.

4.2. *Imperfection scenarios.* Three different imperfection scenarios that characterize shell structures in general and concrete shells in particular are considered. The first scenario is a case where the imperfection is of the form of the critical buckling mode under axisymmetric loading. Such a scenario is typical for the sensitivity study of shell structures and is recommended by many design codes [Xirouchakis and Jones 1980; Hong and Teng 2008]; thus

$$\hat{w}(\varphi) = \xi h \times \text{buckling mode}, \tag{35}$$

where ξ is the imperfection amplitude, and the buckling mode is plotted in Figure 2c.

The second imperfection scenario, which is almost impossible to be avoided in concrete structures but is also typical to any other structure, results from inaccuracies in the construction process that may lead to small departures from sphericity. A nonaxisymmetric geometric imperfection of the following shape is considered [Kao 1981]:

$$\hat{w}(\varphi, \theta) = \xi h \times \left(1 - \left(\frac{\sin(\varphi)}{\sin(\bar{\varphi})}\right)^2\right)^3 \cos(n\theta). \tag{36}$$

The third imperfection scenario is more unique to concrete domes, and accounts for the potential varying stiffness of the dome in the circumferential direction. Such varying stiffness may result from preloading shrinkage cracks that are parallel to the meridians direction and result from tensioning in the circumferential direction, from a nonuniform thickness of the dome due to construction inaccuracies, or from nonuniform material moduli. The varying stiffness of the dome is introduced here through a symmetrically reduced effective thickness that sinusoidally varies in the circumferential direction (where the combined extensional-bending rigidity is zero) and takes the form

$$h(\theta) = \left(1 - \frac{\xi}{2}\right)h_o + \frac{1}{2}\xi h_o \cos(n\theta). \tag{37}$$

Here, h_o is the nominal (designed) thickness of the dome shell, and ξ corresponds to the reduction factor of the membrane rigidity. Mathematically, this imperfection is also treated using the truncated Fourier series as was shown in Equations (24)–(29). Thus, the thickness profile of the dome becomes

$$h(\varphi, \theta) = \sum_{m=0}^{2F_h} h_m(\varphi)g_m(\theta), \tag{38}$$

where F_h is the number of terms in the Fourier series, and $h_m(\varphi)$ is a constant function in the case studied here in the meridional direction; yet it varies with the corresponding Fourier term (see Equation (37)), while $g_m(\theta)$ introduces the variation in the circumferential direction.

Note that other imperfection scenarios than those examined here may lead to different and even greater drop of the critical load; see for example [Zarghamee and Heger 1983; Błachut and Galletly 1990; 1995]. Yet, this aspect is not investigated here. Nevertheless, using the proposed model, many imperfection scenarios can be studied.

The short-term behaviour of imperfect domes was extensively studied in many research works including the development of theoretical models and numerical tools for their analysis; see for example [Muc 1992; Błachut and Galletly 1990; 1995; Teng and Song 2001; Wunderlich and Albertin 2002]. Therefore, for brevity and clarity, and in order to focus on the goals of this paper, the short-term behaviour of imperfect domes is not presented here.

4.3. *Long-term behaviour of imperfect dome.* The long term behaviour under the three imperfection scenarios described above is studied here. In practice, structures are seldom fully loaded at one time, and the loading process usually takes hours and sometimes even days. In this sense, a gradually loading history, which is presented in Figure 3, is considered. For this, the dome is first loaded at age of 7 days by its self-weight, followed by a linearly increasing load at the age of 28 days for a period of one week to reach a magnitude of 50% of its vertical buckling pressure ($23.5\times$ self-weight). The load is then held constant. In the following discussion, the time is measured from the age of first loading when the age of the concrete is 7 days, assuming that the structure is fully supported during the first 7 days for curing. The behaviour at $t = 0$ actually corresponds to the instantaneous response of the dome to its self weight without any long-term effects. Because the stresses induced by shrinkage prior loading depends on the supporting scheme before loading and thus on the construction technique, these stresses are ignored before the time of first loading (that is, shrinkage is taken to commence at $t = 0$).

First imperfection scenario: axisymmetric. The variation of the peak perpendicular deflection (observed at $\varphi = 0.316$ rad (18.1°) according to Figure 2c) with time is shown in Figure 4 for the case where the dome is loaded according to Figure 3 and with an axisymmetric imperfection according to the buckling mode as given by Equation (35) and Figure 2c. Different values for the imperfection amplitude ξ are examined; the response with $\xi = 0$ corresponds to the perfect dome. The results reveal that the ultimate time for creep buckling of the perfect dome, where the rate of deformation of the system begins to increase rapidly and becomes infinite, equals 206 days. In reality, at this point the system tends to snap toward a far more stable equilibrium position with a potential development of circumferential nonaxisymmetric deformations. Yet, due to the brittleness and the limited deformability of the concrete material, the dome will generally collapse at the ultimate time once the deformations become large, and does not exhibit a snap through behaviour [Gioncu 1979].

The results presented in Figure 4 show that the ultimate time significantly decreases with the increase of the imperfection amplitude. Thus, thin-walled concrete domes are very sensitive to the existence of geometric imperfections. Despite the use of the load-disturbance method, which allows for the development of bifurcation points and mode switching, no bifurcation point is observed here and the deformation
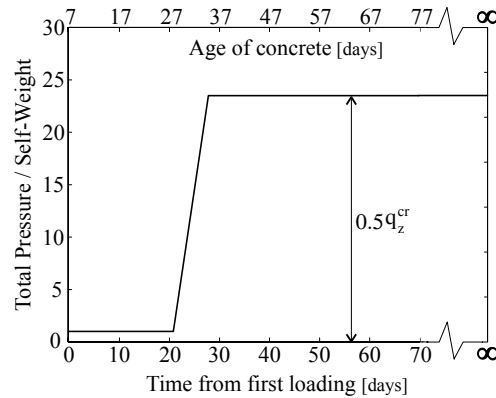
Figure 3. Loading history.
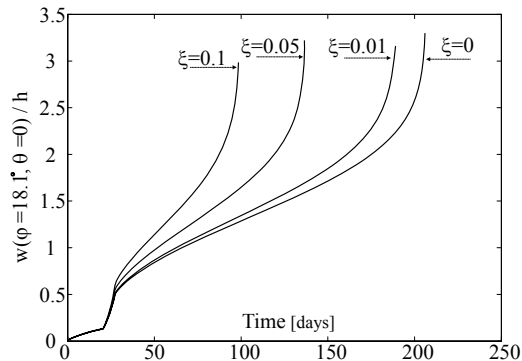
Figure 4. Axisymmetric imperfection: variation in time of peak deflection with different imperfection amplitudes of the buckling mode.

pattern of the dome remains axisymmetric through the entire time domain. The nonlinear sensitivity of the dome to small imperfections indicates the importance of considering these effects through detailed and comprehensive computational models.

Note that with $\xi = 0$, for instance, the rapid increase of the deflection at $t < 50$ days results from the gradual loading and from the nature of creep of the concrete material, which is higher in the first few days after loading. On the other hand, the rapid increase at $t > 180$ days results from the geometric nonlinearity. Comparing the long-term limit deflections that develop at the ultimate time with the short-term limit deflections obtained in Figure 2, it can be seen that the peak deflections develop under a sustained pressure that is half of the vertical buckling pressure are about three times the peak deflections that develop under the full short-term vertical buckling pressure. The normalized peak deflection at $\varphi = 18.1°$ obtained in Figure 2c is 0.93, while the level of normalized deflection in which buckling starts in Figure 4 equals 3.2. Thus, while under short-term loading the structure loses its stability by a combination of large forces and relatively moderate deflections, under sustained load, the structure loses its stability by a combination of moderate forces and relatively large deflections that result from creep and nonlinear coupling as well.

Second imperfection scenario: nonaxisymmetric. The time-dependent behaviour of the dome under the loading history described in Figure 3 and with a nonaxisymmetric imperfection according to Equation (36) is shown in Figure 5 for different imperfection amplitudes. The results show that the amplitude of the nonaxisymmetric imperfection significantly affects the time-dependent behaviour of the dome and should be considered in their design. The response with $\xi = 0.05$ and $\xi = 0.1$ reveals a sudden change in the slope of the curve at certain points, that is, $t = 162$ days and 92 days respectively. These points are considered as critical points, in which the deformation at $\varphi = 18.1°$ sharply increases and becomes affected by nonaxisymmetric deformations. To clarify this, consider Equation (23), which indicates that the total solution is obtained by a summation of the effects of different Fourier harmonics. Figure 6 shows the ratio between the axisymmetric term of the solution w_0 (obtained with $m = 0$) and the total solution. The results show that with $\xi = 0.05$ this ratio is very close to 1 up to $t = 162$ days. At this point, this ratio jumps to 1.12, which reflects a negative contribution of the higher Fourier harmonics on the deflection at $\varphi = 18.1°$ and $\theta = 45°$. A similar behaviour is observed at $t = 92$ days with $\xi = 0.1$.

Because in general, bifurcation or fork points do not necessarily mean a failure of the structure [Obrecht 1977], the effect of these critical points at a different location ($\varphi = 8.0°$ and $\theta = 0$) is examined in Figure 7. The results show that the deflection becomes very large beyond these critical points. Such a level of deflections in concrete structures, which is of the order of 5 to 9 times the thickness of the dome, definitely leads to failure of the structure, and so the critical points observed here can be considered as points that cause creep buckling and failure of the dome. The results presented in Figures 5 and 7 show that in order to identify these *critical* points in a full nonlinear analysis, the deformation-time curve should be examined at multiple points along the surface of the dome. Another approach for identifying these critical points is by using energy methods as proposed by Murakami and Tanaka [1976] and Miyazaki [1986]; yet it is not considered here.

For completeness and clarity, the behaviour of the dome at three different times (namely: $t = 28$, $t = 150$, and $t = 180$ days) obtained with $\xi = 0.05$ is depicted in Figure 8. The behaviour at $t = 28$ days corresponds to the response immediately after the gradual loading, and the behaviours at $t = 150$ and
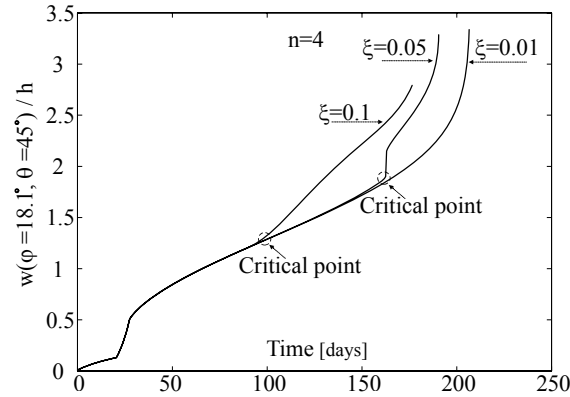
Figure 5. Nonaxisymmetric imperfection with $n = 4$ (scenario 2): variation in time of selected deflection with different imperfection amplitudes.
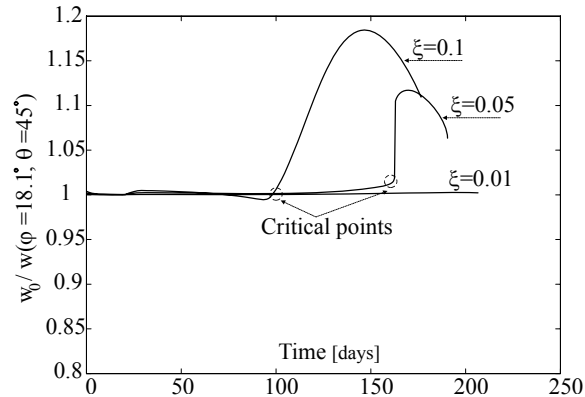
Figure 6. Nonaxisymmetric imperfection (scenario 2): ratio between the axisymmetric term and total solution.
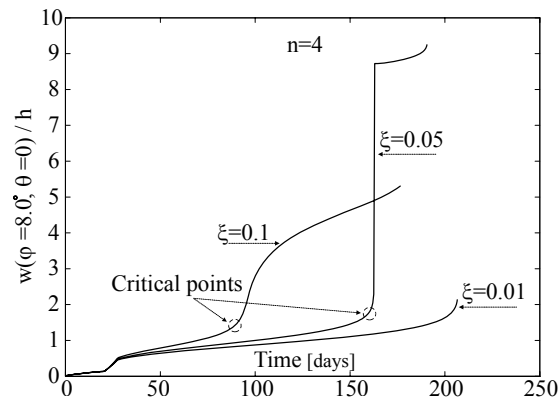
Figure 7. Nonaxisymmetric imperfection with $n = 4$ (scenario 2): variation in time of peak deflection with different imperfection amplitudes.

180 days correspond to the response before and after the critical point. Figure 8 shows that the time-dependent effects significantly increase and modify the distribution of the perpendicular deformations and internal forces. The distribution in the circumferential direction is governed by the characteristic circumferential wave number of the imposed imperfection, which equals 4. Figure 8b shows that at $t = 28$ days, the ratio between the deflection at any given circumferential angle θ to that at $\theta = 0$ is close to 1.0. However, this ratio decreases in time and becomes almost 0.05 at $t = 180$ days, which reflects the effect of the nonaxisymmetric harmonics on the overall response. It is also seen that the internal forces become relatively large at $t = 180$ days, and specifically, the circumferential forces change from compression to tension in some locations. These tension forces cause cracking and eventually initiate the failure of the dome. Finally, note that due to the geometric nonlinearity and the combined action of creep and shrinkage, and their interaction, the location of the peak response varies along the meridian (Figures 8a, 8c, and 8e). These effects highlight the need to use detailed theoretical models for the nonlinear long-term analysis of concrete domes.

The effect of the characteristic circumferential wave number n on the response of the dome is studied in Figure 9 for the nonaxisymmetric geometric imperfection given by (36) with $\xi = 0.05$. In order to approximately identify the ultimate time for creep buckling failure, the variation of the deflection at two critical locations is plotted. Figure 9a shows that with $n = 6$, a critical point develops at around $t = 65$ days compared to 162 days with $n = 4$, and Figure 9b shows that a critical point with $n = 5$ develops at $t = 130$ days. As discussed earlier, these critical points, which are associated with relatively large deformations, are considered as failure points in concrete structures, and so the long-term behaviour and ultimate time of shallow concrete domes are also affected by the characteristic wave number.
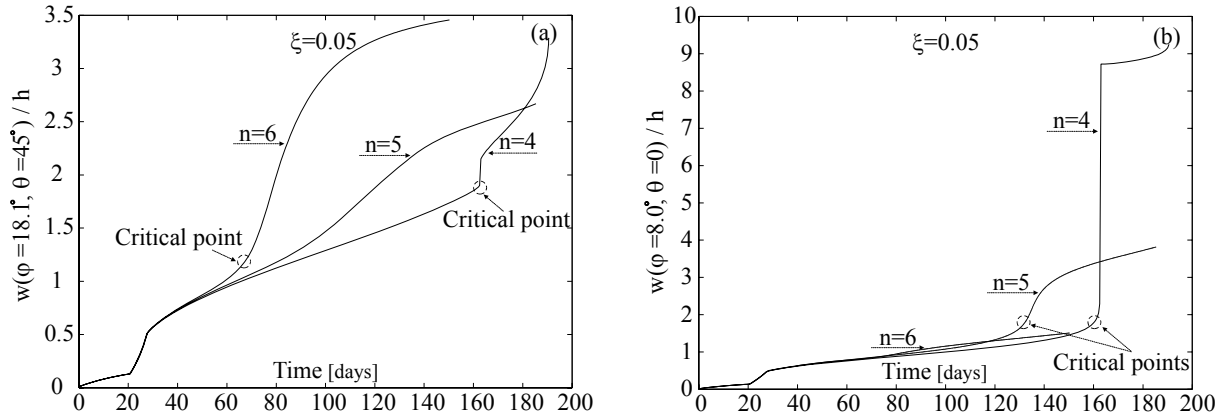
Third imperfection scenario: variable stiffness. Figure 10 shows the effect of sinusoidally varying stiffness according to (37). Different magnitudes of the imperfection parameter (ξ, the reduction factor of the membrane rigidity) and the circumferential wave number n are examined. The results show that relatively small reductions in the effective thickness of the dome and the corresponding membrane and bending rigidities significantly decrease the ultimate time for creep buckling of the dome. It is also seen that the characteristic circumferential wave number in this case significantly and nonlinearly affects the nonlinear creep behaviour of the dome. These effects play important roles in the structural behaviour of thin-walled concrete domes, and should be carefully considered in their design.

5. Conclusions

The creep buckling behaviour of thin-walled imperfect shallow concrete domes has been studied and some of the main aspects that characterize their behaviour have been revealed and clarified. This has been achieved by the development of a theoretical model for their nonlinear long-term analysis. The variational principle of virtual work and the principle of superposition, which accounts for the aging of the concrete material and the variation of stresses and geometry of the dome in time, have been used for the derivation of the governing equations. An incremental time-stepping approach has been used for the solution in time, while the truncated Fourier series and the multiple shooting method have been used for the solution in space allowing for different boundary conditions, loading schemes, and imperfection scenarios.
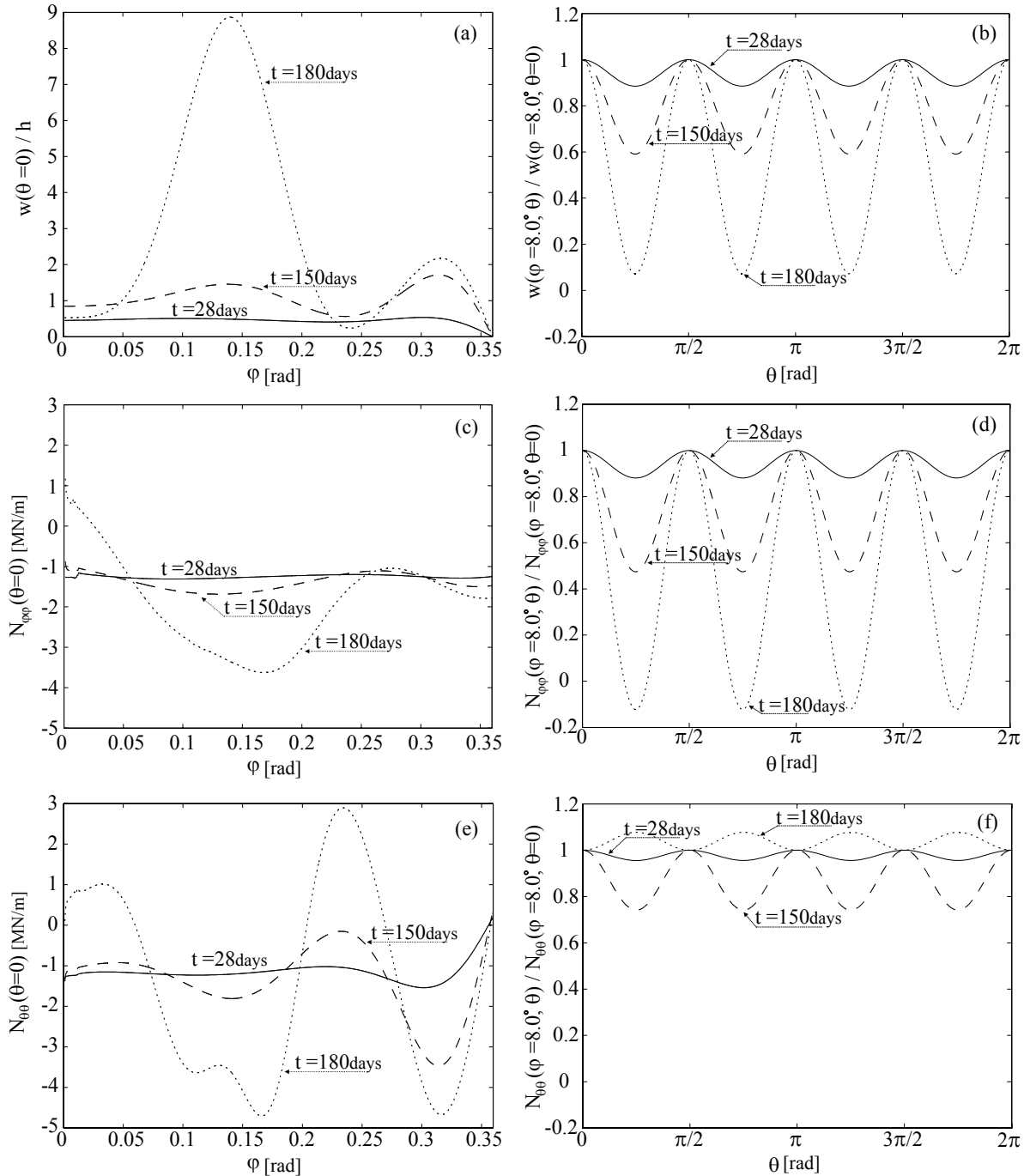
Figure 8. Structural response at three different times of a dome with nonaxisymmetric geometric imperfection ($\xi = 0.05$, $n = 4$): (a, b) perpendicular deformation; (c, d) radial force; (e, f) circumferential force. Solid line: $t = 28$ days; dashed line: $t = 150$ days; dotted line: $t = 180$ days.

Figure 9. Behaviour in time under nonaxisymmetric imperfection (scenario 2) with $\zeta = 0.05$ and different circumferential wave numbers: (a) deflection at $\varphi = 18.1°$ and $\theta = 45$; (b) deflection at $\varphi = 8.0°$ and $\theta = 0$.
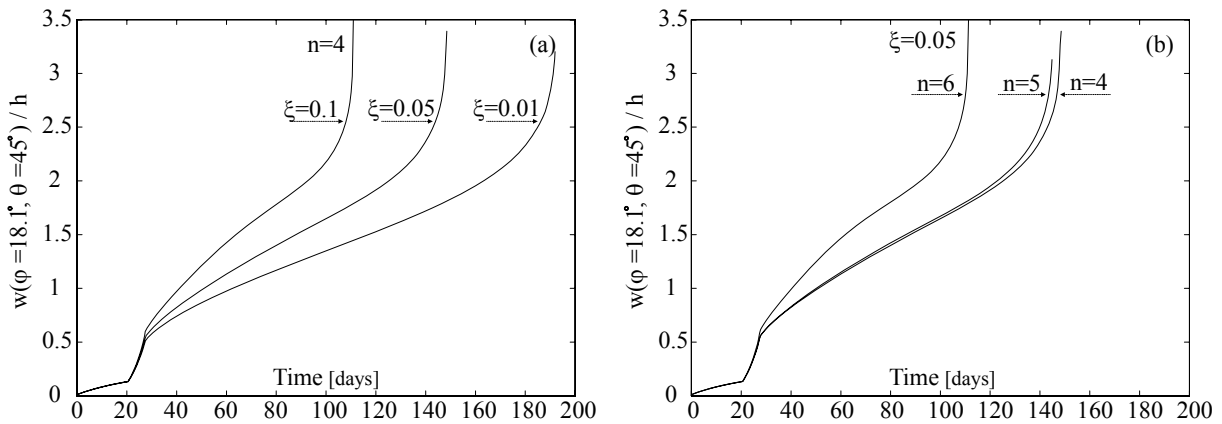
Figure 10. Varying stiffness imperfection (scenario 3): (a) variation in time of peak deflection with $n = 4$ and different imperfection amplitudes; (b) variation in time of peak deflection with $\zeta = 0.05$ and different circumferential wave numbers.

Since the geometric imperfection in a dome to be constructed is not known at the design stage, both the form and the amplitude of the expected imperfection have been considered in the numerical study including an imperfection case that approximately simulates the effect of varying rigidities due to radial preloading shrinkage cracks or other construction inaccuracies, which are unique to domes made of concrete. It has been quantitatively shown that small departures from sphericity and the potential varying rigidities of the dome in the circumferential direction, significantly affect the long-term nonlinear behaviour and structural safety of shallow spherical concrete domes. Both the shape and amplitude of the imperfection have affected the behaviour and led to significant reductions in the ultimate time for creep buckling. Because in reality such imperfections cannot be avoided and are more prominent in concrete structures in general, and in curved concrete members in particular, a reliable prediction of the

imperfection effects is required. In addition, more imperfection scenarios than those examined in this paper should be considered for a detailed design of shallow concrete domes.

This paper contributes to the establishment of a foundation of theoretical knowledge required for long-term reliable analysis, effective design, and safe use of shallow concrete domes and general thin-walled concrete structures considering their potential imperfect shape. The results presented here show that the long-term effects of creep and shrinkage have a critical effect on the safety and the design life of shallow concrete domes. Finally, the modelling concepts and numerical tools and algorithms developed here can be further enhanced and generalized for the nonlinear long-term analysis of general thin-walled concrete structures, while the material nonlinearity and the development of a perturbation analysis for the characterization of bifurcation points are also considered for future research work.

References

[ACI 1982] ACI Committee 209, "Prediction of creep, shrinkage, and temperature effects in concrete structures", ACI Committee Report 209R-82, American Concrete Institute, Detroit, MI, 1982.

[Arbabi-Kanjoori and Leonard 1979] F. Arbabi-Kanjoori and J. Leonard, "Creep of non-symmetrically loaded shells of revolution", *Eng. Struct.* **1**:3 (1979), 145–152.

[Arnold et al. 1989] S. M. Arnold, D. N. Robinson, and A. F. Saleeb, "Creep buckling of cylindrical shell under variable loading", *J. Eng. Mech.* (*ASCE*) **115**:5 (1989), 1054–1074.

[AS 3600 2001] *Concrete structures*, 3rd ed., Australian Standard **AS 3600-2001**, The Association, Homebush, NSW, 2001.

[Bažant 1972] Z. P. Bažant, "Numerical determination of long-range stress history from strain history in concrete", *Mater. Struct.* **5**:3 (1972), 135–141.

[Bažant 1987] Z. P. Bažant, "Limitations of strain-hardening model for concrete creep", *Cem. Concr. Res.* **17**:3 (1987), 505–509.

[Bažant 1988] Z. P. Bažant, *Mathematical modeling of creep and shrinkage of concrete*, Wiley, New York, 1988.

[Bažant and Chern 1984] Z. P. Bažant and J.-C. Chern, "Rate-type concrete creep law with reduced time", *J. Eng. Mech.* (*ASCE*) **110**:3 (1984), 329–340.

[Billington 1982] D. P. Billington, *Thin shell concrete structures*, McGraw-Hill, New-York, 1982.

[Błachut and Galletly 1990] J. Błachut and G. D. Galletly, "Buckling strength of imperfect spherical caps: some remarks", *AIAA J.* **28**:7 (1990), 1317–1319.

[Błachut and Galletly 1995] J. Błachut and G. D. Galletly, "Buckling strength of imperfect steel hemispheres", *Thin-Walled Struct.* **23**:1–4 (1995), 1–20.

[Bockhold and Petryna 2008] J. Bockhold and Y. S. Petryna, "Creep influence on buckling resistance of reinforced concrete shells", *Comput. Struct.* **86**:7–8 (2008), 702–713.

[Bushnell 1976] D. Bushnell, "BOSOR5: program for buckling of elastic-plastic complex shells of revolution including large deflections and creep", *Comput. Struct.* **6**:3 (1976), 221–239.

[Bushnell 1977] D. Bushnell, "A strategy for the solution of problems involving large deflections, plasticity and creep", *Int. J. Numer. Methods Eng.* **11**:4 (1977), 683–708.

[Buyukozturk and Shareef 1985] O. Buyukozturk and S. S. Shareef, "Constitutive modeling of concrete in finite element analysis", *Comput. Struct.* **21**:3 (1985), 581–610.

[DPW NSW 1978] Department of Public Works, New South Wales, *Construction of Binishell reinforced concrete domes: New South Wales, Australia*, DPW, Sydney, 1978.

[Dulácska and Kollár 1995] E. Dulácska and L. Kollár, "Design procedure for the buckling analysis of reinforced concrete shells", *Thin-Walled Struct.* **23**:1–4 (1995), 313–321.

[Gilbert 1988] R. I. Gilbert, *Time effects in concrete structures*, Elsevier, Amsterdam, 1988.

[Gioncu 1979] V. Gioncu, *Thin reinforced concrete shells: special analysis problems*, Wiley, Chichester, 1979.

[Gould 1988] P. L. Gould, *Analysis of shells and plates*, Springer, New York, 1988.

[Grigolyuk and Lopanitsyn 2003] E. I. Grigolyuk and Y. A. Lopanitsyn, "The non-axisymmetric postbuckling behaviour of shallow spherical domes", *J. Appl. Math. Mech.* **67**:6 (2003), 809–818.

[Hamed et al. 2008] E. Hamed, M. A. Bradford, and R. I. Gilbert, "Effects of boundary conditions on the non-linear long-term behaviour of spherical shallow concrete domes", in *Proceedings of the 6th International Conference on Computation of Shell and Spatial Structures* (*IASS-IACM 2008*)*: Spanning nano to mega* (Ithaca, NY, 2008), edited by J. F. Abel and J. R. Cooke, Cornell University, Ithaca, NY, 2008. CD-ROM.

[Hamed et al. 2009a] E. Hamed, M. A. Bradford, and R. I. Gilbert, "Nonlinear time-dependent behaviour of spherical shallow concrete domes: shallowness effect", pp. 823–827 in *Futures in mechanics of structures and materials: proceedings of the 20th Australasian Conference on the Mechanics of Structures and Materials* (*ACMSM20*) (Toowoomba, 2008), edited by T. Aravinthan et al., CRC, Boca Raton, FL, 2009.

[Hamed et al. 2009b] E. Hamed, M. A. Bradford, and R. I. Gilbert, "Time-dependent and thermal behaviour of spherical shallow concrete domes", *Eng. Struct.* **31**:9 (2009), 1919–1929.

[Hamed et al. 2010] E. Hamed, M. A. Bradford, and R. I. Gilbert, "Nonlinear long-term behaviour of spherical shallow thin-walled concrete shells of revolution", *Int. J. Solids Struct.* **47**:2 (2010), 204–215.

[Hoff 1968] N. J. Hoff, "Axially symmetric creep buckling of circular cylindrical shells in axial compression", *J. Appl. Mech.* (*ASME*) **35**:3 (1968), 530–538.

[Hong and Teng 2002] T. Hong and J. G. Teng, "Non-linear analysis of shells of revolution under arbitrary loads", *Comput. Struct.* **80**:18–19 (2002), 1547–1568.

[Hong and Teng 2008] T. Hong and J. G. Teng, "Imperfection sensitivity and postbuckling analysis of elastic shells of revolution", *Thin-Walled Struct.* **46**:12 (2008), 1338–1350.

[Huang 1965] N. C. Huang, "Axisymmetrical creep buckling of clamped shallow spherical shells", *J. Appl. Mech.* (*ASME*) **32**:2 (1965), 323–330.

[Kao 1981] R. Kao, "Nonlinear creep buckling analysis of initially imperfect shallow spherical shells", *Comput. Struct.* **14**:1–2 (1981), 111–122.

[Litle et al. 1970] W. A. Litle, F. J. Forcier, and P. H. Griggs, "Can plastic models represent the buckling behavior of reinforced concrete shells?", pp. 265–288 in *Models for concrete structures*, ACI Special Publication **24**, American Concrete Institute, Detroit, MI, 1970.

[Marcinowski 2007] J. Marcinowski, "Stability of relatively deep segments of spherical shells loaded by external pressure", *Thin-Walled Struct.* **45**:10–11 (2007), 906–910.

[Minahen and Knauss 1993] T. M. Minahen and W. G. Knauss, "Creep buckling of viscoelastic structures", *Int. J. Solids Struct.* **30**:8 (1993), 1075–1092.

[Miyazaki 1986] N. Miyazaki, "On the finite element formulation of bifurcation mode of creep buckling of axisymmetric shells", *Comput. Struct.* **23**:3 (1986), 357–363.

[Miyazaki et al. 1991] N. Miyazaki, S. Hagihara, and T. Munakata, "Creep buckling under varying loads", *J. Pressure Vessel Technol.* (*ASME*) **113**:1 (1991), 41–45.

[Moncarz et al. 2007] P. D. Moncarz, M. Griffith, and P. Noakowski, "Collapse of a reinforced concrete dome in a wastewater treatment plant digester tank", *J. Perform. Constr. Facil.* (*ASCE*) **21**:1 (2007), 4–12.

[Muc 1992] A. Muc, "On the buckling of composite shells of revolution under external pressure", *Compos. Struct.* **21**:2 (1992), 107–119.

[Murakami and Tanaka 1976] S. Murakami and E. Tanaka, "On the creep buckling of circular cylindrical shells", *Int. J. Mech. Sci.* **18**:4 (1976), 185–194.

[Obrecht 1977] H. Obrecht, "Creep buckling and postbuckling of circular cylindrical shells under axial compression", *Int. J. Solids Struct.* **13**:4 (1977), 337—355.

[Reissner 1946] E. Reissner, "Stresses and small displacements of shallow spherical shells", *J. Math. Phys.* (*MIT*) **25** (1946), 80–85 and 279–300.

[Sheinman 1981] I. Sheinman, "Application of DSISR program to recessed shells of revolution", *Comput. Struct.* **14**:5–6 (1981), 361–368.

[Sheinman and Jabareen 2005] I. Sheinman and M. Jabareen, "Postbuckling of laminated cylindrical shells in different formulations", *AIAA J.* **43**:5 (2005), 1117–1123.

[Shi et al. 1970] J. J. J. Shi, C. D. Johnson, and N. R. Bauld, Jr., "Application of the variational theorem for creep of shallow spherical shells", *AIAA J.* **8**:3 (1970), 469–476.

[Stoer and Bulirsch 2002] J. Stoer and R. Bulirsch, *Introduction to numerical analysis*, 3rd ed., Texts in Applied Mathematics **12**, Springer, New York, 2002.

[Sundararajan and Noah 1997] P. Sundararajan and S. T. Noah, "Dynamics of forced nonlinear systems using shooting/arc-length continuation method: application to rotor systems", *J. Vib. Acoust.* (*ASME*) **119**:1 (1997), 9–20.

[Takeuchi et al. 2004] H. Takeuchi, S. Taketomi, S. Samukawa, and A. Nanni, "Renovation of concrete water tank in Chiba prefecture, Japan", *Pract. Period. Struct. Des. Constr.* **9**:4 (2004), 237–241.

[Teng and Hong 2006] J. G. Teng and T. Hong, "Postbuckling analysis of elastic shells of revolution considering mode switching and interaction", *Int. J. Solids Struct.* **43**:3–4 (2006), 551–568.

[Teng and Lou 1997] J. G. Teng and Y. F. Lou, "Post-collapse bifurcation analysis of shells of revolution by the accumulated arc-length method", *Int. J. Numer. Methods Eng.* **40**:13 (1997), 2369–2383.

[Teng and Rotter 1992] J. G. Teng and J. M. Rotter, "Geometrically and materially nonlinear analysis of reinforced concrete shells of revolution", *Comput. Struct.* **42**:3 (1992), 327–340.

[Teng and Song 2001] J. G. Teng and C. Y. Song, "Numerical models for nonlinear analysis of elastic shells with eigenmode-affine imperfections", *Int. J. Solids Struct.* **38**:18 (2001), 3263–3280.

[Vandepitte and Lagae 1986] D. Vandepitte and G. Lagae, "Buckling of spherical domes made of microconcrete and creep buckling of such domes under long-term loading inelastic behaviour of plates and shells", pp. 291–311 in *Inelastic behaviour of plates and shells: proceedings of IUTAM Symposium* (Rio de Janeiro, 1985), edited by L. Bavilacqua et al., Springer, Berlin, 1986.

[Wunderlich and Albertin 2002] W. Wunderlich and U. Albertin, "Buckling behaviour of imperfect spherical shells", *Int. J. Non-Linear Mech.* **37**:4–5 (2002), 589–604.

[Xirouchakis and Jones 1980] P. C. Xirouchakis and N. Jones, "Axisymmetric and bifurcation creep buckling of externally pressurised spherical shells", *Int. J. Solids Struct.* **16**:2 (1980), 131–148.

[Zarghamee and Heger 1983] M. S. Zarghamee and F. J. Heger, "Buckling of thin concrete domes", *ACI Struct. J.* **80**:6 (1983), 487–500.

EHAB HAMED: e.hamed@unsw.edu.au
Centre for Infrastructure Engineering and Safety, School of Civil and Environmental Engineering,
The University of New South Wales, Sydney, NSW 2052, Australia

MARK A. BRADFORD: m.bradford@unsw.edu.au
Centre for Infrastructure Engineering and Safety, School of Civil and Environmental Engineering,
The University of New South Wales, Sydney, NSW 2052, Australia

R. IAN GILBERT: I.Gilbert@unsw.edu.au
Centre for Infrastructure Engineering and Safety, School of Civil and Environmental Engineering,
The University of New South Wales, Sydney, NSW 2052, Australia

INFLUENCE OF MATRIX PLASTICITY AND RESIDUAL THERMAL STRESS ON INTERFACIAL DEBONDING OF A SINGLE FIBER COMPOSITE

YI PAN AND ASSIMINA A. PELEGRI

Fiber/matrix interfacial debonding in a single short-fiber reinforced polymer composite is investigated using finite elements and a cohesive zone model. The glass fiber is modeled as an isotropic, linear elastic material. The matrix is modeled as a linear elastic/elastoplastic material characterized by incremental isotropic hardening. A cohesive zone model governed by the traction-separation law describes the fiber/matrix interface. The simulated stress field of the single fiber debonded and perfectly bonded composites are compared. The results indicate that the interfacial shear stress decreases to zero on the debonded interface. It increases to its maximum value over a small processing zone and decreases exponentially to zero at the fiber midpoint. The debonding length growth in the plastic model is larger than that in the elastic model at small applied strain levels, but the trend is reversed as the applied strain level increases. The influence of factors such as residual thermal stress, interfacial strength, and fracture toughness on the debonding process of a single fiber composite are discussed.

1. Introduction

Fiber/matrix interfacial properties and the mechanical properties of the matrix are key factors that influence the stress-strain behavior and fracture toughness of short fiber reinforced composites (SFRC) [Mandell et al. 1982; Norman and Robertson 2003]. Fiber/matrix interfacial debonding is one of the primary damage mechanisms in the fragmentation test of a single fiber composite (SFC) [Cheng et al. 1993; Galiotis 1993; Yallee and Young 1998; Kim and Nairn 2002] and in the fracture test of random SFRCs [Mandell et al. 1982; Norman and Robertson 2003].

Galiotis [1993] has demonstrated that the load transfer mechanism in fiber reinforced composites is activated in the vicinity of discontinuities such as fiber ends and fiber breaks. In the case of SFRCs with fiber axes parallel to the direction of loading, the mechanism of load transfer from the matrix to the fiber is through interfacial shear stress. Fiber/matrix interfacial debonding, governed by the interfacial shear strength (IFSS) and fracture toughness, changes the stress transfer mechanism in the composite by altering the stress field around the fiber. Furthermore, Kim and Nairn [2002] observed that interfacial debonding occurred simultaneously with fiber breakage when they performed fragmentation tests on continuous SFCs. They also noted that further increases in the applied strain resulted in debonding propagation.

The determination of interfacial properties through an analysis of the stress field around a discontinuous fiber has been thoroughly studied [Galiotis 1993; Yallee and Young 1998; Kim and Nairn 2002]. It was reported that the number of instantaneous debonded interfaces accompanied by fiber breakage

increased at low applied strains and then decreased at higher strains, while the total debonded length enlarged as the applied strain increased.

Analytical and numerical studies have been performed to determine the stresses in the fiber and along the fiber/matrix interface in a perfectly bonded discontinuous fiber composite. The shear-lag model [Cox 1952], widely applied in the fragmentation test in order to determine the interfacial strength and fracture toughness [Galiotis 1993; Yallee and Young 1998], predicts that the maximum interfacial shear stress occurs at both ends of a discontinuous fiber and it decreases exponentially to zero at the fiber midpoint. It also predicts that the minimum normal stress in the fiber occurs at both ends of the discontinuous fiber and increases exponentially to its maximum value at the midpoint.

Carrara and McGarry [1968] studied the stress field of a discontinuous fiber composite in order to identify the optimal fiber-end geometry that would minimize the matrix shear stress concentration. They ascertained that at the fiber-end the stress theoretically predicted by the Cox shear-lag model (which does not account for stress concentrations) is only about half of the value obtained using a FEM that incorporates the stress concentration effect.

Daoust et al. [1993] performed a finite element (FE) analysis on a SFC fragmentation test and modeled the fiber sizing (thin coating layer) as an interphase with low modulus. The soft interphase layer decreased the stress at the ends of the fragment. The effect became more prominent when the thickness of the interphase layer was increased. Daoust's group introduced the gap elements, which only transmit compressive stress, to describe fiber discontinuities due to fiber breakage. The stress field obtained in their model is more realistic than that predicted by the Cox analytical model.

All the aforementioned studies assume a perfectly bonded interface and elastic behavior for the fiber and matrix materials. For matrices with remarkable elastoplastic behavior, Tripathi et al. [1996] introduced matrix plasticity to their FEM to illustrate the limitations of that assumption. Without considering fiber/matrix interfacial debonding, these authors found that the shear stress value near the fiber-end forms a plateau with value less than the maximum shear stress at the interface. The length of this plateau is enlarged as the applied strain increases. Their work is useful in determining the IFSS when no fiber/matrix interface debonding occurs in a single SFC fragmentation test. However, the stress pattern changes and the stress field becomes more complex as partially and/or fully interfacial debonding occurs [Yallee and Young 1998; Kim and Nairn 2002].

In the present study, we model the interfacial debonding of a SFC by a cohesive element using ABAQUS 6.8. Matrix plasticity is accounted for by the elastoplastic model. The model follows the isotropic hardening rule within the framework of incremental theory, where it is assumed that the mechanical strain rate is decomposed into an elastic part and a plastic part. Residual thermal stress (RTS) prevails in the fiber reinforced polymer composite due to the mismatch of thermal expansion coefficients (CTEs) of the fiber and matrix. The effects of interfacial strength, interfacial fracture toughness, and RTS on the interfacial debonding are investigated.

2. Finite element model

The model consists of a cylindrical short fiber centered within a cylindrical matrix. The fiber and the matrix are assumed to be isotropic materials. The cylindrical composite is loaded with a uniform tensile displacement. Since the loading and the geometry are both axisymmetric and the interfacial debonding
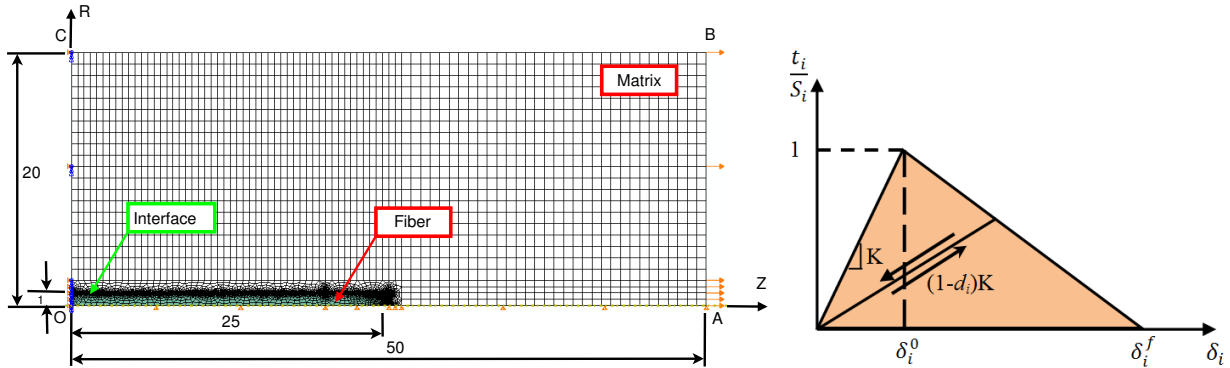
Figure 1. Schematic illustration of a single fiber embedded in the matrix (left, showing the finite element model) and of the traction-separation response (right).

on the lateral surface only undergoes mode II fracture, it is possible to model the physical problem using a two-dimensional axisymmetric model.

Geometric model. The geometry and meshing are illustrated in Figure 1, left. R is the radial direction and Z is the direction of the axis of symmetry along the fiber's centerline. The problem is symmetric about the midplane perpendicular to the Z-axis. Symmetric boundary conditions are applied on the edge OC. Axisymmetric boundary conditions are applied to the fiber centerline, the edge OA. The edge BC is a free edge. A uniform tensile displacement condition is applied on the edge AB. The radius of the fiber r is of unit value and the total length of the fiber l is equal to 50 (only one half of the fiber is shown due to symmetry). The radius of the cylindrical composite, R_0, is set to 20 and the composite length is twice the length of the fiber. A fictitious thin layer with thickness of 0.2% of the fiber radius is inserted between the fiber and the matrix to model the interface.

Material properties and the mesh. A cohesive zone model using cohesive elements governed by the traction-separation law [Camanho and Dávila 2002; Camanho et al. 2003; Turon et al. 2005; 2007; ABAQUS 2008; Dávila et al. 2008] is employed to describe the interface. The four-node axisymmetric element, CAX4, is used for the fiber and the matrix, while the four-node axisymmetric cohesive element, COHAX4, is used for the interface. A fine mesh is applied on the vicinity of the fiber/matrix interface and the mesh becomes coarser away from the interface, see Figure 1, left. The fiber, the interface, and the matrix are meshed using 9746, 2080, and 10303 elements, respectively. A relatively coarse mesh (double the size of the mesh reported here) was also used to study the solution dependency on mesh size. Both the coarse mesh (not reported) and the fine mesh (reported) in this study converged to the same solution. The Young's modulus, E_f, and the Poisson's ratio, v, of the linearly elastic fiber are 72 GPa and 0.22, respectively. Two types of constitutive behavior of the epoxy matrix are used, one of which is the linear elastic behavior with $E_m = 3.22$ GPa and $v = 0.35$. The other is the elastoplastic behavior governed by the same the elastic constants as the linear elastic behavior, a von Misses yield surface, and the isotropic hardening rule [ABAQUS 2008]. Even though the polymers in general have higher compressive yield strengths than tensile yield strengths and their hydrostatic stress dependent yielding behavior may be represented more precisely with other models such as the Drucker–Prager model, one

may use von Misses yield criterion to predict the yield point of epoxy resins with acceptable accuracy. That is because the hydrostatic stress is not prominent in the loading cases in this study. The strain hardening curve for elastoplastic epoxy resin input into ABAQUS is shown in Figure 2; the data is from [Tripathi et al. 1996]. The predicted stress/plastic strain curve is in good agreement with the experimental data.

Bilinear traction-separation law. The traction-separation law, one of the constitutive behaviors available for the cohesive element, was described in great detail in [ABAQUS 2008, Section 27.5]. It relates the traction to the displacement jump (separation) across the interface. The bilinear softening model is shown in Figure 1, right, and can be defined as

$$
t_i = \begin{cases} K\delta_i, & \text{if } \delta_i^{\max} \leq \delta_i^0, \\ (1-d_i)K\delta_i, & \text{if } \delta_i^0 < \delta_i^{\max} < \delta_i^f, \\ 0, & \text{if } \delta_i^{\max} = \delta_i^f, \end{cases} \tag{2-1}
$$

and

$$
d_i = \frac{\delta_i^f (\delta_i^{\max} - \delta_i^0)}{\delta_i^{\max}(\delta_i^f - \delta_i^0)}, \qquad i = 1, 2, 3, \quad d_i \in [0, 1], \tag{2-2}
$$

where t and δ are the traction and separation of the interface, respectively. The subscript i refers to the normal loading and the first and second shear loadings, respectively. The initial response is linear, characterized by the penalty stiffness K with no damage. After the interfacial normal, or the shear, tractions attain their corresponding interfacial tensile, or shear strengths, the stiffness is gradually reduced to zero. The damage onset separations can be computed as: $\delta_i^0 = S_i/K$, where S_1, S_2, and S_3 are the interfacial tensile strength and the interfacial shear strength in the first and the second shear directions, respectively. The area under the traction-separation curves is the corresponding mode I, II, and III fracture
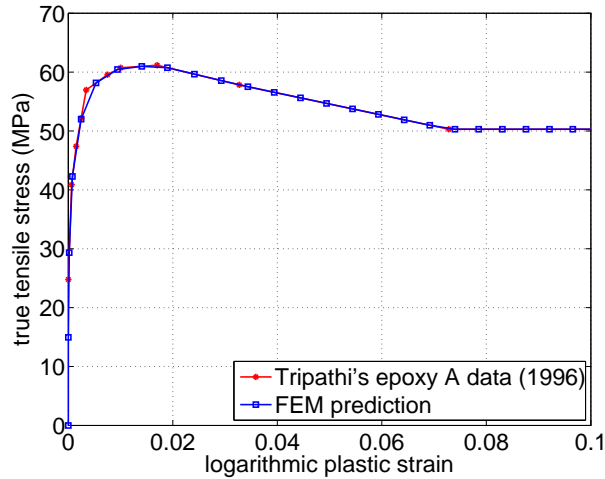
Figure 2. Strain hardening curve for epoxy resin.

toughness, G_{IC}, G_{IIC} and G_{IIIC}, respectively. The final separations can be defined as

$$\delta_1^f = 2G_{\mathrm{IC}}/S_1, \quad \delta_2^f = 2G_{\mathrm{IIC}}/S_2, \quad \delta_3^f = 2G_{\mathrm{IIIC}}/S_3.$$

The variable d_i, denoting the corresponding damage state, depends on the maximum separation, $\delta_i^{\max}$, attained during the loading history.

3. Finite element results and comparison to shear-lag model prediction

Galiotis [1993], Yallee and Young [1998], and Kim and Nairn [2002] found in experiments that partial or full interfacial debonding occurs in fragmentation test of SFCs due to the high interfacial shear stress at the tip of embedded short fibers or broken fibers. The IFSS, on the order of $\sim$10 to $\sim$100 MPa for the glass (or carbon) fiber/epoxy system in which we are interested, depends greatly on the fiber/matrix system and the fiber's surface treatment. The critical interfacial fracture energy is approximately 100 J/m^2. A penalty stiffness of $K = 10^6$ N/mm^3 is used for the traction-separation law. Guidelines for determining K can be found in [Turon et al. 2007]. The effect of matrix properties on the stress field of a SFC is being studied here by using the linear elastic and the isotropic hardening plastic models. The uncoupled traction-separation law is applied in our study. Damage initiation is governed by the maximum stress criterion, and damage evolution is governed by the effective displacement, δ_i^f, at complete failure of the interfacial layer modeled by the cohesive element [ABAQUS 2008]. Results of the FE simulations and the shear-lag predictions of the perfectly bonded interface model are also compared to those of the debonding interface model. The effects of residual thermal stress are addressed in Section 4.

Finite element results. Finite element results of the elastic and the elastoplastic matrix models with a perfectly bonded interface and a debonding interface are presented in this section. Two phenomena are investigated: damage initiation, when damage of the first interfacial cohesive element starts, which is governed by the strength, and crack initiation, when total failure of the first interfacial cohesive element occurs, which is governed by the interfacial fracture toughness.

Perfectly bonded interface model. In the case of a perfectly bonded interface, the fiber axial stress and the interfacial shear stress obtained from the FE analysis are shown in Figure 3. In the case of the elastic matrix model, both the interfacial shear stress (top left) and the axial stress (top right) in the fiber increase with the applied strain at the fiber tip. The fiber axial stress attains its maximum at the fiber midpoint and the interfacial shear stress decreases along the length of the fiber and reduces to zero at the fiber midpoint. For the model with the elastoplastic matrix, the shear stress profile (Figure 3, bottom left) almost coincides with the elastic model at small applied strains (less than 0.6%) except the small region around the fiber end. At higher applied strains, it is observed that the shear stress value near the fiber end forms a plateau and the value of the plateau is less than the maximum shear stress at the interface. The length of this plateau is enlarged as the applied strain increases. Similar results were reported in [Termonia 1987] for the elastic matrix model and in [Tripathi et al. 1996] for the elastoplastic matrix model. The results are presented here for the purpose of completeness and comparison to the debonding interface model. Due to the plateau of the interfacial shear stress, the fiber axial stress (Figure 3, bottom right) is almost linear in that region since the axial load in the fiber is transferred by the interfacial shear stress.

Interfacial shear stress   Fiber axial stress
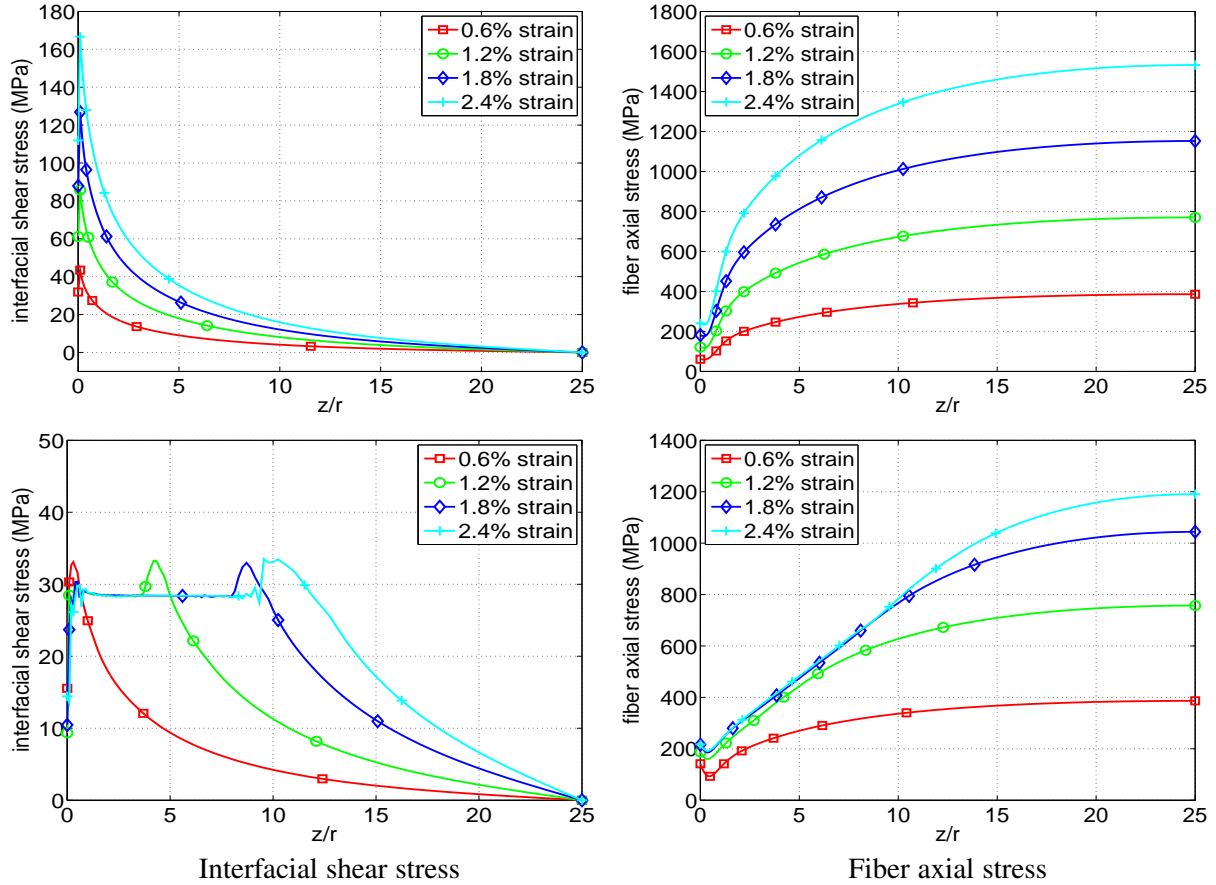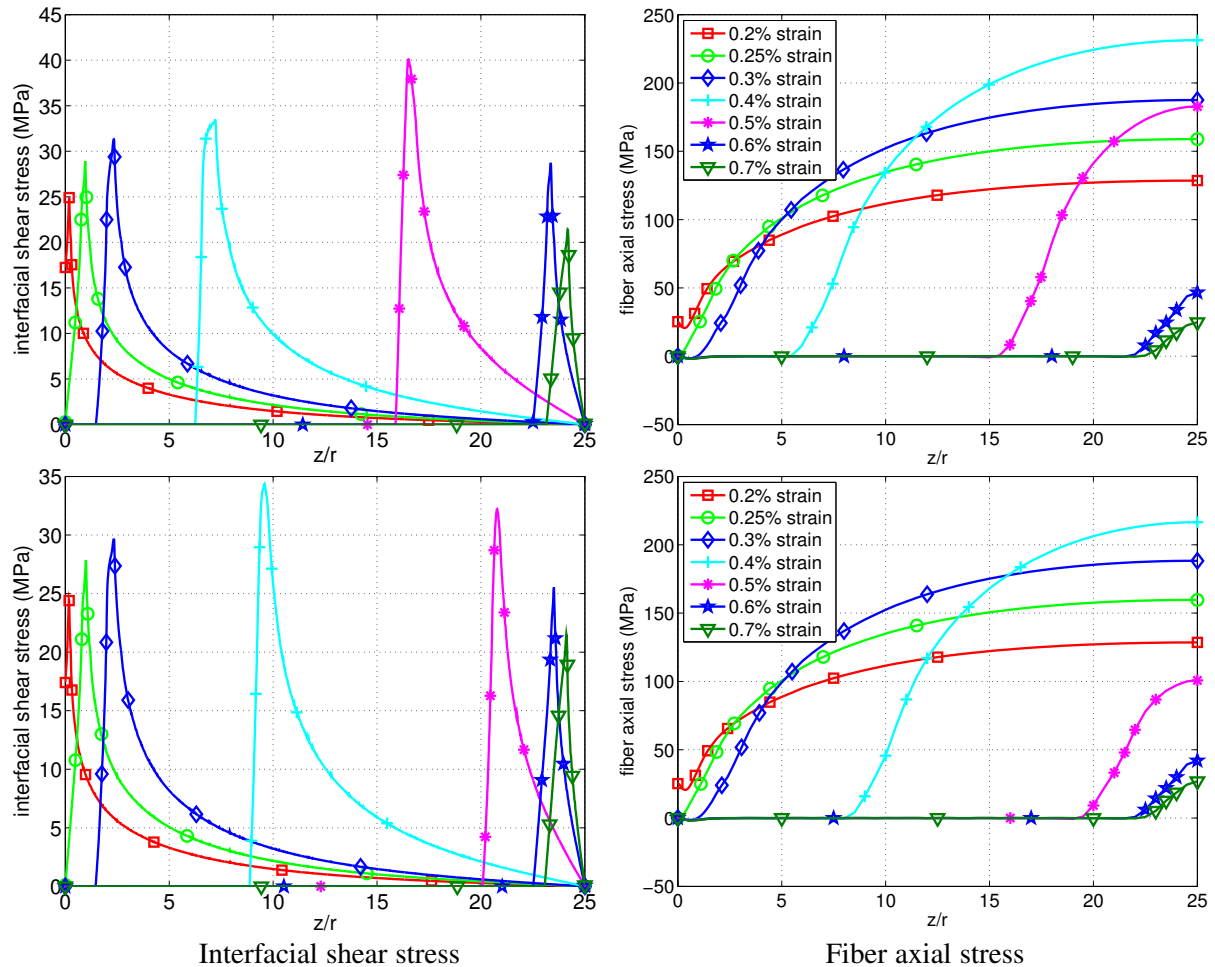
Figure 3. Interfacial shear stress (left column) and fiber axial stress (right column) of
FEM results of perfectly bonded interface model with elastic matrix (top) and elastoplas-
tic matrix (bottom).

Interfacial debonding model. Stress concentration at fiber ends due to the fiber-end geometry [Carrara
and McGarry 1968] and material mismatch results in interfacial debonding. Stress/strain profiles change
greatly when interfacial debonding is accounted for, compared to the perfectly bonded interface model.
The interfacial shear stress profiles and fiber axial stress profiles are shown in Figure 4.

A disparity between the stress profiles of the debonding and the perfectly bonded models is observed.
In the interfacial debonding model ($S_2 = 20$ MPa, $G_{\text{IIC}} = 100$ J/m^2) the shear stresses on the debonded
interface reduce to zero when the interfacial debonding occurs (a fully damaged interface, meaning the
damage variable d is equal to 1 at all integration points). It increases from zero to its maximum value
over the damage processing zone, where the damage of the cohesive element is activated ($0 < d < 1$), see
Figure 4, left. At the fiber tip, the axial stresses increase with the applied strain only before the interfacial
debonding initiates. At a certain applied strain, at which the interfacial shear stress equals the interfacial
strength, interfacial damage occurs. The axial stresses at the fiber tip gradually reduce to zero due to the
progressive interfacial debonding, see Figure 4, right.

Figure 4. Stress profiles of interfacial debonding models with elastic matrix (top) and elastoplastic matrix (bottom). The left two graphs share the legends of the right two.

Moreover, the maximum interfacial shear stress in the model is overestimated (almost twice the IFSS in the elastic model) due to the introduction of viscosity regularization in order to improve convergence [ABAQUS 2008]. The extra shear stress results in overestimation of the fiber axial stress. It is known that the portion of the debonding interface fails to transfer load from the matrix to the fiber. It is expected that the maximum fiber axial stress does not increase once the debonded interface has propagated, if the maximum shear stress does not exceed the interfacial shear strength.

Comparison of the shear-lag model and the FE model with a perfectly bonded and a debonding interface. Stress profiles predicted by the FE model with perfectly bonded and debonded interfaces are compared to that obtained by the shear-lag model [Cox 1952], as shown in Figure 5. The maximum interfacial shear stress from the shear-lag prediction is less than half of the value of the FE results with a perfectly bonded interface. For the debonding model with either an elastic or elastoplastic matrix, the shear stress is zero over the debonded interface region, increases to its maximum value over a small

Interfacial shear stress

Fiber axial stress
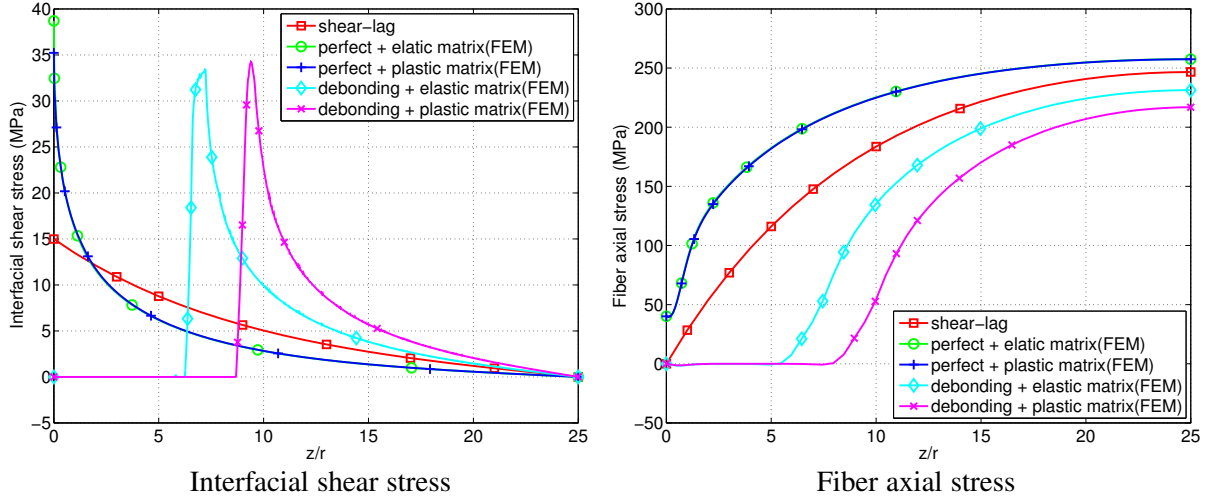
Figure 5. Stress profiles of the shear-lag model, the perfectly bonded interface model, and the debonding interface model with elastic and elastoplastic matrices at the same applied strain $\epsilon_m = 0.4\%$.

processing zone, and then decreases exponentially to zero at the fiber midpoint along the fiber length, see Figure 4, left. In contrast, in the perfect interface model with an elastoplastic matrix the shear stress near the fiber-end forms a plateau followed by a bulge containing the maximum shear stress (Figure 3, bottom left). In the perfect interface model with an elastic matrix the shear stress at the fiber tip increases with increasing applied strain level (Figure 3, top left). The fiber axial stress approximates zero over the debonded interface. The maximum axial stress of the fiber predicted by the shear-lag model is less than that of the perfectly bonded interface model, but exceeds that of the debonding interface model (Figure 5, right).

Effect of matrix plasticity. The effect of matrix plasticity on the interfacial shear stress along the fiber interface in the debonding interface model is illustrated in Figure 4, left, for the models with a linear elastic matrix and with a elastoplastic matrix, respectively. The IFSS of $S_2 = 20\,\mathrm{MPa}$ and the toughness of $G_{\mathrm{IIC}} = 100\,\mathrm{J/m}^2$ are kept constant in both cases.

At small applied strain levels, the corresponding stress profiles of both models almost coincide at the same applied strain level (see the curves with the square, circle, and diamond marks in Figure 4, left. As the applied strain level increases and the interfacial debonding propagates, separation of the two corresponding profiles (the curves marked with plus sign and asterisk symbols) implies that the debonding length is different at the same applied strain level for the two models. The debonding length of the elastic model increases slower than that of the plastic model at lower applied strain levels. However, this trend reverses at higher applied strain levels. The total debonding lengths are plotted against different applied strain levels in Figure 6. It is illustrated that the debonding length growth rate (that is, the slope) increases at lower applied strain levels and it decreases at higher applied strain levels for both models. Experimental data of E-glass/epoxy SFC in [Kim and Nairn 2002] show a similar trend of debonding length growth with increasing applied strain. In their work, an applied strain increase from 1.8% (fragmentation) to
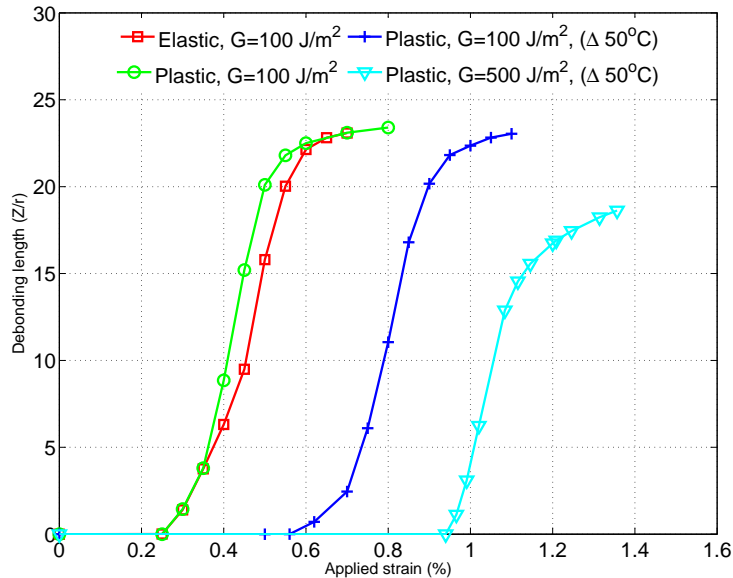
Figure 6. Comparison of debonding length at different levels of applied strain of models with an elastic matrix and an elastoplastic matrix and the effect of RTS.

3.3% (a net applied strain increase of 1.5%) caused an increase of $26r$ in the debonding length. In our modeling, an increase of the applied strain from 0.23% to 0.7% (a net applied strain increase of 0.47%) causes an increase of $22r$ in the debonding length. The average debonding growth in our model is faster than that presented in Kim and Narin's results. The discrepancy may be attributed to the low fracture toughness in our model, the absence of frictional force on the interface in our model, and the negligence of the initial RTS effect that will be accounted for in the next section. The frictional force counteracts the interfacial shear stress that drives the interface to damage and failure.

Effect of the interfacial strength on the debonding process. The effect of IFSS within the practical range, $S_2 \in (10, 100)$ MPa, on the debonding process of both the elastic and elastoplastic matrix models is studied, where the toughness of $G_{\text{IIC}} = 100$ J/m^2 is kept constant in each case. The parameters and results are tabulated in Table 1. It is shown that the stronger the interfacial strength, the higher the applied strain that is needed to initiate the damage.

It is concluded that the applied strain to initiate the damage of the interface is linearly proportional to the interfacial strength. The increments of applied strain needed to fully damage the first cohesive element along the interface from the fiber end in the elastic model (after the damage is initiated) are 0.22%, 0.17%, and 0.17%, respectively. For the case of $S_2 = 80$ MPa, it is 0.16%. Similar results are found in the elastoplastic model. These incremental applied strains are roughly identical (except the first one) since the fracture toughness is kept constant.

Effect of the interfacial fracture toughness on the debonding process and the stress profiles. To study the effect of the interfacial fracture toughness on the debonding process and the stress profiles, three cases are studied. The interfacial shear strengths (S_2) of these cases are kept constant (20 MPa), while

Effect of IFSS				
$(G_{\mathrm{IIC}} = 100\,\mathrm{J/m^2})$	Applied strain to initiate damage		Applied strain to initiate crack	
τ_0 (MPa)	Elastic matrix	Elastoplastic matrix	Elastic matrix	Elastoplastic matrix
10	0.04%	0.04%	0.26%	0.25%
20	0.07%	0.07%	0.24%	0.24%
30	—	0.10%	—	0.26%
40	0.14%	0.14%	0.31%	0.30%
80	0.27%	—	0.43%	—
Effect of fracture toughness				
$(\tau_0 = 20\,\mathrm{MPa})$	Applied strain to initiate damage		Applied strain to initiate crack	
G_{IIC} (J/m^2)	Elastic matrix	Elastoplastic matrix	Elastic matrix	Elastoplastic matrix
20	0.07%	0.07%	0.16%	0.16%
100	0.07%	0.07%	0.24%	0.24%
500	0.07%	0.07%	0.56%	0.56%

Table 1. Effect of IFSS and fracture toughness on the debonding process.

the fracture toughnesses (G_{IIC}) are set to $20\,\mathrm{J/m^2}$, $100\,\mathrm{J/m^2}$, and $500\,\mathrm{J/m^2}$, respectively. The applied strains to initiate the element damage are all 0.07% while the applied strains to initiate the crack are 0.16%, 0.24%, and 0.56%, respectively. Since the IFSS is below the yield stress of the elastoplastic matrix, the same applied strains are needed to initiate the damage. With increase of the interfacial fracture toughness, a higher applied strain is needed to propagate the crack. The influence of the fracture toughness on the debonding process is also recorded in Table 1.

The interfacial shear stress profiles for these three cases for both models are illustrated in Figure 7. It is observed that the length of the processing zone (where the elements are partially damaged) increases with the interfacial fracture toughness. At the same crack length, the maximum interfacial shear stress of the elastic model is slightly higher than that of the elastoplastic model.
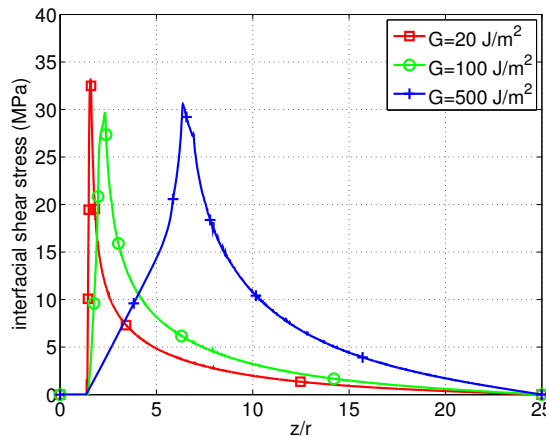
Figure 7. Fracture toughness effect on the interfacial shear stress profiles.

4. Effect of residual thermal stress

For a piece of material, a change in temperature will result in a contraction or expansion of the material due to its thermal properties. It is commonly seen that RTSs developed in a fiber reinforced composite that has undergone a thermal curing process are due to the mismatch of the CTEs of the fiber and matrix and the constraint of the bonded interface. The generic CTEs for the E-glass fiber and the epoxy matrix are $5 \times 10^{-6} \, /°C$ and $81 \times 10^{-6} \, /°C$, respectively. A temperature drop from an elevated temperature to room temperature during the cooling process is considered in this study. For the model with an elastoplastic matrix and a perfect bonded interface, the RTSs induced by a temperature drop of $50 \,°C$ are $-20.5 \, \text{MPa}$ and $33.2 \, \text{MPa}$, for the normal stress (compressive) and the shear stress along the interface, respectively. Larger temperature changes will result in higher RTSs. This is a general model used to demonstrate the effect of RTS on the interfacial debonding. The creep effect, which depends on the thermal and mechanical behavior of the matrix and may mitigate the RTS field, however, is not accounted for during the cooling process in this model. The residual thermal shear stress along the perfect interface is shown in Figure 8 (the solid curve without markers).

The residual thermal shear stress developed during the curing process may cause the damage to the interface [Rodriguez 1989]. In the case where the interfacial shear strength equals 20 MPa, the residual thermal shear stress exceeds the IFSS and it causes the damage initiation. As shown in Figure 8 (the dashed curve), the RTS induces damage initiation along the interface with a damage initiation length of $1.8 \, r$, for an IFSS of 20 MPa. Moreover, the residual thermal shear stress on the interface is pointing from the fiber tip toward the center of the fiber at the matrix side. Once a tensile strain is applied to the SFC, the RTS needs to be counteracted and then reverse shear stress will develop as the applied strain increases. This results in a higher applied strain level to debond the interface than that in the model without the RTS effect as shown in Figure 8. The combined effect of the RTS and the interfacial fracture toughness is also shown in Figure 6. It needs an even higher applied strain level to debond a tougher
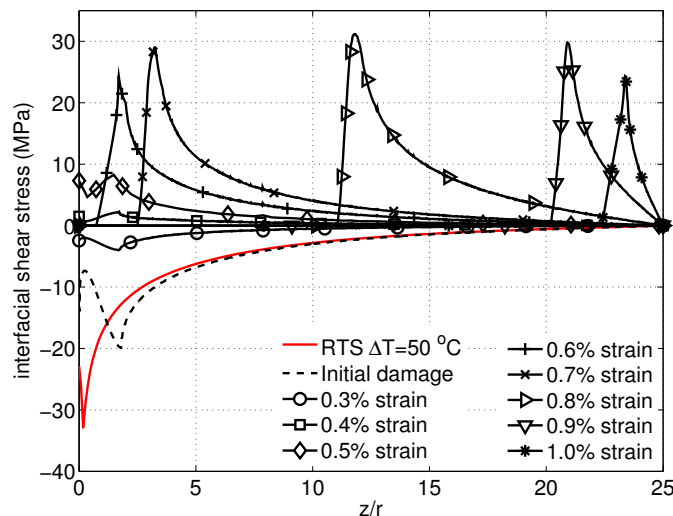
Figure 8. Interfacial shear stress with effect residual thermal stress for a debonding interface model.

interface. It is noted that the local (around the debonding tip) elastoplastic matrix becomes softened when the applied strain level reaches about 1.2% in the case where G_{IIC} equals 500 J/m^2 and the RTS effect is considered (the curve marked with $\triangledown$s in Figure 6). Instability issues caused by material softening are analyzed using the Riks method implemented in [ABAQUS 2008]. Also to be noted is that when the applied strain increases the crack tip propagates and the matrix on the wake of the crack tip is subjected to unloading. This process enables the propagation of the debonding tip instead of further yielding of the matrix. However, the propagation rate of the crack tip decreases as more external work is consumed in the form of plastic dissipation by the matrix and less external work is used to debond the interface.

Once the RTS effect is considered, an increase of applied strain from 0.56% to 1.1% (a net applied strain increase of 0.54%) causes an increase of $23r$ in the debonding length for $G_{\text{IIC}} = 100$ J/m^2. If the RTS and a higher fracture toughness value ($G_{\text{IIC}} = 500$ J/m^2) are considered, an increase of applied strain from 0.94% to 1.36% (a net applied strain increase of 0.42%) causes an increase in the debonding length of $18.6r$.

5. Conclusions

Finite element results of composite materials consisting of a single short glass fiber (modeled as an isotropic, linear elastic material) with elastic and elastoplastic matrices (characterized by an incremental isotropic hardening model) are presented. Two types of interfaces, perfectly bonded and debonded, are studied. Comparison of the simulation results with published experimental results concludes the following:

- The stress profiles of the debonding interface model differ significantly from those of the perfectly bonded interface model. The interfacial shear stress reduces to zero on the debonded interface. It increases to its maximum value over a small processing zone and decreases exponentially to zero at the fiber midpoint.

- The maximum interfacial shear stress of the elastoplastic matrix model is smaller than that of the elastic matrix model at the same applied strain level.

- For both models, the growth of the debonding length (the slope of the debonding length versus the applied strain curve) increases at lower applied strain levels and decreases at higher applied strain levels.

- The growth of the debonding length in the plastic model is larger than that in the elastic model at small applied strain levels. The trend reverses as the applied strain level increases.

- The applied strain level to initiate the damage of the cohesive element is approximately linearly proportional to the interfacial shear strength.

- When the specimen is subjected to tensile loading, the effect of the residual thermal stress offsets the applied strain level required to initiate damage to the interface, since the residual thermal shear stress needs to be first counteracted so that damage at the interface may occur.

Acknowledgements

References

[ABAQUS 2008] *Abaqus User's Manual*, Version 6.8, Dassault Systèmes/SIMULIA, Providence, RI, 2008.

[Camanho and Dávila 2002] P. P. Camanho and C. G. Dávila, "Mixed-mode decohesion finite elements for the simulation of delamination in composite materials", technical report TM-2002-211737, NASA, 2002, Available at http://paginas.fe.up.pt/ demegi/Avaliacao/Pp_Camanho_Davila.pdf.

[Camanho et al. 2003] P. P. Camanho, C. G. Dávila, and M. F. D. Moura, "Numerical simulation of mixed-mode progressive delamination in composite materials", *J. Compos. Mater.* **37**:16 (2003), 1415–1438.

[Carrara and McGarry 1968] A. S. Carrara and F. J. McGarry, "Matrix and interface stresses in a disconinuous fiber composite model", *J. Compos. Mater.* **2**:2 (1968), 222–243.

[Cheng et al. 1993] T.-H. Cheng, F. R. Jones, and D. Wang, "Effect of fiber conditioning on the interfacial shear strength of glass-fibre composites", *Compos. Sci. and Technology* **48** (1993), 89–96.

[Cox 1952] H. L. Cox, "The elasicity and strength of paper and other fiberous materials", *British J. Appl. Phys.* **3** (1952), 72–79.

[Daoust et al. 1993] J. Daoust, T. Vu-Khanh, C. Ahlstrom, and J. F. Gerard, "A finite element model of the fragmentation test for the case of a coated fiber", *Compos. Sci. and Technology* **48** (1993), 143–149.

[Dávila et al. 2008] C. G. Dávila, P. P. Camanho, and A. Turon, "Effective simulation of delamination in aeronautical structures using shells and cohesive elements", *J. Aircraft* **45**:2 (2008), 663–672.

[Galiotis 1993] C. Galiotis, "A study of mechanisms of stress transfer in continuous- and discontinuous-fibre model composites by laser Raman Spectroscopy", *Compos. Sci. and Technology* **48** (1993), 15–28.

[Kim and Nairn 2002] B. W. Kim and J. A. Nairn, "Observations of fiber fracture and interfacial debonding phenomena using the fragmentation test in single fiber composites", *J. Compos. Mater.* **36**:15 (2002), 1825–1858.

[Mandell et al. 1982] J. F. Mandell, D. D. Huang, and F. J. . McGarry, "Crack propagation modes in injection molded fiber reinforced thermoplastics", in *Short fiber reinforced composite materials* (STP 772), edited by B. A. Sanders, ASTM, Philadelphia, 1982.

[Norman and Robertson 2003] D. A. Norman and R. E. Robertson, "The effect of fiber orientation on the toughening of short fiber-reinforced polymers", *J. Appl. Polymer Sci.* **90** (2003), 2740–2751.

[Rodriguez 1989] E. L. Rodriguez, "Microdelamination due to resin shrinkage in filament-wound fibreglass composites", *J. Mater. Sci. Lett.* **8** (1989), 116–118.

[Termonia 1987] Y. Termonia, "Theoretical study of the stress transfer in single fibre composites", *J. Mater. Sci.* **22** (1987), 504–508.

[Tripathi et al. 1996] D. Tripathi, F. Chen, and F. R. Jones, "The effect of matrix plasticity on the stress fields in a single filament composite and the value of interfacial shear strength obtained from the fragmentation test", *Proc. Royal Soc. A* **452**:1946 (1996), 621–653.

[Turon et al. 2005] A. Turon, C. G. Dávila, P. P. Camanho, and J. Costa, "An engineering solution for using coarse meshes in the simulation of delamination with cohesive zone models", technical report TM-2005-213547, NASA, 2005.

[Turon et al. 2007] A. Turon, C. G. Dávila, P. P. Camanho, and J. Costa, "An engineering solution for mesh size effects in the simulation of delamination using cohesive zone models", *Engin. Fracture Mech.* **74** (2007), 1665–1682.

[Yallee and Young 1998] R. B. Yallee and R. J. Young, "Evaluation of interface fracture energy for single-fibre composites", *Compos. Sci. and Technology* **58** (1998), 1907–1916.

YI PAN: yipan@eden.rutgers.edu
Department of Mechanical and Aerospace Engineering, Rutgers University, 98 Brett Road, Piscataway, NJ 08854-8058, United States

ASSIMINA A. PELEGRI: pelegri@jove.rutgers.edu
Department of Mechanical and Aerospace Engineering, Rutgers University, 98 Brett Road, Piscataway, NJ 08854-8058, United States
http://cronos.rutgers.edu/~pelegri/

FREE FLEXURAL VIBRATIONS OF MASONRY BEAM-COLUMNS

MARIA GIRARDI AND MASSIMILIANO LUCCHESI

We present an analytical study of the free transverse vibrations of masonry beam-columns, focusing on the role of the material's inability to sustain traction in modifying the dynamic behavior of such structures. In particular, for periodic oscillations, an analytical method is presented for obtaining an explicit relation between the fundamental frequency of the beam and the displacement amplitude.

1. Introduction

In recent years, the dynamic response of age-old masonry structures and buildings has attracted growing interest, particularly in Italy, where the extraordinary historical architectural heritage is regularly threatened by violent earthquakes. Much effort has been devoted to evaluating the seismic vulnerability of such structures. The methods developed are based mainly on a classification of the damage mechanisms consequent to earthquakes [Petrini et al. 1999; MiBAC 2006] and application of some simplification procedures, which have been adopted by Italian regulations [Norme tecniche 2008]. A number of mechanical models have been developed and implemented in numerical codes, involving a limited number of degrees of freedom and developed for the most part by defining macro-elements [Petrini et al. 1999; Gambarotta and Lagomarsino 1997].

The dynamic behavior of masonry structures is heavily influenced by a variety of parameters, such as construction technique, construction geometry, material characteristics, and type of accelerations applied to the structural supports. Moreover, masonry structures respond differently to tensile and compressive stresses.

In the 1980s [Del Piero 1989; Di Pasquale 1992], a constitutive equation was formulated to describe the behavior of a class of materials, termed no-tension or masonry-like, that is able to withstand compressive stresses but only limited or null tensile stresses. This approach appeared to provide a satisfactory description of the main aspects of the static behavior of old masonry buildings [De Falco and Lucchesi 2002; Lucchesi et al. 2008].

A numerical model was proposed in [Lucchesi and Pintucchi 2007] to describe the dynamic behavior of slender masonry structures, such as columns or towers, by means of one-dimensional finite elements. This model is based on a no-tension constitutive equation expressed in terms of generalized stresses and strains [Zani 2004]. The nonlinear elastic material described by the model provides satisfactory

predictions for the dynamic behavior of such structures. The model mainly predicts flexural oscillations and does not include material damage under cyclic stresses.

In this paper, we present a study of the flexural dynamic behavior of slender masonry structures with the aim of finding an explicit relation between a beam's fundamental frequency and the total energy of the system. We begin with the constitutive law described in [Zani 2004] and used in [Lucchesi and Pintucchi 2007].

The spread of cracks along a beam reduces the stiffness of a structure and gives rise to interactions between the natural beam oscillation frequencies and the amplitude of the cracked zone. These effects strongly alter the dynamic behavior of slender masonry structures, which are characterized by a response to acceleration that deviates considerably from linearity.

Relations between frequencies and amplitudes have been found for several types of softening systems [Nayfeh and Mook 1995; Nayfeh 2000] mainly by using perturbation methods, such as the multiple scales method or averaging techniques. However, such relations may be obtained directly from the equations of motion, as shown in [Whitham 1974] for the propagation of waves in dispersive media.

This work is divided into three parts. Section 2 presents an equation describing the dynamic equilibrium of a one-dimensional continuous beam composed of an elastic material. Then, under suitable hypotheses regarding the form of the solution, a relation between the fundamental frequency and the energy of the system is deduced.

In the two subsequent sections, comprising the second part of the paper, we apply this relation to a masonry beam. Section 3 is dedicated to materials described by the no-tension constitutive equation, and Section 4 introduces a simplified cubic polynomial constitutive law that can approximate the no-tension relation for curvature values near the elastic limit.

Lastly, Section 5 presents some example applications and makes a comparison between the analytical results and the corresponding numerical solutions obtained via the code described in [Lucchesi and Pintucchi 2007].

All results presented here were obtained assuming conservative systems and free vibrations. Future work will study forced and damped oscillations; some results of this kind can already be found in [Girardi 2009; Girardi and Lucchesi 2006].

2. Formulation of the dynamic problem

Consider a rectilinear beam with length l and rectangular cross-section characterized by height h and width b, subjected to a uniform axial force N. Let χ be the curvature of the beam and $M(\chi) : R \to R$ be the bending moment, a continuous differentiable function with a second derivative that is assumed to be piecewise continuous. Let E and ρ denote the Young modulus and density of the material, respectively, and $J = bh^3/12$ denotes the moment of inertia of the beam's cross-section.

To work with dimensionless quantities, if x and v are, respectively, the abscissa along the beam's axis and the transverse flexural displacement of the beam (see Figure 1), and t denotes time, we define

$$\xi = \frac{x}{l}, \quad \tau = \frac{t}{T_c}, \quad u = \frac{v}{l}, \quad \kappa = \chi l, \tag{2-1}$$

where $T_c = l^2/c$ and $c = \sqrt{\dfrac{EJ}{\rho bh}}$ are the elastic constants of the beam.
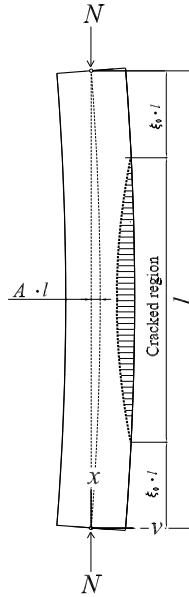
Figure 1. A masonry beam-column: model and notations.

We assume the effects of both the shear strain and the rotary inertia to be negligible. Moreover, we limit ourselves to considering situations in which the flexural displacement $u(\xi, \tau)$ and its derivative $u_\xi(\xi, \tau)$ are small, so that we can neglect the effects of the axial force on the dynamic equilibrium of the beam, and write

$$\kappa(\xi, \tau) = -u_{\xi\xi}(\xi, \tau). \tag{2-2}$$

Under these hypotheses, set

$$f(\kappa) = \frac{l}{EJ} M(\kappa/l), \tag{2-3}$$

the equation of motion is

$$\frac{\partial^2 u}{\partial \tau^2} - \frac{\partial^2 (f \circ \kappa)}{\partial \xi^2} = 0, \tag{2-4}$$

which coincides with the Euler equation

$$\frac{\partial}{\partial \tau} \left(\frac{\partial L}{\partial u_\tau} \right) - \frac{\partial^2}{\partial \xi^2} \left(\frac{\partial L}{\partial u_{\xi\xi}} \right) = 0, \tag{2-5}$$

corresponding to the Lagrangian

$$L = \frac{1}{2} (u_\tau)^2 - F(-u_{\xi\xi}), \tag{2-6}$$

where F is the primitive of f such that $F(0) = 0$, as can be easily verified. The goal is to find approximate solutions to (2-4) of the form [Nayfeh and Mook 1995; Nayfeh 2000]

$$u(\xi, \tau) = \sum_{i=1}^{n} \phi_i(\xi) \eta_i(\tau), \tag{2-7}$$

where the functions ϕ_i are twice continuously differentiable and satisfy the orthogonality condition

$$\int_0^1 \phi_i \phi_j = \delta_{ij} \qquad \text{for} \quad i, j \in 1 \ldots n. \tag{2-8}$$

From (2-6), we deduce that

$$L = L(\phi_i, \phi_i'', \eta_i, \eta_i') = \frac{1}{2}\left(\sum_{i=1}^n \phi_i \eta_i'\right)^2 - F\left(-\sum_{i=1}^n \phi_i'' \eta_i\right), \tag{2-9}$$

where the primes denote differentiation.

Let us introduce the averaged Lagrangian $\bar{L}$ over the normalized length of the beam

$$\bar{L}(\eta_i, \eta_i') = \int_0^1 L(\phi_i, \phi_i'', \eta_i, \eta_i')d\xi = \frac{1}{2}\int_0^1 \left(\sum_{i=1}^n \phi_i \eta_i'\right)^2 d\xi - \int_0^1 F\left(-\sum_{i=1}^n \phi_i'' \eta_i\right) d\xi. \tag{2-10}$$

By virtue of (2-8), we can write

$$\bar{L}(\eta, \eta') = \frac{1}{2}\sum_{i=1}^n \eta_i'^2 - V(\eta_i), \tag{2-11}$$

where

$$V(\eta_i) = \int_0^1 F\left(-\sum_{i=1}^n \phi_i'' \eta_i\right) d\xi. \tag{2-12}$$

First, we will verify that each function η_i satisfies the equation

$$\frac{\partial}{\partial \tau}\frac{\partial \bar{L}}{\partial \eta_i'} - \frac{\partial \bar{L}}{\partial \eta_i} = 0. \tag{2-13}$$

To this aim, we observe that

$$\frac{\partial L}{\partial u_\tau} = \sum_{j=1}^n \frac{1}{\phi_j}\frac{\partial L}{\partial \eta_j'}, \qquad \frac{\partial L}{\partial u_{\xi\xi}} = \frac{1}{n}\sum_{j=1}^n \frac{1}{\eta_j}\frac{\partial L}{\partial \phi_j''}, \tag{2-14}$$

and, thus, from (2-5), we obtain

$$\sum_{j=1}^n \frac{1}{\phi_j}\frac{\partial}{\partial \tau}\left(\frac{\partial L}{\partial \eta_j'}\right) - \frac{1}{n}\sum_{j=1}^n \frac{1}{\eta_j}\frac{\partial^2}{\partial \xi^2}\left(\frac{\partial L}{\partial \phi_j''}\right) = 0. \tag{2-15}$$

Now, multiplying (2-15) by each ϕ_i and integrating over $[0, 1]$, we obtain the set of equations

$$\frac{\partial}{\partial \tau}\left(\frac{\partial \bar{L}}{\partial \eta_i'}\right) + \sum_{j \neq i}\int_0^1 \frac{\phi_i}{\phi_j}\frac{\partial}{\partial \tau}\frac{\partial L}{\partial \eta_j'} - \frac{1}{n}\int_0^1 \phi_i \sum_{j=1}^n \frac{1}{\eta_j}\frac{\partial^2}{\partial \xi^2}\frac{\partial L}{\partial \phi_j''} d\xi = 0. \tag{2-16}$$

In view of (2-9) and (2-8), equation (2-16) becomes

$$\frac{\partial}{\partial \tau}\left(\frac{\partial \bar{L}}{\partial \eta_i'}\right) + \sum_{j \neq i}\int_0^1 \frac{\phi_i}{\phi_j}\frac{\partial}{\partial \tau}(\phi_j^2 \eta_j') - \frac{1}{n}\int_0^1 \phi_i \sum_{j=1}^n \frac{1}{\eta_j}\frac{\partial^2 f}{\partial \xi^2}\eta_j d\xi = \frac{\partial}{\partial \tau}\frac{\partial \bar{L}}{\partial \eta_i'} - \int_0^1 \frac{\partial^2 f}{\partial \xi^2}\phi_i d\xi = 0, \tag{2-17}$$

where, for the sake of brevity, we write $\partial^2 f/\partial \xi^2$ for $\partial^2 (f \circ \kappa)/\partial \xi^2$.

Now, under the assumption that $f'\phi_i = \phi'_i f = 0$ at the ends of the beam, we obtain

$$\frac{\partial}{\partial \tau} \frac{\partial \bar{L}}{\partial \eta'_i} - \int_0^1 \frac{\partial^2 f}{\partial \xi^2} \phi_i \, d\xi = \frac{\partial}{\partial \tau} \frac{\partial \bar{L}}{\partial \eta'_i} - \frac{\partial f}{\partial \xi} \phi_i \Big|_0^1 + \int_0^1 \frac{\partial f}{\partial \xi} \phi'_i \, d\xi$$

$$= \frac{\partial}{\partial \tau} \frac{\partial \bar{L}}{\partial \eta'_i} + f \phi'_i \Big|_0^1 - \int_0^1 f \phi''_i \, d\xi = \frac{\partial}{\partial \tau} \frac{\partial \bar{L}}{\partial \eta'_i} - \int_0^1 f \phi''_i \, d\xi. \tag{2-18}$$

From (2-10), we deduce that

$$\frac{\partial \bar{L}}{\partial \eta_i} = -\frac{\partial}{\partial \eta_i} \int_0^1 F(-\sum_{j=1}^n \phi''_j \eta_j) \, d\xi = \int_0^1 f \phi''_i \, d\xi, \tag{2-19}$$

and (2-13) follows from (2-18).

Because $f(\kappa)$ is, in general, a nonlinear function, the corresponding equations (2-13) are coupled. For our purposes, it is sufficient to limit ourselves to unimodal solutions of the form

$$u(\xi, \tau) = \phi(\xi)\eta(\tau), \tag{2-20}$$

and, thus, (2-13) reduces to

$$\frac{\partial}{\partial \tau} \frac{\partial \bar{L}}{\partial \eta'} - \frac{\partial \bar{L}}{\partial \eta} = 0. \tag{2-21}$$

If we set

$$\eta = \eta(\theta), \qquad \theta_\tau = \omega, \tag{2-22}$$

where the frequency ω indicates a slowly varying system parameter [Whitham 1974], and

$$\bar{L}_1 = \frac{\partial \bar{L}}{\partial \eta'}, \qquad \bar{L}_2 = \frac{\partial \bar{L}}{\partial \eta}, \tag{2-23}$$

then equation (2-21) becomes $\omega \frac{\partial \bar{L}_1}{\partial \theta} - \bar{L}_2 = 0$. Multiplying this by $\frac{\partial \eta}{\partial \theta}$, and recalling that

$$\frac{\partial \bar{L}}{\partial \theta} = \omega \frac{\partial^2 \eta}{\partial \theta^2} \bar{L}_1 + \bar{L}_2 \frac{\partial \eta}{\partial \theta}, \tag{2-24}$$

we obtain

$$\omega \frac{\partial \bar{L}_1}{\partial \theta} \frac{\partial \eta}{\partial \theta} - \frac{\partial \bar{L}}{\partial \theta} + \bar{L}_1 \omega \frac{\partial^2 \eta}{\partial \theta^2} = \frac{\partial}{\partial \theta} \left(\omega \bar{L}_1 \frac{\partial \eta}{\partial \theta} \right) - \frac{\partial \bar{L}}{\partial \theta} = 0, \tag{2-25}$$

whose first integral is

$$\omega \bar{L}_1 \frac{\partial \eta}{\partial \theta} - \bar{L} = a, \tag{2-26}$$

where a is the total energy of the system, which is constant with respect to θ and is related to the amplitude of the motion.

In view of (2-11), with $i = 1$, equation (2-26) becomes

$$\frac{1}{2} \omega^2 \left(\frac{\partial \eta}{\partial \theta} \right)^2 + V(\eta) = a, \tag{2-27}$$

from which we have $\dfrac{d\theta}{d\eta} = \dfrac{\omega}{\sqrt{2(a - V(\eta))}}$. Then,

$$\frac{2\pi}{\omega} = \oint \frac{d\eta}{\sqrt{2(a - V(\eta))}}, \tag{2-28}$$

where the integral is taken over a complete loop of the motion [Whitham 1974].

Equation (2-28) links the frequency ω to the total energy a of the system and is exactly the relation we are seeking.
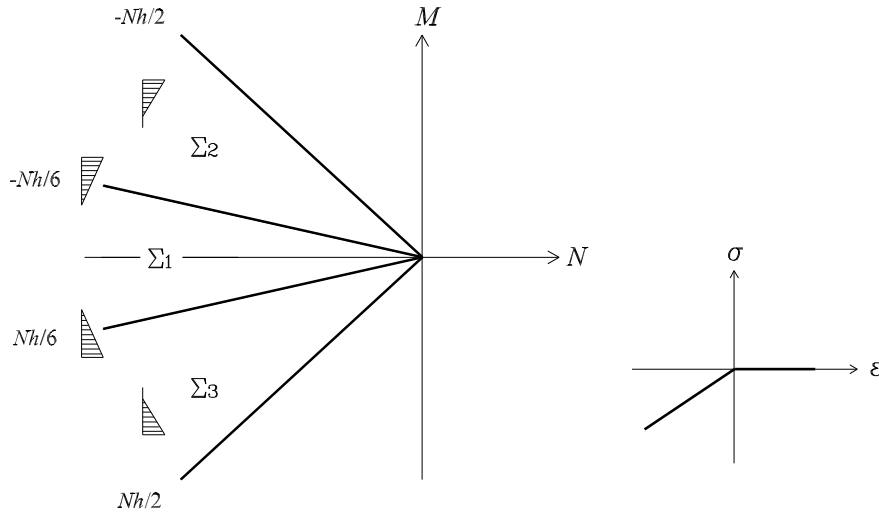
3. No-tension material

3A. *The constitutive equation.* Let the beam described in Section 2 be composed of a no-tension material with zero tensile strength and infinite compressive strength (see Figure 2).

Let ε denote an infinitesimal axial deformation. Under the classical Euler–Bernoulli hypothesis, we can deduce a relation between the generalized deformations ε and χ and the generalized stresses N and M. For each normal section of the beam, let

$$\Sigma = \left\{ (N, M) : N \leq 0, \tfrac{1}{2}Nh \leq M \leq -\tfrac{1}{2}Nh \right\} \tag{3-1}$$

be the set of all admissible generalized stresses, and let us consider the subsets of Σ (see Figure 2)

$$\begin{aligned}
\Sigma_1 &= \left\{ (N, M) \in \Sigma : \tfrac{1}{6}Nh \leq M \leq -\tfrac{1}{6}Nh \right\}, \\
\Sigma_2 &= \left\{ (N, M) \in \Sigma : -\tfrac{1}{6}Nh \leq M \leq -\tfrac{1}{2}Nh \right\}, \\
\Sigma_3 &= \left\{ (N, M) \in \Sigma : \tfrac{1}{2}Nh \leq M \leq \tfrac{1}{6}Nh \right\}.
\end{aligned} \tag{3-2}$$

Figure 2. The σ-ε relation for a no-tension material with infinite compressive strength and zero tensile strength and the admissible generalized stresses M, N for a rectangular section of height h.

Then, we can write the constitutive equation [Zani 2004]:

$$
\begin{aligned}
(N, M) \in \Sigma_1 : \quad & \varepsilon = \frac{N}{Ebh}, & \chi &= \frac{12M}{Ebh^3}, \\
(N, M) \in \Sigma_2 : \quad & \varepsilon = \frac{8}{9Eb} \frac{N^2(Nh + 3M)}{(Nh + 2M)^2}, & \chi &= -\frac{8}{9Eb} \frac{N^3}{(Nh + 2M)^2}, \\
(N, M) \in \Sigma_3 : \quad & \varepsilon = \frac{8}{9Eb} \frac{N^2(Nh - 3M)}{(Nh - 2M)^2}, & \chi &= -\frac{8}{9Eb} \frac{N^3}{(Nh - 2M)^2}.
\end{aligned}
\tag{3-3}
$$

(N, M) in Σ_1 corresponds to a fully compressed section. Σ_2 and Σ_3 correspond to regions in which the section is only partially compressed. The outer boundaries of Σ_2 and Σ_3 are reached when the eccentricity M/N in the section is equal to $-h/2$ and $h/2$, respectively, corresponding to a situation that is allowed given that the material is assumed to have infinite compressive strength.

Equations (3-3) can be inverted to obtain $N = N(\varepsilon, \chi)$, $M = M(\varepsilon, \chi)$. To this aim, we introduce the subsets of the set E of all generalized strains (ε, χ):

$$
\begin{aligned}
E_1 &: \big\{ (\varepsilon, \chi) \in E : 2\varepsilon \leq \chi h \leq -2\varepsilon, \ \varepsilon \leq 0 \big\}, \\
E_2 &: \big\{ (\varepsilon, \chi) \in E : \chi h > 2\,|\varepsilon|, \ \chi > 0 \big\}, \\
E_3 &: \big\{ (\varepsilon, \chi) \in E : \chi h < 2\,|\varepsilon|, \ \chi < 0 \big\}.
\end{aligned}
\tag{3-4}
$$

Then, from (3-3) we obtain

$$
\begin{aligned}
(\varepsilon, \chi) \in E_1 : \quad & N = Ebh\varepsilon, & M &= \frac{Ebh^3}{12}\chi, \\
(\varepsilon, \chi) \in E_2 : \quad & N = -\frac{Eb(\chi h - 2\varepsilon)^2}{8\chi}, & M &= \frac{Eb(\varepsilon + \chi h)(\chi h - 2\varepsilon)^2}{24\chi^2}, \\
(\varepsilon, \chi) \in E_3 : \quad & N = \frac{Eb(\chi h + 2\varepsilon)^2}{8\chi}, & M &= -\frac{Eb(\varepsilon - \chi h)(\chi h + 2\varepsilon)^2}{24\chi^2}.
\end{aligned}
\tag{3-5}
$$

If the axial force N acting on the section is a known quantity, then from (3-5) we can obtain a relation $M = M(\chi, N)$ between the bending moment and the curvature. To this aim, we define

$$
\chi_0 = -\frac{2N}{Ebh^2},
\tag{3-6}
$$

the curvature corresponding to the elastic limit. Therefore, from (3-5), we have

$$
\frac{M(\chi)}{\rho bh} = \begin{cases} c^2\chi & \text{for } |\chi| \leq \chi_0, \\ c^2\chi_0 \,\text{sign}(\chi)\big(3 - 2\sqrt{\chi_0/|\chi|}\,\big) & \text{for } |\chi| > \chi_0, \end{cases}
\tag{3-7}
$$

which represents the constitutive equation we are looking for.

The function (3-7) is plotted in Figure 3. For increasing values of χ in the nonlinear region, we see that the stiffness of the section decreases quickly and the bending moment tends toward its limit value $|Nh/2|$. Moreover, we observe that $M(\chi)$ is continuous with its first derivative, whereas the second derivative undergoes a jump in value for $|\chi| = \chi_0$.
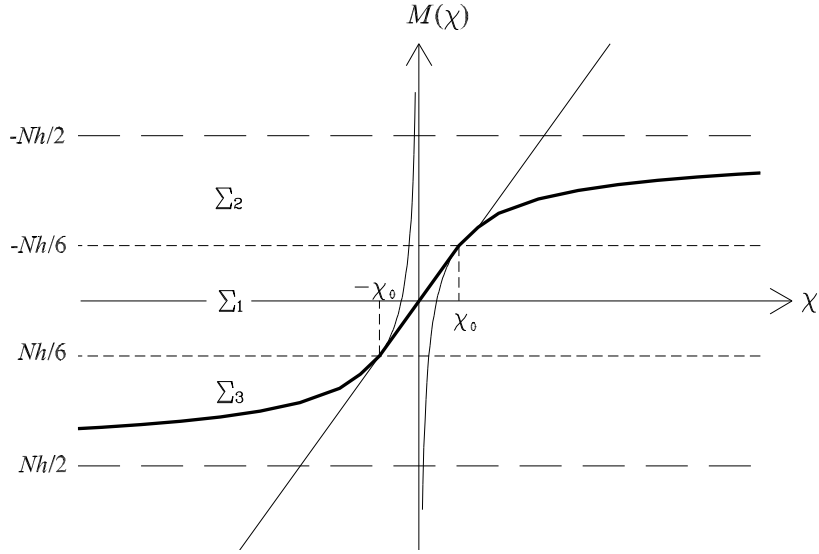
Figure 3. The constitutive equation $M\text{-}\chi$ for a rectangular section made of no-tension material with infinite compressive strength.

3B. *The dynamic problem.* From (3-7), we can obtain the nondimensionalized equation

$$F(\kappa) = \begin{cases} \frac{1}{2}\kappa^2 & \text{for } \xi \leq \xi_0, \\ \kappa_0 \left(3\,|\kappa| - 4\sqrt{\kappa_0\,|\kappa|}\right) + \frac{3}{2}\kappa_0^2 & \text{for } \xi > \xi_0, \end{cases} \tag{3-8}$$

where F is the primitive of $f = Ml/(EJ)$ such that $F(0) = 0$, $\kappa_0 = -2Nl/(Ebh^2)$ represents the dimensionless limit of the elastic curvature of the section, and $\xi_0(\tau)$ is the dimensionless abscissa along the beam of the section in which κ_0 is reached (see Figure 1).

We assume that the beam is hinged at its ends and that the axial force N is constant along the axis. As a first approximation, provided that no internal resonance is allowed in the first mode [Nayfeh and Mook 1995; Nayfeh 2000], we choose a solution of the form

$$u(\xi, \tau) = \sqrt{2}\sin(\pi\xi)\eta(\tau). \tag{3-9}$$

Then, from (2-6) and (3-8), taking into account the symmetry of the problem, the averaged Lagrangian $\bar{L}$ becomes

$$\bar{L}(\tau) = 2\int_0^{\frac{1}{2}} \frac{1}{2}\left(\frac{\partial u}{\partial \tau}\right)^2 d\xi - 2\int_0^{\xi_0} \frac{1}{2}\left(\frac{\partial^2 u}{\partial \xi^2}\right)^2 d\xi - 2\int_{\xi_0}^{\frac{1}{2}} \kappa_0\left(3\left|-\frac{\partial^2 u}{\partial \xi^2}\right| - 4\sqrt{\kappa_0\left|-\frac{\partial^2 u}{\partial \xi^2}\right|} + \frac{3}{2}\kappa_0\right) d\xi, \tag{3-10}$$

from which we obtain

$$\bar{L}(\tau) = \frac{1}{2}[\eta'(\tau)]^2 - \pi^4\eta^2(\tau)\xi_0 + \frac{1}{2}\pi^3\eta^2(\tau)\sin(2\pi\xi_0) + -6\sqrt{2}\pi\kappa_0\,|\,\eta(\tau)|\cos(\pi\xi_0)$$
$$+ \frac{16}{\pi}\sqrt{2\kappa_0^3\pi^2\,|\eta(\tau)|}\,E\left(\tfrac{\pi}{4}(1 - 2\xi_0), 2\right) + 3\kappa_0^2\xi_0 - \tfrac{3}{2}\kappa_0^2, \tag{3-11}$$

where we have used the elliptic integral

$$E\left(\tfrac{\pi}{4}(1 - 2\xi_0), 2\right) = \int_0^{\frac{\pi}{4}(1-2\xi_0)} \frac{1}{\sqrt{1 - 2\sin^2 \zeta}}\, d\zeta. \tag{3-12}$$

We can find the abscissa ξ_0 from the relation

$$|\kappa(\xi_0, \tau)| = \kappa_0, \tag{3-13}$$

such that with the help of (2-2) and (3-9), we obtain

$$\xi_0(\eta) = \frac{1}{\pi} \arcsin \frac{\kappa_0}{\pi^2 \sqrt{2}\,|\eta|} \qquad \text{for } |\eta| \geq \frac{\kappa_0}{\pi^2 \sqrt{2}}. \tag{3-14}$$

Moreover, when the beam is entirely in the elastic field, we have

$$\xi_0(\eta) = \tfrac{1}{2} \qquad \text{for } |\eta| < \frac{\kappa_0}{\pi^2 \sqrt{2}}. \tag{3-15}$$

Now, in view of (2-11), the potential function $V(\eta)$ for $|\eta| < \dfrac{\kappa_0}{\pi^2 \sqrt{2}}$ becomes

$$V_{el}(\eta) = \frac{\pi^4 \eta^2}{2}, \tag{3-16}$$

and the potential function for $|\eta| \geq \dfrac{\kappa_0}{\pi^2 \sqrt{2}}$ becomes

$$V_{nl}(\eta) = \pi^4 \eta^2(\tau)\xi_0 - \tfrac{1}{2}\pi^3 \eta^2(\tau) \sin(2\pi \xi_0) + 6\sqrt{2}\pi \kappa_0 |\eta(\tau)| \cos(\pi \xi_0)$$
$$- \frac{16}{\pi} \sqrt{2\kappa_0^3 \pi^2 |\eta(\tau)|}\, E\left(\tfrac{\pi}{4}(1 - 2\xi_0), 2\right) - 3\kappa_0^2 \xi_0 + \tfrac{3}{2}\kappa_0^2. \tag{3-17}$$

In Figure 4, V is plotted as a function of η for different values of κ_0 and compared with the linear elastic case, represented by a parabolic curve.

We can now apply equations (3-16) and (3-17) to relation (2-28) and write

$$\omega = \frac{\pi}{2} \Big/ \int_0^{R_1} \frac{d\eta}{\sqrt{2(a - V_{el}(\eta))}} = \pi^2 \qquad\qquad\qquad \text{for } \eta \leq \frac{\kappa_0}{\pi^2 \sqrt{2}},$$
$$\omega = \frac{\pi}{2} \Big/ \left(\int_0^{\frac{\kappa_0}{\pi^2 \sqrt{2}}} \frac{d\eta}{\sqrt{2(a - V_{el}(\eta))}} + \int_{\frac{\kappa_0}{\pi^2 \sqrt{2}}}^{R_2} \frac{d\eta}{\sqrt{2(a - V_{nl}(\eta))}} \right) \quad \text{for } \eta > \frac{\kappa_0}{\pi^2 \sqrt{2}}, \tag{3-18}$$
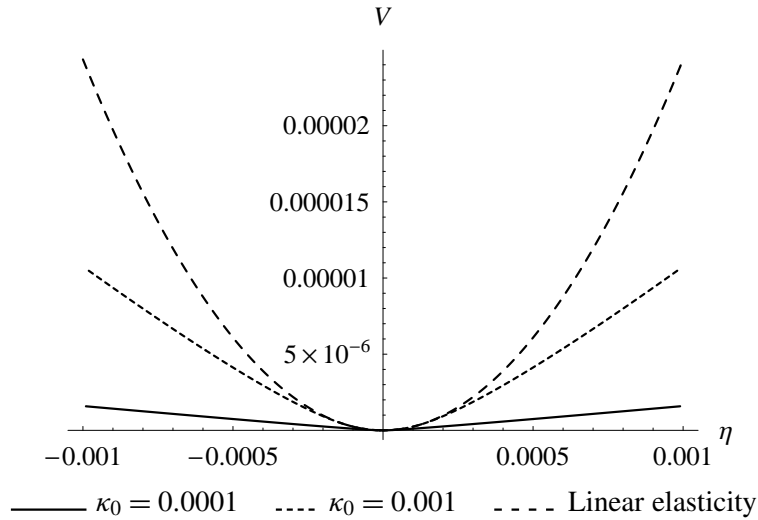
where R_1, R_2 are roots of the equation
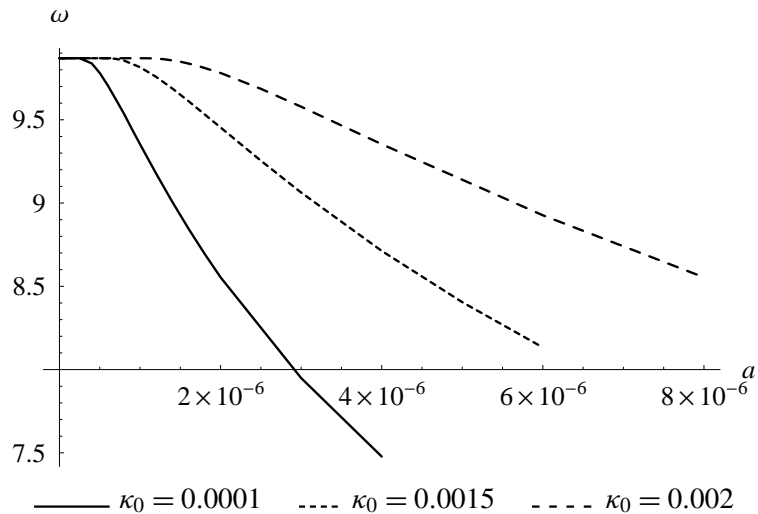
$$a - V(\eta) = 0. \tag{3-19}$$

Equations (3-18) can be solved numerically for different values of the total energy a and the elastic bending limit κ_0 to obtain the curves shown in Figure 5.

By way of example, let us now consider a hinged-hinged beam subjected to an initial deformed shape

$$u(\xi, 0) = A\, \sin(\pi \xi), \qquad A > 0. \tag{3-20}$$

Figure 4. The potential function $V(\eta)$ for different values of κ_0.

Figure 5. The function ω as a function of a, as given by (3-18), for different values of the limit-elastic curvature κ_0.

The deformed shape of the beam is represented in Figure 1 on page 145, where $l\xi_0$ and $l(1 - \xi_0)$ delimit the cracked region.

The particular form chosen for the initial deformed shape, together with the absence of internal resonances in the first mode [Nayfeh and Mook 1995; Nayfeh 2000], allows us to describe the motion of the beam using the unimodal expression (3-9).

We can write the total energy a of the beam as a function of the amplitude A of the motion, observing that

$$\eta(0) = A/\sqrt{2}, \qquad \eta'(0) = 0. \tag{3-21}$$

Therefore, from (3-16), we have

$$a(A, \kappa_0) = V(0) = \tfrac{1}{2}\pi^4 A^2 \bar{\bar{\xi}}_0 - \tfrac{1}{4}\pi^3 A^2 \sin(2\pi \bar{\bar{\xi}}_0) + 6\pi \kappa_0 A \cos(\pi \bar{\bar{\xi}}_0)$$

$$- \frac{16}{\pi}\sqrt{\kappa_0^3 A \pi^2}\, E\left(\tfrac{\pi}{4}(1 - 2\bar{\bar{\xi}}_0), 2\right) - 3\kappa_0^2 \bar{\bar{\xi}}_0 + \tfrac{3}{2}\kappa_0^2, \quad (3\text{-}22)$$

the initial cracked region being delimited by $1 - 2\bar{\bar{\xi}}_0$ and

$$\bar{\bar{\xi}}_0(A, \kappa_0) = \frac{1}{\pi} \arcsin \frac{\kappa_0}{\pi^2 A}. \tag{3-23}$$

Now, from (3-18) we can find the frequency ω of the oscillations as a function of A and κ_0.

4. The cubic approximation

Next, we present a simpler constitutive law that approximates equation (3-7) for values of χ near χ_0. To this aim, we introduce the cubic equation

$$\frac{M_c(\chi)}{\rho bh} = c^2 \chi \left(1 - \bar{\sigma}\chi^2\right), \tag{4-1}$$

where $\bar{\sigma}$ is a positive parameter that depends on the axial force N, which can approximate (3-7) for values of χ in the range $-\sqrt{1/3\bar{\sigma}} \le \chi \le \sqrt{1/3\bar{\sigma}}$, where the cubic function is increasing. Figure 6 shows a comparison of the behavior of equations (3-7) and (4-1) for a given value of N.

From (4-1), we obtain the dimensionless equation

$$F_c(\kappa) = \tfrac{1}{2}\kappa^2 - \sigma \tfrac{1}{4}\kappa^4, \tag{4-2}$$

where $\sigma = \bar{\sigma}/l^2$. This represents a classical cubic nonlinearity problem for softening systems.

If the displacement $u(\xi, \tau)$ is again expressed by (3-9), we can write the potential

$$V(\eta) = \tfrac{1}{2}\pi^4 \eta^2 - \tfrac{3}{8}\sigma \pi^8 \eta^4. \tag{4-3}$$
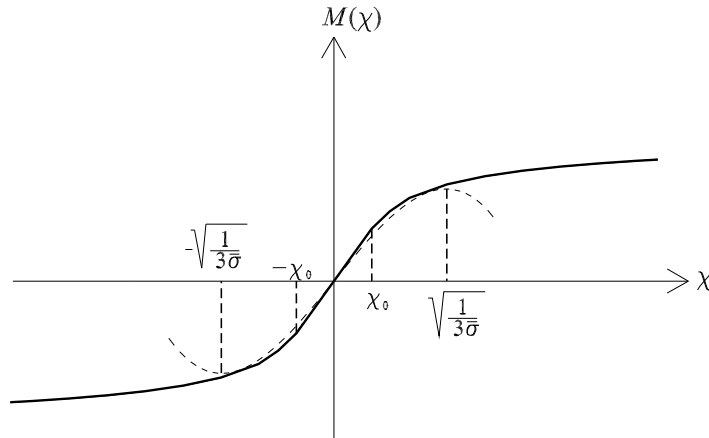
Figure 6. Comparison between equations (3-7) and (4-1).
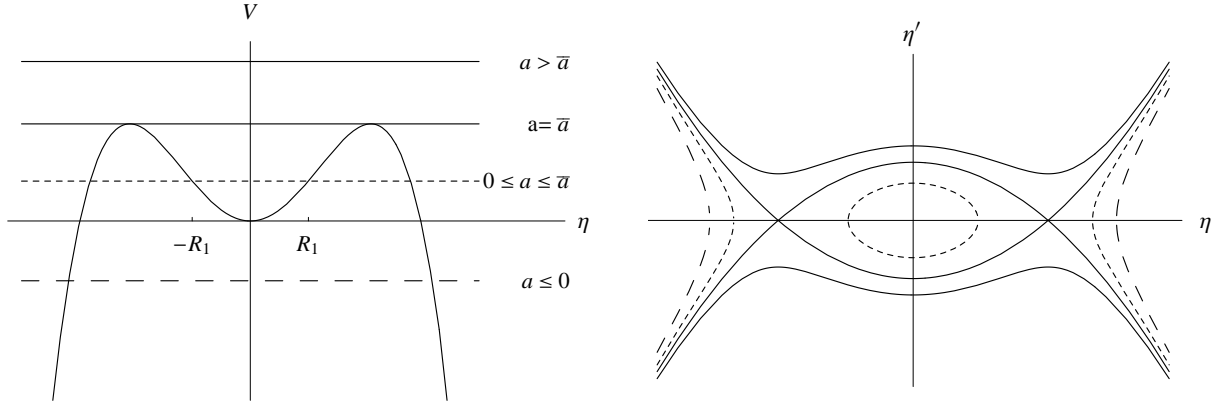
Figure 7. Solutions to the equations of motion for the cubic equation with different values of the total energy a.

Then

$$\omega = 2\pi \Big/ \oint \frac{d\eta}{\sqrt{2(a - \frac{1}{2}\pi^4\eta^2 + \frac{3}{8}\sigma\pi^8\eta^4)}} = \frac{\pi}{2} \Big/ \int_0^{R_1} \frac{d\eta}{\sqrt{2(a - \frac{1}{2}\pi^4\eta^2 + \frac{3}{8}\sigma\pi^8\eta^4)}}, \qquad (4\text{-}4)$$

by (2-28), where

$$R_1 = \frac{\sqrt{2}}{\pi^2}\sqrt{\frac{1 - \sqrt{1 - 6a\sigma}}{3\sigma}} \qquad (4\text{-}5)$$

is the smallest positive root of the equation

$$a - V(\eta) = 0. \qquad (4\text{-}6)$$

If we draw the graph of the function $V(\eta)$ and represent different values of energy a by horizontal lines (see Figure 7), the condition $a \geq V(\eta)$ can be easily studied in the phase plane $(\eta\text{-}\eta')$, observing that, from (2-11), we have

$$\eta' = \sqrt{2(a - V(\eta))}. \qquad (4\text{-}7)$$

For no-tension materials and under the present hypotheses (neglecting geometric nonlinearities and assuming an infinite material compressive strength), periodic motion is possible for every positive value of a, because V, given by (3-16) and (3-17), is a convex function. In this case, we see that periodic solutions, represented by closed trajectories in Figure 7, are possible only for

$$0 \leq a \leq \bar{a} \qquad \text{and} \qquad -R_1 \leq \eta \leq R_1. \qquad (4\text{-}8)$$

From Figure 8, where ω is plotted as a function of a for different values of σ using (4-4), we see that the frequency is a decreasing function of the total energy. All curves originate from the value of the fundamental frequency of the linear beam.

For increasing values of the axial force N, corresponding to decreasing values of σ, the nonlinear behavior becomes weaker.

Let us now consider a hinged-hinged beam subjected to an initial deformation of the form (3-20). With the help of (4-3) and (3-21), we can express the total energy a of the beam as a function of the maximum
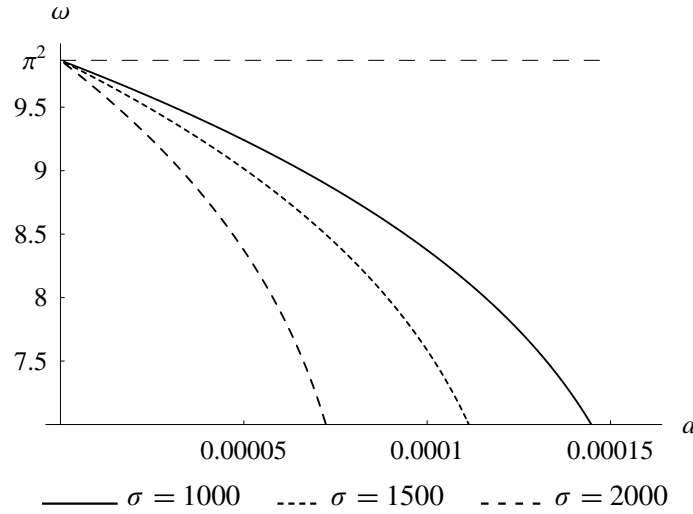
Figure 8. Frequency ω as a function of a for different values of σ.

amplitude A of the motion, $a(A) = V(0) = \frac{1}{4}\pi^4 A^2 - \frac{3}{32}\sigma\pi^8 A^4$. A relation between the fundamental frequency ω and the amplitude A of the motion along the beam can now be obtained by substituting this equality into (4-4).

5. Example applications
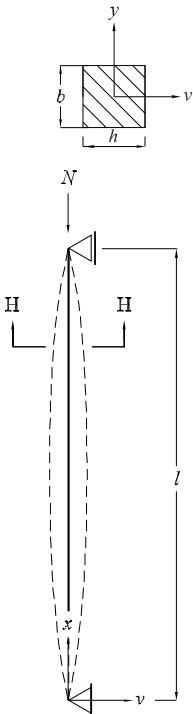
Consider a masonry column, of length l, with a square cross-section, hinged at its supports, as in the figure on the left. Let its dimensions and material properties be $l = 7$ m (beam length), $h = b = 0.6$ m (side of cross section), $\rho = 1800$ kg/m³ (material density), and $E = 3 \cdot 10^9$ Pa (modulus of elasticity). We consider an axial force $N = 10^5$ N applied as shown.

Under the previous hypotheses, we can predict the dynamic characteristics of the beam using the relations (3-18) for no-tension materials and, for curvature values near the elastic limit, relation (4-4) for the cubic constitutive equation.

We choose the following parameter values:

$$c = \sqrt{EJ/(\rho bh)} = 223.607 \text{ m}^2 \text{ / s} \quad \text{elastic constant of the beam}$$
$$\chi_0 = 2N/(Ebh^2) = 0.0003086 \text{ m}^{-1} \quad \text{limit elastic curvature}$$
$$T = 2l^2/(\pi c) = 0.1395 \text{ s} \quad \text{fundamental elastic period}$$
$$\nu = 1/T = 7.17 \text{ Hz} \quad \text{fundamental elastic frequency}$$

Figure 9 shows a plot of the constitutive equation (3-7) together with the corresponding cubic approximation (4-1) for $\bar{\sigma} = 528400$ m². Such a value of $\bar{\sigma}$ is obtained by minimizing the function

$$K(\bar{\sigma}) = \int_0^{\sqrt{1/3\bar{\sigma}}} \left| M_{nt}(\chi) - M_c(\chi, \bar{\sigma}) \right| d\chi,$$
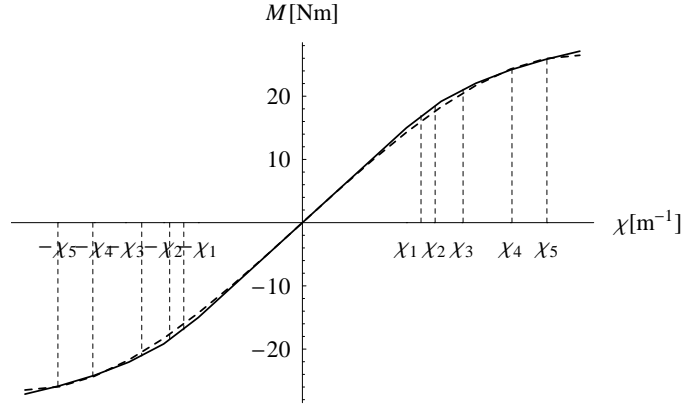
Figure 9. Constitutive equations for the beam section: N.T.M. (solid) and cubic approximation (dashed).

where M_{nt} and M_c are given by (3-7), and (4-1), respectively. We assign the initial displacement

$$v(x, 0) = \bar{A} \sin \frac{\pi x}{l}, \tag{5-1}$$

and consider five cases:

$$\bar{A}_1 = 0.0017 \,\text{m} \quad \chi_1 = \bar{A}_1 \pi^2 / l^2 = 0.00034 \,\text{m}^{-1}$$
$$\bar{A}_2 = 0.0019 \,\text{m} \quad \chi_2 = \bar{A}_2 \pi^2 / l^2 = 0.00038 \,\text{m}^{-1}$$
$$\bar{A}_3 = 0.0023 \,\text{m} \quad \chi_3 = \bar{A}_3 \pi^2 / l^2 = 0.00046 \,\text{m}^{-1}$$
$$\bar{A}_4 = 0.0030 \,\text{m} \quad \chi_4 = \bar{A}_4 \pi^2 / l^2 = 0.00060 \,\text{m}^{-1}$$
$$\bar{A}_5 = 0.0035 \,\text{m} \quad \chi_5 = \bar{A}_5 \pi^2 / l^2 = 0.00070 \,\text{m}^{-1}$$

For beams composed of no-tension materials, the fundamental frequency $v_{nt} = \omega/(2\pi T_c)$ is obtained from the relations (3-18) and (3-22), with

$$\kappa_0 = l\chi_0 = 0.0021605, \qquad A = \frac{\bar{A}}{l}. \tag{5-2}$$

In this way, we obtain for the fundamental frequencies

$$v_{1nt} = 7.166 \,\text{Hz} \quad v_{1nt}/v = 0.999 \qquad (v_{1c} = 7.042 \,\text{Hz} \quad v_{1c}/v = 0.982)$$
$$v_{2nt} = 7.151 \,\text{Hz} \quad v_{2nt}/v = 0.998 \qquad (v_{2c} = 7.010 \,\text{Hz} \quad v_{2c}/v = 0.978)$$
$$v_{3nt} = 7.074 \,\text{Hz} \quad v_{3nt}/v = 0.986 \qquad (v_{3c} = 6.935 \,\text{Hz} \quad v_{3c}/v = 0.967)$$
$$v_{4nt} = 6.849 \,\text{Hz} \quad v_{4nt}/v = 0.955 \qquad (v_{4c} = 6.766 \,\text{Hz} \quad v_{4c}/v = 0.944)$$
$$v_{5nt} = 6.662 \,\text{Hz} \quad v_{5nt}/v = 0.929 \qquad (v_{5c} = 6.613 \,\text{Hz} \quad v_{5c}/v = 0.922)$$

where the corresponding values for the cubic approximation, given by (4-4), are supplied in parentheses.

The results were compared with those obtained by the numerical methods described in [Lucchesi and Pintucchi 2007]. The displacements of the midpoint of the beam have been analyzed via Fourier transform, and the following fundamental frequencies were found:

$$\nu_{1num} = 7.14\,\text{Hz} \quad \nu_{1num}/\nu = 0.999$$
$$\nu_{2num} = 7.12\,\text{Hz} \quad \nu_{2num}/\nu = 0.993$$
$$\nu_{3num} = 7.02\,\text{Hz} \quad \nu_{3num}/\nu = 0.979$$
$$\nu_{4num} = 6.76\,\text{Hz} \quad \nu_{4num}/\nu = 0.943$$
$$\nu_{5num} = 6.54\,\text{Hz} \quad \nu_{5num}/\nu = 0.912$$

Figure 10 (which shows, by way of example, the Fourier transform of the numerical data corresponding to $\bar{A}_4$) highlights the lower amplitude peaks at the expense of the predominant peak of the fundamental frequency ν_{4num}. Other superharmonic terms are observable near $\nu = 7\nu_4$, the amplitude of which is just 100 times lower than the amplitude of the fundamental. Therefore, the numerical results appear to confirm that the displacements of the beam can be represented by the unimodal expression (3-9), by using the fundamental frequency obtained from (3-18).
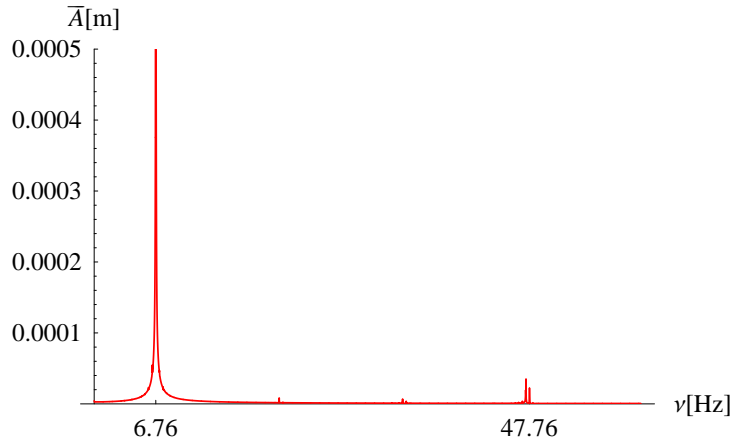
Figure 10. The discrete Fourier transform of the numerical data for $\bar{A} = 0.003$m.
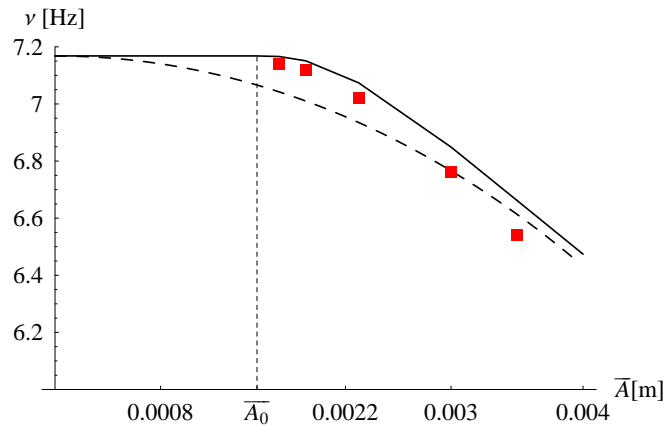
Figure 11. Frequencies obtained via the cubic equation (dashed curve) and the no-tension equation (solid) are compared with the numerical solution (red squares).
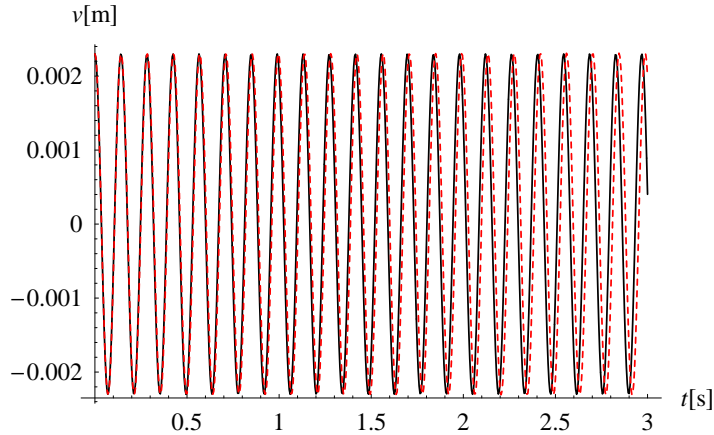
Figure 12. Midpoint displacement of the no-tension material beam for an initial amplitude of $\bar{A}_3 = 0.0023$ m. Solid curve: analytic solution, given by $v(t) = \bar{A}_3 \cos(2\pi v_{3nt})$. Dashed curve: numerical calculation. The curves are indistinguishable in the scale of the graph for the first few cycles.

Figure 11 compares the fundamental frequencies obtained using the no-tension equation, the cubic approximation, and the numerical code. The behavior of the cubic equation exhibits more marked softening for small values of $\bar{A}$ due to the absence of the linear elastic region. This difference is reduced for larger values of the amplitude. The numerical results start at values near the no-tension curve and exhibit a more rapid frequency decrease for greater values of $\bar{A}$.

Lastly, Figure 12 shows the displacement of the midpoint of the beam as a function of time, comparing the explicit solution with the numerical solution.

6. Conclusions

The method presented in this paper yields an explicit relation between the fundamental frequency and the amplitude of the motion for freely vibrating beams composed of nonlinear elastic materials. This method has been applied to slender masonry structures using the constitutive equation for no-tension materials [Zani 2004]. The frequencies, determined analytically for some example applications, are in good agreement with the frequencies predicted from applications of the numerical method presented in [Lucchesi and Pintucchi 2007].

Acknowledgements

References

[De Falco and Lucchesi 2002] A. De Falco and M. Lucchesi, "Stability of columns with no tension strength and bounded compressive strength and deformability, I: Large eccentricity", *Int. J. Solids Struct.* **39**:25 (2002), 6191–6210.

[Del Piero 1989] G. Del Piero, "Constitutive equation and compatibility of the external loads for linear elastic masonry-like materials", *Meccanica* (*Milano*) **24**:3 (1989), 150–162.

[Di Pasquale 1992] S. Di Pasquale, "New trends in the analysis of masonry structures", *Meccanica* (*Milano*) **27**:3 (1992), 173–184.

[Gambarotta and Lagomarsino 1997] L. Gambarotta and S. Lagomarsino, "Damage models for the seismic response of brick masonry shear walls, II: The continuum model and its applications", *Earthquake Eng. Struct. Dyn.* **26**:4 (1997), 441–462.

[Girardi 2009] M. Girardi, "Analytical and numerical methods for the dynamic analysis of slender masonry structures", in *Atti del XIX Congresso dell'Associazione Italiana di Meccanica Teorica ed Applicata* (Paper 103, session ST-09b; full version on accompanying CD), edited by S. Lenci, Aras Edizioni, Ancona, 2009.

[Girardi and Lucchesi 2006] M. Girardi and M. Lucchesi, "Sulle vibrazioni flessionali di travi costituite da materiale non resistente a trazione", pp. 135–144 in *WONDERmasonry–Workshop on Design for Rehabilitation of Masonry Structures: tecniche di modellazione e progetto per interventi sul costruito in muratura* (Firenze, 2006), edited by P. Spinelli, Polistampa, Firenze, 2006.

[Lucchesi and Pintucchi 2007] M. Lucchesi and B. L. Pintucchi, "A numerical model for non-linear dynamic analysis of slender masonry structures", *Eur. J. Mech. A Solids* **26**:1 (2007), 88–105.

[Lucchesi et al. 2008] M. Lucchesi, C. Padovani, G. Pasquinelli, and N. Zani, *Masonry constructions: mechanical models and numerical applications*, Lecture Notes in Applied and Computational Mechanics **39**, Springer, Berlin, 2008.

[MiBAC 2006] Ministero per i Beni e le Attività Culturali, *Linee guida per la valutazione e riduzione del rischio sismico del patrimonio culturale con riferimento alle norme tecniche per le costruzioni*, edited by L. Moro, Gangemi, Roma, 2006.

[Nayfeh 2000] A. H. Nayfeh, *Nonlinear interactions: analytical, computational, and experimental methods*, Wiley, New York, 2000.

[Nayfeh and Mook 1995] A. H. Nayfeh and D. T. Mook, *Nonlinear oscillations*, Wiley, New York, 1995.

[Norme tecniche 2008] Ministero delle Infrastrutture, "Nuove norme tecniche per le costruzioni", *Gazz. Uff.* **29**:Suppl. Ordinario n. 30 (2008).

[Petrini et al. 1999] V. Petrini, S. Casolo, and F. Doglioni, "Models for vulnerability analysis of monuments and strengthening criteria", pp. 179–198 in *Proceedings of the Eleventh European Conference on Earthquake Engineering: invited lectures* (Paris, 1998), edited by P. Bisch et al., Balkema, Rotterdam, 1999.

[Whitham 1974] G. B. Whitham, *Linear and nonlinear waves*, Wiley, New York, 1974.

[Zani 2004] N. Zani, "A constitutive equation and a closed-form solution for no-tension beams with limited compressive strength", *Eur. J. Mech. A Solids* **23**:3 (2004), 467–484.

MARIA GIRARDI: *Istituto di Scienza e Tecnologie dell'Informazione "A. Faedo", CNR, Via G. Moruzzi 1, 56124 Pisa, Italy*
Maria.Girardi@isti.cnr.it

MASSIMILIANO LUCCHESI: *Università di Firenze, Dipartimento di Costruzioni, Piazza Brunelleschi 6, 50121 Firenze, Italy*
massimiliano.lucchesi@unifi.it

MULTISCALE ANALYSIS OF NANOSCALE THIN FILM CONSIDERING SURFACE EFFECTS: THERMOMECHANICAL PROPERTIES

JINBOK CHOI, MAENGHYO CHO AND WONBAE KIM

The classical model for a thin film, based on continuum theory, is independent of size, and ignores surface effects. But the surface-to-bulk ratio becomes very large in small-scale structures such as nanofilms, nanowires, and nanobeams, and surface effects play an important role. Molecular dynamics simulation has been a conventional way to analyze these ultrathin structures, but structures in the range between submicro and micro are difficult to analyze by molecular dynamics simulation due to the restrictions of computing resources and time. In the present study, a continuum-based, size-dependent model is developed for predicting the thermomechanical properties of nanoscale structures, especially thin films. The proposed continuum-based thin plate finite element is efficient and reliable for the prediction of nanoscale film behavior.

1. Introduction

As the applications of nanosized structures such as thin films, nanobeams, and nanowires have increased in the field of electromechanical systems, the analysis of the physical and thermomechanical properties of these structures has been an issue in the design of these devices and the prediction of their performance.

The properties of nanosized structures can differ sharply from the bulk properties of the same material [Dingreville et al. 2005; Shenoy 2005], because surface effects, which are negligible in macrosized materials, play a dominant role as the surface-to-volume ratio becomes larger. These phenomena have been investigated in previous works with both experiments and molecular dynamics (MD) simulations. Cuenot et al. [2004] studied the surface tension effect on the mechanical properties of nanomaterials with electrostatic resonant-contact atomic force microscopy. The elastic properties of a silicon nanocantilever were calculated via molecular dynamics techniques, and it was shown that the elastic modulus decreases as the thickness of the specimen decreases [Park et al. 2005]. Miller and Shenoy [2000] and Cammarata and Sieradzki [1989] demonstrated that this size dependence arises due to the increasing importance that surfaces play as structures become smaller. It was shown by Cammarata [1994] that for a solid with one or more dimensions under 10 nm, the surface stress could be a principal factor in determining behavior. It was also shown that several kinetic and thermodynamic properties of thin polymer film could be changed by decreasing the film thickness, due to the surface and interface effects [Lang et al. 2006]. The elastic properties of ZnO nanofilms with different film thicknesses, surface orientations, and loading directions were investigated in Cao and Chen [2008] using molecular mechanics. Song and Huang [2009] studied

the effects of surface stress on bending behavior of nanowires with incremental deformation theory and a high-order continuum model was developed by Song et al. [2010] to study wave propagation in nanowires with surface effects. Some other researchers also considered size-dependent elasticity of nanowires due to nonlinearity [Liang et al. 2005; Park and Klein 2008]. But in this study we are focusing on prediction of the thermoelastic properties of thin film structures under the assumption of linear elasticity considering small deformation and temperature change.

Recently, it has become possible to simulate these nanosized structures with MD simulations because of the improvement in their numerical techniques and today's computing power, but it is still difficult to simulate structures in the range between the submicro and microscale due to restrictions of computing resources and time. MD simulations are still limited to problems of several million atoms for just a few nanoseconds. But it is often necessary to repeatedly analyze such structures to get an optimized design in practical applications. It is not efficient to apply the classical MD simulations to these problems. Therefore, continuum methods are appropriate for these problems where it is not tractable to apply the classical MD simulation. There have been several approaches to analyzing nanostructures based on continuum theories. Gao et al. [2006] suggested a finite element model to describe the size-dependent mechanical properties of nanostructures but did not try to obtain the surface elastic constants, and temperature effects were not considered in their formulation. An energy-based continuum model for the analysis of nanostructures was developed by Park et al. [2006] by adopting theories utilized in the Cauchy–Born rules. They also decomposed the total potential energy of the system into a bulk energy component and a surface energy component, but define the strain energy in terms of a relatively simple pair potential.

In the present study, the continuum-based method is considered to predict the overall thermomechanical properties of nanoscale structures. A general model for elastically isotropic solids with surface stress was suggested by [Gurtin and Murdoch 1975a; 1975b; 1978]. This model was adopted recently by some authors to analyze the elastic responses of nanoscale thin films [Lim and He 2004; Lu et al. 2006]. We especially focus on the investigation of the thermomechanical properties in thin film with a thickness ranging from a few nanometers to several tens of nanometers, and the finite element method (FEM) for the thin film structure is also implemented based on the continuum model. The proposed continuum-based thin film FEM is efficient and reliable for the prediction of nanoscale film behavior. Basically, the governing equations of this continuum model are based on the modified Kirchhoff plate theory, including surface effects [Lim and He 2004; Lu et al. 2006]. These equations can describe the dominant surface effects as the thickness of the thin film becomes very small [Miller and Shenoy 2000]. The conventional thin plate continuum model does not contain the surface energy term because this effect is negligibly small in the macroscale, as mentioned above; however, the surface energy needs to be considered in these nanosized structures. The present continuum model considering the size effect needs three surface parameters to represent the surface effects of the thin film. In this study, the necessary surface parameters are obtained from the MD simulations. Reliable and accurate surface parameters are essential for guaranteeing the accuracy of the solution of the continuum-based thin film FEM.

(a)   (b)
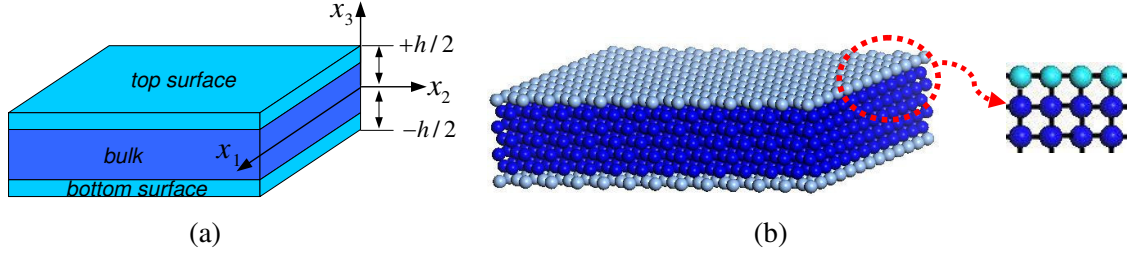
Figure 1. Thin film structures for the continuum model (a) and atomistic structure of thin film (b): the alignments of bond chains of an atom in the surface and bulk are different.

2. Equilibrium equation of the thin film considering surface effects

Kirchhoff plate theory considering surface effects. For a thin film structure with a very small length scale in the thickness direction, a midplane, along with top and bottom surface layers of S^+ and S^- at $x_3 = \pm h/2$, can be defined, as shown in Figure 1a. In the figure the top and bottom surfaces are shown with finite thickness, to stress that additional surface energy has to be added to the classical Kirchhoff thin plate theory in order to consider the surface effects, but in fact, the surface layers do not have thickness in our continuum model.

The reason we consider the surface and bulk energy separately is that the atoms in the surface layers have fewer neighbors and consequently excess energy over atoms in the bulk (see Figure 1b). This energy difference results in unique and interesting properties of nanosized thin film structures.

In Kirchhoff thin plate theory, the displacement fields of the bulk layer are defined as

$$u_\alpha = u_\alpha^0 - x_3 u_{3,\alpha}^0, \qquad u_3 = u_3^0. \tag{1}$$

The displacements of the top and bottom surface layers (s^+, s^-) are u_α^{S+}, u_α^{S-}, u_3^{S+}, and u_3^{S-}. The displacement continuity conditions at the interface between the interior layer and surface layers can be represented as

$$
\begin{aligned}
u_\alpha^{s-} &= u_\alpha\big|_{x_3=-h/2} = (u_\alpha^o - x_3 w_{,\alpha})\big|_{x_3=-h/2} = u_\alpha^o + \frac{h}{2} w_{,\alpha}, & u_3^{s+} &= w, \\
u_\alpha^{s+} &= u_\alpha\big|_{x_3=h/2} = (u_\alpha^o - x_3 w_{,\alpha})\big|_{x_3=h/2} = u_\alpha^o - \frac{h}{2} w_{,\alpha}, & u_3^{s-} &= w.
\end{aligned}
\tag{2}
$$

Temperature effects are considered in this study, so the temperature field is assumed to be linear through the thickness as $\Delta T(x_1, x_2) = \Delta T_1 + x_3 \Delta T_2$. The temperature change of the upper (ΔT^+) and lower (ΔT^-) surfaces of the thin film are given in the following form, respectively:

$$\Delta T^+ = \Delta T_1 + \frac{h}{2} \Delta T_2, \qquad \Delta T^- = \Delta T_1 - \frac{h}{2} \Delta T_2. \tag{3}$$

The virtual work principle is adopted to derive the governing equation of the thin film including the surface energy contribution. The total virtual work is given in the following form for a static problem: $\delta\Pi = \delta U - \delta W_E$, where δU is the variation of the internal strain energy, and the variation of the external

virtual work is given as

$$\delta W_E = \int_\Omega p_\alpha \, \delta u_\alpha^0 + p_3 \, \delta w \, dA, \quad \text{where} \quad dA = dx_1 \, dx_2, \tag{4}$$

where p_α is the tangential force intensity per unit area on the reference surface and p_3 is the transversal force intensity to the reference surface. The variation of the internal strain energy (δU) consists of the bulk energy and surface energy variations: $\delta U = \delta U_{\text{bulk}} + \delta U_{\text{surf}}$. The internal virtual bulk energy of the plate under the Kirchhoff assumption is written as

$$
\begin{aligned}
\delta U_{\text{bulk}} &= \int_v \sigma_{ij} \, \delta \varepsilon_{ij} \, dv = \int_\Omega \int_{-h/2}^{h/2} \sigma_{\alpha\beta} (\delta \varepsilon_{\alpha\beta}^0 - x_3 \, \delta w_{,\alpha\beta}) \, dx_3 dA \\
&= \int_\Omega \int_{-h/2}^{h/2} \sigma_{\alpha\beta} \frac{1}{2} (\delta u_{\alpha,\beta}^0 + \delta u_{\beta,\alpha}^0) - \sigma_{\alpha\beta} x_3 \, \delta w_{,\alpha\beta} \, dx_3 dA \\
&= \int N_{\alpha\beta} \, \delta u_{\alpha,\beta}^0 - M_{\alpha\beta} \, \delta w_{,\alpha\beta} \, dA, \quad \text{where} \quad \int_{-h/2}^{h/2} (\sigma_{\alpha\beta}, \sigma_{\alpha\beta} x_3) \, dx_3 = (N_{\alpha\beta}, M_{\alpha\beta}).
\end{aligned}
\tag{5}
$$

The surface internal virtual energy is expressed by

$$\delta U_{\text{surf}} = \int_{\Omega^+} \tau_{\alpha\beta}^+ \, \delta \varepsilon_{\alpha\beta}^{s+} + \tau_{\alpha3}^+ \, \delta \gamma_{\alpha3}^{s+} dA + \int_{\Omega^+} \tau_{\alpha\beta}^- \, \delta \varepsilon_{\alpha\beta}^{s-} + \tau_{\alpha3}^- \, \delta \gamma_{\alpha3}^{s-} \, dA. \tag{6}$$

Using the strain-displacement relationship in the surface, the surface internal virtual work can be written as

$$
\begin{aligned}
\delta U_{\text{surf}} &= \int_{\Omega^+} \tau_{\alpha\beta}^+ \, \delta \varepsilon_{\alpha\beta}^{s+} + \tau_{\alpha3}^+ \delta (u_{\alpha,3}^{s+} + u_{3,\alpha}^{s+}) \, dA + \int_{\Omega^+} \tau_{\alpha\beta}^- \delta \varepsilon_{\alpha\beta}^{s-} + \tau_{\alpha3}^- \delta (u_{\alpha,3}^{s-} + u_{3,\alpha}^{s-}) \, dA \\
&= \int_{\Omega^+} \tau_{\alpha\beta}^+ \delta \varepsilon_{\alpha\beta}^{s+} + \tau_{\alpha3}^+ \delta (u_{3,\alpha}^{s+}) \, dA + \int_{\Omega^+} \tau_{\alpha\beta}^- \delta \varepsilon_{\alpha\beta}^{s-} + \tau_{\alpha3}^- \delta (u_{3,\alpha}^{s-}) \, dA.
\end{aligned}
\tag{7}
$$

By replacing the surface displacements $u_i^{s\pm}$ in (7) with the bulk displacements u_α and w using the displacement continuity conditions in (2), the final surface virtual work becomes

$$\delta U_{\text{surf}} = \int_{\Omega^+} \tau_{\alpha\beta}^+ \, \delta \left(u_{\alpha,\beta}^0 - \frac{h}{2} w_{,\alpha\beta} \right) + \tau_{\alpha3}^+ \, \delta (u_{3,\alpha}^{s+}) \, dA + \int_{\Omega^+} \tau_{\alpha\beta}^- \left(u_{\alpha,\beta}^0 + \frac{h}{2} w_{,\alpha\beta} \right) + \tau_{\alpha3}^- \, \delta (u_{3,\alpha}^{s-}) \, dA. \tag{8}$$

Here, the domains Ω^+ and Ω^- are defined at $x_3 = +h/2$ and $x_3 = -h/2$, respectively, but are all equal to the midplane domain (Ω) for plate configurations. Therefore, the surface virtual work can be rewritten as

$$\delta U_{\text{surf}} = \int_{\Omega^+} (\tau_{\alpha\beta}^+ + \tau_{\alpha\beta}^-) \, \delta u_{\alpha,\beta}^0 + \frac{h}{2} (-\tau_{\alpha\beta}^+ + \tau_{\alpha\beta}^-) \, \delta w_{,\alpha\beta} + (\tau_{\alpha3}^+ + \tau_{\alpha3}^-) \, \delta (w_{,\alpha}) \, dA. \tag{9}$$

Then, we can get the final variational equation as follows:

$$
\begin{aligned}
\delta \Pi &= \delta U (\delta U_{\text{bulk}} + \delta U_{\text{surf}}) - \delta W_E \\
&= \int_\Omega (N_{\alpha\beta} + \tau_{\alpha\beta}^+ + \tau_{\alpha\beta}^-) \, \delta u_{\alpha,\beta}^o - \left\{ M_{\alpha\beta} + \frac{h}{2} (\tau_{\alpha\beta}^+ - \tau_{\alpha\beta}^-) \right\} \delta w_{,\alpha\beta} \\
&\qquad\qquad + (\tau_{\alpha3}^+ + \tau_{\alpha3}^-) \, \delta w_{,\alpha} \, dA - \int_\Omega p_\alpha \, \delta u_\alpha^0 + p_3 \, \delta w \, dA.
\end{aligned}
\tag{10}
$$

From (10), the following equilibrium equations can be obtained (see the Appendix):

$$N_{\alpha\beta,\beta} + \tau_{\alpha\beta,\beta}^{+} + \tau_{\alpha\beta,\beta}^{-} + p_\alpha = 0, \qquad M_{\alpha\beta,\alpha\beta} + \frac{h}{2}(\tau_{\alpha\beta,\alpha\beta}^{+} - \tau_{\alpha\beta,\alpha\beta}^{-}) + (\tau_{\alpha3,\alpha}^{+} + \tau_{\alpha3,\alpha}^{-}) + p_3 = 0. \quad (11)$$

If we set $N_{\alpha\beta}^{*} = N_{\alpha\beta} + \tau_{\alpha\beta}^{+} + \tau_{\alpha\beta}^{-}$ and $M_{\alpha\beta}^{*} = M_{\alpha\beta} + \frac{h}{2}(\tau_{\alpha\beta}^{+} + \tau_{\alpha\beta}^{-})$, (11) can be simplified as

$$N_{\alpha\beta,\beta}^{*} + p_\alpha = 0, \quad M_{\alpha\beta,\alpha\beta}^{*} + (\tau_{\alpha3,\alpha}^{+} + \tau_{\alpha3,\alpha}^{-}) + p_3 = 0. \tag{12}$$

The boundary conditions can be of the following forms:

- u_α^0 prescribed or $N_{\alpha\beta}^{*} n_\beta$ specified.

- $\dfrac{\partial w}{\partial n}$ prescribed or $M_{\alpha\beta}^{*} n_\alpha n_\beta$ specified.

- w prescribed or $\dfrac{\partial (M_{\alpha\beta}^{*} t_\beta)}{\partial t} + M_{\alpha\beta,\beta}^{*} + (\tau_{\alpha3}^{+} + \tau_{\alpha3}^{-})$ specified.

Constitutive equations for the bulk and surface layers. If the bulk and surface layers are assumed to be homogeneous and isotropic material, the constitutive equation for the bulk layers can be expressed as

$$\sigma_{ij} = \lambda \varepsilon_{kk} \delta_{ij} + 2\mu \varepsilon_{ij} + \frac{E\alpha}{1-\nu} \Delta T \delta_{ij}, \tag{13}$$

where λ and μ are Lamé's constants, α is the coefficient of thermal expansion, and ΔT is the temperature change. In addition, the face-centered cubic crystal structures exhibit elastic anisotropy, which means the modulus is dependent on orientation. Therefore, the following stress-strain relationship is used for the bulk in this study:

$$\begin{Bmatrix} \sigma_{11} \\ \sigma_{22} \\ \tau_{12} \end{Bmatrix} = \begin{bmatrix} E/(1-\nu^2) & E\nu/(1-\nu^2) & 0 \\ E\nu/(1-\nu^2) & E/(1-\nu^2) & 0 \\ 0 & 0 & G \end{bmatrix} \begin{Bmatrix} \varepsilon_{11} \\ \varepsilon_{22} \\ \gamma_{12} \end{Bmatrix} + \frac{E\alpha}{1-\nu} \begin{Bmatrix} \Delta T \\ \Delta T \\ 0 \end{Bmatrix}, \tag{14}$$

where E and G are the Young's modulus and shear modulus, respectively, and ν is the Poisson's ratio. The constitutive equations for the surface layers are given by [Gurtin and Murdoch 1975a; 1975b; 1978], and these surface constitutive equations are modified to consider the temperature effects by including the surface thermal constant (Θ) [Murdoch 1976]. If the top and bottom surface layers consist of the same material, the equations are expressed as

$$\tau_{\alpha\beta}^{\pm} = \tau_0 \delta_{\alpha\beta} + (\mu_0 - \tau_0)(u_{\alpha,\beta}^{\pm} + u_{\beta,\alpha}^{\pm}) + (\lambda_0 + \tau_0)u_{\gamma,\gamma}^{\pm} \delta_{\alpha\beta} + \tau_0 u_{\alpha,\beta}^{\pm} - \Theta \Delta T^{\pm} \delta_{\alpha\beta}, \quad \tau_{\alpha3}^{\pm} = \tau_0 u_{3,\alpha}^{\pm}, \tag{15}$$

where τ_0 is the surface residual tension, and μ_0 and λ_0 are the surface Lamé's constants.

The surface stress is usually defined as $\tau_{\alpha\beta} = \tau_0 \delta_{\alpha\beta} + S_{\alpha\beta\gamma\delta}\varepsilon_{\gamma\delta}$ [Miller and Shenoy 2000], where $\tau_{\alpha\beta}$ is the surface stress, $S_{\alpha\beta\gamma\delta}$ is surface elastic modulus tensor, and τ_0 is the surface residual tension when the bulk is unstrained. Therefore, the surface stress $\tau_{\alpha\beta}$ depends on the strain but the constant τ_0 does not change with the relaxation of the thin film with different thicknesses. We obtained this surface residual tension τ_0 from the MD simulations and used it in our finite element model. A rigorous formed surface constitutive relation can be obtained through the surface-Cauchy–Born rule considering atomic potential [Park et al. 2006]. However, the present approach is valid for linearized small deformation problems.

3. Finite element formulation including surface effects

The finite element formulation is derived from the variational equation (10). Before writing the final variational equation for the stiffness matrix, we introduce the necessary notation. First set

$$T_1 = \{\Delta T_1, \Delta T_1, 0\}^T, \qquad T_2 = \{\Delta T_2, \Delta T_2, 0\}^T, \qquad T_m = \{2\tau_0, 2\tau_0, 0\}^T.$$

Then write the generalized resultant forces N^* and moments M^* in matrix form as

$$\begin{Bmatrix} N_{11}^* \\ N_{22}^* \\ N_{12}^* \end{Bmatrix} = \begin{Bmatrix} 2\tau_0 \\ 2\tau_0 \\ 0 \end{Bmatrix} - \left(\frac{Eh\alpha}{1-\nu} + 2\Theta \right) T_1 + C_m \begin{Bmatrix} u_{1,1} \\ u_{2,2} \\ u_{1,2} + u_{2,1} \end{Bmatrix}, \tag{16}$$

$$\begin{Bmatrix} M_{11}^* \\ M_{22}^* \\ M_{12}^* \end{Bmatrix} = -\frac{h^2}{2} \Theta T_2 - C_b \begin{Bmatrix} w_{,11} \\ w_{,22} \\ w_{,12} + w_{,21} \end{Bmatrix}, \tag{17}$$

where the constitutive matrices C_m and C_b for the membrane and bending parts are given by

$$C_m = \begin{bmatrix} \dfrac{Eh}{1-\nu^2} + 4\mu_0 + 2\lambda_0 & \dfrac{E\nu h}{1-\nu^2} + 2\lambda_0 + 2\tau_0 & 0 \\ \dfrac{E\nu h}{1-\nu^2} + 2\lambda_0 + 2\tau_0 & \dfrac{Eh}{1-\nu^2} + 4\mu_0 + 2\lambda_0 & 0 \\ 0 & 0 & Gh + 2\mu_0 - \tau_0 \end{bmatrix}, \tag{18}$$

$$C_b = \begin{bmatrix} \dfrac{Eh^3}{12(1-\nu^2)} + \dfrac{h^2}{2}(2\mu_0 + \lambda_0) & \dfrac{E\nu h^3}{12(1-\nu^2)} + \dfrac{h^2}{2}(\lambda_0 + \tau_0) & 0 \\ \dfrac{E\nu h^3}{12(1-\nu^2)} + \dfrac{h^2}{2}(\lambda_0 + \tau_0) & \dfrac{Eh^3}{12(1-\nu^2)} + \dfrac{h^2}{2}(2\mu_0 + \lambda_0) & 0 \\ 0 & 0 & \dfrac{Gh^3}{12} + \dfrac{h^2}{2}\mu_0 \end{bmatrix}. \tag{19}$$

We next introduce the vectors

$$\vec{q} = \{u_i, v_i\}^T \quad \text{and} \quad \vec{d} = \{w_i, \theta_{xi}, \theta_{yi}\}^T,$$

representing respectively the nodal degrees of freedom for the membrane components and the element degrees of freedom for the bending components.

Using the area coordinates L_1, L_2, L_3 as interpolation functions, we can write

$$\vec{u} = \sum_{i=1}^{3} \begin{bmatrix} L_i & 0 \\ 0 & L_i \end{bmatrix} \begin{Bmatrix} u_i \\ v_i \end{Bmatrix} = N_m \vec{q} \quad \text{and} \quad w = \sum_{i=1}^{3} \begin{bmatrix} N_i & N_{xi} & N_{yi} \end{bmatrix} \begin{Bmatrix} w_i \\ \theta_{xi} \\ \theta_{yi} \end{Bmatrix} = N_b^T \vec{d} \tag{20}$$

for the interpolation of in-plane displacements $\vec{u}$ (using isoparametric mapping) and the out-of-plane displacement w (using subparametric mapping).

We can now write the final variational equation for the stiffness matrix as

$$\delta\Pi = \delta U - \delta W_E = \int_\Omega \boldsymbol{N}^* \, \delta\vec{\varepsilon} + \boldsymbol{M}^* \, \delta\vec{\psi} + 2\tau_0 \, \delta\vec{\phi} \, dA - \int_\Omega \vec{p} \, \delta\vec{u} + \vec{p}_3 \, \delta\vec{w} \, dA$$

$$= \int_\Omega \delta\vec{q}^T \boldsymbol{B}_m^T \boldsymbol{T}_m + \delta\vec{q}^T \boldsymbol{B}_m^T \boldsymbol{C}_m \boldsymbol{B}_m \vec{q} - \delta\vec{q}^T \boldsymbol{B}_m^T \Big(\frac{Eh\alpha}{1-\nu} + 2\Theta\Big) \boldsymbol{T}_1 - \delta\vec{d}^T \boldsymbol{B}_b^T \boldsymbol{C}_b \boldsymbol{B}_b \vec{d} + 2\tau_0 \, \delta\vec{d}^T \boldsymbol{B}^T$$

$$-\delta\vec{d}^T \boldsymbol{B}_b^T \frac{h^2}{2} \Theta \boldsymbol{T}_2 \, dA - \int_\Omega \delta\vec{q}^T \boldsymbol{N}_m^T \vec{p} + \delta\vec{d}^T \boldsymbol{N}_b^T \vec{p}_3 \, dA = 0, \quad (21)$$

where

$$\vec{\varepsilon} = \begin{Bmatrix} \partial u/\partial x \\ \partial v/\partial y \\ \partial v/\partial x + \partial u/\partial y \end{Bmatrix} = \sum_{i=1}^{3} \begin{bmatrix} \partial L_i/\partial x & 0 \\ 0 & \partial L_i/\partial y \\ \partial L_i/\partial y & \partial L_i/\partial x \end{bmatrix} \begin{Bmatrix} u_i \\ v_i \end{Bmatrix} \equiv \boldsymbol{B}_m^T \vec{q}, \quad (22)$$

$$\vec{\psi} = \begin{Bmatrix} \partial^2 w/\partial x^2 \\ \partial^2 w/\partial y^2 \\ 2\partial^2 w/\partial x\partial y \end{Bmatrix} = \sum_{i=1}^{3} \begin{bmatrix} \partial^2 N_i/\partial x^2 & \partial^2 N_{xi}/\partial x^2 & \partial^2 N_{yi}/\partial x^2 \\ \partial^2 N_i/\partial y^2 & \partial^2 N_{xi}/\partial y^2 & \partial^2 N_{yi}/\partial y^2 \\ 2\partial^2 N_i/\partial x\partial y & 2\partial^2 N_{xi}/\partial x\partial y & 2\partial^2 N_{yi}/\partial x\partial y \end{bmatrix} \begin{Bmatrix} w_i \\ \theta_{xi} \\ \theta_{yi} \end{Bmatrix} = \boldsymbol{B}_b^T \vec{d}, \quad (23)$$

$$\vec{\phi} = \begin{Bmatrix} \partial w/\partial x \\ \partial w/\partial y \end{Bmatrix} = \sum_{i=1}^{3} \begin{bmatrix} \partial N_i/\partial x & \partial N_{xi}/\partial x & \partial N_{yi}/\partial x \\ \partial N_i/\partial y & \partial N_{xi}/\partial y & \partial N_{yi}/\partial y \end{bmatrix} \begin{Bmatrix} w_i \\ \theta_{xi} \\ \theta_{yi} \end{Bmatrix} = \boldsymbol{B}^T \vec{d}. \quad (24)$$

The vector $\vec{\psi}$ represents the curvature. The load vectors resulting from the temperature change are

$$\int_\Omega \boldsymbol{B}_m^T \Big(\frac{Eh\alpha}{1-\nu} + 2\Theta\Big) \boldsymbol{T}_1 \, dA, \qquad \int_\Omega \boldsymbol{B}_b^T \Big(\frac{h^2}{2}\Big) \Theta \boldsymbol{T}_2 \, dA,$$

for the membrane and bending components in (21).

In Kirchhoff plate theory, the governing differential equations require transverse displacement and slope continuity across the element boundary, so a nonconforming C^1 continuity finite element is used [Specht 1988; Cho and Parmerter 1994; Oh and Cho 2004; Oh et al. 2008].

In the present study, the thermomechanical surface parameters τ_0, λ_0, μ_0, and Θ are determined by fitting them into the results of MD simulations. The detailed procedure is given in the next section. Once these parameters are determined, the thermomechanical behavior of the nanofilm can be easily analyzed by the present finite element for various thermal and mechanical loading cases.

The geometry and coordinates for the triangular element are shown in Figure 2. For this bending element, the nodal displacement vector $\vec{d}$ is

$$\vec{d}^T = \{w_i, \theta_{xi}, \theta_{yi}\}, \quad (25)$$

where $\theta_{xi} = w_{,y}$ and $\theta_{yi} = -w_{,x}$. The primary unknowns are expressed in terms of nodal variables and shape functions as

$$w = \sum_{i=1}^{3} w_i N_i + \theta_{xi} N_{xi} + \theta_{yi} N_{yi}, \quad (26)$$

where the shape functions N_i, N_{xi}, and N_{yi}, for $i = 1, 2, 3$, can be written as

$$N_i = n_{3i-2}, \qquad N_{xi} = n_{3i-1}, \qquad N_{yi} = n_{3i}.$$

The basis of shape functions in the area coordinate system is given by

$$n_a = \sum_{a=1}^{9} Z_{ar}^{-1} z_r, \qquad a = 1, 2, \ldots, 9, \tag{27}$$

where

$$
\begin{aligned}
&z_1 = L_1, &&z_2 = L_2, &&z_3 = L_3, \\
&z_4 = L_1 L_2, &&z_5 = L_2 L_3, &&z_6 = L_3 L_1, \\
&z_7 = L_1^2 L_2 + \tfrac{1}{2} L_1 L_2 L_3 \big(3(1-\mu_3)L_1 - (1+3\mu_3)L_2 + (1+3\mu_3)L_3\big), \\
&z_8 = L_2^2 L_3 + \tfrac{1}{2} L_1 L_2 L_3 \big(3(1-\mu_1)L_2 - (1+3\mu_1)L_3 + (1+3\mu_1)L_1\big), \\
&z_9 = L_3^2 L_1 + \tfrac{1}{2} L_1 L_2 L_3 \big(3(1-\mu_2)L_3 - (1+3\mu_2)L_1 + (1+3\mu_2)L_2\big),
\end{aligned}
\tag{28}
$$

with

$$\mu_1 = \frac{l_3^2 - l_2^2}{l_1^2}, \qquad \mu_2 = \frac{l_1^2 - l_3^2}{l_2^2}, \qquad \mu_3 = \frac{l_2^2 - l_1^2}{l_3^2} \tag{29}$$

(recall from Figure 2 that l_1, l_2, and l_3 are the triangle side lengths), and where the inverse transformation matrix is given by

$$Z_{ar}^{-1} = \begin{bmatrix}
1 & 0 & 0 & -1 & 0 & 1 & 2 & 0 & -2 \\
0 & 0 & 0 & 0 & 0 & a_{12} & -a_{13} & 0 & -a_{12} \\
0 & 0 & 0 & 0 & 0 & a_{22} & -a_{23} & 0 & -a_{22} \\
0 & 1 & 0 & 1 & -1 & 0 & -2 & 2 & 0 \\
0 & 0 & 0 & a_{13} & 0 & 0 & -a_{13} & -a_{11} & 0 \\
0 & 0 & 0 & a_{23} & 0 & 0 & -a_{23} & -a_{21} & 0 \\
0 & 0 & 1 & 0 & 1 & -1 & 0 & -2 & 2 \\
0 & 0 & 0 & 0 & a_{11} & 0 & 0 & -a_{11} & -a_{12} \\
0 & 0 & 0 & 0 & a_{21} & 0 & 0 & -a_{21} & -a_{22}
\end{bmatrix}, \tag{30}$$
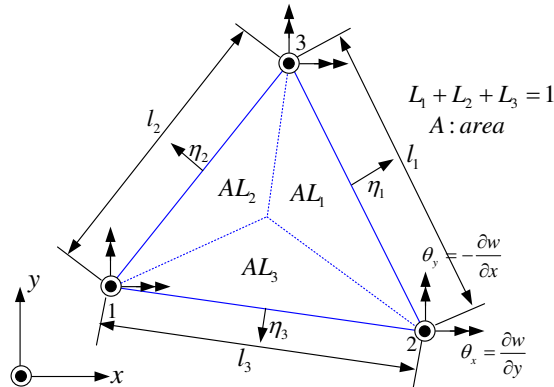
Figure 2. Geometry and coordinates for plate bending element with nine degrees of freedom.

with

$$[a_{ij}] = \left[2A\frac{\partial L_j}{\partial x_i}\right] = \begin{bmatrix} y_2 - y_3 & y_3 - y_1 & y_1 - y_2 \\ x_3 - x_2 & x_1 - x_3 & x_2 - x_1 \end{bmatrix}.$$

The determination of z_7, z_8, and z_9 is based on the following considerations. From the boundary conditions, the energy associated with interelement jumps can be written

$$\Delta U_{\Gamma_s} = \int_{\Gamma_s} M_{nn}^* \Delta\left(\frac{\partial w}{\partial n}\right) d\Gamma + \int_{\Gamma_s} M_{ns}^* \Delta\left(\frac{\partial w}{\partial s}\right) d\Gamma. \tag{31}$$

Physically, there should be no energy associated with these interelement discontinuities; so we set both terms of (31) to zero.

Since $w(s)$ is uniquely determined from the two node data, $\Delta w_{,s}$ is equal to zero. For a constant state of bending moments, the following condition should be required to pass the bending patch test:

$$M_{nn}^* \int_{\Gamma_s} \Delta\left(\frac{\partial w}{\partial n}\right) d\Gamma = 0. \tag{32}$$

Thus the quadric polynomials z_7, z_8, and z_9 are determined to satisfy (32). The transformation matrix Z_{ar} is regular for an arbitrary geometry of the triangle.

As is seen above, each of the constitutive matrices for the membrane and bending components contains the surface parameters which represent the surface effects. The membrane and bending stiffness matrices, which are required for the finite element implementation, can be expressed as follows from (21):

$$\boldsymbol{K}_m = \int_\Omega \boldsymbol{B}_m^T \boldsymbol{C}_m \boldsymbol{B}_m \, dA, \qquad \boldsymbol{K}_b = \int_\Omega \boldsymbol{B}_b^T \boldsymbol{C}_b \boldsymbol{B}_b \, dA. \tag{33}$$

4. Molecular dynamics simulations

Determination of surface parameters. The accuracy of the solution obtained from the finite element analysis based on the continuum model, which considers surface effects, is dependent on the reliability of the surface parameters τ_0, μ_0, and λ_0.

Generally, these parameter values can be provided by experiments or MD simulations. In this study, the necessary surface parameters are obtained from MD simulations with open source code [LAMMPS 2008].

Figure 3 shows the configuration of the unit cell of copper thin film. The periodic boundary conditions are applied along the x_1 and x_2 directions, and the free boundary condition is applied in the x_3 direction. The dimensions of the unit cell are about 20 nm for the x_1 and x_2 directions, and 4.3 nm in the x_3
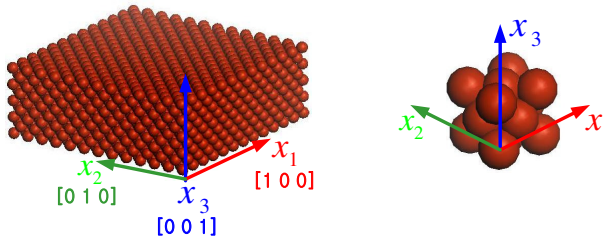
Figure 3. Molecular dynamics simulation model for copper thin film with (100) surface.

direction. The simulation temperature is 0.1 K. The surface crystallographic orientation of the unit cell is the (100). The simulation cell size to get the bulk properties of copper is about 20 nm in all directions and the simulation cell satisfies the periodic boundary conditions in the x_1 [100], x_2 [010] and x_3 [010] directions respectively. The surface parameter values (τ_0, μ_0, and λ_0) are provided by MD simulations with the embedded atom method potential for the copper thin film. To determine the surface stress, energy minimization is performed for the atoms at the surface to obtain their equilibrium positions. The simulation cell, shown in Figure 3, is then strained to calculate the total energy. The total energy of the thin film consists of the strain energy in the bulk and on the surface; therefore, the surface energy must be extracted from the total energy. If the area of the surface is defined as A ($= dx_1 dx_2$), the total energy can be expressed as a function of strain [Shenoy 2005]: $E_{\text{total}} = E_{\text{surface}} + E_{\text{bulk}} = 2AE_s(\varepsilon) + hAE_b(\varepsilon)$, where $E_s(\varepsilon)$ and $E_b(\varepsilon)$ are the surface energy and bulk energy, respectively. The total energy is linear with respect to the thickness h of the thin film. Therefore, the linear fit, which is made with the E_{total} and h data, can give the surface energy. Once the total surface energy is obtained, the surface stress can be obtained from the definition of surface stress: $\tau_{ij}^0 = 1/A(\partial E_{\text{surface}}/\partial \varepsilon_{ij})_{\varepsilon=0}$ [Haiss 2001]. The obtained surface residual tension for copper with a (100) surface is $\tau_0 = 1.0398$ N/m.

The MD simulation is performed as well and two elastic constants (C_{11} and C_{12}) can be obtained. A thin film with (100) surface orientation has the same directional properties in the x_1 [100] and x_2 [010] directions. Therefore, it is possible to calculate both C_{11} and C_{22} just with one simulation because the thin film structure has the same C_{11} and C_{22} components in this orientation. But, the thin film with (110) surface orientation has different directional properties along the [100] and [110] directions. So, the values of C_{11} and C_{22} are different from each other. Two times the strain tests with respect to ε_{11} and ε_{22} are required to calculate C_{11}, C_{22}, and C_{12} respectively. The simulation cell is strained along the x_1 direction, that is, ε_{11} has a specific value while constraining the deformation along the x_2 direction ($\varepsilon_{22} = 0$). The correlation between components of the constitutive matrix for the membrane part of the finite element model (see (18)) and the corresponding two elastic constants from the MD simulations yield the equations

$$C_{11} = \frac{Eh}{1-\nu^2} + 4\mu_0 + 2\lambda_0, \qquad C_{12} = \frac{E\nu h}{1-\nu^2} + 2\lambda_0 + 2\tau_0. \tag{34}$$

Here all variables except μ_0 and λ_0 are already known, so the two unknown surface constants are easily determined to be $\mu_0 = -8.755$ N/m and $\lambda_0 = 15.843$ N/m at the matching point. The surface parameter values do not vary significantly as shown in Table 1 for the films with different thicknesses. Here, the surface residual tension is assumed to be constant as mentioned above.

thickness (Å)	τ_0	μ_0	λ_0
14.72	1.0398	−8.571	15.432
29.25	1.0398	−8.643	15.638
43.75	1.0398	−8.755	15.843

Table 1. Surface parameter values.

After the three surface constants are determined, the surface thermal constant is also obtained from the results of the MD simulations. The temperature is increased from 0 K to 500 K, and the thermal strains are calculated at every 100 K increment during the simulations.

A certain amount of deviation in the results cannot be avoided due to the nature of MD simulations; this deviation tends to be larger as the temperature increases. This is the reason why MD simulations are usually performed several times and averaged values taken. Here, the average of thermal strain can be considered to be uniform in a relatively low temperature range as shown in the graph (the black solid line in Figure 4a). Consequently, the averaged strain values are obtained as $u_{1,1} = 0.001291$ and $u_{2,2} = 0.001268$ (see Table 2). From the constitutive relation about the membrane components described in (16), we obtain the following relation:

$$N_{11}^* = 2\tau_0 - \left(\frac{Eh\alpha}{1-\nu} + 2\Theta\right)\Delta T_1 + \left(\frac{Eh}{1-\nu^2} + 4\mu_0 + 2\lambda_0\right)u_{1,1} + \left(\frac{E\nu h}{1-\nu^2} + 2\lambda_0 + 2\tau_0\right)u_{2,2}. \qquad (35)$$

Here, because N_{11}^* is zero due to the stress free condition and all other variables are known except the surface thermal constant (Θ), the surface thermal constant is determined to be $\Theta = -3.216 \times 10^{-4}$. A more detailed procedure for finding the equilibrium state and straining process can be found in the next section.

We could also observe an almost constant coefficient of thermal expansion (CTE) of the copper thin film in the temperature range lower than 500 K from the MD simulations in Figure 4b. It is thus reasonable to use the proposed model in the smaller temperature range assuming small temperature variance.

Modulus computations of copper thin film with thickness variations. The mechanical properties of thin films with different thicknesses, such as the Young's modulus, the shear modulus, and the Poisson's ratio, are provided by the MD simulations and compared with the FEM results. In this study, we consider two configurations: (100) surface orientation and [100] loading direction ((100)/[100]) and (100) surface orientation and [110] loading direction ((100)/[110]). Figure 6 shows the simulation configurations and coordinate systems. The simulation conditions are basically the same as those explained in the previous section except for thickness variations.

We have five simulation models for the thin film with different thicknesses:

$$h = 14.64, 29.11, 43.62, 58.23, 115.98 \, (\text{Å}).$$

The first step of MD simulation is to find the equilibrium states of the simulation cells. To this end, the NPT ensemble (the number of atoms, pressure, and temperature of the system will remain

| Temp. (K)	$\varepsilon_{11}(u_{1,1})$	$\varepsilon_{22}(u_{2,2})$
100	0.001252	0.001281
200	0.001257	0.001234
300	0.001402	0.001228
400	0.001079	0.001421
500	0.001466	0.001178
Avg.	0.001291	0.001268

Table 2. Strains caused by temperature change.
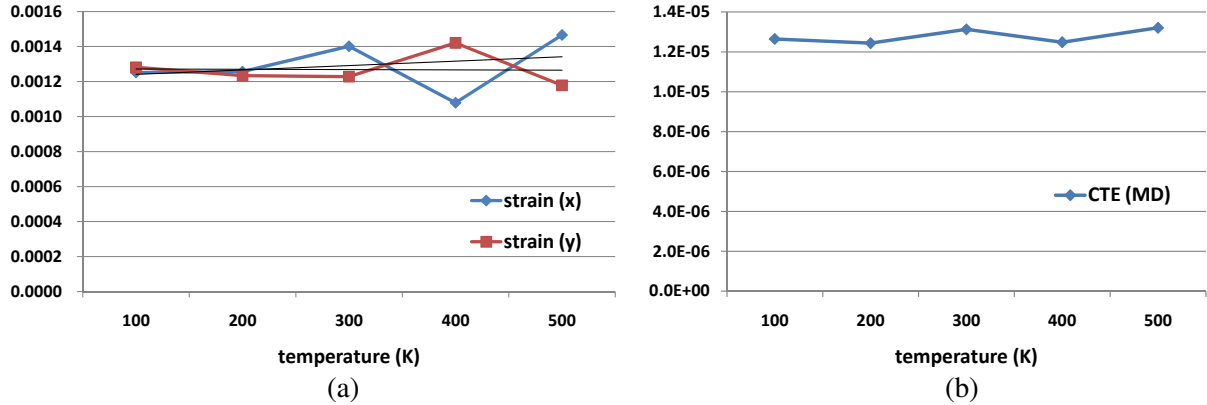
Figure 4. Strain variance (a) and CTE variance (b) where the simulation cell thickness is 3.62 nm (matching point).
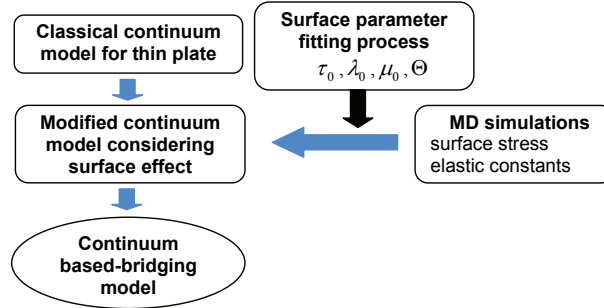
Figure 5. Overall process of continuum based-bridging model development.
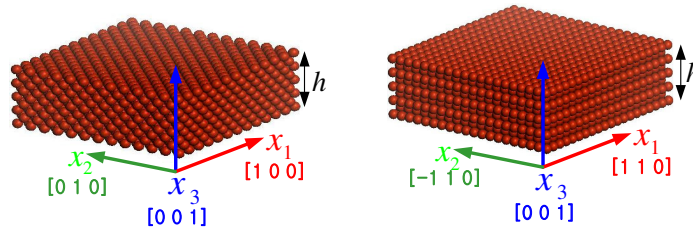
Figure 6. MD simulation model for the copper thin film: under (100)/[100] configuration (left) and (100)/[110] configuration (right).

constant) is adopted and we set the initial conditions of temperature, pressure, and lattice constant (a_0) as $T = 0.1$ K, $P = 0$ bar, and $a_0 = 0.362$ nm, respectively. As mentioned in the previous section, the simulation cell boundary lateral surfaces satisfy periodic boundary conditions and the bounding surface in the x_3 direction is free. MD simulation up to 100 ps is performed with the NPT ensemble to get the equilibrium state, followed by the NVT ensemble (where the number of atoms, volume, and temperature of the system will remain constant) for 50 ps to obtain the initial stresses. Then the simulation cell is strained as $\varepsilon = 0.01$ for 100 ps in each step and the averaged stress is calculated under the equilibrium

state. Finally, the mechanical properties of the thin film are computed based on the obtained stress and strain relation. The simulation results are given in the following chapter for both thin film configurations.

5. Numerical examples

Mechanical properties: Young's modulus, shear modulus, and Poisson's ratio. The elastic properties of thin film can be different with respect to the surface orientation and loading direction. In this study, the elastic properties are obtained from FEM simulation and compared with MD simulation results under two configurations as mentioned in the previous chapter.

A tensile test for the Cu thin film is performed to compute the Young's modulus and Poisson's ratio with the proposed FEM based on continuum theory considering surface effects. The pure shear test is also carried out to compute the shear modulus. As explained in the previous section, the surface parameter values are obtained from the MD simulations when the thickness of the copper thin film is about 43 Å, that is, this is the matching point between the finite element model and the MD simulations. If the necessary surface parameters are determined at this point, we do not need to do any more MD simulations about the thin film with other thickness dimensions to determine surface parameters. This means that the suggested continuum model does not require excessive computing time and can give us the mechanical response of the thin film in a very short period of time. The rest of the moduli of the thin film with different thicknesses can be calculated by the continuum based-finite element model with the fitted surface parameter values.

In each simulation, 200 finite elements are used as depicted in Figure 7, which also represents the deformed configuration of the thin film model due to surface effects only. When there are no externally applied forces, the thin film with positive surface stress shrinks to be in a relaxed state. As is shown in the left part of Figure 8, the modulus of the thin film with (100) surface and [100] loading direction is smaller than that of the bulk material by 23% when the thickness is about 14 Å. However, the modulus
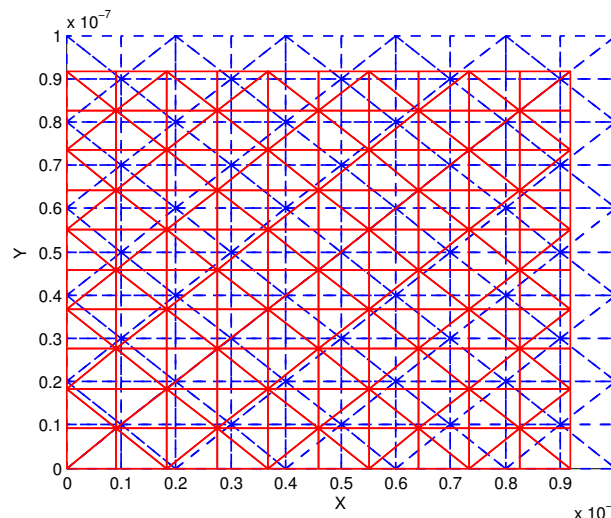
Figure 7. Initial finite element mesh configuration (blue dashed line) and relaxation due to surface effects only (red solid line).
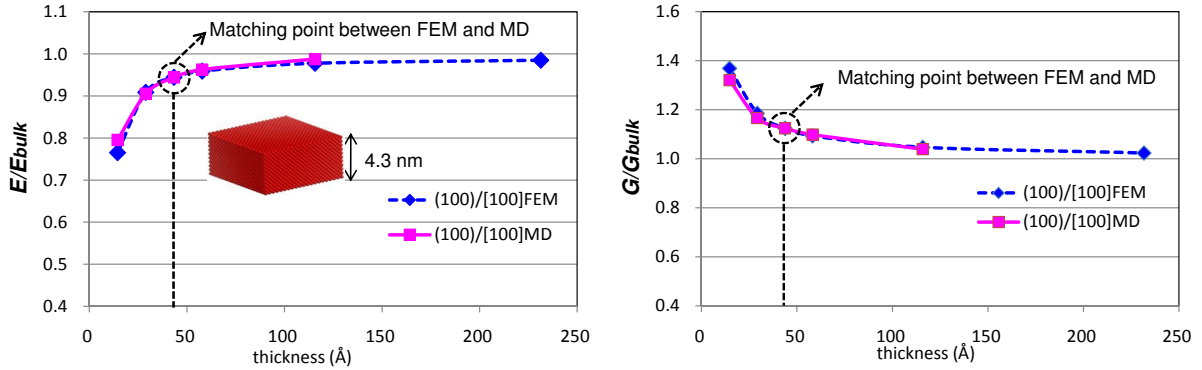
Figure 8. Young's modulus (left) and shear modulus (right) of a copper thin film with (100) surface, and under [100] loading.

converges to the bulk counterpart as the thickness increases. The moduli calculated by the FEM agree well with the results from the MD simulation. This softening phenomenon can be explained by the atomic coordination. The atomic coordination is low on the surfaces compared to the bulk and the modulus tends to be softer. From MD simulations, the elastic constant of a surface with the (100)/[100] configuration is negative due to the bond loss. Considering that total stiffness is equal to bulk stiffness plus surface stiffness, negative surface stiffness causes the overall stiffness of thin film to be smaller than the bulk counterpart. Moreover, this effect becomes more dominant as the thickness gets smaller as shown in Figure 8, left. Similar phenomena have also been observed by other researchers [Miller and Shenoy 2000; Gao et al. 2006]. The bulk Young's modulus (E) of a single crystal structured copper, which is used in this study, is about 62.09 GPa and the bulk shear modulus (G) is 76.46 GPa. The Poisson's ratio (ν) is 0.424. These values are obtained by MD simulation for the bulk copper material and are very close to the reference values [Simmons and Wang 1971].

Figure 8, right, compares the shear moduli predicted by the FEM and MD calculations. Unlike the Young's modulus, the shear modulus is larger for thin films that its bulk value, and it converges to its bulk counterpart as the thickness increases. To our knowledge, the literature does not so far contain predictions of shear modulus for a thin film. The shear modulus is calculated by the relation $\tau = G\gamma$ where τ, G, and γ are the virial stress, shear modulus, and engineering shear strain. The MD simulation is carried out in the shear strained unit cell configuration. Virial stress is obtained as a result of the MD simulation, and increases as the thickness gets smaller, because the pairwise interaction forces between atoms increase due to the contraction effect caused by surface stress.

The results of the Poisson's ratio of a copper thin film with (100) surface are plotted in Figure 9. For a thin film under [100] loading direction, the Poisson's ratio becomes larger than the bulk counterpart when the thickness gets smaller. The Poisson's ratio is defined as $\nu = -\varepsilon_{yy}/\varepsilon_{xx}$, where ε_{xx} and ε_{yy} are the strains along the x and y directions. In the case of a thin film with the (100)/[100] configuration, greater contraction in the y direction and less extension in the x direction are observed due to positive surface stress, because a thin film with positive surface stress shrinks in a relaxed state. Therefore, when the thickness of the thin film is smaller, a larger Poisson's ratio is observed. The results of the FEM agree with those of the MD simulations.

h (Å)	MD			FEM		
	C_{11}, C_{22}	C_{12}	C_{66}	C_{11}, C_{22}	C_{12}	C_{66}
14.64	99.59	70.70	100.98	100.68	73.16	106.77
29.11	87.63	52.48	89.18	87.99	52.72	91.18
43.62	83.73	45.86	85.95	83.73	45.86	85.95
58.23	81.11	41.60	84.01	81.60	42.42	83.33
115.98	77.52	35.44	79.46	78.38	37.24	79.38

**Table 3.** Elastic constants of single crystal copper thin film with (100) surface orientation and [100] loading direction.

In this study, we consider a face centered cubic (FCC) material which has cubic symmetry. The elastic deformation of this material can be represented by the three constants C_{11}, C_{12}, and C_{66} in the Voigt notation. These elastic constants of a single crystal copper thin film with (100) surface orientation and [100] loading direction are computed by MD simulations and FEM according to the change in the thickness and are tabulated in Table 3. The corresponding elastic constants from the MD simulation and FEM are almost the same.

For a thin film under the (100)/[110] configuration, the stiffness of the thin film can be regarded as a 45° rotation of the (100)/[100] thin film configuration, as depicted in Figure 10. So it is expected that the elastic constants from MD simulations about the (100)/[110] configuration would be the same as those computed by using the elastic constants of the (100)/[100] thin film configuration through the stiffness transformation relationship between the two configurations [Tsai and Hahn 1980].

The MD simulation for copper thin film with the (100)/[110] configuration is performed and elastic constants are obtained (MD (I)). These are compared with the transformed elastic constants (MD (II)) of the thin film with the (100)/[100] configuration in Table 4. The corresponding quantities are similar
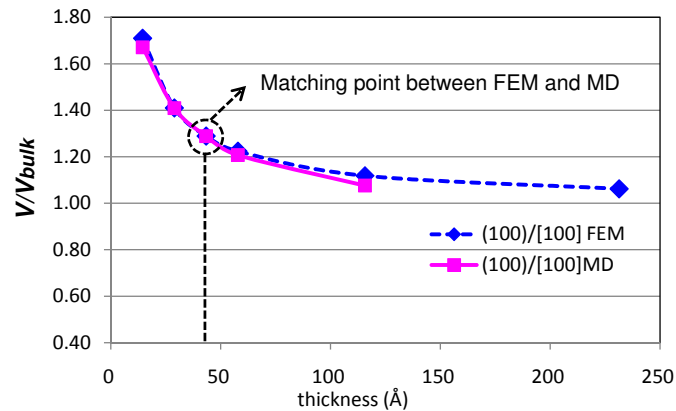
Figure 9. Poisson's ratio of a copper thin film with (100) surface and under [100] loading direction, where a dotted circle indicates the matching point between the result of the FEM and that of the MD simulations.

h (Å)	MD (I)			MD (II)			FEM		
	C_{11}, C_{22}	C_{12}	C_{66}	C_{11}, C_{22}	C_{12}	C_{66}	$C_{11} C_{22}$	C_{12}	C_{66}
14.64	179.11	−17.70	14.65	186.12	−15.83	14.44	193.69	−19.84	13.76
29.11	153.39	−20.19	17.91	159.24	−19.12	17.57	161.54	−20.83	17.64
43.62	145.46	−20.87	18.57	150.74	−21.15	18.94	150.74	−21.15	18.94
58.23	143.35	−21.20	19.12	145.36	−22.65	19.75	145.34	−21.32	19.59
115.98	134.57	−22.10	20.61	135.93	−22.98	21.04	137.19	−21.57	20.57

Table 4. Elastic constants of single crystal copper thin film with (100) surface orientation and [110] loading direction.

to each other and the elastic constants obtained by FEM are also close to both the MD (I) and MD (II) simulation results in the thin film with different thicknesses.

The comparison of the Young's modulus and shear modulus of thin film with (100) surface orientation and [110] loading direction between the MD simulations and FEM is shown in Figure 11. But the trend of variations of the Young's modulus and shear modulus is opposite to those of the thin film with the (100)/[100] configuration. Especially for the Young's modulus, the modulus gets larger than bulk counterpart as the thickness becomes smaller. FEM results also show good agreement with those of the MD simulations.

From the results shown above, there is an obvious size effect for mechanical properties of nanosized thin film with thickness variations. In addition, the mechanical properties for a single crystal structure are strongly dependent on the loading directions.

Bending rigidity and the coefficient of thermal expansion. The surface effects are also introduced in bending as an additional force. The flexural rigidity of the bulk thin plate is $D_b = \frac{1}{12} E h^3 / (1 - \nu^2)$ and the flexural rigidity of thin film is $D_f = \frac{1}{12} E h^3 / (1 - \nu^2) + \frac{1}{2} h^2 (2\mu_0 + \lambda_0)$, while the nondimensional flexural rigidity is plotted in Figure 12. The quantity $(D_f - D_b)/D_b$ for the thin film with the (100)/[100] configuration becomes small with decreasing thickness because negative surface stiffness also softens the flexural rigidity. But it tends to converge in the opposite way in the case of the thin film with the (100)/[110] configuration. Figure 13 shows the comparison of the CTE from the FEM and MD simulations. The bulk value of the CTE is obtained as 1.65×10^{-5}/K from the MD simulations, which is
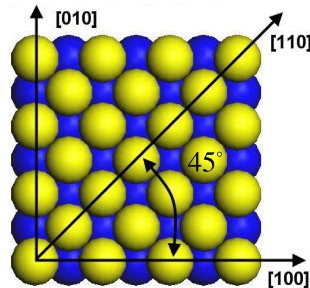
Figure 10. Top view of the (100) surface of FCC copper thin film.
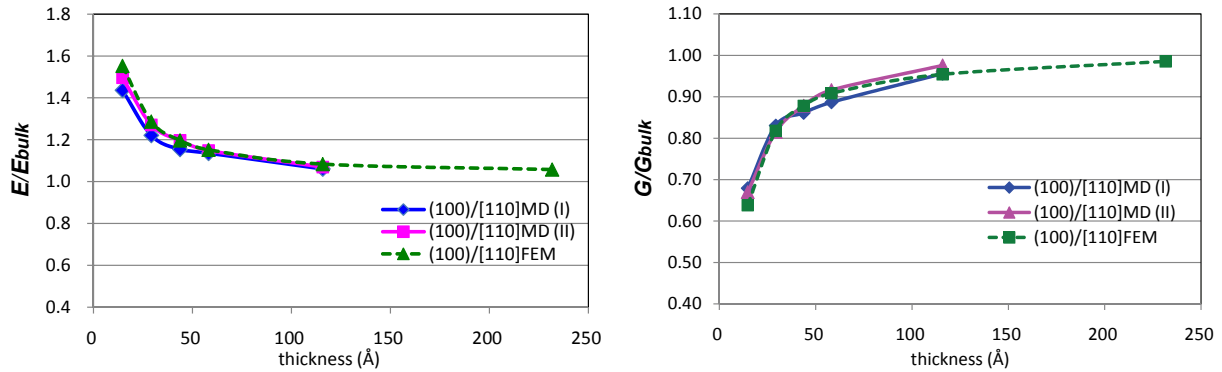
Figure 11. Young's modulus of a copper thin film (left) and shear modulus with (100) surface and under [110] loading direction (right).
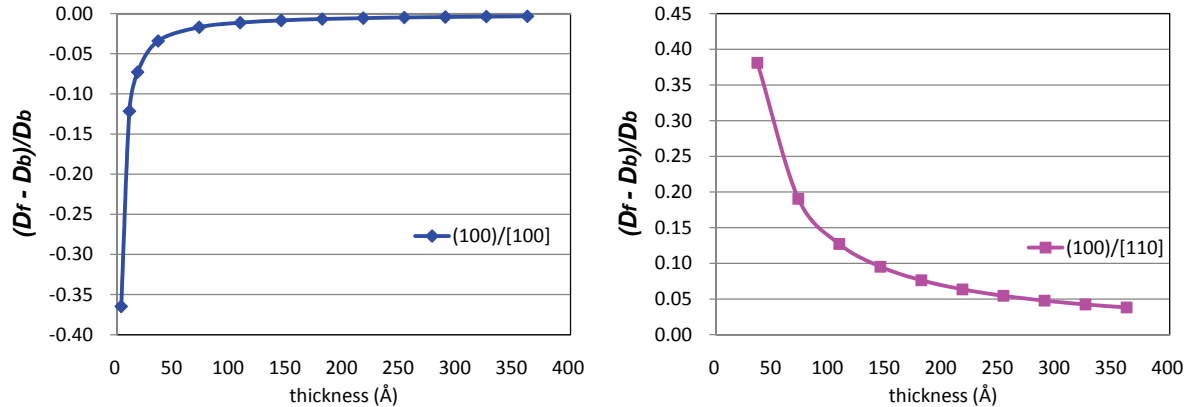

Figure 12. Nondimensional flexural rigidity: copper thin film with (100)/[100] configuration (left) and copper thin film with (100)/[110] configuration (right).

almost the same as the reference value [Shackelford and Alexander 2000]. The CTE of a copper thin film with (100) surface decreases as the thickness of the film decreases [Pathak and Shenoy 2005]. Generally, the change in the film area with temperature can be written as $\Delta A / A_0 = \alpha \Delta T$, where ΔA is the change of area, A_0 is the initial area, and α is the CTE. Temperature rise usually expands the size of the thin film. But when the thickness gets smaller, the role of surface stress becomes more prominent and the positive surface stress tends to shrink the thin film. Therefore, the area of the film is decreased and the CTE of the thin film becomes smaller than that of the bulk. For a thin film with FCC (100) surface orientation, it exhibits in-plane symmetry so that the CTE does not change with respect to the directions.

Buckling analysis. To investigate how the surface effect affects the buckling behavior of the nano thin film, the buckling analysis is carried out for free standing copper thin film.

For a thin film, the strain energy subjected to in-plane forces can be written as $U = U_b + U_s$, where U_b is the strain energy due to the bending including surface effects and U_s is the strain energy due to the
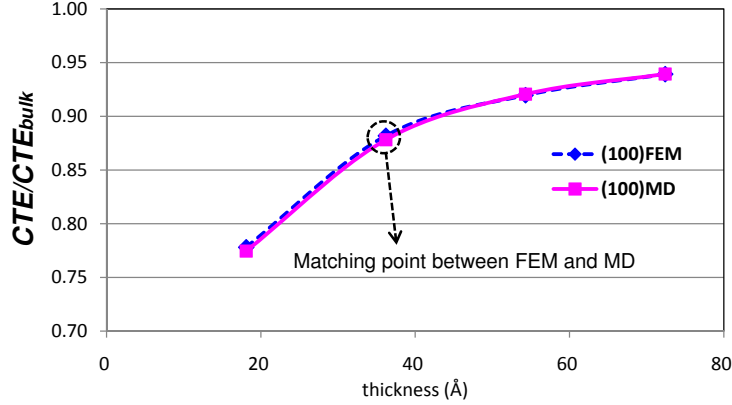
Figure 13. CTE of a copper thin film with a (100) surface. $(\text{CTE}_{\text{bulk}}(\alpha_{\text{bulk}}) = 1.65 \times 10^{-5} /\text{K})$.

in-plane forces, given by [Abbas and Thomas 1977]

$$U_s = \frac{1}{2} \int_\Omega \left[N_{11} \left(\frac{\partial w}{\partial x_1} \right)^2 + N_{22} \left(\frac{\partial w}{\partial x_2} \right)^2 + 2 N_{12} \left(\frac{\partial w}{\partial x_1} \right) \left(\frac{\partial w}{\partial x_2} \right) \right] dA, \qquad N_{\alpha\beta} = \int_{-h/2}^{h/2} \sigma_{\alpha\beta} \, dz, \quad (36)$$

or, in matrix form,

$$U_s = \frac{1}{2} \int_\Omega \begin{bmatrix} \frac{\partial w}{\partial x_1} & \frac{\partial w}{\partial x_2} \end{bmatrix} \begin{bmatrix} N_{11} & N_{12} \\ N_{12} & N_{22} \end{bmatrix} \begin{bmatrix} \frac{\partial w}{\partial x_1} \\ \frac{\partial w}{\partial x_2} \end{bmatrix} dA. \tag{37}$$

By using the derivative of the lateral displacement w given in (20), we have

$$U_s = \frac{1}{2} \int_\Omega \{\vec{d}\}^T \boldsymbol{B}^T [N] \boldsymbol{B} \{\vec{d}\} \, dA. \tag{38}$$

The differentiation in (38) with respect to the nodal displacements gives a geometric stiffness:

$$[\boldsymbol{K}_s] = \int_\Omega \boldsymbol{B}^T [N] \boldsymbol{B} \, dA. \tag{39}$$

We assemble the element matrices to get the static stability matrix equation

$$([\boldsymbol{K}_b] - \lambda [\boldsymbol{K}_s]) \{\vec{d}\} = 0, \tag{40}$$

where λ is the buckling load. Equation (40) was solved for a thin film structure with simply supported boundary conditions, and the results are shown in Figure 14. For copper thin film with a (100) surface orientation, the buckling parameter $K = N^* b^2 / (\pi^2 D)$ of the film becomes smaller as the thickness decreases, due to surface effects. The surface effects do not change the fundamental buckling mode shape, shown in Figure 15. As the thickness increases, the buckling parameter value converges to the bulk value obtained by ignoring surface effects.

The buckling of a thin film with high aspect ratio $(a/b = 10)$ was considered next, and the results are shown in Figure 16. All edges are clamped in the left half of the figure and simply supported the right half. Again, there is no change in fundamental buckling mode shape due to the surface effects, but the

buckling parameter values of the thin film considering surface effects are lower than those of the bulk when the thickness becomes smaller, as shown in Figures 14 and 16.

The postbuckling behavior of the nano thin film is quite different from that of the proposed continuum plate behavior with the size effect. The atomistic potential behavior is totally different from the continuum linear elastic behavior because the atomic behavior includes the highly geometric nonlinear effect as well as the inelastic effects such as twining and slip. However, the onset of instability can be reasonably well described by the linear elastic buckling analysis. Thus the linear buckling analysis of nanoscale thin films can provide a guideline for the onset of structural instability.

6. Conclusions

In this study, a continuum model considering of the surface effects of thin film is suggested and a finite element formulation is also implemented. Because this continuum model is properly modified for nano sized thin film by adding the surface energy contribution to the classical thin plate theory in the
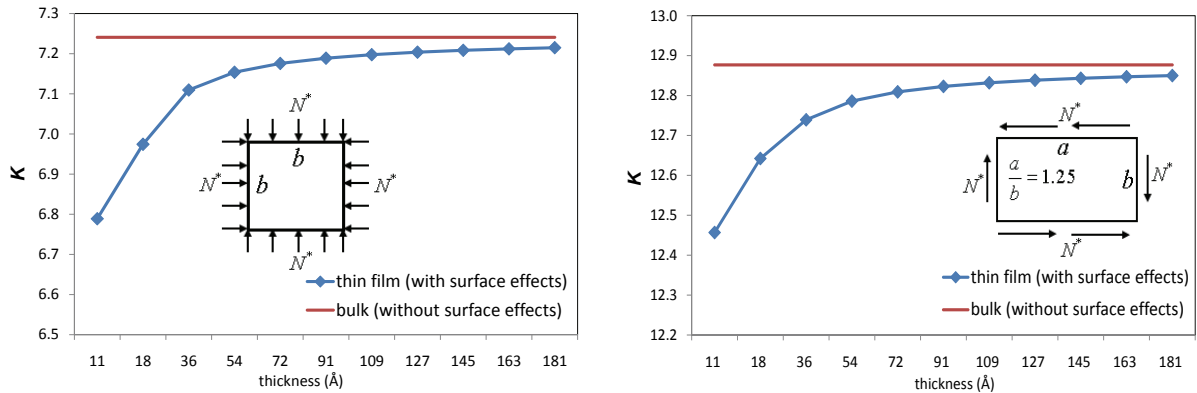
Figure 14. Buckling parameter K for a roughly square copper thin film with a (100) surface is clamped on all edges and compressed biaxially (left), or simply supported on all edges and subjected to pure shear (right).
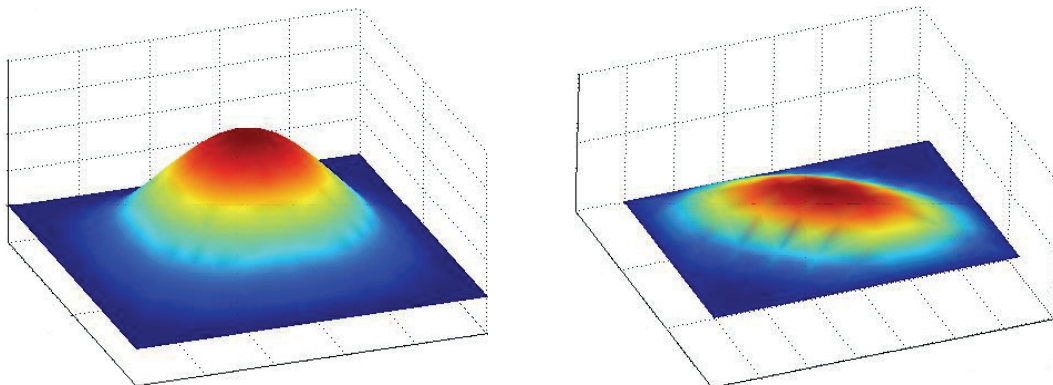
Figure 15. Shape of fundamental buckling mode for the experiments of Figure 14.
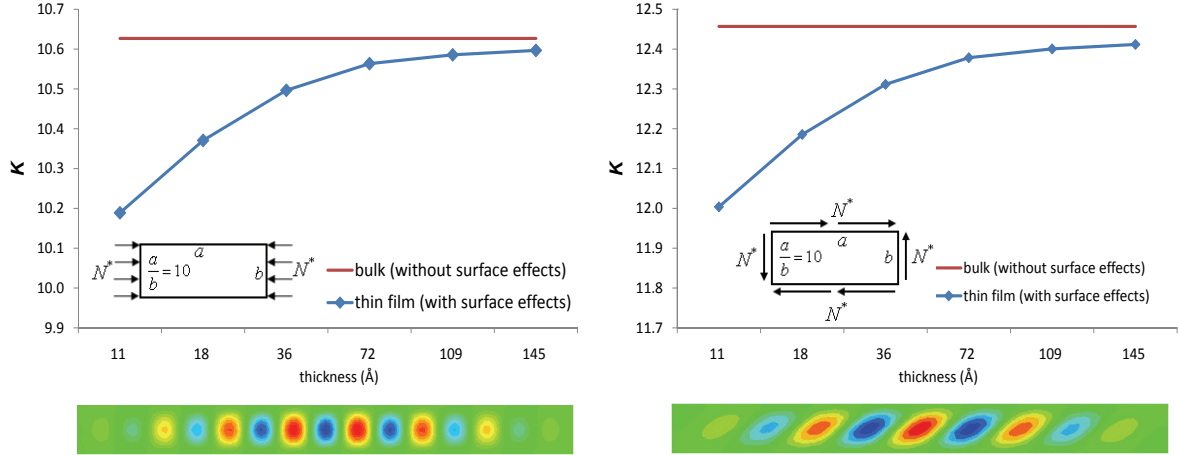
Figure 16. A strip of copper thin film with a (100) surface is clamped on all edges and compressed uniaxially (left), or alternatively simply supported on all edges and subjected to pure shear (right). Top: buckling parameters; bottom: shape of fundamental buckling mode.

macroscale, it can represent the dominant surface effects which should be considered in nanoscale thin film structures.

The suggested continuum model should serve as a useful alternative method to overcome the limitations of conventional molecular dynamics (MD) simulations, such as excessive required computing resources and time. The proposed continuum model can also be used when we need to carry out the design modification and analysis process repeatedly for practical applications in the mesoscale range. To accurately predict the properties of thin film structures, reliable material constants of its bulk and surface should be known. Therefore, precise measurement techniques and MD simulation methods are essential factors. The thermomechanical responses of the thin film with other surface orientations will be addressed in future.

Appendix: Equilibrium equations and boundary conditions

The principle of virtual work states that the stress, body force, and traction are in equilibrium if and only if the internal virtual work equals the external virtual work for every virtual displacement field. Therefore, the following equation can be derived by applying integration by parts and the divergence theorem to obtain the equilibrium equations from (10):

$$\delta\Pi = \int_{\Omega} -(N_{\alpha\beta,\beta} + \tau^{+}_{\alpha\beta,\beta} + \tau^{-}_{\alpha\beta,\beta})\,\delta u^{o}_{\alpha} - \left\{ M_{\alpha\beta,\alpha\beta} + \frac{h}{2}(\tau^{+}_{\alpha\beta,\alpha\beta} - \tau^{-}_{\alpha\beta,\alpha\beta}) \right\}\delta w$$
$$- (\tau^{+}_{\alpha3,\alpha} + \tau^{-}_{\alpha3,\alpha})\,\delta w - p_{\alpha}\,\delta u^{o}_{\alpha} - p_{3}\,\delta w\, dA + \text{Boundary Conditions.} \quad \text{(A.1)}$$

The boundary terms are summarized as the following. First, the boundary conditions of the bulk part are considered:

$$\delta U^{\text{boundary}}_{\text{bulk}} = \int_{\partial S} N_{\alpha\beta}n_{\beta}\,\delta u^{0}_{\alpha} + M_{\alpha\beta,\beta}n_{\beta}\,\delta w - M_{\alpha\beta}n_{\beta}\,\delta w,_{\alpha}\, dS. \quad \text{(A.2)}$$

The boundary conditions are usually expressed in terms of directions that are normal and tangent to the boundaries. Therefore, the derivatives of w in Cartesian coordinates can be represented in terms of derivatives in the normal direction ($\partial w/\partial n$) and the tangent direction ($\partial w/\partial t$) of the boundary:

$$w,_\alpha = \frac{\partial w}{\partial n}n_\alpha + \frac{\partial w}{\partial t}t_\alpha. \tag{A.3}$$

Substituting (A.3) into (A.2) we obtain

$$\begin{aligned} \delta U_{\text{bulk}}^{\text{boundary}} &= \int_{\partial S} N_{\alpha\beta}n_\beta\,\delta u_\alpha^0 + M_{\alpha\beta,\beta}n_\beta\,\delta w - M_{\alpha\beta}n_\beta\,\delta w,_\alpha\ dS \\ &= \int_{\partial S} N_{\alpha\beta}n_\beta\,\delta u_\alpha^0 + M_{\alpha\beta,\beta}n_\beta\,\delta w - M_{\alpha\beta}n_\beta\,\delta\left(\frac{\partial w}{\partial n}n_\alpha + \frac{\partial w}{\partial t}t_\alpha\right) dS \\ &= \int_{\partial S} N_{\alpha\beta}n_\beta\,\delta u_\alpha^0 + M_{\alpha\beta,\beta}n_\beta\,\delta w - M_{\alpha\beta}n_\beta n_\alpha\,\delta\left(\frac{\partial w}{\partial n}\right) - M_{\alpha\beta}n_\beta t_\alpha\left(\frac{\partial w}{\partial t}\right) dS, \end{aligned} \tag{A.4}$$

where the fourth term can be changed to the following form through integration by parts:

$$\int_{\partial S} M_{\alpha\beta}n_\beta t_\alpha\left(\frac{\partial w}{\partial t}\right) dS = \left[M_{\alpha\beta}n_\beta t_\alpha\left(\frac{\partial w}{\partial t}\right)\right]_{S_1}^{S_2} - \int_{\partial S}\left(\frac{\partial M_{\alpha\beta}n_\beta t_\alpha}{\partial t}\right)\delta w\,dS. \tag{A.5}$$

If the boundary is a closed smooth curve, the start and end points are the same and the first term vanishes in above equation. Therefore, the final form of the boundary condition for the bulk part is given as

$$\delta U_{\text{bulk}}^{\text{boundary}} = \int_{\partial S} N_{\alpha\beta}n_\beta\,\delta u_\alpha^0 - M_{\alpha\beta}n_\beta n_\alpha\,\delta\left(\frac{\partial w}{\partial n}\right) + \left(\frac{\partial(M_{\alpha\beta}n_\beta t_\alpha)}{\partial t} + M_{\alpha\beta,\beta}n_\beta\right)\delta w\,dS. \tag{A.6}$$

Next, the boundary conditions about surface layers are considered:

$$\begin{aligned} \delta U_{\text{surface}}^{\text{boundary}} &= \int_{\partial S}(\tau_{\alpha\beta}^+ - \tau_{\alpha\beta}^-)n_\beta\,\delta u_\alpha^0 - \frac{h}{2}(\tau_{\alpha\beta}^+ - \tau_{\alpha\beta}^-)n_\beta\,\delta w,_\alpha \\ &\qquad\qquad + \frac{h}{2}(\tau_{\alpha\beta,\beta}^+ - \tau_{\alpha\beta,\beta}^-)n_\alpha\,\delta w + (\tau_{\alpha3}^+ + \tau_{\alpha3}^-)n_\alpha\,\delta w\,dS \\ &= \int_{\partial S}(\tau_{\alpha\beta}^+ - \tau_{\alpha\beta}^-)n_\beta\,\delta u_\alpha^0 - \frac{h}{2}(\tau_{\alpha\beta}^+ - \tau_{\alpha\beta}^-)n_\alpha n_\beta\,\delta\left(\frac{\partial w}{\partial n}\right) \\ &\qquad\qquad + \left\{\frac{h}{2}\frac{\partial(\tau_{\alpha\beta}^+ - \tau_{\alpha\beta}^-)}{\partial t}t_\alpha n_\alpha + (\tau_{\alpha3}^+ + \tau_{\alpha3}^-)n_\alpha + \frac{h}{2}(\tau_{\alpha\beta,\beta}^+ - \tau_{\alpha\beta,\beta}^-)n_\alpha\right\}\delta w\,dS. \end{aligned} \tag{A.7}$$

Finally, the boundary conditions of the bulk and surface layers are assembled to give

$$\begin{aligned} \delta U^{\text{boundary}} &= \int_{\partial S}(N_{\alpha\beta} + \tau_{\alpha\beta}^+ - \tau_{\alpha\beta}^-)n_\beta\,\delta u_\alpha^0 - \left(M_{\alpha\beta} + \frac{h}{2}(\tau_{\alpha\beta}^+ - \tau_{\alpha\beta}^-)\right)n_\beta n_\alpha\,\delta\left(\frac{\partial w}{\partial n}\right) \\ &\quad + \left\{\left(\frac{\partial M_{\alpha\beta}}{\partial t} + \frac{h}{2}\frac{\partial(\tau_{\alpha\beta}^+ - \tau_{\alpha\beta}^-)}{\partial t}\right)t_\beta + M_{\alpha\beta,\beta} + \frac{h}{2}(\tau_{\alpha\beta,\beta}^+ - \tau_{\alpha\beta,\beta}^-) + (\tau_{\alpha3}^+ + \tau_{\alpha3}^-)\right\}n_\alpha\,\delta w\,dS. \end{aligned} \tag{A.8}$$

From (A.1), the following equilibrium equations can be obtained:

$$\begin{aligned} N_{\alpha\beta,\beta} + \tau_{\alpha\beta,\beta}^+ + \tau_{\alpha\beta,\beta}^- + p_\alpha &= 0, \\ M_{\alpha\beta,\alpha\beta} + \frac{h}{2}(\tau_{\alpha\beta,\alpha\beta}^+ - \tau_{\alpha\beta,\alpha\beta}^-) + (\tau_{\alpha3,\alpha}^+ + \tau_{\alpha3,\alpha}^-) + p_3 &= 0. \end{aligned} \tag{A.9}$$

If we set $N^*_{\alpha\beta} = N_{\alpha\beta} + \tau^+_{\alpha\beta} + \tau^-_{\alpha\beta}$ and $M^*_{\alpha\beta} = M_{\alpha\beta} + \dfrac{h}{2}(\tau^+_{\alpha\beta} + \tau^-_{\alpha\beta})$, (A.9) can be simplified as

$$N^*_{\alpha\beta,\beta} + p_\alpha = 0, \qquad M^*_{\alpha\beta,\alpha\beta} + (\tau^+_{\alpha3,\alpha} + \tau^-_{\alpha3,\alpha}) + p_3 = 0. \qquad (A.10)$$

This leads to the following possibilities for the boundary conditions:

- u^0_α prescribed or $N^*_{\alpha\beta} n_\beta$ specified.

- $\dfrac{\partial w}{\partial n}$ prescribed or $M^*_{\alpha\beta} n_\alpha n_\beta$ specified.

- w prescribed or $\dfrac{\partial(M^*_{\alpha\beta} t_\beta)}{\partial t} + M^*_{\alpha\beta,\beta} + (\tau^+_{\alpha3} + \tau^-_{\alpha3})$ specified.

References

[Abbas and Thomas 1977] B. A. H. Abbas and J. Thomas, "Static stability of plates using fully conforming element", *Int. J. Numer. Methods Eng.* **11**:6 (1977), 995–1003.

[Cammarata 1994] R. C. Cammarata, "Surface and interface stress effects in thin films", *Prog. Surf. Sci* **46**:1 (1994), 1–38.

[Cammarata and Sieradzki 1989] R. C. Cammarata and K. Sieradzki, "Effects of surface stress on the elastic moduli of thin films and superlattices", *Phys. Rev. Lett.* **62**:17 (1989), 2005–2008.

[Cao and Chen 2008] G. Cao and X. Chen, "Size dependence and orientation dependence of elastic properties of ZnO nanofilms", *Int. J. Solids Struct.* **45**:13 (2008), 3821–3844.

[Cho and Parmerter 1994] M. Cho and R. Parmerter, "Finite element for composite plate bending based on efficient higher order theory", *AIAA J.* **32**:11 (1994), 2241–2248.

[Cuenot et al. 2004] S. Cuenot, C. Frétigny, S. Demoustier-Champagne, and B. Nysten, "Surface tension effect on the mechanical properties of nanomaterials measured by atomic force microscopy", *Phys. Rev. B* **69**:16 (2004), 165410.

[Dingreville et al. 2005] R. Dingreville, J. Qu, and M. Cherkaoui, "Surface free energy and its effect on the elastic behavior of nano-sized particles, wires and films", *J. Mech. Phys. Solids* **53**:8 (2005), 1827–1854.

[Gao et al. 2006] W. Gao, S. Yu, and G. Huang, "Finite element characterization of the size-dependent mechanical behaviour in nanosystems", *Nanotechnology* **17**:4 (2006), 1118–1122.

[Gurtin and Murdoch 1975a] M. E. Gurtin and A. I. Murdoch, "Addenda to our paper: a continuum theory of elastic material surfaces", *Arch. Ration. Mech. An.* **59**:4 (1975), 389–390.

[Gurtin and Murdoch 1975b] M. E. Gurtin and A. I. Murdoch, "A continuum theory of elastic material surfaces", *Arch. Ration. Mech. An.* **57**:4 (1975), 291–323.

[Gurtin and Murdoch 1978] M. E. Gurtin and A. I. Murdoch, "Surface stress in solids", *Int. J. Solids Struct.* **14**:6 (1978), 431–440.

[Haiss 2001] W. Haiss, "Surface stress of clean and adsorbate-covered solids", *Rep. Prog. Phys.* **64**:5 (2001), 591–648.

[LAMMPS 2008] S. Plimpton, P. Crozier, and A. Thompson, "LAMMPS: large-scale atomic/molecular massively parallel simulator", Sandia National Laboratories, 2008, Available at http://lammps.sandia.gov.

[Lang et al. 2006] X. Y. Lang, Y. F. Zhu, and Q. Jiang, "Size and interface effects on several kinetic and thermodynamic properties of polymer thin films", *Thin Solid Films* **515**:4 (2006), 2765–2770.

[Liang et al. 2005] H. Liang, M. Upmanyu, and H. Huang, "Size-dependent elasticity of nanowires: nonlinear effects", *Phys. Rev. B* **71**:24 (2005), 241403.

[Lim and He 2004] C. W. Lim and L. H. He, "Size-dependent nonlinear response of thin elastic films with nano-scale thickness", *Int. J. Mech. Sci.* **46**:11 (2004), 1715–1726.

[Lu et al. 2006] P. Lu, L. H. He, H. P. Lee, and C. Lu, "Thin plate theory including surface effects", *Int. J. Solids Struct.* **43**:16 (2006), 4631–4647.

[Miller and Shenoy 2000] R. E. Miller and V. B. Shenoy, "Size-dependent elastic properties of nanosized structural elements", *Nanotechnology* **11**:3 (2000), 139–147.

[Murdoch 1976] A. I. Murdoch, "A thermodynamical theory of elastic material interfaces", *Q. J. Mech. Appl. Math.* **29**:3 (1976), 245–275.

[Oh and Cho 2004] J. Oh and M. Cho, "A finite element based on cubic zig-zag plate theory for the prediction of thermo-electric-mechanical behaviors", *Int. J. Solids Struct.* **41**:5–6 (2004), 1357–1375.

[Oh et al. 2008] J. Oh, M. Cho, and J.-S. Kim, "Buckling analysis of a composite shell with multiple delaminations based on a higher order zig-zag theory", *Finite Elem. Anal. Des.* **44**:11 (2008), 675–685.

[Park and Klein 2008] H. S. Park and P. A. Klein, "Surface stress effects on the resonant properties of metal nanowires: the importance of finite deformation kinematics and the impact of the residual surface stress", *J. Mech. Phys. Solids* **56**:11 (2008), 3144–3166.

[Park et al. 2005] S. H. Park, J. S. Kim, J. H. Park, J. S. Lee, Y. K. Choi, and O. M. Kwon, "Molecular dynamics study on size-dependent elastic properties of silicon nanocantilevers", *Thin Solid Films* **492**:1–2 (2005), 285–289.

[Park et al. 2006] H. S. Park, P. A. Klein, and G. J. Wagner, "A surface Cauchy–Born model for nanoscale materials", *Int. J. Numer. Methods Eng.* **68**:10 (2006), 1072–1095.

[Pathak and Shenoy 2005] S. Pathak and V. B. Shenoy, "Size dependence of thermal expansion of nanostructures", *Phys. Rev. B* **72**:11 (2005), 113404.

[Shackelford and Alexander 2000] J. F. Shackelford and W. Alexander (editors), *CRC materials science and engineering handbook*, 3rd ed., CRC Press, Boca Raton, FL, 2000.

[Shenoy 2005] V. B. Shenoy, "Atomistic calculations of elastic properties of metallic fcc crystal surfaces", *Phys. Rev. B* **71**:9 (2005), 094104.

[Simmons and Wang 1971] G. Simmons and H. Wang, *Single crystal elastic constants and calculated aggregate properties: a handbook*, MIT Press, Cambridge, MA, 1971.

[Song and Huang 2009] F. Song and G. L. Huang, "Modeling of surface stress effects on bending behavior of nanowires: incremental deformation theory", *Phys. Lett. A* **373**:43 (2009), 3969–3973.

[Song et al. 2010] F. Song, G. L. Huang, and V. K. Varadan, "Study of wave propagation in nanowires with surface effects by using a high-order continuum theory", *Acta Mech.* **209**:1–2 (2010), 129–139.

[Specht 1988] B. Specht, "Modified shape functions for the three-node plate bending element passing the patch test", *Int. J. Numer. Methods Eng.* **26**:3 (1988), 705–715.

[Tsai and Hahn 1980] S. W. Tsai and H. T. Hahn, *Introduction to composite materials*, Technomic, Lancaster, PA, 1980.

JINBOK CHOI: jbchoi95@snu.ac.kr
WCU Program of Multiscale Mechanical Design, School of Mechanical and Aerospace Engineering, Seoul National University, San56-1, Shillim-dong, Kwanak-gu, Seoul 151-742, Republic of Korea

MAENGHYO CHO: mhcho@snu.ac.kr
WCU Program of Multiscale Mechanical Design, School of Mechanical and Aerospace Engineering, Seoul National University, San56-1, Shillim-dong, Kwanak-gu, Seoul 151-742, Republic of Korea

WONBAE KIM: wbkim@snu.ac.kr
WCU Program of Multiscale Mechanical Design, School of Mechanical and Aerospace Engineering, Seoul National University, San56-1, Shillim-dong, Kwanak-gu, Seoul 151-742, Republic of Korea

SUBMISSION GUIDELINES

ORIGINALITY

Authors may submit manuscripts in PDF format on-line. Submission of a manuscript acknowledges that the manuscript is *original and has neither previously, nor simultaneously, in whole or in part, been submitted elsewhere.* Information regarding the preparation of manuscripts is provided below. Correspondence by email is requested for convenience and speed. For further information, consult the web site at http://www.jomms.org or write to

jomms.steele@stanford.edu

LANGUAGE

Manuscripts must be in English. A brief abstract of about 150 words or less must be included. The abstract should be self-contained and not make any reference to the bibliography. Also required are keywords and subject classification for the article, and, for each author, postal address, affiliation (if appropriate), and email address if available. A home-page URL is optional.

FORMAT

Authors are encouraged to use LaTeX and the standard article class, but submissions in other varieties of TeX, and, exceptionally in other formats, are acceptable. Electronic submissions are strongly encouraged in PDF format only; after the refereeing process we will ask you to submit all source material.

REFERENCES

Bibliographical references should be listed alphabetically at the end of the paper and include the title of the article. All references in the bibliography should be cited in the text. The use of BibTeX is preferred but not required. Tags will be converted to the house format (see a current issue for examples), however, in the manuscript, the citation should be by first author's last name and year of publication, e.g. "as shown by Kramer, et al. (1994)". Links will be provided to all literature with known web locations and authors are encoraged to provide their own links on top of the ones provided by the editorial process.

FIGURES

Figures prepared electronically should be submitted in Encapsulated PostScript (EPS) or in a form that can be converted to EPS, such as GnuPlot, Maple, or Mathematica. Many drawing tools such as Adobe Illustrator and Aldus FreeHand can produce EPS output. Figures containing bitmaps should be generated at the highest possible resolution. If there is doubt whether a particular figure is in an acceptable format, the authors should check with production by sending an email to

production@mathscipub.org

Each figure should be captioned and numbered so that it can float. Small figures occupying no more than three lines of vertical space can be kept in the text ("the curve looks like this:"). It is acceptable to submit a manuscript with all figures at the end, if their placement is specified in the text by comments such as "Place Figure 1 here". The same considerations apply to tables.

WHITE SPACE

Forced line breaks or page breaks should not be inserted in the document. There is no point in your trying to optimize line and page breaks in the original manuscript. The manuscript will be reformatted to use the journal's preferred fonts and layout.

PROOFS

Page proofs will be made available to authors (or to the designated corresponding author) at a web site in PDF format. Failure to acknowledge the receipt of proofs or to return corrections within the requested deadline may cause publication to be postponed.